Search for Admixture of Scalar Top in the $t\bar{t}$ Lepton+Jets Final State at $\sqrt{s} = 1.96$ TeV

by

Su-Jung Park

Submitted in Partial Fulfillment
of the
Requirements for the Degree
Doctor of Philosophy

Supervised by
Professor Regina Demina
Department of Physics and Astronomy
The College
Arts and Sciences

University of Rochester
Rochester, New York
2007

For my parents and for my godparents

Curriculum Vitae

The author attended the Rheinische Friedrich-Wilhems-Universit¨at Bonn from 1997 to 2004, and graduated with a Diplom in Physics in 2004. She came to the University of Rochester in March 2004 and began her graduate studies in Physics. She received a doctoral fellowship from the German National Academic Foundation from June 2005 to December 2007 and a Marshak Graduate Fellowship from the Department of Physics and Astronomy at the University of Rochester from 2004 to 2006. She pursued her research in Experimental High Energy Physics under the direction of Professor Regina Demina, and moved to Fermi National Accelerator Laboratory in June 2005 for this purpose. She received the Master of Arts degree from the University of Rochester in October 2005.

Acknowledgements

Above all I would like to thank my advisor Prof. Regina Demina for her guidance, invaluable advice, and support, that made all this possible. I am also most grateful to Prof. Tom Ferbel for his insight and for improving my writing style.

I would like to thank the Rochester group at DØ, foremost Dr. Jochen Cammin and Dr. Amnon Harel for patiently answering countless questions and spending a lot of their time helping me, Dr. Michael Begel, Dr. Charly Garcia, Dr. George Ginther, Prof. Paul Slattery, and Dr. Marek Zielinski for their ideas and advice.

I thank the Top Physics group, its past and current conveners, and especially Dr. Marc-André Pleier for the continuous support of my work.

I am grateful to the Studienstiftung des deutschen Volkes for their generous financial support throughout the complete course of my studies.

Many thanks to my friends Jennifer and Jiyeon, without whom I could not have endured. I am also thankful to Jörg, Christian, Matthias, Yvonne, Björn, Alex, and the many other Germans who kept me company and ate my cakes.

Finally, I would like to thank the most important people in my life for their constant love and support: my parents, Su-In, Su-Nam, my godparents, and Olav.

Abstract

A search for pair production of scalar top (stop) quarks has been performed in the lepton+jets channel in $\approx$1 fb^{-1} of data at the DØ experiment. Kinematic differences between $\tilde{t}_1\bar{\tilde{t}}_1$ and the dominant $t\bar{t}$ process are used to separate the two reactions. For stop-quark masses of 145–175 GeV, and chargino masses of 105–135 GeV, to which the stop quarks decay ($\tilde{t}_1 \rightarrow \tilde{\chi}_1^+ b$), we obtain upper limits on the $\tilde{t}_1\bar{\tilde{t}}_1$ cross section at 95% confidence, that are a factor of $\approx$7–12 larger than expected from the Minimal Supersymmetric Standard Model (MSSM), as calculated in a next-to-leading-order (NLO) approximation in quantum chromodynamics (QCD).

Contents

Curriculum Vitae **iii**

Acknowledgements **iv**

Abstract **v**

1. Introduction **1**

2. Theory **3**

2.1. The Standard Model 3

2.2. Supersymmetry 6

2.3. The Top Quark and the Scalar Top Quark 11

2.3.1. Production 11

2.3.2. Decay 14

2.3.3. Sources of Background 19

2.3.4. Current Limits on Scalar Top-Quark Production 22

2.4. Setting Limits 23

3. Experimental Setup **26**

3.1. The Tevatron Collider 27

3.2. The DØ Detector 27

3.2.1. Central Tracking System 29

3.2.2. Calorimeter System 33
3.2.3. Muon System 39
3.2.4. Forward Proton Detector 43
3.2.5. Luminosity Monitor 43
3.2.6. Trigger System 45

4. Object Identification and Event Reconstruction 48
4.1. Track Reconstruction 48
4.2. Primary Vertex 50
4.3. Electrons 51
4.4. Muons 56
4.5. Jets 58
4.5.1. Jet Energy Scale 60
4.6. B-Jets 64
4.7. Missing Transverse Energy 66

5. Data Sample and Monte Carlo Simulation 68
5.1. Data Sample 68
5.1.1. Electron Channel 68
5.1.2. Muon Channel 70
5.2. Monte Carlo Simulation 70
5.2.1. Simulation of Signal 72
5.2.2. Simulation of Background 74

6. Search for Pair Production of Scalar Top Quarks 76
6.1. Event Selection 76
6.2. Sample Composition 83
6.2.1. Multijet Background 83
6.2.2. W+jets Background 86

6.3. Extraction of Signal 88
6.3.1. Variables for Discriminating Signal from Background 91
6.3.2. Likelihood Discriminant 95
6.3.3. Expected Limits 97
6.4. Closure Tests 101
6.5. Systematic Uncertainties 103
6.5.1. Systematic Uncertainties on Yields 104
6.5.2. Systematic Uncertainties Affecting the Shape of the Likelihood 109

7. Result and Conclusions **111**

Bibliography **117**

A. Tables of Preselection Efficiencies **128**

B. Control Plots **141**

C. Likelihood Discriminant **148**
C.1. Variables for Discriminating Signal from Background 148
C.2. Comparison of Input Variables in Data and MC 158
C.3. Likelihood Discriminant 163

D. Posterior Probabilities **168**
D.1. Expected Posterior Probabilities 168
D.2. Observed Posterior Probabilities 178

E. Results of Ensemble Tests **187**

List of Tables

2.1. Overview of particles in the MSSM. 8
2.2. Cross section for $\tilde{t}_1\bar{\tilde{t}}_1$ production at $\sqrt{s}$ =1.96 TeV for different stop-quark masses, as calculated using the PROSPINO program. 15
2.3. Branching ratios for the e+jets and μ+jets channel for the top and stop samples. 19

3.1. Test-beam results for calorimeter resolution. 39

5.1. Trigger names and integrated luminosities by version of trigger list for the e+jets channel. 69
5.2. Trigger names and integrated luminosities by version of trigger list for the μ+jets channel. 71
5.3. MSSM parameters that differ from the default values in PYTHIA. . 73
5.4. Mass points used in the analysis, with their cross section in pb, and SUSY parameters and SUSY particle masses given in GeV. 74

6.1. Exclusive preselection efficiencies and correction factors in % for all signal mass points in $\tilde{t}_1\bar{\tilde{t}}_1 \rightarrow e$+jets events, with only statistical uncertainties included. 81
6.2. Exclusive preselection efficiencies and correction factors in % for all signal mass points in $\tilde{t}_1\bar{\tilde{t}}_1 \rightarrow \mu$+jets events, with only statistical uncertainties included. 82

6.3. Expected number of signal events after all preselections for 913 pb^{-1} of data in the e+jets channel and 871 pb^{-1} in the μ+jets channel. The uncertainties are based only on those from the preselection efficiencies. 83

6.4. ε_{sig} with their statistical and systematic errors for different jet multiplicities, and ε_{QCD} with combined statistical and systematic uncertainties. 85

6.5. Normalization factor α_W for W+jets, and yields of background and data, before b-tagging in the e+jets channel. 88

6.6. Normalization factor α_W for W+jets, and yields of background and data, before b-tagging in the μ+jets channel. 89

6.7. Normalization factor α_W for W+jets, and yields of background and data, after b-tagging in the e+jets channel. 89

6.8. Normalization factor α_W for W+jets, and yields of background and data, after b-tagging in the μ+jets channel. 91

6.9. Variables used in the likelihood discriminant for different signal mass points. 95

6.10. Expected Bayesian limits at 95% confidence on the $\tilde{t}_1\bar{\tilde{t}}_1$ cross section in pb, without and with systematic uncertainties, assuming a $t\bar{t}$ cross section of 6.77 pb. 99

6.11. Expected Bayesian limits at 95% confidence on the $\tilde{t}_1\bar{\tilde{t}}_1$ cross section, and the expected $t\bar{t}$ cross section in pb, without and with systematic uncertainties. 101

6.12. Summary of systematic uncertainties and their % effect in the e+jets channel. 105

6.13. Summary of systematic uncertainties and their % effect in the μ+jets channel. 106

7.1. Observed Bayesian limits at 95% confidence on the $\tilde{t}_1\bar{\tilde{t}}_1$ cross section in pb, without and with systematic uncertainties, assuming a $t\bar{t}$ cross section of 6.77 pb. 112

7.2. Observed Bayesian limits at 95% confidence on the $\tilde{t}_1\bar{\tilde{t}}_1$ cross section, and the measured $t\bar{t}$ cross section in pb, without and with systematic uncertainties. 114

A.1. Preselection efficiencies and corresponding κ factors in % in $\tilde{t}_1\bar{\tilde{t}}_1 \rightarrow$ e+jets events for the 175/135 mass point. Only statistical uncertainties are included. 129

A.2. Preselection efficiencies and corresponding κ factors in % in $\tilde{t}_1\bar{\tilde{t}}_1 \rightarrow$ μ+jets events for the 175/135 mass point. Only statistical uncertainties are included. 130

A.3. Preselection efficiencies and corresponding κ factors in % in $\tilde{t}_1\bar{\tilde{t}}_1 \rightarrow$ e+jets events for the 175/120 mass point. Only statistical uncertainties are included. 131

A.4. Preselection efficiencies and corresponding κ factors in % in $\tilde{t}_1\bar{\tilde{t}}_1 \rightarrow$ μ+jets events for the 175/120 mass point. Only statistical uncertainties are included. 132

A.5. Preselection efficiencies and corresponding κ factors in % in $\tilde{t}_1\bar{\tilde{t}}_1 \rightarrow$ e+jets events for the 175/105 mass point. Only statistical uncertainties are included. 133

A.6. Preselection efficiencies and corresponding κ factors in % in $\tilde{t}_1\bar{\tilde{t}}_1 \rightarrow$ μ+jets events for the 175/105 mass point. Only statistical uncertainties are included. 134

A.7. Preselection efficiencies and corresponding κ factors in % in $\tilde{t}_1\bar{\tilde{t}}_1 \rightarrow$ e+jets events for the 160/120 mass point. Only statistical uncertainties are included. 135

A.8. Preselection efficiencies and corresponding κ factors in % in $\tilde{t}_1\bar{\tilde{t}}_1 \rightarrow$ μ+jets events for the 160/120 mass point. Only statistical uncertainties are included. 136

A.9. Preselection efficiencies and corresponding κ factors in % in $\tilde{t}_1\bar{\tilde{t}}_1 \rightarrow$ e+jets events for the 160/105 mass point. Only statistical uncertainties are included. 137

A.10. Preselection efficiencies and corresponding κ factors in % in $\tilde{t}_1\bar{\tilde{t}}_1 \rightarrow$ μ+jets events for the 160/105 mass point. Only statistical uncertainties are included. 138

A.11. Preselection efficiencies and corresponding κ factors in % in $\tilde{t}_1\bar{\tilde{t}}_1 \rightarrow$ e+jets events for the 145/105 mass point. Only statistical uncertainties are included. 139

A.12. Preselection efficiencies and corresponding κ factors in % in $\tilde{t}_1\bar{\tilde{t}}_1 \rightarrow$ μ+jets events for the 145/105 mass point. Only statistical uncertainties are included. 140

List of Figures

2.1. Examples of one-loop Feynman diagrams by fermions (a) or scalars (b), that lead to quadratically divergent contributions to the Higgs mass. 5

2.2. Evolution of gauge couplings as a function of energy in the Standard Model and the MSSM, where α_1 reflects the coupling of hypercharge, α_2 the weak coupling, and α_3 the strong coupling [6]. 10

2.3. Feynman diagrams for lowest-order $t\bar{t}$ production. Top: quark-antiquark annihilation, bottom: gluon fusion. 12

2.4. Results of measurements of the $t\bar{t}$ cross section at the Tevatron. Left: CDF results for up to 760 pb^{-1} [9], right: DØ results for up to 1050 pb^{-1} [10]. 13

2.5. Examples of higher-order Feynman diagrams for stop-quark production that introduce a dependence on SUSY parameters other than that from the stop-quark mass [12]. 13

2.6. Production cross section for stop-quark pairs as a function of stop-quark mass. 14

2.7. "Pie chart" of $t\bar{t}$ decay channels. The branching ratios correspond to the theoretical predictions at tree level. 16

2.8. A selection of stop-quark decay channels: a) and b) are two-body decays, c) and e) are three-body decays, and d) a four-body decay. . 17

2.9. Feynman diagram of a W+0jet event. 20
2.10. Feynman diagrams of W+1jet events. 21
2.11. Feynman diagrams of W+2jets events. 21

3.1. The accelerator chain at Fermilab. 28
3.2. Side view of the DØ detector. 29
3.3. Longitudinal section of the DØ tracking and preshower systems. . . 30
3.4. 3-D view of the Silicon Vertex Detector. 31
3.5. Cross section of a Silicon Vertex Detector barrel, showing its layered structure. 32
3.6. Isometric view of the calorimeter. 36
3.7. Sections of a quarter of the DØ calorimeter. 37
3.8. Unit cell in the liquid-argon DØ calorimeter. 38
3.9. Exploded view of the muon drift chambers. 40
3.10. Exploded view of the muon scintillation detectors. 41
3.11. Photograph of the C layer of muon scintillation counters of the forward muon system. 43
3.12. Schematic view of the luminosity counters showing the PMTs as small filled circles. 44
3.13. The DØ trigger and data acquisition system. 45
3.14. The Level 1 and Level 2 trigger system. 46

4.1. Average number of hits as a function of track η [39]. Left: in the SMT, right: in the CFT. 49
4.2. Impact parameter resolution as a function of track p_T [39]. 49

4.3. Efficiency of the likelihood discriminant for electrons in data as a function of the cut value in the central calorimeter (CC) region for different choices of input parameters [46]. The one used in this analysis is shown as rectangles. Left: in $Z \to e^+e^-$ events, right: in multijet background events. 55
4.4. Sketch of the evolution of a hard-scattered parton to a jet in the calorimeter. 61
4.5. Absolute response in data, after offset and relative response corrections, as a function of partly corrected jet energy for jets with cone size $\Delta R = 0.7$. 63
4.6. Fractional uncertainty on transverse energy as a function of uncorrected transverse energy, for jets with a cone size of $\Delta R = 0.5$ and $\eta \approx 0$. 63
4.7. Neural Net output for direct $b\bar{b}$ (red) and multijet production (green). 66

6.1. Transverse mass of the W boson (for ℓ and $\not\!\!E_T$) in data and in Monte Carlo events for the e+jets channel, before b-tagging. Top left: events with 1 jet, top right: 2 jets, bottom left: 3 jets, bottom right: 4 or more jets. 87
6.2. Transverse mass of the W boson (for ℓ and $\not\!\!E_T$) in data and in Monte Carlo events for the μ+jets channel, after b-tagging. Top left: In events with 1 jet, top right: 2 jets, middle left: 3 jets, middle right: 4 or more jets, bottom: 4 or more jets, after convergence in HITFIT. 90
6.3. Missing transverse energy in the e+jets channel in $\tilde{t}_1\bar{\tilde{t}}_1$ 175/135 (solid line) and $t\bar{t}$ events (dashed line). 92
6.4. Input variables for the 175/135 mass point in the μ+jets channel. . 96
6.5. Input variables used in the likelihood discriminant for the 175/135 mass point in data and MC in the e+jets channel. 97

6.6. Likelihood discriminant for the 175/135 mass point. The distribution for the 175/135 mass point has been enhanced by a factor of ten and overlaid. Top: in the e+jets channel, bottom: in the μ+jets channel. 98

6.7. Expected posterior probability as a function of the $\tilde{t}_1\bar{\tilde{t}}_1$ cross section for the 175/135 mass point. Left: For the e+jets channel, middle: for the μ+jets channel, right: for both channels combined. 99

6.8. Expected posterior probability for the 175/135 mass point. Top: as a function of the $\tilde{t}_1\bar{\tilde{t}}_1$ cross section, bottom: as a function of the $t\bar{t}$ cross section. 100

6.9. Results for limits in experiments with no signal content for the 175/135 mass point. The expected limit is shown as solid line, the observed limit is shown as dashed line. 102

6.10. Results for cross sections in experiments when the theoretical signal content for the 175/135 mass point is raised by a factor of ten. The input cross section is shown as a line. 103

7.1. Observed posterior probability as a function of the $\tilde{t}_1\bar{\tilde{t}}_1$ cross section for the 175/135 mass point. 111

7.2. Observed and expected Bayesian limits at 95% confidence, and the theoretical cross section for $\tilde{t}_1\bar{\tilde{t}}_1$ at each mass point, assuming a $t\bar{t}$ cross section of 6.77 pb. 113

7.3. Observed posterior probability for the 175/135 mass point. Top: as a function of the $\tilde{t}_1\bar{\tilde{t}}_1$ cross section, bottom: as a function of the $t\bar{t}$ cross section. 115

7.4. Top: Observed and expected Bayesian limits at 95% confidence on the $\tilde{t}_1\bar{\tilde{t}}_1$ cross section, and the theoretical cross section for $\tilde{t}_1\bar{\tilde{t}}_1$ at each mass point. Bottom: Observed, expected and theoretical cross section for $t\bar{t}$. 116

B.1. Comparison of data and MC in the e+jets channel for $\geq$4 jets, before b-tagging. 142
B.2. Comparison of data and MC in the μ+jets channel for $\geq$4 jets, before b-tagging. 143
B.3. Comparison of data and MC in the e+jets channel for $\geq$4 jets, after b-tagging. 144
B.4. Comparison of data and MC in the μ+jets channel for $\geq$4 jets, after b-tagging. 145
B.5. Comparison of data and MC in the e+jets channel for $\geq$4 jets, after b-tagging and after obtaining convergence in Hitfit. 146
B.6. Comparison of data and MC in the μ+jets channel for $\geq$4 jets, after b-tagging and after obtaining convergence in Hitfit. 147

C.1. Input variables for the 175/135 mass point in the e+jets channel. . 149
C.2. Input variables for the 175/135 mass point in the μ+jets channel. . 149
C.3. Input variables for the 175/120 mass point in the e+jets channel. . 150
C.4. Input variables for the 175/120 mass point in the μ+jets channel. . 150
C.5. Input variables for the 175/105 mass point in the e+jets channel. . 151
C.6. Input variables for the 175/105 mass point in the μ+jets channel. . 152
C.7. Input variables for the 160/120 mass point in the e+jets channel. . 153
C.8. Input variables for the 160/120 mass point in the μ+jets channel. . 153
C.9. Input variables for the 160/105 mass point in the e+jets channel. . 154
C.10. Input variables for the 160/105 mass point in the μ+jets channel. . 155
C.11. Input variables for the 145/105 mass point in the e+jets channel. . 156

C.12. Input variables for the 145/105 mass point in the μ+jets channel. . 157
C.13. Input variables used in the likelihood discriminants in data and MC in the e+jets channel. 159
C.14. Input variables used in the likelihood discriminants in data and MC in the e+jets channel. 160
C.15. Input variables used in the likelihood discriminants in data and MC in the μ+jets channel. 161
C.16. Input variables used in the likelihood discriminants in data and MC in the μ+jets channel. 162
C.17. Likelihood discriminants in the e+jets channel for different mass points. Top: Stop 175/135, middle: Stop 175/120, bottom: Stop 175/105. 164
C.18. Likelihood discriminants in the e+jets channel for different mass points. Top: Stop 160/120, middle: Stop 160/105, bottom: Stop 145/105. 165
C.19. Likelihood discriminants in the μ+jets channel for different mass points. Top: Stop 175/135, middle: Stop 175/120, bottom: Stop 175/105. 166
C.20. Likelihood discriminants in the μ+jets channel for different mass points. Top: Stop 160/120, middle: Stop 160/105, bottom: Stop 145/105. 167

D.1. Expected posterior probability as a function of the $\tilde{t}_1\bar{\tilde{t}}_1$ cross section for the 175/135 mass point. 169
D.2. Expected posterior probability as a function of the $\tilde{t}_1\bar{\tilde{t}}_1$ cross section for the 175/120 mass point. 169
D.3. Expected posterior probability as a function of the $\tilde{t}_1\bar{\tilde{t}}_1$ cross section for the 175/105 mass point. 170

D.4. Expected posterior probability as a function of the $\tilde{t}_1\bar{\tilde{t}}_1$ cross section for the 160/120 mass point. 170
D.5. Expected posterior probability as a function of the $\tilde{t}_1\bar{\tilde{t}}_1$ cross section for the 160/105 mass point. 171
D.6. Expected posterior probability as a function of the $\tilde{t}_1\bar{\tilde{t}}_1$ cross section for the 145/105 mass point. 171
D.7. Expected posterior probability for the 175/135 mass point. Top: as a function of the $\tilde{t}_1\bar{\tilde{t}}_1$ cross section, bottom: as a function of the $t\bar{t}$ cross section. 172
D.8. Expected posterior probability for the 175/120 mass point. Top: as a function of the $\tilde{t}_1\bar{\tilde{t}}_1$ cross section, bottom: as a function of the $t\bar{t}$ cross section. 173
D.9. Expected posterior probability for the 175/105 mass point. Top: as a function of the $\tilde{t}_1\bar{\tilde{t}}_1$ cross section, bottom: as a function of the $t\bar{t}$ cross section. 174
D.10. Expected posterior probability for the 160/120 mass point. Top: as a function of the $\tilde{t}_1\bar{\tilde{t}}_1$ cross section, bottom: as a function of the $t\bar{t}$ cross section. 175
D.11. Expected posterior probability for the 160/105 mass point. Top: as a function of the $\tilde{t}_1\bar{\tilde{t}}_1$ cross section, bottom: as a function of the $t\bar{t}$ cross section. 176
D.12. Expected posterior probability for the 145/105 mass point. Top: as a function of the $\tilde{t}_1\bar{\tilde{t}}_1$ cross section, bottom: as a function of the $t\bar{t}$ cross section. 177
D.13. Observed posterior probability as a function of the $\tilde{t}_1\bar{\tilde{t}}_1$ cross section for the 175/135 mass point. 178
D.14. Observed posterior probability as a function of the $\tilde{t}_1\bar{\tilde{t}}_1$ cross section for the 175/120 mass point. 178

D.15. Observed posterior probability as a function of the $\tilde{t}_1\bar{\tilde{t}}_1$ cross section for the 175/105 mass point. 179
D.16. Observed posterior probability as a function of the $\tilde{t}_1\bar{\tilde{t}}_1$ cross section for the 160/120 mass point. 179
D.17. Observed posterior probability as a function of the $\tilde{t}_1\bar{\tilde{t}}_1$ cross section for the 160/105 mass point. 180
D.18. Observed posterior probability as a function of the $\tilde{t}_1\bar{\tilde{t}}_1$ cross section for the 145/105 mass point. 180
D.19. Observed posterior probability for the 175/135 mass point. Top: as a function of the $\tilde{t}_1\bar{\tilde{t}}_1$ cross section, bottom: as a function of the $t\bar{t}$ cross section. 181
D.20. Observed posterior probability for the 175/120 mass point. Top: as a function of the $\tilde{t}_1\bar{\tilde{t}}_1$ cross section, bottom: as a function of the $t\bar{t}$ cross section. 182
D.21. Observed posterior probability for the 175/105 mass point. Top: as a function of the $\tilde{t}_1\bar{\tilde{t}}_1$ cross section, bottom: as a function of the $t\bar{t}$ cross section. 183
D.22. Observed posterior probability for the 160/120 mass point. Top: as a function of the $\tilde{t}_1\bar{\tilde{t}}_1$ cross section, bottom: as a function of the $t\bar{t}$ cross section. 184
D.23. Observed posterior probability for the 160/105 mass point. Top: as a function of the $\tilde{t}_1\bar{\tilde{t}}_1$ cross section, bottom: as a function of the $t\bar{t}$ cross section. 185
D.24. Observed posterior probability for the 145/105 mass point. Top: as a function of the $\tilde{t}_1\bar{\tilde{t}}_1$ cross section, bottom: as a function of the $t\bar{t}$ cross section. 186

E.1. Results for limits in experiments with no signal content for the 175/135 mass point. The expected limit is shown as solid blue line, the observed limit is shown as dashed red line. 187
E.2. Results for limits in experiments with no signal content for the 175/120 mass point. The expected limit is shown as solid blue line, the observed limit is shown as dashed red line. 188
E.3. Results for limits in experiments with no signal content for the 175/105 mass point. The expected limit is shown as solid blue line, the observed limit is shown as dashed red line. 188
E.4. Results for limits in experiments with no signal content for the 160/120 mass point. The expected limit is shown as solid blue line, the observed limit is shown as dashed red line. 189
E.5. Results for limits in experiments with no signal content for the 160/105 mass point. The expected limit is shown as solid blue line, the observed limit is shown as dashed red line. 189
E.6. Results for limits in experiments with no signal content for the 145/105 mass point. The expected limit is shown as solid blue line, the observed limit is shown as dashed red line. 190
E.7. Results for cross sections in experiments when the theoretical signal content for the 175/135 mass point is raised by a factor of ten. The input cross section is shown as purple line. 190
E.8. Results for cross sections in experiments when the theoretical signal content for the 175/120 mass point is raised by a factor of ten. The input cross section is shown as purple line. 191
E.9. Results for cross sections in experiments when the theoretical signal content for the 175/105 mass point is raised by a factor of ten. The input cross section is shown as purple line. 191

E.10. Results for cross sections in experiments when the theoretical signal content for the 160/120 mass point is raised by a factor of ten. The input cross section is shown as purple line. 192
E.11. Results for cross sections in experiments when the theoretical signal content for the 160/105 mass point is raised by a factor of ten. The input cross section is shown as purple line. 192
E.12. Results for cross sections in experiments when the theoretical signal content for the 145/105 mass point is raised by a factor of ten. The input cross section is shown as purple line. 193

1. Introduction

Elementary Particle Physics is based on studies of the fundamental building blocks of nature and their interactions. The Standard Model of Particle Physics is the most complete and successful theory to describe all observed particle phenomena [1]. It has also made successful quantitative predictions for interaction rates and couplings, as well as for the existence of particles such as the τ neutrino and the top quark, that were observed subsequently. The latter was found in 1995 at Fermi National Accelerator Laboratory (Fermilab) by the CDF and DØ collaborations [2].

In spite of the tremendous success of the Standard Model, we know that it is incomplete. To name a few shortcomings, the Standard Model does not include gravity, does not provide explanations for the choice of its parameters, does not account for dark matter and dark energy, and there is the notorious fine-tuning problem due to radiative corrections to the Higgs-boson mass [3]. While the Standard Model successfully unifies the electromagnetic and the weak interactions, the strong and the gravitational forces are still decoupled. For decades, the ultimate goal of particle physics has been to unify all interactions in one Grand Unified Theory.

One possible extension to the Standard Model involves Supersymmetry (SUSY), a symmetry between fermions and bosons [3]. Every Standard-Model boson (fermion) acquires a yet undiscovered fermionic (bosonic) supersymmetric partner. This aesthetically appealing theory not only solves the fine-tuning problem of radiative

corrections, but it also provides a candidate for dark matter, it has gauge couplings unifying at large energy scales, and there is even a connection to gravity. However, Supersymmetry cannot be the final theory either, as it also leaves unanswered questions.

If Supersymmetry is realized in nature, and indeed provides solutions to the fine-tuning problem and unifies the gauge couplings, the masses of supersymmetric particles must be between 100 GeV and 10 TeV. There are reasons to believe that the supersymmetric partner of the top quark, the scalar top quark ($\tilde{t}$), is the lightest supersymmetric quark [4]. That means it could already be produced at the Tevatron. The specific scalar top-quark decay explored in the analysis presented in this work leads to an event signature identical to that of the top quark. Hiding among top quark events, scalar top quarks could not only have escaped detection, but also distorted precision measurements of the top quark production cross section and properties. The objective of this analysis is to search for the possible scalar top-quark admixture in top quark events.

The thesis is organized as follows: Chapter 2 gives an introduction to the Standard Model, Supersymmetry, and the physics of the top quark and the scalar top quark. It also discusses the procedure for setting limits on production processes. Chapter 3 describes the experimental environment, that is, the Tevatron collider and the DØ detector. Chapter 4 describes how the physics objects in an event are reconstructed. Chapter 5 gives details on the data and the Monte-Carlo simulated events used in the analysis. Chapter 6 presents the main analysis, documenting the search for a scalar top quark in the top-quark sample. Chapter 7 summarizes the results and provides conclusions.

2. Theory

The Standard Model describes our current understanding of elementary particles and their interactions. One possible extension to the theory is Supersymmetry, a symmetry between fermions and bosons. This chapter gives an introduction to both theories and discusses the physics of the top quark and the scalar top quark. It ends with a description of our procedure for setting limits on cross sections.

2.1. The Standard Model

In the Standard Model (SM), all matter is believed to consist of two kinds of elementary particles: leptons and quarks, each of which can be classified into three generations of identical configuration [1]. The leptons are comprised of the electron (e), the electron neutrino (ν_e), the muon (μ), the muon neutrino (ν_μ), the tau (τ), and the tau neutrino (ν_τ). The six quarks are the up (u), down (d), charm (c), strange (s), top (t) and bottom (b) quark. Each particle has an antiparticle with the same properties but opposite quantum numbers, e.g. electric charge. Quarks come in three different "colors", which reflect their strong interactions. Another property of all particles is their chirality, left-handed fermions come in weak-isospin doublets, whereas right-handed fermions are singlets, as indicated below. In the Standard Model, neutrinos do not carry mass, which is an excellent approximation.

$$\text{Leptons:} \quad \begin{array}{ccc} \begin{pmatrix} \nu_e \\ e \end{pmatrix}_L & \begin{pmatrix} \nu_\mu \\ \mu \end{pmatrix}_L & \begin{pmatrix} \nu_\tau \\ \tau \end{pmatrix}_L \\ e_R & \mu_R & \tau_R \end{array}$$

$$\text{Quarks:} \quad \begin{array}{ccc} \begin{pmatrix} u \\ d \end{pmatrix}_L & \begin{pmatrix} c \\ s \end{pmatrix}_L & \begin{pmatrix} t \\ b \end{pmatrix}_L \\ u_R & c_R & t_R \\ d_R & s_R & b_R \end{array}$$

The Standard Model describes three of the four fundamental forces. Gravity is ignored in the theory, but it is very weak in the normal realm of elementary particles. The other three, the strong, the weak, and the electromagnetic interaction are described by a non-Abelian gauge theory based on the group:

$$SU(3)_C \times SU(2)_L \times U(1)_Y,$$

where C refers to the "color" of quarks, L to the third weak-isospin component of left-handed particles, and Y to the hypercharge. Quantum Chromodynamics (QCD) describes the strong interaction, which is mediated by eight massless gluons, the gauge bosons of the $SU(3)_C$ group. The weak and the electromagnetic interaction are unified and described by the electroweak model of the $SU(2)_L \times U(1)_Y$ group, which is mediated by the massive W^+, W^-, and Z bosons and the massless photon (γ).

Only particles with strong color charge participate in the strong interaction of QCD, and, of all the matter fermions, only quarks carry color. Electrically charged particles participate in the electromagnetic interaction, which means all quarks and the charged leptons: the electron, muon, and τ. For the weak interaction, only left-handed particles have weak isospin, so that only the left-handed weak-isospin doublets participate in weak interactions.

Local gauge invariance of the theory is inconsistent with the presence of massive gauge bosons, yet the Z and W bosons are, in fact, massive. Although the mechanism for generating the gauge boson masses is unconfirmed, the generally accepted theory is referred to as the Higgs mechanism [5]. This introduces a complex scalar doublet, the Higgs field, which leads to spontaneous symmetry breaking of the $SU(2)_L \times U(1)_Y$ group to the $U(1)_Q$ group, where Q refers to the electric charge. Three of the four degrees of freedom of the Higgs field give masses to the Z and W bosons, and one gives mass to a new spin 0 particle, the Higgs boson. Fermion masses can also be generated through Yukawa interactions between the Higgs ground state and the fermions. The couplings are proportional to the fermion mass. Finding the yet undiscovered Higgs boson would confirm the current theory of mass generation.

Radiative corrections to the Higgs boson mass introduce a flaw into the Standard Model, which is referred to as the "fine-tuning problem". The Higgs mass receives quadratically divergent corrections, both from fermion and boson loop diagrams, as shown in Fig. 2.1. These corrections are of the order $\mathcal{O}(\Lambda^2)$, where Λ is the

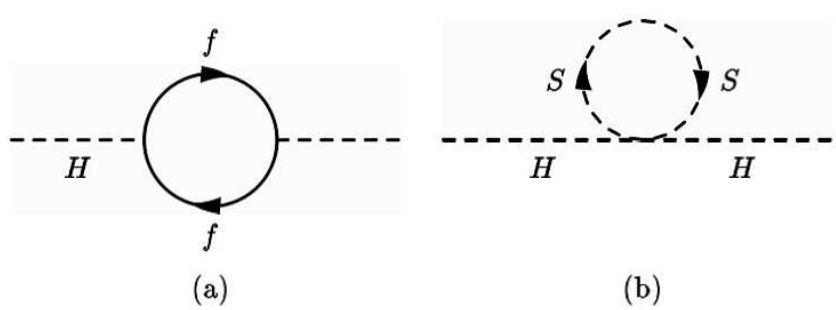

Figure 2.1.: Examples of one-loop Feynman diagrams by fermions (a) or scalars (b), that lead to quadratically divergent contributions to the Higgs mass.

energy scale up to which the Standard Model is expected to be valid: for example, the Planck scale $\Lambda_P \approx 10^{18}$ GeV. But electroweak precision measurements indicate

that the physical Higgs mass should be of order $\mathcal{O}(100\text{ GeV})$. This requires fine-tuning the bare Higgs mass to cancel the enormous radiative corrections over many orders of magnitude. It is interesting that contributions from fermion loops have the opposite sign of boson contributions. If fermion and boson couplings were related, they could, in principle, cancel even to higher-order corrections.

Apart from the fine-tuning problem, there are other reasons to believe that the Standard Model is incomplete. Connected to the fine-tuning is the hierarchy problem, which is the question why the Planck scale is so much larger than the weak scale. The Standard Model also does not explain why there are three generations of fermions, it does not predict particle masses or the elements of the Cabibbo-Kobayashi-Maskawa mixing matrix or the values of any of the coupling constants. It offers no explanation for dark matter and dark energy and it does not include gravity, which becomes important for interactions at higher energies, and certainly at the Planck scale.

2.2. Supersymmetry

One possible extension to the Standard Model involves Supersymmetry (SUSY), which postulates a symmetry between fermions and bosons [3]. Since the Lagrangian is required to be invariant under this symmetry transformation, every fermionic degree of freedom needs a bosonic degree of freedom, and vice versa. These fermion-boson pairs do not exist within the Standard Model, so that the theory implies the existence of new particles, the superpartners of Standard-Model particles. Every Standard-Model boson (fermion) acquires a fermionic (bosonic) supersymmetric partner. In addition, Supersymmetry requires at least two Higgs doublets, resulting in several Higgs bosons and their superpartners. We already know that Supersymmetry must be a broken symmetry, because we have not observed any particle pairs with same properties, except for spin.

A multiplicative quantum number called R-parity can be introduced in SUSY, and is defined as follows:

$$R = (-1)^{3(B-L)+2S}, \tag{2.1}$$

where B is the baryon number, L the lepton number and S the spin. All Standard-Model fermions, gauge bosons, and both Higgs doublets have R-parity +1, while their superpartners have R-parity –1. Both R-parity conserving and R-parity violating supersymmetric models are possible, the analysis presented in this thesis assumes that R-parity is conserved in SUSY processes. This has two important consequences:

- Supersymmetric particles can only be produced in pairs.
- The lightest supersymmetric particle (LSP) has to be stable, thereby providing a candidate for dark matter.

The simplest supersymmetric model with the smallest number of new particles and interactions is known as the Minimal Supersymmetric Standard Model (MSSM) [3]. Table 2.1 provides an overview of the particle content. The naming convention gives superpartners of fermions an "s" in front of their normal name, and are known as "sfermions". For example, the partner of the top quark is called the stop quark. Superpartners of bosons receive an "ino" at the end of their names, the Higgs bosons have "higgsino" partners, and the superpartners of the gauge bosons are called "gauginos".

However, except for the gluino, which is the only color-octet fermion, gauginos and higgsinos have the same quantum numbers, and will therefore mix to form the physical particles. The neutral higgsinos, the photino, and the Zino form the four neutralinos $\tilde{\chi}_i^0$ (i=1,2,3,4), and the charged higgsinos and the Wino form the charginos $\tilde{\chi}_i^\pm$ (i=1,2). For the sfermions, since the original fermion has two degrees of freedom, there will be two spinless superpartners for each fermion, which are

R-parity=+1			R-parity=-1		
Particle	Symbol	Spin	Particle	Symbol	Spin
Lepton	ℓ	$\frac{1}{2}$	Slepton	$\tilde{\ell}_L, \tilde{\ell}_R$	0
Neutrino	ν	$\frac{1}{2}$	Sneutrino	$\tilde{\nu}$	0
Quark	q	$\frac{1}{2}$	Squark	$\tilde{q}_L, \tilde{q}_R$	0
Gluon	g	1	Gluino	$\tilde{g}$	$\frac{1}{2}$
Photon	γ	1	Photino	$\tilde{\gamma}$	$\frac{1}{2}$
W/Z	$W^{\pm}, Z$	1	Wino/Zino	$\tilde{W}^{\pm}, \tilde{Z}$	$\frac{1}{2}$
Higgs	$H^0, H^{\pm}$	0	Higgsino	$\tilde{H}_1^0, \tilde{H}_2^+$	$\frac{1}{2}$
	h^0, A^0	0		$\tilde{H}_1^-, \tilde{H}_2^0$	$\frac{1}{2}$

Table 2.1.: Overview of particles in the MSSM.

sometimes loosely referred to as left-handed and right-handed sfermions, although they have no standard handedness or chirality. Since sfermions also have identical quantum numbers, they will mix to form the physical particles. The mixing depends on the mass of the Standard-Model fermion, and the third-generation sfermions will mix most. For example, for the stop quark, the mixing matrix is given by [3]:

$$\begin{pmatrix} m_{\tilde{t}_L}^2 + m_t^2 + D(\tilde{t}_L) & m_t(-A_t + \mu \cot\beta) \\ m_t(-A_t + \mu \cot\beta) & m_{\tilde{t}_R}^2 + m_t^2 + D(\tilde{t}_R) \end{pmatrix}, \tag{2.2}$$

and

$$\begin{aligned} D(\tilde{t}_L) &= M_Z^2 \cos 2\beta(\frac{1}{2} - \frac{2}{3}\sin^2\theta_W), \\ D(\tilde{t}_R) &= M_Z^2 \cos 2\beta(+\frac{2}{3}\sin^2\theta_W), \end{aligned}$$

where m_t is the mass of the top quark, $m_{\tilde{t}_L}$ the mass of the left-stop quark, $m_{\tilde{t}_R}$ the mass of the right-stop quark, A_t a trilinear coupling, μ the higgsino mass term, $\tan\beta$ the ratio of the vacuum expectation values of the two Higgs doublets, M_Z

the mass of the Z boson, and θ_W the weak mixing angle. This matrix can be diagonalized and the physical stop quarks $\tilde{t}_1$ and $\tilde{t}_2$ are given by:

$$\begin{pmatrix} \tilde{t}_1 \\ \tilde{t}_2 \end{pmatrix} = \begin{pmatrix} \cos\theta_t & -\sin\theta_t \\ \sin\theta_t & \cos\theta_t \end{pmatrix} \begin{pmatrix} \tilde{t}_L \\ \tilde{t}_R \end{pmatrix}, \tag{2.3}$$

where $\tilde{t}_1$ is the lighter stop-quark mass eigenstate and $\tilde{t}_2$ is the heavier one. The stop-quark mixing angle θ_t is defined by:

$$\tan\theta_t = \frac{m^2_{\tilde{t}_L} + m_t^2 + M_Z^2 \cos 2\beta(\frac{1}{2} - \frac{2}{3}\sin^2\theta_W) - m^2_{\tilde{t}_1}}{m_t(-A_t + \mu\cot\beta)}. \tag{2.4}$$

Supersymmetry possesses many desirable features [3]:

- By introducing fermion-boson pairs related by a symmetry, the fine-tuning problem of the Standard Model is solved. For each divergent fermion (boson) loop contribution, there will be a boson (fermion) loop contribution with opposite sign, so that the two will cancel to all orders. It is possible to construct a breaking of supersymmetry, and therefore have the fermion mass differ from the boson mass, while keeping the cancellation of quadratic divergences intact. This is called "soft" supersymmetry breaking, and it leads to masses of supersymmetric particles in the range 100 GeV–10 TeV.

- In the Standard Model, the running gauge couplings do not unify when they are extrapolated to higher energies, as shown in Fig. 2.2. In the MSSM, however, they unify at an energy near 10^{16} GeV, if the masses of the supersymmetric particles are in the range 100 GeV–10 TeV, which coincides with the range needed to resolve the fine-tuning problem.

- All supersymmetric models that conserve R-parity have a stable lightest supersymmetric particle. This LSP is usually neutral and weakly interacting,

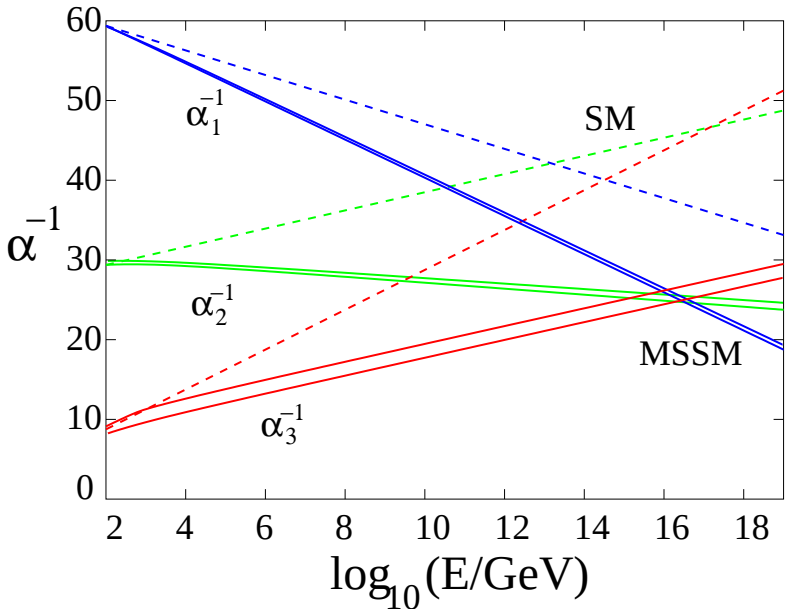

Figure 2.2.: Evolution of gauge couplings as a function of energy in the Standard Model and the MSSM, where α_1 reflects the coupling of hypercharge, α_2 the weak coupling, and α_3 the strong coupling [6].

and provides an excellent candidate for the observed dark matter in the universe.

- In the Standard Model, electroweak symmetry-breaking has to be induced through a specific choice of parameters in the Higgs potential. In a variety of supersymmetric models, electroweak symmetry-breaking occurs naturally, if the mass of the top quark m_t is $\approx$ 100–200 GeV.

- By demanding gauge invariance under local supersymmetric transformations, a spin-2 massless gauge field is introduced in the theory. This graviton and its supersymmetric partner, the gravitino, mediate gravitational interactions. Unfortunately, the Supergravity theory is not renormalizable.

- Another interesting motivation derives from electroweak baryogenesis, which

is excluded in the Standard Model, but is feasible in a supersymmetric model when the stop quark is lighter than the top quark [7].

Despite of all these promising features, Supersymmetry cannot be the final theory of particle phenomena. Like the Standard Model, it does not resolve the hierarchy problem, why there are three generations of fermions, and it does not predict particle masses and mixing angles. Instead, it introduces many new parameters. Even the MSSM contains 124 parameters. And, lastly, there is no evidence as yet for the presence of Supersymmetry in nature.

2.3. The Top Quark and the Scalar Top Quark

The top quark is the heaviest known elementary particle, and the Tevatron is still the only place where it can be produced and studied. Apart from being interesting in its own right, the top quark also influences other analyses. The Higgs boson couples most strongly to it, and top-quark production is an important background to a lot of searches for new physics.

Because of the large mass of the top quark the mixing between the left-stop and right-stop can be substantial, as mentioned in the previous section. This provides a large difference in the mass eigenvalues of the stop quark, with the possibility of the lighter stop quark ($\tilde{t}_1$) being the lightest squark, and well within reach at the Tevatron.

2.3.1. Production

At the Tevatron, top quarks are produced mainly in pairs via the strong interaction. The lowest-order processes are shown in Fig. 2.3, with quark-antiquark annihilation dominating the production at the Tevatron (85 %, and 15 % for gluon fusion).

The predicted cross section for a top quark with a mass of 175 GeV, including

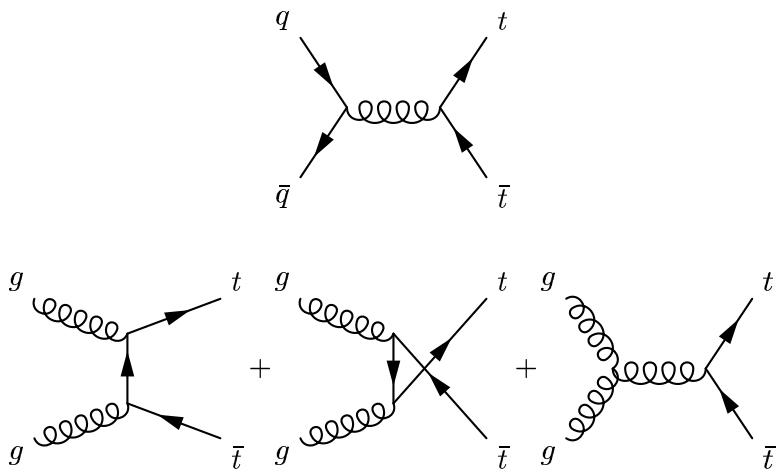

Figure 2.3.: Feynman diagrams for lowest-order $t\bar{t}$ production. Top: quark-antiquark annihilation, bottom: gluon fusion.

next-to-next-to-leading order (NNLO) soft-gluon corrections, next-to-next-to-next-to-leading-logarithm (NNNLL) corrections, and certain virtual terms is [8]:

$$\sigma^{p\bar{p}\to t\bar{t}}(m_t = 175 \text{ GeV}, \sqrt{s} = 1.96 \text{ TeV}) = (6.77 \pm 0.42) \text{ pb}$$

The results of recent measurements by the CDF and DØ Collaborations are summarized in Fig. 2.4.

Evidence has recently been found for the more rare single-top production process via charged-current weak interaction [11].

Stop quarks at the Tevatron are produced mainly in diagonal $\tilde{t}_1\bar{\tilde{t}}_1/\tilde{t}_2\bar{\tilde{t}}_2$ pairs and production of mixed pairs is suppressed [12]. At lowest order in QCD, the production processes involve quark-antiquark annihilation or gluon-gluon fusion, just as for the case of top-quark pair-production, as shown in Fig. 2.3. The cross section depends primarily on the stop-quark mass, although there is also a weak dependence on gluino mass, the mixing angle, and other squark masses, all arising from higher-order corrections, two of which are shown in Fig. 2.5.

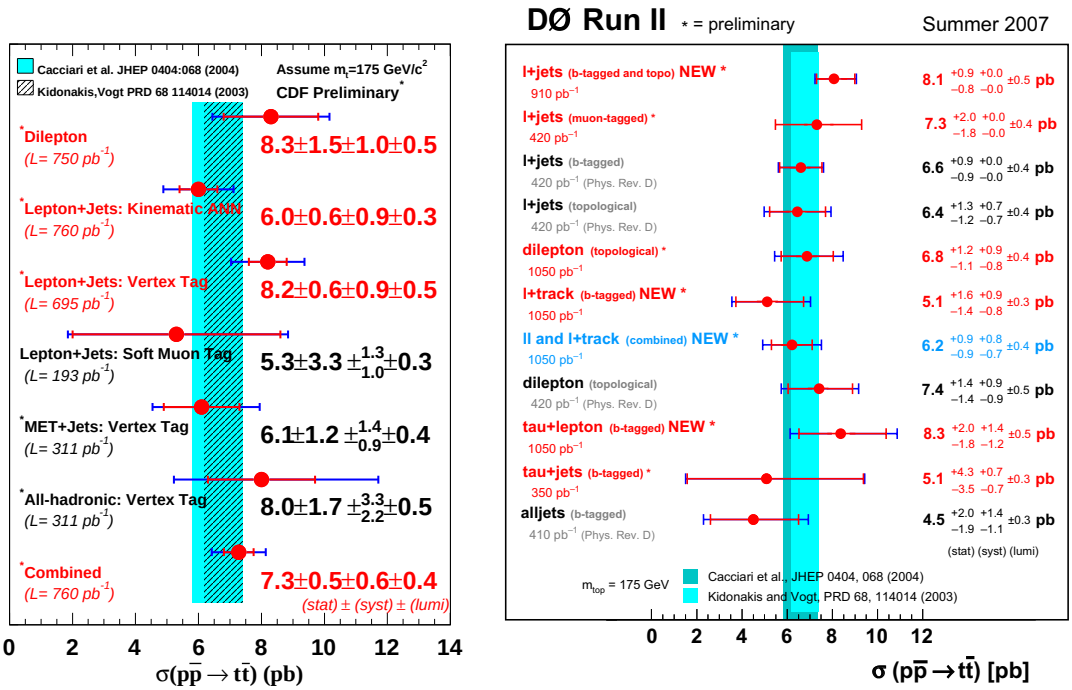

Figure 2.4.: Results of measurements of the $t\bar{t}$ cross section at the Tevatron. Left: CDF results for up to 760 pb^{-1} [9], right: DØ results for up to 1050 pb^{-1} [10].

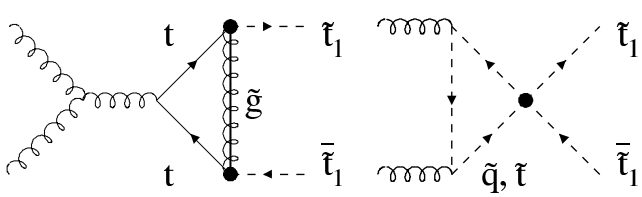

Figure 2.5.: Examples of higher-order Feynman diagrams for stop-quark production that introduce a dependence on SUSY parameters other than that from the stop-quark mass [12].

Since stop-quark pair-production takes place through the color force (QCD), the rate can be calculated relatively reliably. Next-to-leading order (NLO) calculations already exist, and are even incorporated in tools such as PROSPINO, which provides NLO cross sections for supersymmetric particles [13]. Figure 2.6 shows the dependence of the $\tilde{t}_1\bar{\tilde{t}}_1$ NLO cross section on the stop-quark mass for $\tilde{t}_1$ masses of 100–200 GeV. At a mass of 175 GeV, the cross section is only about a tenth of the

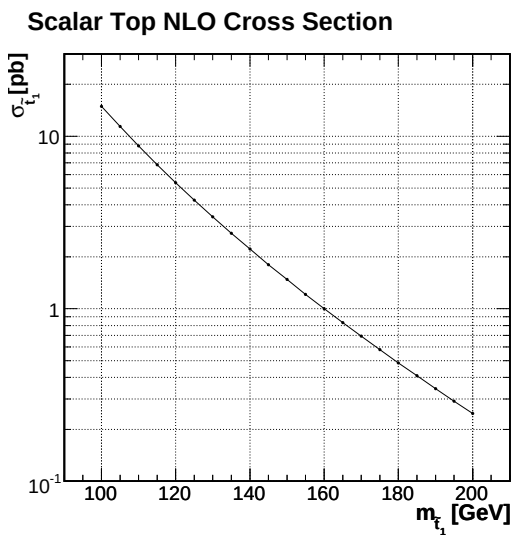

Figure 2.6.: Production cross section for stop-quark pairs as a function of stop-quark mass.

$t\bar{t}$ cross section. The suppression in production arises from the stop quark's having spin-0, as opposed to spin-$\frac{1}{2}$ for the top quark. Table 2.2 lists the cross sections for stop-quark masses considered in this analysis.

2.3.2. Decay

The top quark has an extremely short lifetime of only $\approx 10^{-25}$ seconds, and subsequently decays via the charged-current weak interaction, before hadronizing. In the Standard Model, it almost always decays to a W boson and a b-quark, with

$m_{\tilde{t}_1}$	$\sigma_{\tilde{t}_1\bar{\tilde{t}}_1}$
145 GeV	1.80 pb
160 GeV	1.00 pb
175 GeV	0.579 pb

Table 2.2.: Cross section for $\tilde{t}_1\bar{\tilde{t}}_1$ production at $\sqrt{s}$ =1.96 TeV for different stop-quark masses, as calculated using the PROSPINO program.

a predicted branching fraction of BR($t \to Wb$) > 0.998. Each W boson can decay either into a lepton and a neutrino or into two quarks, and the final state of top-quark pair-production is determined by the decays of the two W bosons. If both W bosons decay into quarks, which subsequently hadronize, the final state is called the "all-hadronic" or "all-jets" channel, and when both W bosons decay leptonically it is called the "dilepton" channel. This analysis studies "lepton+jets" (ℓ+jets) channels, where one W boson decays leptonically and one "hadronically". All channels and their approximate theoretical branching ratios, taking into account only lowest-order Feynman diagrams, are illustrated in Fig. 2.7.

The advantage of the lepton+jets channel is that the presence of the lepton in the event gives a clear signature, which suppresses background, while the branching ratio is still relatively large. The signature of a $t\bar{t}\to$ ℓ+jets event consists of one isolated lepton of large transverse momentum (p_T), large "missing" transverse momentum ($\not{E}_T$) due to the escaping neutrino from the leptonic W-boson decay, two light jets from the "hadronic" W-boson decay, and two b-jets from the hadronization of the b-quarks.

Figure 2.8 shows some of the major stop-quark decay channels [14]. When kinematically possible, the dominant decays will be $\tilde{t}_1 \to t\tilde{\chi}_1^0$ and $\tilde{t}_1 \to b\tilde{\chi}_1^+$ (Fig. 2.8a). When the stop quark is lighter than both the top quark and the chargino ($\tilde{\chi}_1^\pm$), the two-body decay $\tilde{t}_1 \to c\tilde{\chi}_1^0$ (Fig. 2.8b) is usually taken as the main decay channel;

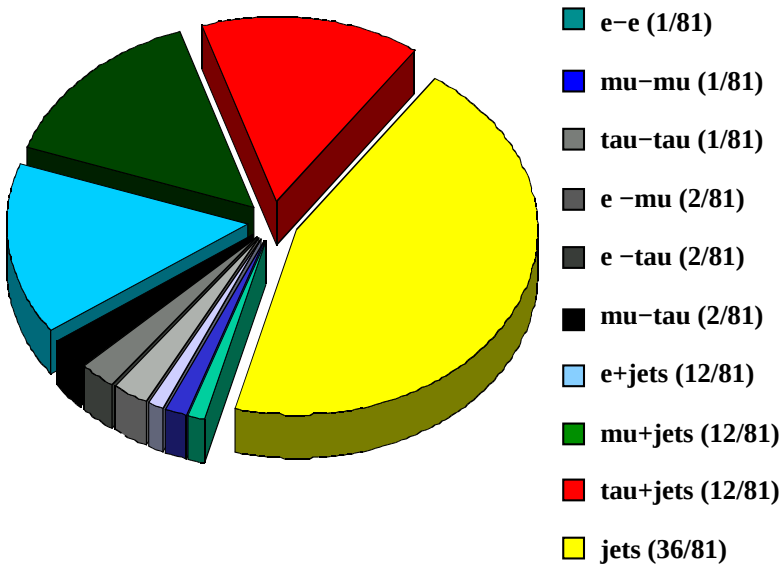

Figure 2.7.: "Pie chart" of $t\bar{t}$ decay channels. The branching ratios correspond to the theoretical predictions at tree level.

but it has been shown that the three-body decays $\tilde{t}_1 \to bW^+\tilde{\chi}_1^0$ or $\tilde{t}_1 \to bH^+\tilde{\chi}_1^0$, involving the charged Higgs H^+ (Fig. 2.8c), or the four-body decay $\tilde{t}_1 \to b\tilde{\chi}_1^0 f\bar{f}'$, involving fermion pairs (Fig. 2.8d), can also dominate under these circumstances. In addition, if sleptons are lighter than squarks, then $\tilde{t}_1 \to b\ell^+\tilde{\nu}_\ell$ and $\tilde{t}_1 \to b\tilde{\ell}^+\nu_\ell$ (Fig. 2.8e) can also play an important role.

In this analysis, we consider only stop-quark masses $m_{\tilde{t}_1} \leq m_t$, with the chargino and neutralino masses close to their current experimental lower limits. In this scenario, the decay $\tilde{t}_1 \to b\tilde{\chi}_1^+$ is allowed and will therefore dominate. Each chargino $\tilde{\chi}_1^\pm$ decays to a W boson and a neutralino $\tilde{\chi}_1^0$. The subsequent decay of the W boson determines the event topology just as for $t\bar{t}$ events. The resulting $\tilde{t}_1\bar{\tilde{t}}_1$ event signature is consequently very similar to the $t\bar{t}$ signature, thereby making it possible for the $\tilde{t}_1\bar{\tilde{t}}_1$ signal to be contained within the $t\bar{t}$ event sample. It should be noted that, depending on the masses of the involved supersymmetric particles, the W boson is not necessarily on its "mass-shell", but the final state is nevertheless

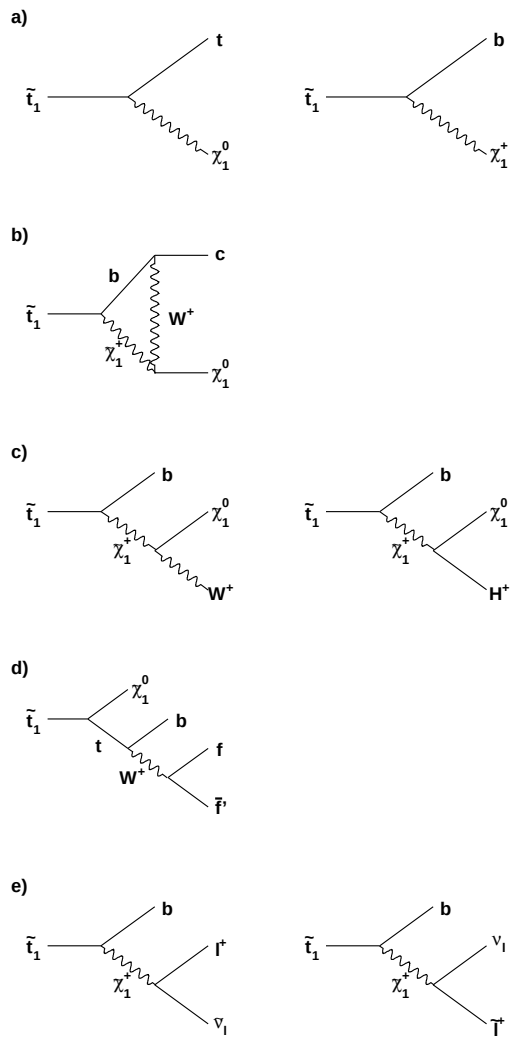

Figure 2.8.: A selection of stop-quark decay channels: a) and b) are two-body decays, c) and e) are three-body decays, and d) a four-body decay.

the same for both cases. In this analysis, the lepton of the lepton+jets channel can be an electron or muon, either directly from the W-boson decay or from a τ, which in turn originates from the W boson. These are called the e+jets and the μ+jets channels, and are analyzed separately until they are combined for the final result.

The branching ratios (B) of the e+jets and μ+jets channel for $t\bar{t}$ events are given by:

$$\begin{aligned} \mathrm{B}(t\bar{t} \to \ell + \mathrm{jets}) &= (\mathrm{B}(t \to Wb))^2 \\ &\cdot 2 \cdot \mathrm{B}(W \to q\bar{q}') \\ &\cdot (\mathrm{B}(W \to \ell\bar{\nu}_\ell) + \mathrm{B}(W \to \tau\bar{\nu}_\tau) \cdot \mathrm{B}(\tau \to \ell\bar{\nu}_\ell\nu_\tau)), \end{aligned}$$

where ℓ is an electron or a muon. Similarly, for stop events with on-shell W bosons:

$$\begin{aligned} \mathrm{B}(\tilde{t}_1\bar{\tilde{t}}_1 \to \ell + \mathrm{jets}) &= (\mathrm{B}(\tilde{t}_1 \to \tilde{\chi}_1^{\pm} b) \cdot \mathrm{B}(\tilde{\chi}_1^{\pm} \to W\tilde{\chi}_1^0))^2 \\ &\cdot 2 \cdot \mathrm{B}(W \to q\bar{q}') \\ &\cdot (\mathrm{B}(W \to \ell\bar{\nu}_\ell) + \mathrm{B}(W \to \tau\bar{\nu}_\tau) \cdot \mathrm{B}(\tau \to \ell\bar{\nu}_\ell\nu_\tau)). \end{aligned}$$

For stop events with an off-shell W boson, the chargino will decay via three-body decays, directly to the fermions and a neutralino:

$$\begin{aligned} \mathrm{B}(\tilde{t}_1\bar{\tilde{t}}_1 \to \ell + \mathrm{jets}) &= (\mathrm{B}(\tilde{t}_1 \to \tilde{\chi}_1^{\pm} b) \cdot \mathrm{B}(\tilde{\chi}_1^{\pm} \to W\tilde{\chi}_1^0))^2 \\ &\cdot 2 \cdot \mathrm{B}(W \to q\bar{q}') \\ &\cdot (\mathrm{B}(W \to \ell\bar{\nu}_\ell) + \mathrm{B}(W \to \tau\bar{\nu}_\tau) \cdot \mathrm{B}(\tau \to \ell\bar{\nu}_\ell\nu_\tau)). \end{aligned}$$

To compute the branching ratios relevant to this analysis, we set $\mathrm{B}(t\bar{t} \to Wb)$=1, and take the best known branching ratios for Standard-Model processes from Ref. [15]. The MC event generator Isajet 7.58 provides the SUSY branching

ratios [16]. For the chosen SUSY parameters, the branching ratio B($\tilde{t}_1 \rightarrow \tilde{\chi}_1^{\pm} b$)=1. In case of an on-shell W boson, the branching ratio B($\tilde{\chi}_1^{\pm} \rightarrow W\tilde{\chi}_1^0$) is >0.99, and for the rest of the analysis assumed to be 1. The branching ratios of the three-body decays of the chargino in case of off-shell W bosons depend on the mass difference between the chargino and the neutralino $\Delta m_W = m_{\tilde{\chi}_1^{\pm}} - m_{\tilde{\chi}_1^0}$. Table 2.3 summarizes the branching ratios of the e+jets and μ+jets channel for the samples used in this analysis.

Sample	B(e+jets)	B(μ+jets)
$t\bar{t}$	0.173	0.169
$\tilde{t}_1\bar{\tilde{t}}_1$ with on-shell W	0.173	0.169
$\tilde{t}_1\bar{\tilde{t}}_1$ with Δm_W=70 GeV	0.158	0.157
$\tilde{t}_1\bar{\tilde{t}}_1$ with Δm_W=55 GeV	0.165	0.164

Table 2.3.: Branching ratios for the e+jets and μ+jets channel for the top and stop samples.

2.3.3. Sources of Background

The main background for $\tilde{t}_1\bar{\tilde{t}}_1 \rightarrow \ell$+jets events is from $t\bar{t}$ production, which is not surprising because of the many similarities. All other background sources are identical to the ones discussed in $t\bar{t}$ lepton+jets analyses. They can be subdivided into two components, an instrumental background and an inherent background. The instrumental background is from strong multijet production, which can mimic the signal signature due to detector imperfections. The inherent background consists of various physical processes that can all result in the same final state as the signal, namely $t\bar{t}$ production, W+jets production, Z+jets production, single-top production and diboson production.

Multijet Background

Multijet events can resemble $\tilde{t}_1\bar{\tilde{t}}_1$ and $t\bar{t}$ events, when $\not{E}_T$ is created by mismeasurements, and isolated leptons correspond to jets that mimic leptons. An electron may be mimicked by a pion within a highly electromagnetic jet or by a photon that converts to an e^+e^- pair in the detector material. A non-isolated muon can arise from a semi-leptonic b-decay. These mismeasurements do not occur often, but multijet production has an overwhelming cross section. The strategy for suppressing this type of background is to select high-quality leptons.

W+Jets Background

The dominant background to $\tilde{t}_1\bar{\tilde{t}}_1$ and $t\bar{t}$ events, however, is W+jets production, where a W boson is produced via the weak interaction, and jets arise from initial state gluon radiation or from an intermediary quark. Figures 2.9, 2.10 and 2.11 show some possible background sources. The cross section for W+jets is still high compared to the signal process. Requiring the presence of b-jets is an efficient way to reduce this background, but because a fraction of the W+jets events contain b- and c-jets, it is not possible to entirely suppress this inherent background.

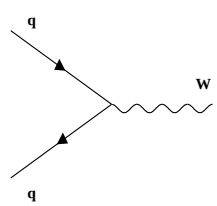

Figure 2.9.: Feynman diagram of a W+0jet event.

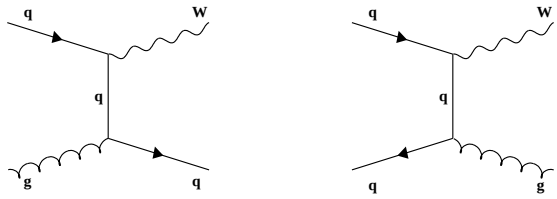

Figure 2.10.: Feynman diagrams of W+1jet events.

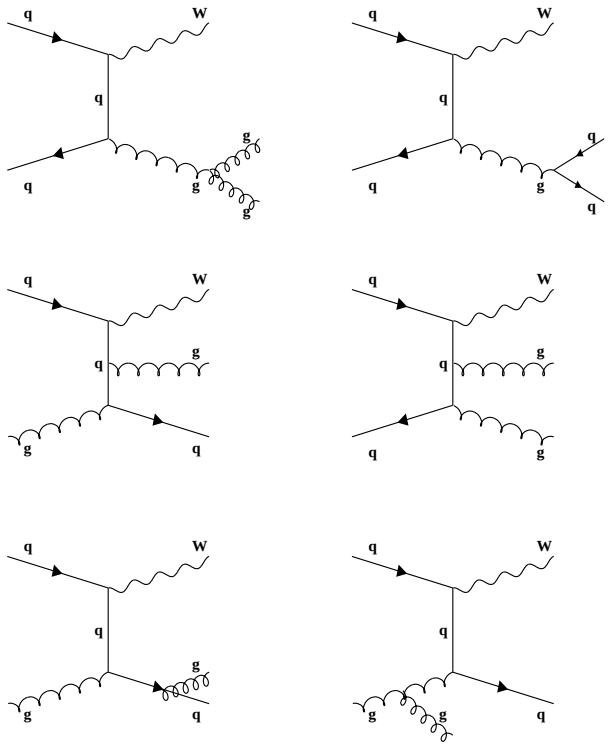

Figure 2.11.: Feynman diagrams of W+2jets events.

Minor Background Processes

Minor contributions to the background arise from Z+jets, single top, and vector-boson pair (diboson) production. Z+jets is produced through essentially the same diagrams as W+jets. When the Z boson decays to lepton pairs, and one lepton is not detected, the signature is the same as for $\tilde{t}_1\bar{\tilde{t}}_1$. Single-top production with a leptonic decay of the W boson from the top quark, and additional jets from initial or final-state radiation also produces the $\tilde{t}_1\bar{\tilde{t}}_1$ signature. Finally, the production of WW, WZ, and ZZ pairs can generate signatures identical to $\tilde{t}_1\bar{\tilde{t}}_1$.

2.3.4. Current Limits on Scalar Top-Quark Production

Limits on masses of supersymmetric particles obtained in experiments at the Large Electron-Positron Collider (LEP), which was a particle accelerator at the European Organization for Nuclear Research (CERN) operating from 1989–2000, can be found in Ref. [17]. In the MSSM with gaugino and sfermion mass unification at the Grand Unified Theory (GUT) scale, at which energy the strong, weak, and electromagnetic coupling constants converge, the lower limit on the mass of the lightest neutralino LSP is 47 GeV. Charginos are excluded up to masses of 103.5 GeV, depending on the model. Stop quarks in the $\tilde{t}_1 \to c\tilde{\chi}_1^0$ and $\tilde{t}_1 \to b\ell^+\tilde{\nu}_\ell$ decay channels are excluded up to masses of 100 GeV. Limits on the stop-quark mass have also been obtained at the Tevatron. For the $\tilde{t}_1 \to b\tilde{\chi}_1^+$ channel, CDF obtained upper limits on the stop-quark production cross section for stop-quark masses between 100 and 120 GeV at a center-of-mass energy of 1.8 TeV [18]. More recently, at a center-of-mass energy of 1.96 TeV, CDF sets a limit in the $\tilde{t}_1 \to c\tilde{\chi}_1^0$ channel at 132 GeV with 295 pb^{-1} of data [19], with 995 pb^{-1}, DØ has a limit of 149 GeV for a neutralino mass of 63 GeV for the same decay channel [20]. Also, using 400 pb^{-1} of data, DØ sets a limit in the $\tilde{t}_1 \to b\ell^+\tilde{\nu}_\ell$ channel of 186 GeV for a sneutrino mass of 71 GeV [21].

2.4. Setting Limits

There are many prescriptions for setting limits and quoting potential signal significances, each with their own advantages and drawbacks. Currently, the following methods are considered to be most robust: the Bayesian method [22], and two variations of the Frequentist approach: the Feldman-Cousins [23] and CL_S [24] methods.

For DØ Run II analyses, as the one presented in this dissertation, it is recommended to either use the DØ Run I Bayesian prescription or the LEP CL_S method [25]. The Bayesian method was chosen for this analysis, using tools developed for the Run II search for single top [26]. In what follows, the method used to set limits on the cross section for signal relies on the Bayesian approach, as implemented in those tools.

The goal is to obtain a Bayesian posterior probability as a function of the cross section for signal, given the observed counts and predicted signal and background yields. These can be provided as just simple numbers, but also as counts in bins in the distribution of some chosen discriminant. Starting with the first option, a likelihood function can be defined that is proportional to the probability to obtain the number of observed counts. The probability to observe D counts, if the mean count is d, is given by the Poisson distribution:

$$P(D|d) = \frac{e^{-d} d^D}{D!}. \tag{2.5}$$

The mean count d is the sum of the predicted signal contribution s and the contribution from the N background sources b_j:

$$d = s + \sum_{j=1}^{N} b_j = \sigma \cdot a + \sum_{j=1}^{N} b_j, \tag{2.6}$$

where σ is the cross section for the signal of interest, and a is the product of integrated luminosity, branching ratio, and all acceptances and efficiencies relevant to the signal.

Using Bayes theorem, the likelihood can be inverted:

$$L(d|D) = \frac{L(D|d)\,\pi(d)}{\int L(D|d)\,\pi(d)\,dd}, \tag{2.7}$$

where $\pi(d)$ is the prior probability that encodes the knowledge about the parameter d. Since the probability is proportional to the likelihood function,

$$P(d|D) = P(\sigma, a, \mathbf{b}|D) \propto L(D|\sigma, a, \mathbf{b})\,\pi(\sigma, a, \mathbf{b}), \tag{2.8}$$

where $\mathbf{b}(= b_1, b_2, \ldots, b_N)$ is an abbreviation for all background sources.

The prior probability $\pi(\sigma, a, \mathbf{b})$ contains the input knowledge about σ, a, and $\mathbf{b}$. Since it can be assumed that any knowledge of a and $\mathbf{b}$ is independent of the signal cross section σ, the prior probability can be factorized:

$$\pi(\sigma, a, \mathbf{b}) = \pi(\sigma)\,\pi(a, \mathbf{b}). \tag{2.9}$$

The prior $\pi(a, \mathbf{b})$ contains the estimates of a and $\mathbf{b}$ (often referred to as "nuisance" parameters) as well as the associated uncertainties from systematics. Conventionally, a flat prior is used for σ:

$$\pi(\sigma) = \begin{cases} \frac{1}{\sigma_{max}} & \text{if } 0 < \sigma < \sigma_{max}, \\ 0 & \text{otherwise}, \end{cases} \tag{2.10}$$

where σ_{max} is any sufficiently high upper bound on the cross section such that the posterior probability for $\sigma > \sigma_{max}$ is negligible.

Given an observed count D, the posterior probability density for the cross section

σ for signal can be obtained by integrating the posterior in Eq. 2.8 over the nuisance parameters a and $\mathbf{b}$:

$$P(\sigma|D) \propto \int \cdots \int L(D|\sigma, a, \mathbf{b})\, \pi(a, \mathbf{b})\, da\, d\mathbf{b}. \tag{2.11}$$

$P(\sigma|D)$ is normalized to satisfy $\int P(\sigma|D) d\sigma = 1$. A Bayesian upper limit σ_{CL} at some confidence level CL is a solution of:

$$\int_0^{\sigma_{CL}} P(\sigma|D)\, d\sigma = CL. \tag{2.12}$$

Alternatively, the measured cross section can be defined as the mean or the mode of $P(\sigma|D)$.

To combine two or more channels, or to use counts in bins of a distribution in a discriminator, the likelihood function in Eq. 2.11 is replaced by a product of the likelihoods over all M bins or channels:

$$L(D|d) = \prod_{i=1}^{M} L(D_i|d_i). \tag{2.13}$$

This method can also be used to set limits on (or measure the cross section for) two different signal processes by constructing a Bayesian posterior probability in a two-dimensional space.

3. Experimental Setup

To probe the realm of truly elementary particles requires high energies to break up ordinary particles such as protons and use part of their energy to produce new and more fundamental particles. These high energies are provided by particle accelerators, which accelerate and then collide the ordinary particles. Fermilab's Tevatron collider is currently the highest-energy collider in the world. It has a radius of ≈ 1 km, and collides beams of protons and antiprotons at a center-of-mass energy of 1.96 TeV. Fermilab is located in Batavia, Illinois, in the western suburbs of Chicago.

Many of the produced particles decay within a very short time. Sometimes they form hadrons before these also decay. Detectors are built to identify and measure the decay products. Multi-purpose detectors usually consist of a tracking system inside a magnetic field, a calorimeter, and an outer muon system. Charged particles can be detected in the inner tracking system and in the calorimeter, and, in the case of muons, in the outer muon system. Neutral particles are detected in the calorimeter, or in some cases, as for neutrinos, not at all. The DØ experiment with its multi-purpose detector is one of two experiments at Fermilab's Tevatron collider. The first data-taking period lasted from 1992 to 1996 (Run I), during which time the CDF and DØ detectors collected ≈ 125 pb^{-1} of data at a center-of-mass energy of 1.8 TeV. After an upgrade of the accelerator and the detectors, Run II started in March 2001, and up to 6-7 fb^{-1} of data is expected by 2009.

This chapter introduces the accelerator and the components of the DØ detector.

3.1. The Tevatron Collider

The Tevatron is the last stage of an accelerator chain that consists of consecutive accelerators of increasing energies [27]. It starts with accelerating negative hydrogen ions to 750 keV in a Cockroft-Walton accelerator, followed by a linear accelerator, which boosts their energy to 400 MeV. After stripping off the electrons, the protons are accelerated to 8 GeV in the Booster synchroton ring and then to 150 GeV in the Main Injector, where the protons are grouped into bunches. Antiprotons are produced by directing some of the proton bunches from the Main Injector at a nickel-copper target. The antiprotons are accumulated and accelerated to 8 GeV before being returned to the Main Injector, where they are also accelerated to 150 GeV. Finally, the Tevatron accelerates the protons and antiprotons from 150 GeV to 980 GeV. Figure 3.1 shows a schematic of the whole accelerator chain.

Both protons and antiprotons are arranged into 36 bunches with a 396 ns bunch spacing, the 36 bunches are again divided into three super-bunches with 2 μs between them. A proton bunch consists of $\approx 3 \times 10^{11}$ protons, whereas an antiproton bunch consists of $\approx 3 \times 10^{10}$ antiprotons. They collide at the two detector positions of CDF and DØ. At DØ, the interaction region along the beam direction is spread out according to a Gaussian distribution with a standard deviation $\approx$ 25 cm.

3.2. The DØ Detector

Figure 3.2 shows a side view of the Run II DØ detector, which is $\approx$ 20 m long and 13 m high. DØ is a multi-purpose detector consisting of several subsystems, which ensure precise measurement of electrons, muons and jets [28]. An inner tracking system resides within a $\approx$ 2 T magnetic field, which is surrounded by a finely grained calorimeter and an outer muon system. There are also luminosity

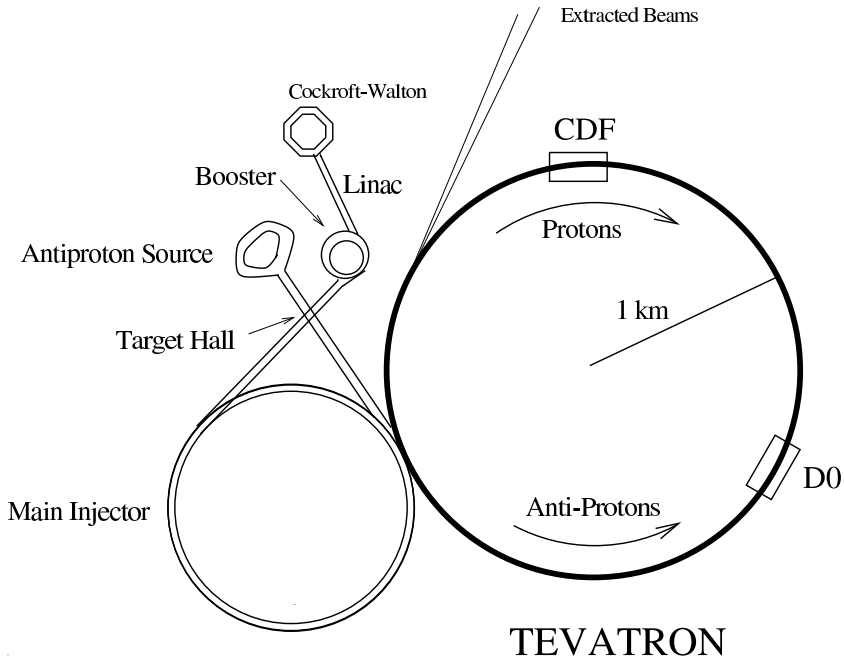

Figure 3.1.: The accelerator chain at Fermilab.

monitors and proton detectors in the very forward regions, and a three-level trigger system for selecting collisions of greatest interest. The upgrade for Run II included the complete tracking system with its solenoid, preshower detectors, forward muon chambers, an improved shielding system, and a faster data acquisition system.

The coordinate system used in DØ analyses is right-handed, with the x-coordinate pointing towards the center of the ring, the y-coordinate upwards and the z-coordinate in the direction of the incident proton. A more useful set of coordinates for parameterizing particle trajectories relies on cylindrical (r, φ, η), defined by:

$$r = \sqrt{x^2 + y^2}, \tag{3.1}$$

$$\phi = \arctan \frac{y}{x}, \quad \text{and} \tag{3.2}$$

$$\eta = -\ln \tan \frac{\theta}{2}, \tag{3.3}$$

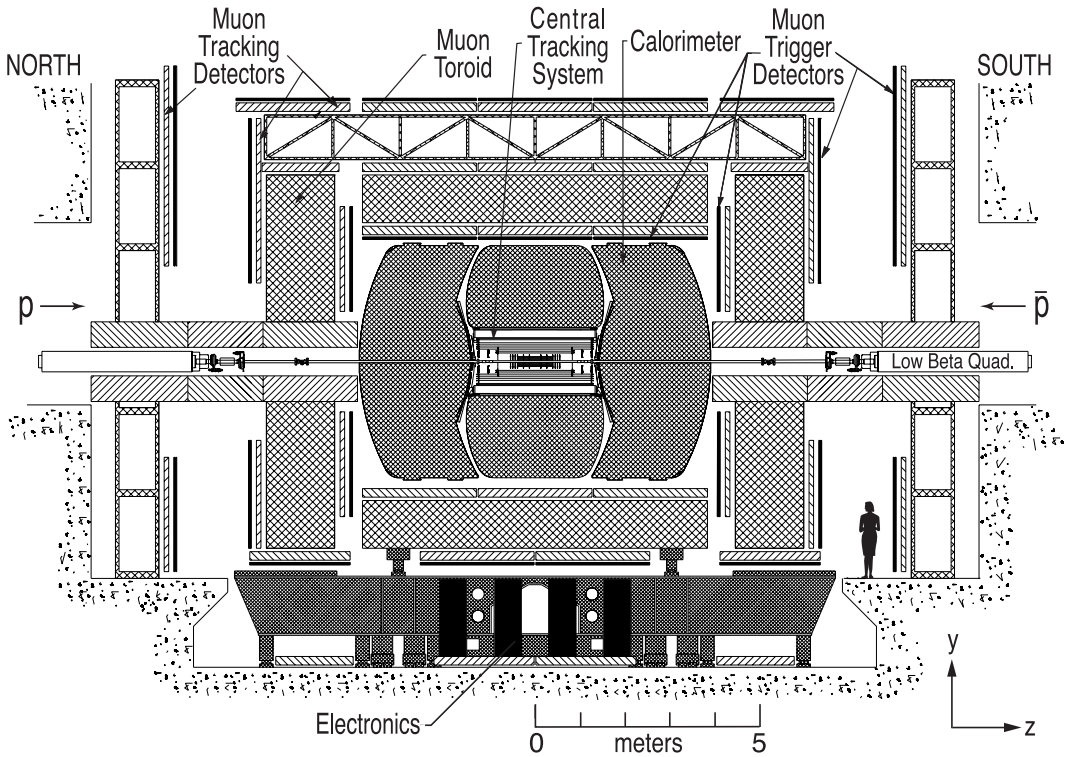

Figure 3.2.: Side view of the DØ detector.

where θ is the angle of any trajectory relative to the z-axis. The pseudorapidity η approximates the rapidity $y = \frac{1}{2}\ln(\frac{E+p_z}{E-p_z})$ when particle mass can be neglected. Usually, the coordinates of any trajectory are given relative to the primary vertex of an event, which in the case of η is called "physics η." Another possibility is to use detector-centered coordinates, defined relative to the center of the detector, which define "detector η_{det}."

3.2.1. Central Tracking System

The central tracking system consists of the Silicon Microstrip Tracker (SMT) and the Central Fiber Tracker (CFT). These elements occupy the radial space up to 52 cm from the center of the beam pipe, and is up to 2.52 m long. The two

detectors are located within a solenoid with a magnetic field of 2 T along the z-direction. Charged particles are deflected in the magnetic field. By measuring the radius of curvature r of the track in the $r - \varphi$ plane, the transverse momentum $p_T = \sqrt{p_x^2 + p_y^2}$ of the particle can be determined:

$$r[\mathrm{m}] = \frac{p_T[\mathrm{GeV}]}{0.3 \cdot B[\mathrm{T}]}. \tag{3.4}$$

Measuring the track inclination in the $r - z$ plane gives the complete three-dimensional information for the track.

Figure 3.3 shows a longitudinal section of the inner detector, along with the tracking system and the preshower detectors.

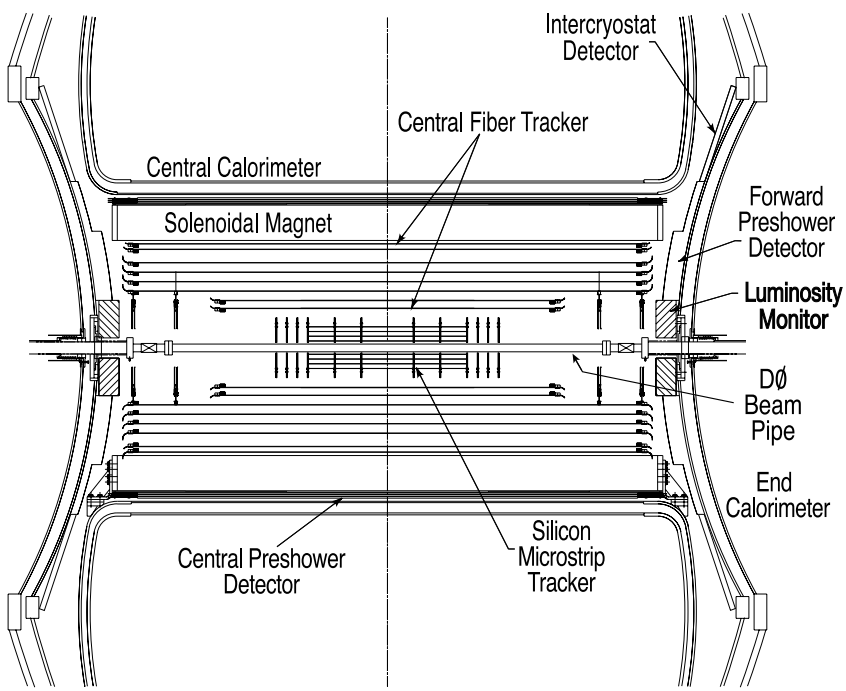

Figure 3.3.: Longitudinal section of the DØ tracking and preshower systems.

Silicon Microstrip Tracker

The Silicon Microstrip Tracker (SMT) is innermost of the detector components [29]. Besides tracking, an important function of the SMT is to reconstruct secondary vertices of hadrons from bottom-quark decays, in order to identify jets originating from bottom quarks, as well as to distinguish them from jets that originate from the fragmentation of light quarks or gluons. The detector is 2.40 m long, and covers the region of $|\eta_{det}| < 3$, almost the full range of the calorimeter and the muon system. Figure 3.4 shows the composition of the SMT, as barrels interspersed with "F"-disks in the center and additional "H"-disks in the forward regions. This

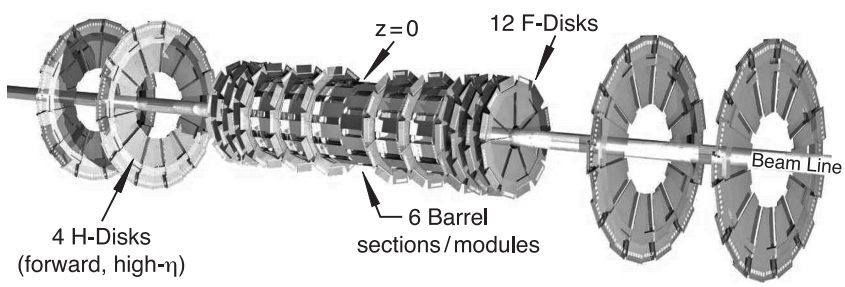

Figure 3.4.: 3-D view of the Silicon Vertex Detector.

construction of barrels and disks provides hits in the detector for tracking over an interaction region of standard deviation ≈ 25 cm. The barrel detectors provide primarily the $r - \varphi$ coordinates, whereas the disks are also sensitive to $r - z$ coordinates.

Each of the six barrels is 12 cm long and has 72 ladders arranged in 4 layers, each of which has two overlapping sublayers. This layer structure can be seen in the cross section of a barrel detector shown in Fig. 3.5. The sensors of the SMT are a combination of single-sided (SS), double-sided (DS), and double-sided double-metal (DSDM) technologies. The two outer barrels use single-sided and double-sided 2° stereo ladders, while the four inner ones have double-sided double-

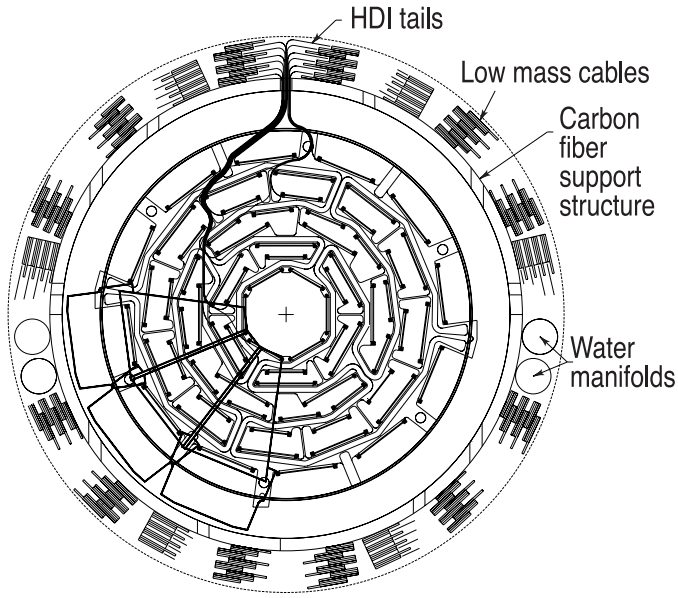

Figure 3.5.: Cross section of a Silicon Vertex Detector barrel, showing its layered structure.

metal 90° stereo and double-sided 2° stereo ladders. There are two types of disks. The 12 F-disks, interspersed between, and at either end of, the barrel section, are made of 12 wedges of double-sided stereo detectors. The 4 H-disks at the ends of the silicon detector have a larger diameter, and are made of 24 pairs of single-sided detectors. While single-sided sensors provide only the axial (φ) position of a hit, double-sided sensors with stereo angles can provide a $\varphi - z$ measurement by pinpointing the intersection of two activated strips. However, this can lead to ambiguities when two hits are close to each other and the activated strips intersect at points with no true hits. Keeping the stereo angles small minimizes this kind of problem.

Scintillating Fiber Tracker

The Scintillating-Fiber Tracker or Central Fiber Tracker (CFT) consists of 76,800 scintillating fibers arranged in eight layers [28]. Each layer is mounted on a con-

centric support cylinder, with radii ranging from 20 cm to 52 cm, as shown in Fig. 3.3. The two innermost layers are 1.66 m long to accommodate the SMT H-disks, whereas the outer layers are 2.52 m long. These provide coverage up to $|\eta_{det}| < 1.6$. Each of the eight layers again consists of two doublet layers, one oriented along the beam axis (axial layer), and the other one at a stereo angle of $\pm 3°$ (stereo layer). The fibers have a diameter of 835 μm, which results in a doublet layer resolution of about 100 μm. The fibers scintillate at $\approx$ 530 nm, which is the yellow-green part of the visible spectrum. Clear fiber light guides, 8 to 12 m long, conduct the light to the "Visible Light Photon Counters" (VLPCs), where the signals are read out. The VLPCs have high quantum efficiency ($\geq$75%), and minimum-ionizing particles produce an average of eight photoelectrons per layer.

Solenoid

A magnetic field of $\approx$ 2 Tesla is provided by a superconducting solenoid magnet that encloses the tracking system [28]. Since the solenoid was added after Run I, its size was constrained by the available space to 2.73 m in length and 1.42 m in diameter, and presents 0.87 radiation lengths of material at $\eta = 0$. The solenoid was designed to optimize the momentum resolution $\Delta p_T/p_T$ and pattern recognition in tracking. The operating temperature is 10 K, the current 4749 A, and 5.3 MJ of energy is stored in the field.

3.2.2. Calorimeter System

The calorimeter system consists of preshower detectors, a uranium/liquid-argon calorimeter and intercryostat detectors that are used to identify and measure energies of electrons, photons and jets, which lose most of their energy through interactions with the calorimeter material. Above a certain energy threshold, which depends on the calorimeter material, electrons lose their energy mainly through

bremsstrahlung. Electrons deflected by atomic nuclei emit photons, which create electron-positron pairs, which then also emit photons. After falling below the energy threshold for bremsstrahlung, the electrons lose their energy through ionization of atoms. The mean distance over which an electron has its energy reduced to $1/e$ of the original value depends on the detector material, and is called the radiation length X_0. Hadronic particles on the other hand produce pions and nucleons by interacting inelastically with nuclei. If their energy is sufficiently high, these secondaries can also interact inelastically with other downstream nuclei, and generate showers of hadronic particles. The characteristic length scale for this process is the nuclear interaction length λ_I, which depends on the detector material. Muons are minimum ionizing particles (MIPs) at energies of the Tevatron, and leave only a very small fraction of their energy in the calorimeter. Their momenta are measured in the muon system. Neutrinos deposit no energy at all in the detector, but their presence in an event can be inferred by any imbalance in momentum in the transverse plane (after correcting for the presence of muons). This quantity is called the "missing transverse energy" ($\not{E}_T$).

Preshower Detectors

Figure 3.3 shows a sketch of the preshower detectors, which are designed to enhance electron and photon identification, as well as background rejection [28].

The Central Preshower Detector (CPS) is located outside the solenoid at a radius of about 72 cm, and covers the region up to a pseudorapidity of $|\eta_{det}| \approx 1.3$. Its purpose is to help restore the electromagnetic energy resolution degraded by the presence of the solenoid. Besides measuring the energy, it also serves as a tracker because of its good spatial resolution. Between the solenoid and the CPS lies a 5.6 mm thick lead radiator, which corresponds to about one radiation length. Together with the solenoid it presents two to four radiation lenghts, depending

on the angle of entry, and initiates the showering of electrons and photons, to distinguish them from pions. The CPS has three layers of scintillating fibers, which are read out by wavelength-shifting (WLS) fiber readouts in 7,680 channels. The signal is conducted by clear light-guide fibers to the VLPCs.

The Forward Preshower Detectors (FPS) are mounted on the end-calorimeter cryostats and cover the pseudorapidity range $1.5 < |\eta| < 2.5$. They consist of two double layers of scintillators, separated by two radiation lengths of lead-stainless-steel absorber. The inner layer is called the MIP layer, where all charged particles tend to leave minimum ionizing signals, and photons tend not to interact at all. Electrons and photons shower in the absorber, producing a signal in the outer layer called the shower layer. By matching the signals in the two layers, electrons can be distinguished from photons.

Calorimeter

Because of its excellent performance, the DØ uranium/liquid-argon calorimeter has not been changed since Run I, but the front-end electronics were upgraded for Run II [28, 30].

Figure 3.6 shows the three parts of the calorimeter, the central calorimeter (CC) and the two end calorimeters (EC). Each is contained in its own cryostat, which maintains the liquid argon at a temperature of $\approx$ 87 K. A longitudinal section of a quarter of the calorimeter, shown in Fig. 3.7, indicates that the CC covers the pseudorapidity range up to $|\eta_{det}| \approx 1$, with the ECs extending the range to $|\eta_{det}| \approx 4$.

Each sector of the calorimeter is divided into electromagnetic and hadronic sections. The central calorimeter has three of these, namely, a front electromagnetic (CCEM), a fine hadronic (CCFH) and a coarse hadronic (CCCH) section. The end calorimeters are divided into four sections, the electromagnetic

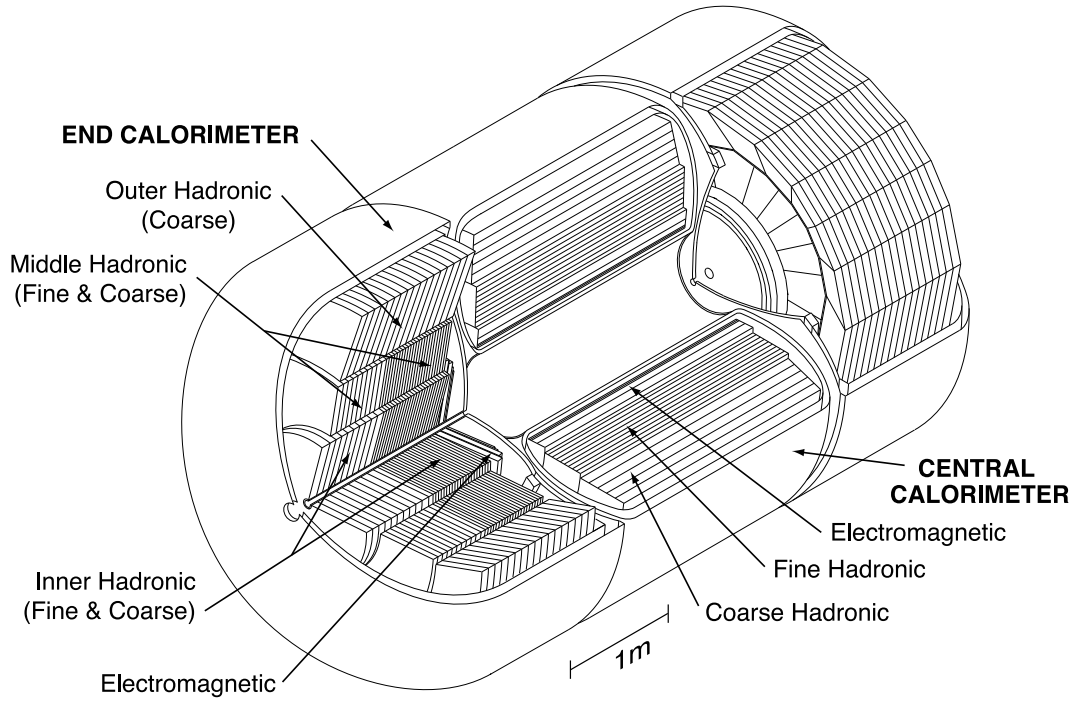

Figure 3.6.: Isometric view of the calorimeter.

(ECEM) section, the inner hadronic (ECIH) covering $2.0 < |\eta_{det}| < 4.2$, the middle hadronic (ECMH) covering $1.5 < |\eta_{det}| < 2.0$ and the outer hadronic (ECOH) $1.1 < |\eta_{det}| < 1.5$ section. These sections are further subdivided into cylindrical floors, the electromagnetic sections into EM1 to EM4, and the hadronic sections into FH1 to FH3 and CH. This subdivision helps to distinguish the "longitudinal" shower profiles of electrons and hadrons. The electromagnetic layers contain 65.5 mm of nearly pure uranium in total, which is equivalent to approximately 20 radiation lengths ($X_0^U \approx 3.2$ mm), so they capture most of the electromagnetic energy. The nuclear interaction length ($\lambda_I^U \approx 10.5$ cm) is much larger, and much of the energy of hadronic particles is therefore deposited in the hadronic layers, which are ≈ 6 nuclear interaction lengths thick.

The calorimeter is divided into towers of $\Delta\eta \times \Delta\varphi = 0.1 \times 2\pi/64 \approx 0.1 \times 0.1$.

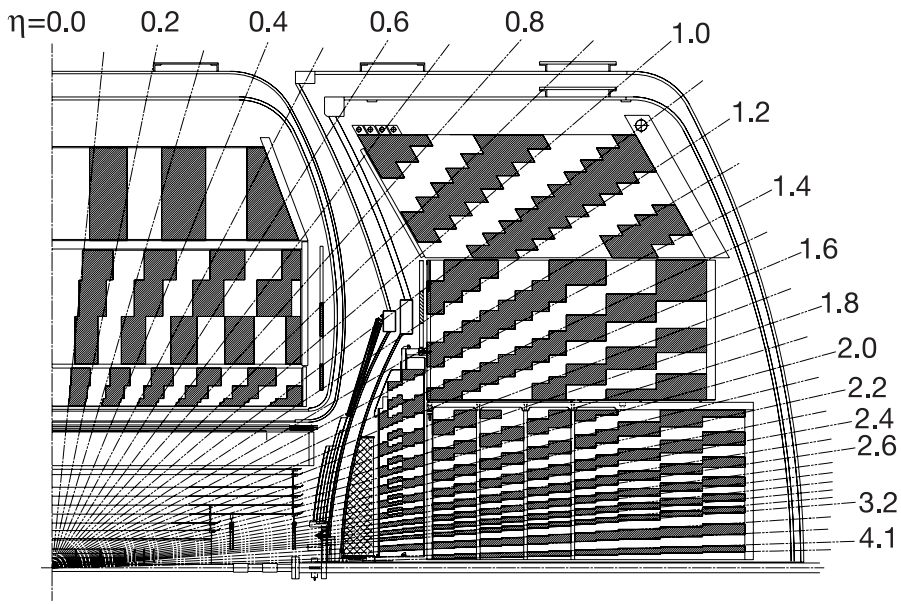

Figure 3.7.: Sections of a quarter of the DØ calorimeter.

In the third EM layers, where the showers are expected to reach their maximum, the cell granularity is doubled in both η and φ. Since typical cone sizes of jets are $\Delta R = \sqrt{\Delta\eta^2 + \Delta\varphi^2} \approx 0.5$, the segmentation is important for characterizing the shape of any jet.

Figure 3.8 shows a unit cell of the calorimeter, which consists of an absorber plate, where the showers develop, a liquid-argon gap, where the ionization is generated, a signal board made of copper with resistive coating, where image charges are sensed, followed by the next liquid-argon gap. While the active medium is always liquid argon, for mechanical reasons and cost, the absorber material differs in different sections. The electromagnetic sections use 3 or 4 mm nearly pure depleted uranium plates, the fine hadronic sections 6 mm uranium-niobium alloy and the coarse hadronic modules contain 46.5 mm thick plates of copper in the CC or stainless steel in the EC. An electric field to collect the ionization is established by

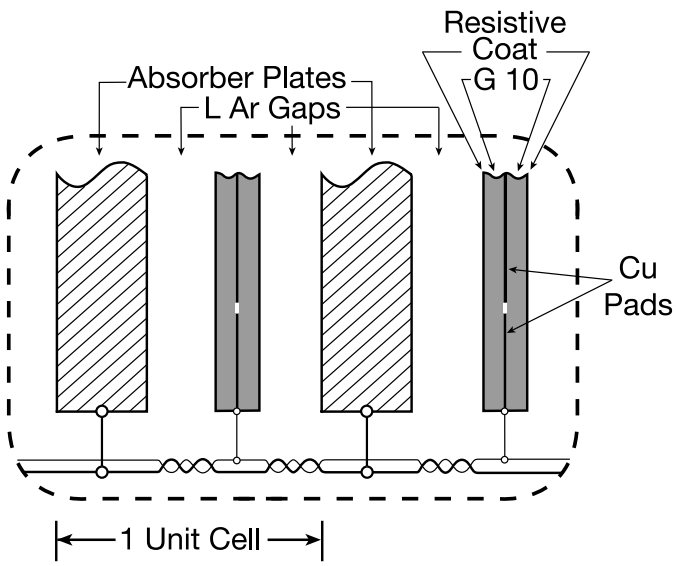

Figure 3.8.: Unit cell in the liquid-argon DØ calorimeter.

grounding the metal absorber plates and connecting the resistive surfaces of the signal boards to a positive high voltage of ≈ 2.0 kV.

The response of the calorimeter is defined by the fraction of deposited energy measured in the calorimeter. This differs for electromagnetic and hadronic particles due to different processes through which they interact in the detector. The ratio of the electromagnetic to hadronic response of the DØ calorimeter ranges 1.02–1.09, which makes it an almost "compensating" calorimeter.

The energy in the calorimeter is measured by integrating the charge produced in the liquid argon, where the signal is proportional to the deposited energy E. Because the count is subject to Poisson sampling fluctuations in the collected charge n $\approx \sqrt{n}$, the relative resolution of the energy measurement should go as:

$$\frac{\Delta E}{E} \propto \frac{\Delta n}{n} = \frac{1}{\sqrt{n}} \propto \frac{1}{\sqrt{E}}. \tag{3.5}$$

Including other contributions, the formula used is [31]:

$$\left(\frac{\Delta E}{E}\right)^2 = C^2 + \frac{S^2}{E} + \frac{N^2}{E^2}, \tag{3.6}$$

where the contributions C, S and N reflect calibration uncertainties, sampling fluctuations and contributions from noise, respectively. Test-beam measurements with electrons and pions gave the results listed in Table 3.1 [31, 32].

Particle	C	S	N
e	$0.0115^{+0.0027}_{-0.0036}$	$(0.135 \pm 0.005)\ \sqrt{\text{GeV}}$	0.43 GeV
π	0.032 ± 0.004	$(0.45 \pm 0.04)\ \sqrt{\text{GeV}}$	0.975 GeV

Table 3.1.: Test-beam results for calorimeter resolution.

Intercryostat Detector

Gaps between the central calorimeter and the end calorimeters, due to the separate cryostats, lead to a deteriorated coverage of the pseudorapidity region $0.8 < |\eta_{det}| < 1.4$. The Intercryostat Detector (ICD) [28] provides layers of scintillating tiles, which are attached to the exterior surface of the end cryostats, and cover the region $1.1 < |\eta_{det}| < 1.4$. In addition, calorimeter readout cells called "massless gaps" are located within both the central and end cryostats in front of the first layers of uranium to improve sampling of showers in that region of η.

3.2.3. Muon System

Muons are minimum-ionizing particles (MIPs) and the only charged particles that can penetrate the calorimeter with high probability and reach the muon detector. The muon system consists of toroidal magnets, a central muon detector and a forward muon detector [28]. An exploded view of the muon detectors is shown in

Figs. 3.9 and 3.10. The central as well as the forward detectors have wire chambers as well as scintillation detectors, and consist of the three A, B, and C layers. The wire chambers or drift tubes are gas-filled rectangular volumes that contain a wire under high voltage. When a charged particle passes through the gas, it ionizes the gas and the resulting ions and electrons drift towards the wire or to the walls of the tube, respectively. The hit position along the wire is extracted using vernier cathode pads on the walls and the difference in arrival times from neighboring wires. Scintillators absorb energy from the ionizing particle and fluoresce lower-energy photons, which are then collected by photomultiplier tubes. The muon system identifies muons, triggers on them and measures their momenta and charge from the curvature of their trajectories in the field of the toroid magnets.

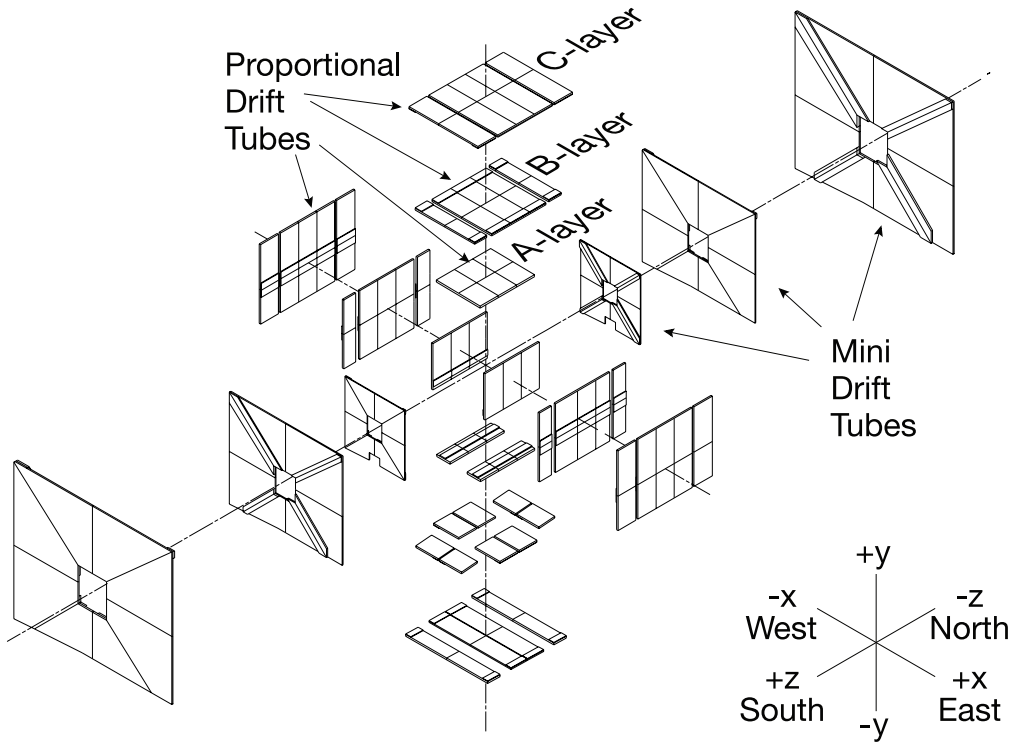

Figure 3.9.: Exploded view of the muon drift chambers.

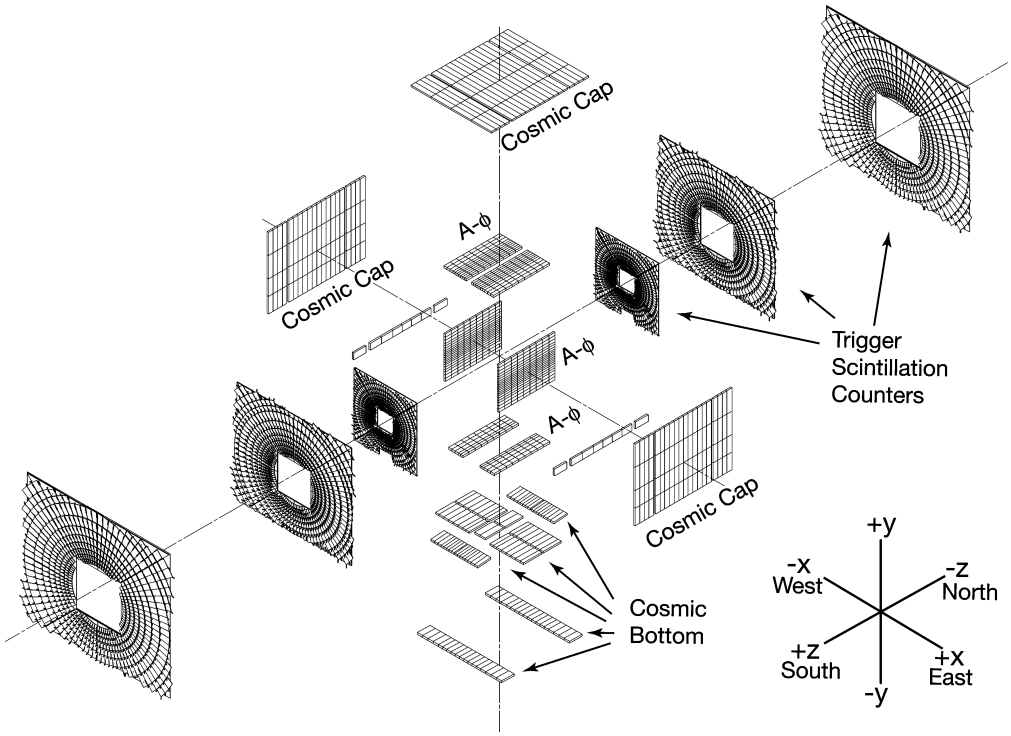

Figure 3.10.: Exploded view of the muon scintillation detectors.

Toroidal Magnets

The toroidal magnets are unchanged from Run I [33], but the operating current has been reduced to 1500 A, which results in a magnetic field of 1.8 T. The magnets are located between layer A and B of the muon detectors, at a radial distance of 317.5 cm from the beam line. The three parts of the toroidal magnet form a square annulus 109 cm thick, and combined weigh 1973 metric tons. The central part is accompanied by two C-shaped sections located at $454 \leq |z| \leq 610$ cm. The magnetic field is either along the x or the y-direction, so that a muon emerging from the center of the detector and hitting the toroid field perpendicularly will be deflected in the z-direction, that is, along the beamline.

Central Muon Detector

The central muon system covers the region up to $|\eta_{det}| \approx 1$. The drift chambers of the central system are called Proportional Drift Tubes (PDTs), and they are typically 2.8×5.6 m^2 in cross section, with a single drift cell being 10.1×5.5 cm^2. The gas mixture used in the PDTs consists of 84% argon, 8% methane, and 8% CF_4, which results in a drift velocity of ≈10 cm/μs, and a maximum drift time of about 500 ns. The drift chamber wires are oriented parallel to the magnetic fields of the toroids, which are along the x-direction on the top and bottom, and along the y-direction on the sides. The scintillation detectors on the top, sides and bottom of the outer C layer of the central muon system are called "cosmic caps" and "bottom counters", and they are positioned with their width along the z-direction and their length along φ. The scintillation counters on the A layer PDTs are called "Aφ" scintillation counters. While all the scintillation counters are used only for triggering, the PDTs are used for obtaining precise coordinate measurements as well as in triggering.

Forward Muon Detector

The forward muon system was added for Run II, it extends muon coverage to $|\eta_{det}| \approx 2$ [28]. The drift chambers are smaller in the forward detector, and are called Mini Drift Tubes (MDTs). Each MDT consists of eight cells, each with a cross section of 9.4×9.4 mm^2. The gas mixture is 90% CF_4 and 10% CH_4. The MDTs do not provide the hit positions along the wire, since the resolution of the scintillators is far superior. The trigger scintillation counters in the forward system cover all three layers, and are arranged in an $r - \varphi$ geometry. A photograph of the outermost layer is shown in Fig. 3.11. As in the central system, the scintillation counters are used for triggering, whereas the MDTs are used for both triggering and coordinate measurements.

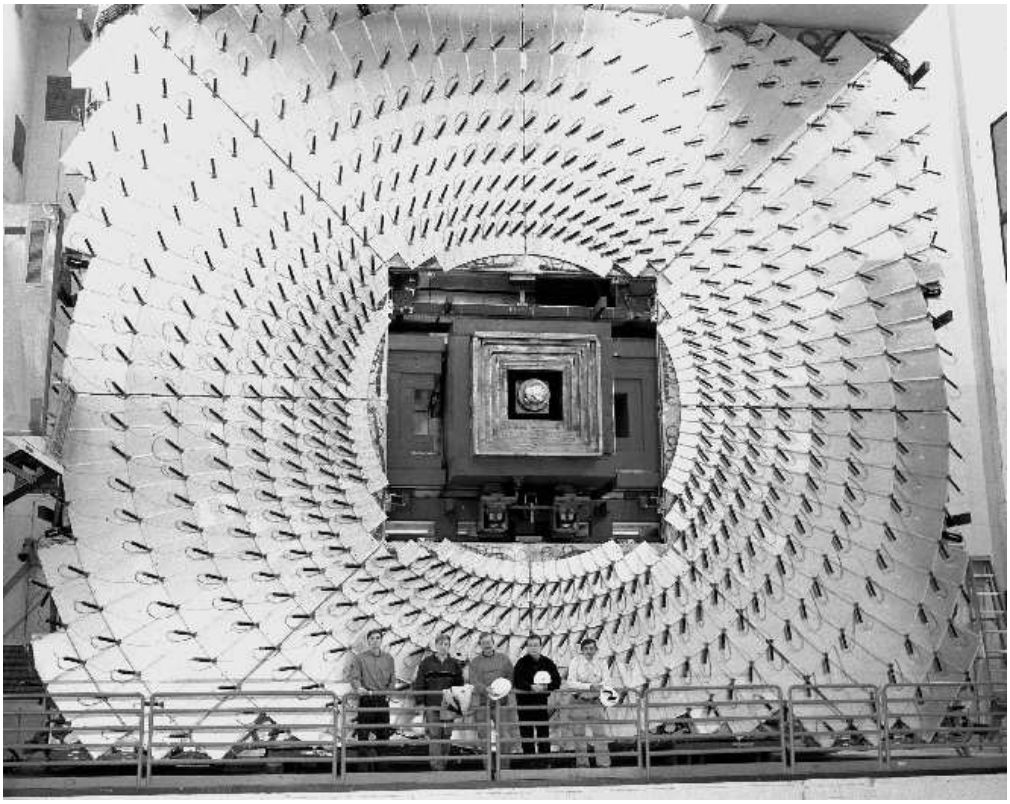

Figure 3.11.: Photograph of the C layer of muon scintillation counters of the forward muon system.

3.2.4. Forward Proton Detector

The Forward Proton Detector (FPD) [28, 34] measures the momenta of protons and antiprotons scattered at small angles of the order of 1 mrad. Such measurements are used in studies of diffractive phenomena.

3.2.5. Luminosity Monitor

Primary purpose of the Luminosity Monitors (LM) [28, 35] is to determine the Tevatron luminosity at the DØ interaction region by detecting inelastic $p\bar{p}$ collisions. The LM also provides information on the beam halo and yields a fast

measurement of the z coordinate of the interaction vertex.

The LM detector consists of two arrays of twenty-four plastic scintillation counters that are read out with photomultipliers (PMT). A schematic drawing of an array is shown in Fig. 3.12. The arrays are located in front of the end calorimeters at $z = \pm 140$ cm, and occupy the region between the beam pipe and the Forward Preshower Detector. The counters are 15 cm long, and cover the pseudorapidity range 2.7< $|\eta_{det}|$ <4.4.

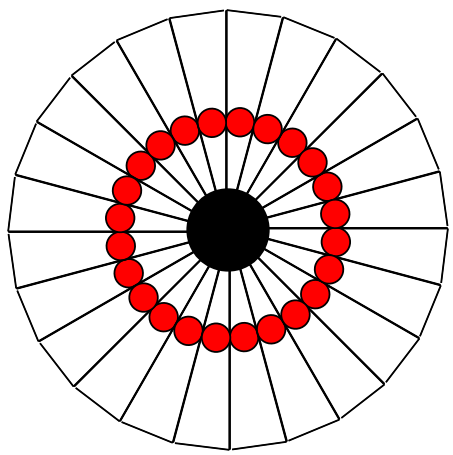

Figure 3.12.: Schematic view of the luminosity counters showing the PMTs as small filled circles.

The instantaneous luminosity $\mathcal{L}$ is determined with the LM detector through the measurement of the rate of inelastic $p\bar{p}$ collisions [36]:

$$\mathcal{L} = \frac{1}{\varepsilon \times A \times \sigma_{p\bar{p}}} \cdot \frac{dN}{dt}(p\bar{p}), \tag{3.7}$$

where $\sigma_{p\bar{p}}$ is the inelastic cross section, A the LM acceptance, and ε the efficiency of the LM detector. Precise time-of-flight measurements are made to distinguish $p\bar{p}$ interactions from background from the beam halo. The z coordinate of the interaction vertex z_v is estimated from the difference in time-of-flight for the two

LM detectors. Beam halo particles traveling along the z direction will have $z_v \approx \mp 140$ cm, and can be eliminated by the requirement of $|z_v| < 100$ cm.

A "luminosity block" is the fundamental unit of time for the luminosity measurement. Each block is indexed by the luminosity block number (LBN). The LBN increases monotonically throughout Run II, and is incremented at least every 60 seconds, which is sufficiently short to assure that the instantaneous luminosity is constant during each luminosity block. Luminosity calculations are made independently for each LBN, and averaged over the luminosity block.

3.2.6. Trigger System

At the Tevatron, a bunch crossing occurs every 396 ns, resulting in a data rate of 2.5 MHz, whereas only 50 Hz of data can be stored [28, 37]. The purpose of the trigger system is to recognize interesting events and initiate their storage. The DØ trigger achieves that with three levels, and the elements of the trigger system are shown in Figs. 3.13 and 3.14. This section gives a general overview of the trigger system. The triggers specific to the presented analysis are discussed in Section 5.1.

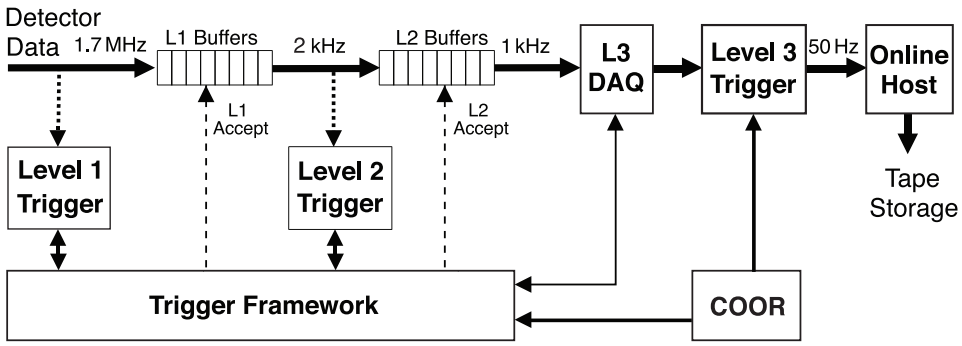

Figure 3.13.: The DØ trigger and data acquisition system.

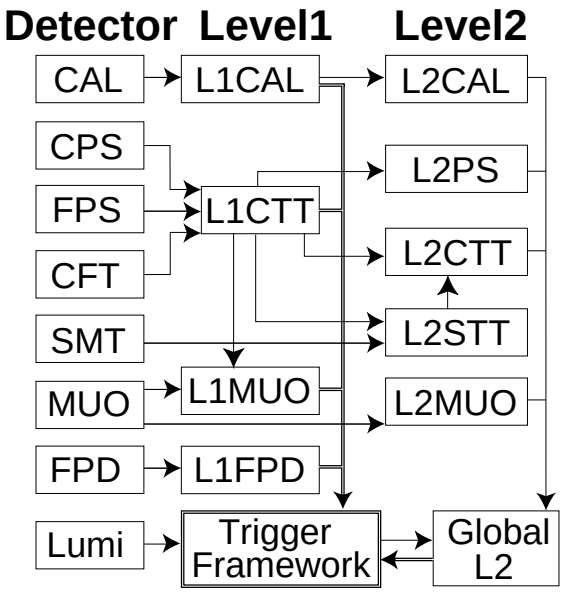

Figure 3.14.: The Level 1 and Level 2 trigger system.

Level 1

The Level-1 (L1) trigger decision is based entirely on hardware. The calorimeter towers, which are defined by $\Delta\eta \times \Delta\varphi = 0.2 \times 0.2$ at L1, have to exceed certain thresholds in transverse energy. Also, the hit patterns found in the preshower detectors, the CFT, and the muon chambers have to match tracks with a transverse momentum (p_T) above a preprogrammed value. Together, these provide electron triggering up to $|\eta_{det}| = 2.5$ and muon triggering up to $|\eta_{det}| = 2.0$. The L1 trigger operates without deadtime, and makes a decision in 3.5 μs, passing on 10 kHz of data to Level 2.

Level 2

The Level-2 (L2) trigger has two stages. In the preprocessor stage, the information from the subsystems is collected separately to form objects such as tracks or energy

clusters. The subsystems included are the calorimeters, the preshower detectors, the CFT, SMT and the muon chambers. All the information is combined at the global-processor stage to form physical objects such as electron candidates, and, based on this information, the trigger decision is made. L2 has a deadtime of 5% at the highest data rates, requires $< 100\mu$s for decision, and reduces the data rate to 1 kHz.

Level 3

At Level 3 (L3), a simplified reconstruction of the entire event is made on farm nodes. This reduces the data rate to the desired 50 Hz, which can then be written to tape for offline analysis. The average event size is ≈ 250 kBytes.

4. Object Identification and Event Reconstruction

The collected data initially consists of about a million channels of outputs, such as signals in trackers, energies, and trigger information. To identify objects and reconstruct events one relies on a collection of algorithms [38]. In the following we describe the reconstruction and identification of key objects and the selection criteria used in the analysis.

4.1. Track Reconstruction

Charged particles passing through the tracking system in the magnetic field of the solenoid leave dot-like hits on their curved path through various layers. Figure 4.1 shows the average number of hits as a function of track η in the two tracking detectors. Because of its geometry, the SMT detects hits up to high pseudorapidity. Using these hits, the tracking algorithm reconstructs the trajectories of charged particles. Two different algorithms are employed, the Histogram Track Finder (HTF) [40] and the Alternative Algorithm (AA) [41], whose results are combined in the end.

The trajectory of a charged particle in a magnetic field can be characterized by the radius of curvature ρ, the distance of closest approach (DCA) to the interaction point, called impact parameter d_0, and the transverse direction ϕ of the track at the

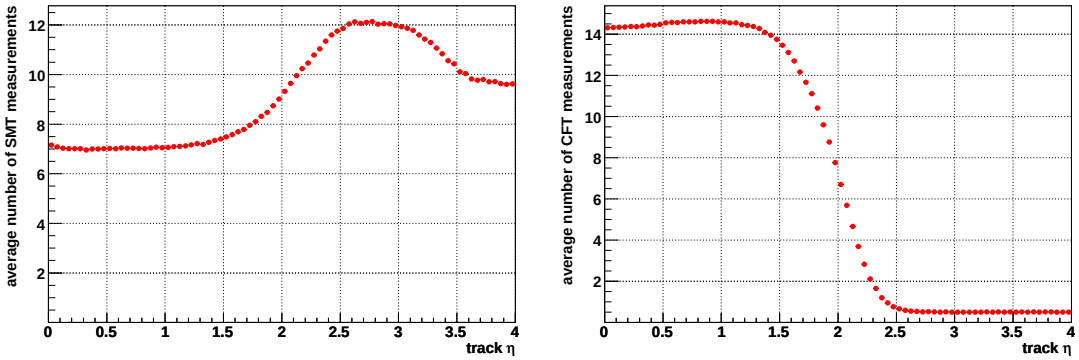

Figure 4.1.: Average number of hits as a function of track η [39]. Left: in the SMT, right: in the CFT.

DCA. Figure 4.2 compares the resolution on the impact parameter as a function of the transverse momentum for tracks in data and MC [39]. For tracks with small

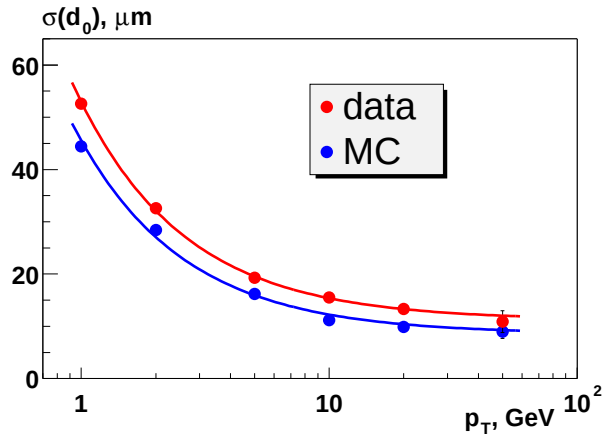

Figure 4.2.: Impact parameter resolution as a function of track p_T [39].

impact parameter $d_0 \approx 0$, this parameter can be neglected, and a track is fully described by ρ and ϕ. Each pair of hits in the tracker provides a candidate track, which corresponds to a point in the $\rho - \phi$ space. True tracks can, in principle, appear as concentrations in a $\rho - \phi$ scatterplot. The HTF method improves on

this idea using the Hough transform. Each hit by itself represents a line in the $\rho - \phi$ space, and intersections of lines yield track candidates.

The Alternative Algorithm starts from a combination of three hits in the silicon tracker (SMT), and extrapolates the trajectory outwards to the next SMT or CFT layer. If there is a hit within this "road" and its χ^2 contribution to track reconstruction is below a certain threshold, the point is added to the track. This is continued until the last CFT layer is reached or if three layers have no matching hits.

In the end, the tracks from the two algorithms are combined using a Kalman algorithm [42].

4.2. Primary Vertex

The primary vertex (PV) is the location of the $p\bar{p}$ collision. A precise reconstruction is especially important when trying to determine which tracks originate from the primary vertex and which from secondary vertices from decays of heavy quarks or from additional overlapping interactions. This is the main problem in vertex reconstruction, and is minimized with the adaptive primary vertex (APV) algorithm [43].

Only tracks with transverse momentum p_T>0.5 GeV and two or more SMT hits, if the track is in the SMT acceptance region, are considered. A z-clustering algorithm groups tracks within 2 cm of each other along the beam direction, assuming they belong to the same interaction. For each z-cluster, an initial procedure preselects tracks based on their χ^2 contribution in a Kalman Filter vertex-fitting algorithm and on their distance of closest approach (dca) to the beam spot.

After preselection, the APV algorithm is applied. This involves an iterative procedure that reweights track errors according to the track's χ^2 contribution to the attempted fit to a vertex. When the track weights converge, the vertex is

stored in a list for subsequent use.

Finally, the primary vertex of the hard scatter is chosen from the list of reconstructed vertices. It is assumed that the other vertices originate from minimum-bias events (MBE), which have lower-p_T tracks. Based on the p_T of the associated tracks, a probability for being an MBE is assigned to each vertex, and the vertex with the lowest probability is chosen as the primary vertex [44].

Additional selections in this analysis require:

- $|z_{PV}| \leq 60$ cm, and
- at least three tracks in the fit to the PV.

4.3. Electrons

The reconstruction of electrons relies on information from the calorimeter and from the tracking system. Better energy resolution is attained with the calorimeter, but angles are measured in the tracker, if the energy deposition in the calorimeter can be matched to a track. Sources of background for electrons are neutral pions, η mesons, photons, charged pions, and unusual fluctuations in the development of jets. Requiring a track-match for an electron candidate leaves mainly background from neutral pions, which decay to photons, which in turn convert to e^+e^- pairs, or are accompanied by a charged particle that mimics an electron track. Also, η mesons, which decay either to neutral pions or photons contribute to background [45].

Electrons start out as calorimeter objects. In the CC, EM clusters are defined by a set of towers adjacent to the tower with highest energy content within a cone of $\Delta R = \sqrt{\Delta\varphi^2 + \Delta\eta^2} < 0.2$. In the EC, EM clusters are defined by a set of adjacent cells with transverse distance of <10 cm from an initial cell of highest energy content. For the cluster to be considered an electron candidate, it has to

meet the following requirements:

- EM cluster $p_T >$ 1.5 GeV.
- True EM clusters are expected to have a large fraction of their energy deposited in the electromagnetic layers of the calorimeter. Electron candidates are therefore required to have an electromagnetic fraction

$$f_{EM} = \frac{E_{EM}}{E_{tot}} > 0.9. \tag{4.1}$$

- Additionally, the cluster is required to be isolated in (η, φ) space, meaning that the total energy in a cone of ΔR <0.4 around the candidate without the EM energy contained in the ΔR <0.2 cone must have <20% of the EM energy deposited within ΔR <0.2:

$$f_{iso} = \frac{E_{tot}(\Delta R < 0.4) - E_{EM}(\Delta R < 0.2)}{E_{EM}(\Delta R < 0.2)} < 0.2. \tag{4.2}$$

In addition, for this analysis, the electron candidates are required to have:

- $p_T >$ 20 GeV.
- $|\eta_{det}| < 1.1$.
- The isolation as defined in Eq. 4.2 is required to be $f_{iso} < 0.15$.
- The shower development of the candidate cluster in the calorimeter is compared to the shower development using electrons from test beams and from W boson events and $Z \to e^+e^-$ decays. A 7×7 covariance matrix is defined for N such electrons, based on seven discriminating variables:

$$M_{ij} = \frac{1}{N} \sum_{n=1}^{N} (x_i^{(n)} - \langle x_i \rangle)(x_j^{(n)} - \langle x_j \rangle), \tag{4.3}$$

where $x_i^{(n)}$ is the value of variable i for electron n, and $\langle x_i \rangle$ is its mean value. The seven discriminating variables are:

- Energy fractions in the first, second, third and fourth EM layer of the calorimeter.
- The width of the shower in $r-\varphi$ in the third EM layer of the calorimeter.
- The shower energy.
- The longitudinal position of the primary vertex divided by its uncertainty $z_{\text{vtx}}/\sigma_{z_{\text{vtx}}}$.

The H-matrix provides a χ^2 function that quantifies how well the shower development of electron candidate k matches that of an electron:

$$\chi^2_{\text{H-matrix}} = \sum_{i,j=1}^{7} (x_i^{(k)} - \langle x_i \rangle) H_{ij} (x_j^{(k)} - \langle x_j \rangle), \tag{4.4}$$

where $H = M^{-1}$. To pass the electron requirement, the H-matrix for the shower must have $\chi^2_{\text{H-matrix}} < 50$.

- Electrons are expected to leave a track in the tracking system that should point to the calorimeter cluster in (η, φ) space, and the transverse energy measured in the calorimeter should be consistent with the transverse momentum of the measured track. A χ^2 is defined:

$$\chi^2_{\text{trackmatch}} = \left(\frac{\Delta\varphi}{\sigma_\varphi}\right)^2 + \left(\frac{\Delta z}{\sigma_z}\right)^2 + \left(\frac{E_T/p_T - 1}{\sigma_{E_T/p_T}}\right)^2, \tag{4.5}$$

where $\Delta\varphi$ (or Δz) is the difference between the φ(or z)-coordinate of the cluster in the EM3 layer of the calorimeter and the φ(or z)-coordinate the track extrapolated to the EM3 layer. E_T/p_T is the ratio of the transverse energy in the calorimeter and the transverse momentum of the track. σ_φ, σ_z and σ_{E_T/p_T} are the root mean squares (RMS) of the three distributions,

respectively. $P(\chi^2_{\text{trackmatch}})$ is the χ^2-probability for a track match in φ, z, and E_T/p_T, and is required to be $P(\chi^2_{\text{trackmatch}}) > 0$.

Electron candidates that fulfill all of the above requirements, are called "loose" electrons. Further confirmation is needed to suppress the overwhelming background from multijet production, and is obtained from requiring the candidate to pass a selection on electron likelihood, which is described in detail in Ref. [45]. It uses the following seven input quantities:

1. χ^2-probability of a spatial track match:

$$\chi^2_{\text{spatial}} = \left(\frac{\Delta\varphi}{\sigma_\varphi}\right)^2 + \left(\frac{\Delta z}{\sigma_z}\right)^2. \tag{4.6}$$

2. E_T/p_T.

3. H-matrix.

4. EM-fraction.

5. Distance of closest approach (DCA) of the selected track relative to the z-axis passing through the primary vertex.

6. Number of tracks in a cone of $\Delta R < 0.05$, including the track of the electron candidate. This variable is sensitive to photon conversions, which can have a second track very close to the track of the electron candidate, and suppresses background from neutral pions.

7. $\sum p_T$ of all tracks in a cone of $\Delta R < 0.4$, excluding the track of the electron candidate. This variable rejects jets, which will have several tracks around that of the electron candidate.

The electron likelihood discriminant has values between 0 and 1, with 0 being background-like and 1 signal-like. If the loose electron has a likelihood discriminant value $\geq$0.85, it is called a "tight" electron.

The likelihood discriminant for electrons from $Z \rightarrow e^+e^-$ events peaks strongly at 1, and for electrons from the multijet background at 0. The performance of the electron likelihood discriminant in signal and in multijet background events is depicted in Fig. 4.3 for different choices of input parameters [46].

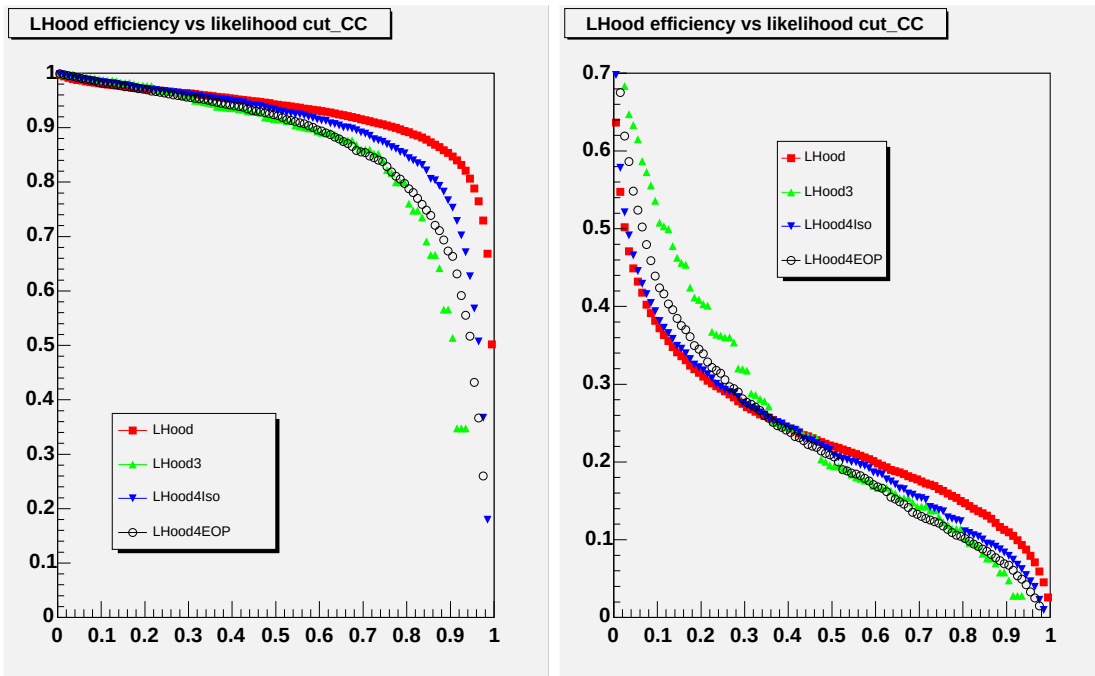

Figure 4.3.: Efficiency of the likelihood discriminant for electrons in data as a function of the cut value in the central calorimeter (CC) region for different choices of input parameters [46]. The one used in this analysis is shown as rectangles. Left: in $Z \rightarrow e^+e^-$ events, right: in multijet background events.

4.4. Muons

Muons are reconstructed using information from the muon system and the inner tracking system [47]. A muon candidate starts out as a so-called "local muon" track, which is formed using the hits in the layers of the muon system. The local muon is then matched to a track from the inner tracking system, taking into account the magnetic fields of the solenoid and the toroid. If the match succeeds, the muon candidate is called "central track-matched muon". Since the resolution of the tracking system is much better than that obtained in the muon system, the former is used to establish muon p_T. In addition, calorimeter information can be used to confirm the presence of a muon through its characteristic minimum-ionizing signature. This "Muon Tracking in the Calorimeter" (MTC) algorithm currently has an efficiency of ≈50% and is still being developed.

A complete description of the identification requirement options for muons can be found in Ref. [48]. For this analysis, muon candidates are required to fulfill the following criteria:

- p_T>20 GeV.
- $|\eta_{det}|$ <2.0.
- The muon candidate is required to be of type $|nseg|$=3, which means it has to have hits in all three layers of the muon system, the inner A layer and the outer B and C layers beyond the toroid.
- "Medium" muon quality, meaning:
  - at least two wire hits in the A layer
  - at least one scintillator hit in the A layer
  - at least two wire hits in the combined BC layers

  - at least one scintillator hit in the combined BC layers (except for central muons with < 4 BC wire hits).

- Timing information from the scintillator hits is used to reject background from cosmic rays. Muons from the collision traverse the muon system shortly after the time of the interaction, and the cosmic veto cut requires scintillator times t_A <10 ns and t_{BC} <10 ns following the central trigger.

- The central track match in this analysis is required to be of "medium" quality, which means that the χ^2 per degree of freedom of the fit has to be χ^2/dof < 4, and the distance of closest approach of the track to the primary vertex |DCA| <0.2 cm, or |DCA| <0.02 cm if the track has a hit in the SMT.

- To reject muons from semileptonic decays of heavy quarks, it is required that the muon candidate is at a distance in (η, φ) space $\Delta R(\mu, \text{jet})$ >0.5 from jets.

Muon candidates that pass all of the above requirements are called "loose" muons. If loose muons fulfill the following additional isolation requirements, they are called "tight" muons:

- The first isolation requirement is a calorimeter isolation requirement. The summed E_T of all calorimeter cells in an annulus of 0.1< ΔR <0.4 is required to have <8% of the muon p_T:

$$\frac{1}{p_T(\mu)} \sum_{cells} E_T < 0.08. \tag{4.7}$$

- The second isolation requirement is a track isolation requirement. It requires the sum of the p_T of all tracks within a cone of ΔR=0.5 around (but not including) the muon to be <6% of the muon p_T:

$$\frac{1}{p_T(\mu)} \sum_{tracks} p_T < 0.06. \tag{4.8}$$

4.5. Jets

Quarks and gluons from the hard scatter form showers of hadrons that can be reconstructed as jets in the calorimeter. An ideal jet algorithm should be infrared safe, that is, work when the emission involves a soft gluon, and collinear safe, which means that it should not be sensitive to situations where the parton energy is split across several cells by collinear radiation.

The DØ Run II "Improved Legacy Cone Algorithm" (ILCA) [49] takes these and other considerations into account, and is the jet algorithm used in the presented analysis. First it forms preclusters using the "Simple Cone Algorithm" as described in the following. From a p_T-ordered list of calorimeter towers, the algorithm starts with the tower of highest p_T. When the selected tower has $p_T > 0.5$ GeV, it is admitted as a precluster. All towers within a cone of $\Delta R = \sqrt{(\Delta\eta)^2 + (\Delta\varphi)^2} < 0.3$ around that tower that have $p_T > 1$ MeV are added to this precluster. The algorithm then proceeds with the tower of next-highest p_T, until all preclusters are formed. To ensure collinear and infrared safety, these preclusters and midpoints between certain preclusters serve as seeds for the clustering of "proto-jets". The proto-jets have a cone size of $\Delta R = 0.5$, and can overlap. To avoid double counting of energy, they undergo a splitting and merging procedure. In the end, all jet candidates with $E_T > 6$ GeV are kept. These can still include electrons, photons and jets from electronics noise, so that additional requirements are needed [50]:

- The ratio of the highest to the next-to-highest cell transverse energies is required to be HotF < 10. This reduces clustering of jets from hot (noisy) cells.

- The number of towers containing 90% of the jet energy has to be n90 > 1. This minimizes the number of jets clustered from a single hot tower.

- To separate jets from electromagnetic objects, there is an upper limit on

the electromagnetic fraction f_{EM} of < 0.95, as defined in Eq. 4.1. There is also a lower limit on f_{EM}, that depends on η_{det}, because of a gap in the electromagnetic calorimeter in the ICD region (see Section 3.2.2):

- $f_{EM} > 0.05$ or
- $||\eta_{det}| - 12.5| + \max[0, 40 \cdot (\sigma_\eta - 0.1)] < 1.3$ (narrow jet in ICD) or
- $f_{EM} > 0.03$ and $11.0 < |\eta_{det}| < 14.0$ (wide jet in ICD) or
- $f_{EM} > 0.04$ and $|\eta| > 2.5$ (forward region),

where η_{det} denotes calorimeter cell coordinates with $\eta_{det} \approx 10 \cdot \eta$ and σ_η is the RMS width of a jet in η.

- Because there is a large amount of noise in the coarse hadronic section of the calorimeter, the fraction of energy deposited in that layer (f_{CH}) is required to be:
  - $f_{CH} < 0.4$, or
  - $f_{CH} < 0.6$ for $8.5 < |\eta_{det}| < 12.5$ and n90<20, or
  - $f_{CH} < 0.44$ for $|\eta| < 0.8$, or
  - $f_{CH} < 0.46$ for $1.5 < |\eta| < 2.5$.
- The presence of a jet has to be confirmed, meaning that the energy from the precision readout must also be present in the L1 trigger. In particular:
  - The scalar sum of the p_T in the L1 trigger tower (L1SET) has to exceed 55 GeV, or
  - using the quantity

$$\mathrm{L1}_{\mathrm{ratio}} := \frac{p_T^{\text{from L1 readout}}}{p_T^{\text{from precision readout}}} \tag{4.9}$$

the requirements, depending on the detector region, are:

    * $L1_{\text{ratio}} > 0.5$, or
    * $L1_{\text{ratio}} > 0.35$ for p_T<15 GeV and $|\eta|$ >1.4, or
    * $L1_{\text{ratio}} > 0.1$ for p_T<15 GeV and $|\eta|$ >3.0, or
    * $L1_{\text{ratio}} > 0.2$ for $p_T \geq$15 GeV and $|\eta|$ >3.0.

  – The L1 trigger coverage for the earliest data was more limited, and, for jets outside that coverage, instead of L1 confirmation, it is required that either f_{CH} <0.15, or that the fraction of the total number of towers that contain 90% of the jet p_T (n90) be < 0.5.

- Jets used in this analysis are also required to fulfill $p_T > 15$ GeV (after energy corrections) and $|\eta_{det}| < 2.5$.

4.5.1. Jet Energy Scale

Figure 4.4 sketches the evolution of a typical parton from the hard scatter into a jet in the calorimeter. Due to non-linearities, dead material, noise and showering effects in the calorimeter, the measured energy of a jet is not equal to the sum of the particle energies nor to the energy of the parton. The Jet Energy Scale (JES) attempts to correct the measured energy back to the stable-particle jet level, before any interactions within the detector [51]. However, this does not account for hard gluon radiation, which can redirect energy at large angles relative to the original parton.

The corrected jet energy is given by:

$$E_{jet}^{corr} = \frac{E_{jet}^{obs} - O}{F_\eta \cdot R \cdot S}, \tag{4.10}$$

where E_{jet}^{obs} is the uncorrected jet energy observed in the calorimeter, O an offset to the energy, F_η the relative response as a function of η_{det}, R the energy-dependent

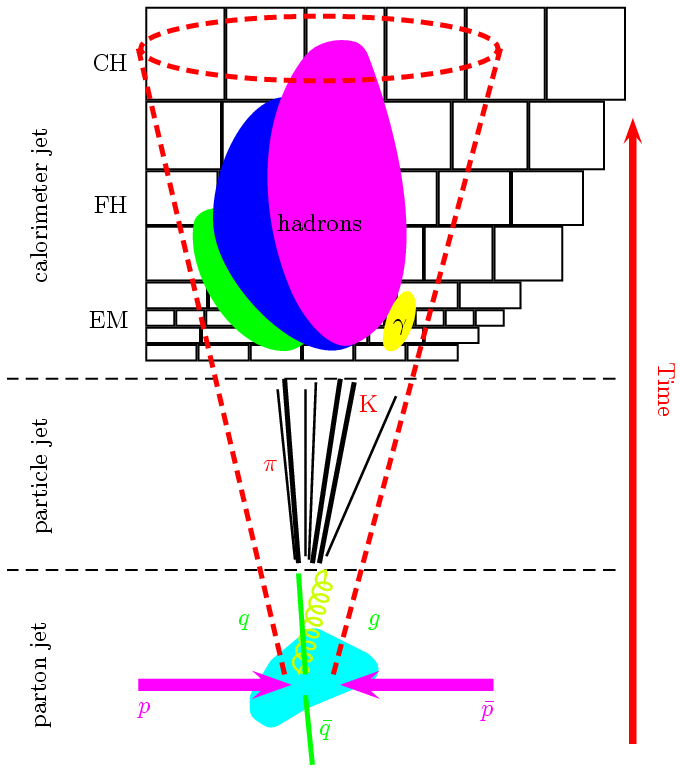

Figure 4.4.: Sketch of the evolution of a hard-scattered parton to a jet in the calorimeter.

correction for absolute response, and S a correction for shower development. In the following, we briefly discuss each of the four corrections.

The offset O is needed to correct for energy deposited within the cone of the jet in the calorimeter that does not originate from the hard scatter. Such "energy" can be caused by electronics and uranium noise, energy pile-up from previous beam crossings, additional $p\bar{p}$ interactions, and the "underlying event", which corresponds to remnants of the interacting hadrons and multiple-parton interactions. This correction is estimated using "minimum bias" events, which are events triggered by the luminosity monitor to provide essentially unrestricted inelastic $p\bar{p}$ collisions.

The goal of the relative response correction, or "η-intercalibration" F_η, is to

provide a uniform response of the entire calorimeter (from the CC to the less instrumented ICD region and the forward EC regions). F_η is based on the "Missing Transverse Energy Projection Fraction" (MPF) method using samples of photon+jet and dijet events. The MPF method relates the relative response between a "probe" jet and a "tag" jet to the observed momentum imbalance in the transverse plane, projected onto the direction of the tagged object.

The MPF method is also applied to measure the absolute correction R to the response of the calorimeter to jets as a function of energy. This is the largest correction (≈30%), and arises mainly from energy loss in uninstrumented regions of the detector and the lower calorimeter response to hadrons compared to electrons or photons. The absolute response measured for jets with cone size $\Delta R = 0.7$ as function of partly corrected (by offset and relative response) jet energy is shown in Fig. 4.5.

The statistical nature of shower development in any calorimeter makes it possible for energy from particles inside some jet cone to leak outside, and vice versa. The showering correction S is intended to compensate for this instrumental effect. It is derived by comparing the profile in the energy density of a jet as a function of the radial distance to the jet axis in photon+jets events and particle-level Monte Carlo simulations.

The total fractional uncertainty on transverse energy for jets with a cone size of $\Delta R = 0.5$ and $\eta \approx 0$ is depicted in Fig. 4.6. Shown are also the contributions from the three main subcorrections, indicating that the uncertainty on the response is greatest of all.

Because the Monte Carlo does not simulate the detector response satisfactorily, a separate jet energy scale is derived and applied for Monte Carlo events.

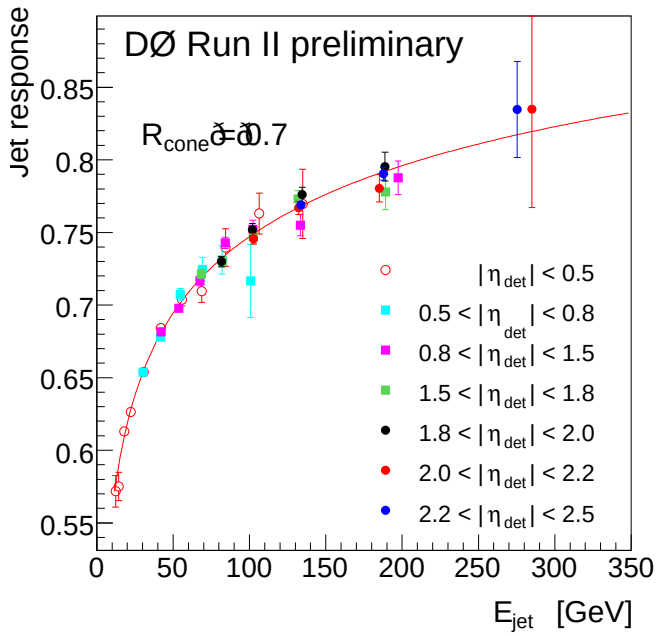

Figure 4.5.: Absolute response in data, after offset and relative response corrections, as a function of partly corrected jet energy for jets with cone size $\Delta R = 0.7$.

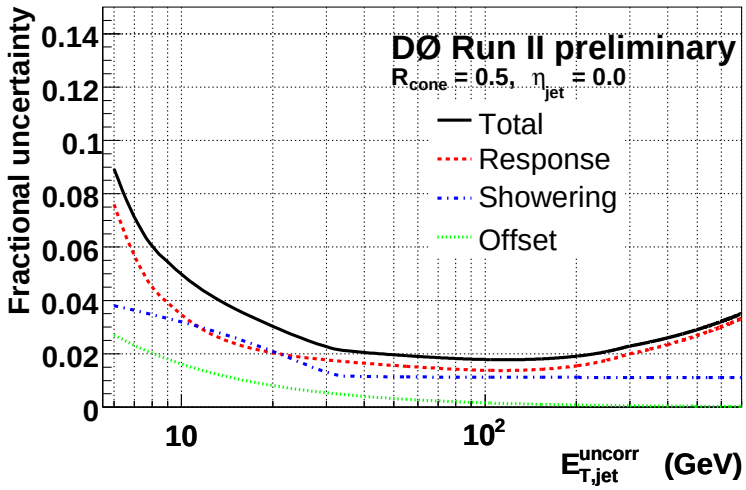

Figure 4.6.: Fractional uncertainty on transverse energy as a function of uncorrected transverse energy, for jets with a cone size of $\Delta R = 0.5$ and $\eta \approx 0$.

4.6. B-Jets

Since stop-pair events always contain two jets originating from b-quarks, whereas only a small fraction of the background processes produce b-jets, it is desirable to employ the detector's capability of distinguishing b-jets from jets originating from gluons or other quark flavors. Two characteristics of heavy flavor jets (c- and b-jets) can be exploited for this purpose:

1. The branching ratio of c and b-hadrons decaying semileptonically is typically $\approx$10% per lepton, and the probability for a light-quark jet to contain a lepton is much smaller. The presence of a soft lepton within the jet cone is therefore a good indicator of heavy flavor.

2. Heavy-flavor hadrons have relatively long lifetimes, so that they travel a measurable distance before decaying. The decay length of the b-quarks in $t\bar{t}$ events averages around 3 mm [52].

Based on these characteristics, several ways have been developed to identify b-jets at DØ:

- The Soft Lepton Tagging (SLT) algorithm identifies soft muons inside a jet cone as a way of tagging b-jets [53]. SLT is the only tagger that relies on semileptonic decays of heavy-flavor hadrons.

- The Counting Signed Impact Parameter (CSIP) algorithm identifies tracks with non-zero impact parameters relative to the primary vertex, the significance of which is determined by the uncertainties on the reconstructed tracks [54]. A sign is also assigned to the impact parameter, which reflects the direction of the impact parameter projected along the jet axis. A minimum number of tracks with significant impact parameter is required for tagging any jet as a b-jet.

- The Secondary Vertex Tagger (SVT) reconstructs the explicit decay vertices of long-lived b-hadrons [52]. It selects tracks with significant impact parameter, and forms from them two-track seed vertices, then adds tracks according to their contribution to the χ^2 fit to a common vertex. The resulting vertices are matched to jets in the calorimeter, and a jet is b-tagged if it contains at least one secondary vertex with some chosen significance in decay length.

- Based on information on impact parameters of tracks in the SMT, the Jet Lifetime Probability (JLIP) algorithm assigns to each jet a probability that it originates from the primary vertex [55]. JLIP therefore requires a low assigned probability for a jet to be tagged as a b-jet.

- The Neural Net (NN) tagging algorithm uses as input seven variables from the three lifetime taggers CSIP, SVT, and JLIP [56]. The tagger returns a value between 0 and 1 for each jet, with an output close to 1 indicating a high probability to be a b-jet. Figure 4.7 shows the NN output for directly produced $b\bar{b}$ Monte Carlo events compared to multijet Monte Carlo events, which contain mostly light jets.

This analysis uses the NN tagging algorithm with NN > 0.775, which corresponds to the "tight" operating point. The average b-tagging efficiency on data is 47% for jets up to $|\eta_{det}|$=2.5, and the average rate for mimicking b-jets is $\approx 0.47\%$ for light jets in the CC region.

Events in data can be tagged directly, but for simulated samples a parametrization, called the Tag Rate Function (TRF), is used. The TRF is derived from data in order to obtain a more realistic estimate of the b-tag efficiency for the simulation. For any jet, the TRF provides a probability for the jet to be tagged as a b-jet. In the presented analysis we need to know if a given jet is b-tagged or not, so each jet is assigned to be b-tagged through a randomized procedure that takes into account the probability given by the TRF.

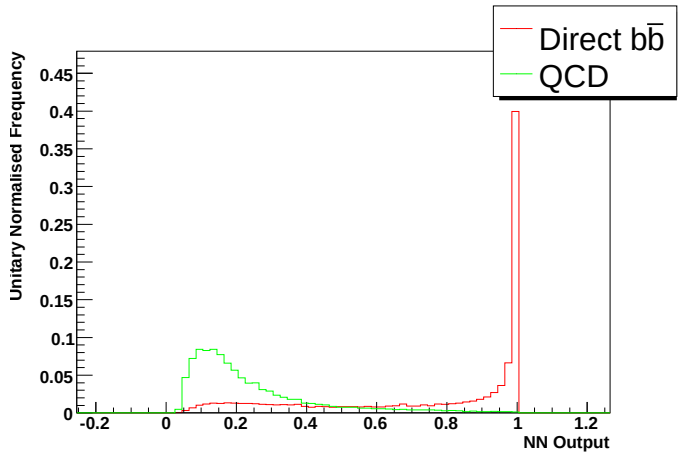

Figure 4.7.: Neural Net output for direct $b\bar{b}$ (red) and multijet production (green).

4.7. Missing Transverse Energy

Neutrinos cannot be detected directly at DØ, instead their presence in an event can only be inferred through momentum conservation. Because the Tevatron is a hadron collider, the z-component of the total momentum in individual partonic collisions is unknown, and so the calculation of any momentum carried away by neutrinos is limited to the transverse plane.

The missing transverse energy $\not\!\!E_T$ is defined by depositions in transverse energy in all calorimeter cells. Depositions greater than 100 MeV are added up vectorially. Because of the high level of noise in the coarse hadronic sections of the calorimeter, the cells in that part are included only if they form part of a good jet. The vector opposite the resulting vector is defined as the initial uncorrected missing transverse energy $\not\!\!E_{T_{\mathrm{uncorr}}}$ in the event.

In the next step, energies of all good jets and EM objects in the event are corrected, as is the resulting missing transverse energy, called the calorimeter missing transverse energy $\not\!\!E_{T_{\mathrm{CAL}}}$.

Finally, the missing transverse energy has to be corrected for the presence of muons in the event. A high-energy muon, being a minimum-ionizing particle, deposits only very little of its energy in the calorimeter. The $\not{E}_T$ is therefore corrected using the measured momentum of the track matched to the outer muon, taking into account the expected deposition of energy in the calorimeter. The resulting $\not{E}_T$ is the fully corrected missing transverse energy.

5. Data Sample and Monte Carlo Simulation

5.1. Data Sample

The data for this analysis was collected between August 2002 and December 2005, and comprises an integrated luminosity of 913 pb^{-1} for the electron channel and 871 pb^{-1} for the muon channel. The quoted integrated luminosity includes recent refinements of its determination at DØ [57]. The triggers require one electron and two jets for the electron channel, where the electron can be triggered simultaneously as an electron and as a jet, and one muon and one jet for the muon channel. The triggers are described in detail in Ref. [58] and will be discussed below. To reduce the size of the initial data sample, additional restrictive requirements are imposed on the quality of the leptons and the jets. A software package was developed at DØ [59] for evaluating and establishing final selection criteria for events in both data and in Monte Carlo simulations.

5.1.1. Electron Channel

The triggers for the e+jets channel use only calorimeter information. Trigger requirements change from time to time to accommodate the needs of analyses or restrictions from recording capabilities. Table 5.1 lists the trigger names for the

e+jets channel for the versions of trigger lists used in this analysis, and the information on integrated luminosity of delivered, recorded, and good-quality data for each. As an example, we will describe the requirements of E1_SHT15_2J_J30, which is used in versions v13.3–v13.9, during which time the most data was collected. At Level 1, the requirement is CEM(1,11), which means that there has to be a trigger tower in the calorimeter with an electromagnetic transverse energy $E_T \geq 11$ GeV. At Level 2, L2CALEM(15,x) is required, which means one calorimeter electron object with transverse energy $E_T \geq 15$ GeV. Finally, at Level 3, the requirement is ELE_NLV_SHT(1,15)_JET(1,30)JET(2,20). The first part asks for a Level-3 electron object with transverse energy $E_T \geq 15$ GeV, an electromagnetic energy fraction $f_{EM} > 0.85$, and cutoffs on the shower widths in the EM layers of the calorimeter. The jet part requires at least one jet with $E_T > 30$ GeV, and at least two jets with $E_T > 20$ GeV (the first jet already fulfills half of the latter jet requirement). The requirements in different versions of trigger lists differ only slightly from the one discussed above.

Trigger Version	Trigger Name	Delivered [pb^{-1}]	Recorded [pb^{-1}]	Good Quality [pb^{-1}]
v8	EM15_2JT15	6	5	5
v9	EM15_2JT15	48	42	25
v10	EM15_2JT15	20	18	10
v11	EM15_2JT15	79	72	63
v12	E1_SHT15_2J20	273	251	227
v13.0–v13.2	E1_SHT15_2J_J25	80	73	55
v13.3–v13.9	E1_SHT15_2J_J30	354	325	294
v14	E1_SHT15_2J_J25	290	271	234
Total Integrated Luminosity		1150	1056	913

Table 5.1.: Trigger names and integrated luminosities by version of trigger list for the e+jets channel.

5.1.2. Muon Channel

For the μ+jets channel, Table 5.2 lists the trigger names for all versions of trigger lists, as well as the integrated luminosity of delivered, recorded, and good-quality data for each of them. The example to be described is MUJ2_JT30_LM3, which is used in versions v13.3–v13.9. At Level 1, the requirement is mu1ptxatlx_CJT(1,5). The first part asks for one muon ("mu1"), with no L1CTT track match or p_T requirement ("ptx"), in any region ("a"), a tight scintillator requirement ("t"), a loose wire-chamber requirement ("l"), and no optional requirement ("x"). The latter part refers to jets, and requires one or more trigger towers with total, that is electromagnetic and hadronic, transverse energy $E_T \geq 5$ GeV. Level 2 requires MUON(1,med)JET(1,8), that is, a medium quality muon and one or more jets with $E_T > 8$ GeV. At Level 3, the requirement is JET(1,30)MUON(1,3,loose), which means one or more jets with $E_T > 30$ GeV, and one or more "loose" Level-3 muons with $p_T > 3$ GeV. The trigger requirements in other versions of trigger lists are similar to the one discussed above.

5.2. Monte Carlo Simulation

A good simulation of events is needed to study signal and background processes in a quantitative way. The complete simulation of an event includes the hard-scattering interaction, initial and final state gluon radiation, hadronization, the "underlying event," detector response, and digitization, which are all discussed in detail below. Since the phase space for simulated events is populated using random numbers, the simulation is referred to as Monte Carlo (MC) simulation and the events as Monte Carlo events [60].

The hard-scattering interaction of the partons inside the proton and antiproton is calculated in perturbative QCD. For the calculation of the matrix element, DØ uses

Trigger Version	Trigger Name	Delivered [pb^{-1}]	Recorded [pb^{-1}]	Good Quality [pb^{-1}]
v8	MU_JT20_L2M0	7	6	6
v9	MU_JT20_L2M0	48	42	25
v10	MU_JT20_L2M0	21	19	11
v11	MU_JT20_L2M0	79	74	65
v12	MU_JT25_L2M0	277	255	231
v13.0–v13.1	MUJ2_JT25	56	39	31
v13.2	MUJ2_JT25_LM3	26	22	16
v13.3–v13.9	MUJ2_JT30_LM3	382	277	252
v14.0–v14.1	MUJ1_JT25_LM3	0	0	0
v14.2	MUJ1_JT25_ILM3	25	23	21
v14.3–v14.9	MUJ1_JT35_LM3	265	248	214
Total Integrated Luminosity		1187	1006	871

Table 5.2.: Trigger names and integrated luminosities by version of trigger list for the μ+jets channel.

Pythia [61], Alpgen [62] or compHEP-singleTOP [63] generators, depending on the process. Since neither the proton or antiproton, but rather the partons within them interact in these hard scatters, the probability to find a certain parton as a function of the fraction x of the momentum carried by the parton, has to be available for these calculations. This is given by the parton distribution functions (PDFs), and the ones used in generating the MC samples are CTEQ6L1 [64].

The perturbative calculation of the radiation of hard gluons can become complicated because of collinear and infrared divergences in the theory. Initial and final-state radiation are therefore modeled by parton showering in Pythia. Since this simplified approach often results in overly soft jets, Alpgen instead calculates higher-order matrix elements for the processes. A jet-matching algorithm, following the MLM prescription [65], is employed to avoid double-counting.

Quarks and gluons carry color charge, and have to be transformed into jets of colorless hadrons. This "hadronization" can be divided into a particle fragmentation

component and particle decays. The fragmentation part is poorly understood, and therefore has to be based on models, which vary among the different generators. DØ uses the string fragmentation model (Lund model) [66], which is implemented into PYTHIA.

Besides the hard scattering, there are several additional interactions that are characterized by the term underlying event. These include interactions of the partonic remnants of the proton and antiproton, which are color-connected to the hard scatter, and do not depend on the $p\bar{p}$ luminosity. These comprise the "soft underlying event." The higher the luminosity, the more multiple proton interactions can take place, which can lead to additional hard scatters. Energy from previous bunch crossings can also remain in the detector, which is called "pile-up." Lastly, there is also electronic or thermal noise from the detector components. The underlying event is added to the simulated events by overlaying "zero-bias" events to the simulation. Zero-bias events are those recorded without any trigger conditions.

Finally, the detector response is simulated in the MC, taking into account the geometry and material of the DØ detector. This is done using the program DØGSTAR [67], which is a full DØ-detector simulation based on GEANT [68]. GEANT is a software package developed for high energy physics, and designed to describe the passage of elementary particles through matter. It encompasses many physical processes for interactions of particles with matter, including Compton scattering, synchrotron radiation, bremsstrahlung, ionization, and hadronic interactions, over a wide range of energies. The simulated data is then digitized by DØSIM [69], and the events are reconstructed by DØRECO, as described in Chapter 4.

5.2.1. Simulation of Signal

The $\tilde{t}_1\bar{\tilde{t}}_1$ signal events in the lepton+jets topology were generated using PYTHIA v6.323 in its general Minimal Supersymmetric Standard Model (MSSM) mode [61].

In this setting, each of the soft SUSY-breaking parameters in the Lagrangian is set by hand, since the exact mechanism of SUSY breaking is unknown. PYTHIA does, however, assume some relations between those parameters, which reduces the number of independent parameters greatly. Table 5.3 lists only the parameters that differ from PYTHIA default values. Another deviation from the default PYTHIA settings is that M_3 is set to be the gluino pole-mass, with effects from squark loops already included. According to PYTHIA, the branching ratio for $\tilde{t}_1 \to \tilde{\chi}_1^+ b$ is 100% for the given set of SUSY parameters.

Parameter	Value
U(1) Gaugino mass M_1	53 GeV
SU(2) Gaugino mass M_2	varies
Gluino mass M_3	500 GeV
Higgsino mass parameter μ	225 GeV
Ratio of expected Higgs expectation values $\tan\beta$	20
Left slepton mass $M_{\tilde{l}_L}$	200 GeV
Right slepton mass $M_{\tilde{l}_R}$	200 GeV
Left squark mass $M_{\tilde{q}_L}$	250 GeV
Right squark mass $M_{\tilde{q}_R}$	250 GeV
Left squark mass for third generation $M_{\tilde{q}_L}$	250 GeV
Right sbottom mass $M_{\tilde{b}_R}$	250 GeV
Right stop mass $M_{\tilde{t}_R}$	250 GeV
Left stau mass $M_{\tilde{\tau}_L}$	200 GeV
Right stau mass $M_{\tilde{\tau}_R}$	200 GeV
Bottom trilinear coupling A_b	200 GeV
Top trilinear coupling A_t	varies
Tau trilinear coupling A_τ	200 GeV
Pseudoscalar Higgs mass parameter M_A	800 GeV

Table 5.3.: MSSM parameters that differ from the default values in PYTHIA.

The masses of the stop quark, the lightest chargino, and the lightest neutralino are determined almost exclusively by the top trilinear coupling A_t, the **SU(2)** gaugino mass M_2, and the **U(1)** gaugino mass M_1, respectively. They were selected

to produce the desired mass points specified in Table 5.4. The naming of the mass points includes the stop-quark mass and the mass of the lightest chargino. The table shows the cross sections for $\tilde{t}_1\bar{\tilde{t}}_1$ production, as calculated in PROSPINO [13], the SUSY parameters, and the resulting SUSY particle masses for each mass point.

Mass point	$\sigma_{\tilde{t}_1\bar{\tilde{t}}_1}$ [pb]	A_t [GeV]	$m_{\tilde{t}_1}$ [GeV]	M_2 [GeV]	$m_{\tilde{\chi}_1^\pm}$ [GeV]	M_1 [GeV]	$m_{\tilde{\chi}_1^0}$ [GeV]
Stop 175/135	0.579	357	175	164	135	53	50
Stop 175/120	0.579	357	175	144	120	53	50
Stop 175/105	0.579	357	175	125	105	53	50
Stop 160/120	1.00	387	160	144	120	53	50
Stop 160/105	1.00	387	160	125	105	53	50
Stop 146/105	1.80	414	146	125	105	53	50

Table 5.4.: Mass points used in the analysis, with their cross section in pb, and SUSY parameters and SUSY particle masses given in GeV.

5.2.2. Simulation of Background

The background Monte Carlo samples for this analysis are identical to those used in standard DØ $t\bar{t}$ analyses, and were produced and are available within DØ.

The $t\bar{t}$ events were generated using PYTHIA, for a top-quark mass of 175 GeV, and the scale $m_t^2 + \sum p_T^2(jets)$. The theoretical next-to-next-to-leading order cross section of 6.77±0.42 pb is assumed for $t\bar{t}$ production [8].

The W+jets samples were generated using ALPGEN, with the MLM matching procedure. The factorization scale is $m_W^2 + p_T^2(W)$. The W+jets samples consist of subsamples sorted by jet flavor: Wjj, $Wc\bar{c}$ and $Wb\bar{b}$, where Wjj includes the Wcj subprocess. It has been shown that the relative contribution of the heavy-flavor samples $Wc\bar{c}$ and $Wb\bar{b}$ has to be scaled up by a factor of $k_{HF} = 1.17 \pm 0.18$ to model

the data [70]. The overall normalization is estimated using data, as described in Section 6.2.2.

The Z+jets samples were also generated using ALPGEN, in the same way and subsamples as for the W+jets samples, as described above. $Z \to ee, \tau\tau, \nu\nu$ decays are considered in the e+jets channel, and $Z \to \mu\mu, \tau\tau, \nu\nu$ in the μ+jets channel. Because ALPGEN does not reproduce the p_T distribution of Z bosons in data, a reweighting is applied to the Z+jets samples [71]. It has also been found that the contributions from both the light-sample Zjj and the heavy-flavor samples $Zc\bar{c}$ and $Zb\bar{b}$ have to be scaled up as [72]:

$$\sigma_{Z+jets} = 1.23 \cdot (\sigma_{Zjj} + 1.35 \cdot (\sigma_{Zc\bar{c}} + \sigma_{Zb\bar{b}})) \tag{5.1}$$

We estimate an uncertainty of 15% on the cross section.

Single-top event samples were generated with the COMPHEP-SINGLETOP Monte Carlo event generator, which produces events whose kinematic distributions match those of NLO calculations [63]. The top-quark mass is set to 175 GeV, the scales are m_t^2 in the s-channel, and $(m_t/2)^2$ in the t-channel. The cross sections are assumed to be $\sigma_{tb} = 0.88 \pm 0.11$ pb for the s-channel and $\sigma_{tqb} = 1.98 \pm 0.25$ pb for the t-channel, which are derived from next-to-leading order calculations [73].

The diboson samples WW, WZ, and ZZ were generated using PYTHIA. The cross sections for these samples are $\sigma_{WW} = 12.0 \pm 0.6(\text{scale}) \pm 0.3(\text{PDF})$ pb, $\sigma_{WZ} = 3.68 \pm 0.22(\text{scale}) \pm 0.12(\text{PDF})$ pb, and $\sigma_{ZZ} = 1.42 \pm 0.06(\text{scale}) \pm 0.05(\text{PDF})$ pb.

6. Search for Pair Production of Scalar Top Quarks

The presented analysis is the first attempt in Run II at the Tevatron to search for stop quark pair production in the channel where the stop quark decays to a chargino and a b-quark ($\tilde{t}_1 \rightarrow \tilde{\chi}_1^+ b$). As described in Section 2.3.2, this particular stop quark decay results in final states that are very similar to the final state of top-quark pair production. The search is conducted in the lepton+jets final state, where the event signature is an isolated high-p_T lepton, large missing transverse energy $\not\!\!E_T$, two b jets and two light-quark jets. Depending on the lepton flavor, the analysis is performed separately in the electron+jets (e+jets) and in the muon+jets (μ+jets) channel, the results of which are combined in the end.

This chapter describes the event selection, the estimation of the background contribution, closure tests, and the determination of systematic uncertainties.

6.1. Event Selection

The event selection is modeled to correspond to the event signature. The goal is to reject a lot of the background described in Section 2.3.3, while still keeping as much as possible of the signal. Because of the similarity of stop quark and top quark events, the event selection will not discriminate between the two processes, and a different method to separate the two will be employed later in the analysis.

Both the e+jets and the μ+jets channels have the following requirements:

- The event has to be declared of good quality, which means that all detector components were fully functional, with no excessive noise at the time of recording of the data.
- Since there are four quarks in the final state, the event is required to contain at least four jets with transverse momentum $p_T > 15$ GeV, and with detector pseudorapidity $|\eta_{det}| < 2.5$.
- The highest-p_T (leading) jet has to have a transverse momentum $p_T > 40$ GeV.
- The primary vertex is required to have at least three tracks pointing to it, and its z-coordinate must be within the region that is accessible to the SMT: $|z_{PV}| \leq 60$ cm.
- To ensure that the leading lepton originates from the primary vertex, its z-coordinate is required to be close to that of the primary vertex $|\Delta z(\ell, PV)| < 1$ cm.

In addition, each channel has specific requirements regarding the lepton, the missing transverse energy, and event vetoes. These vetoes are introduced to avoid including events from the dilepton channels in DØ $t\bar{t}$ analyses, which simplifies combining $t\bar{t}$ results from all channels. Although this analysis is exclusively performed in the lepton+jets channels, such vetoes are adopted along with the rest of the $t\bar{t}$ selections.

For the e+jets channel, the following additional criteria have to be fulfilled:

- The leading electron with $p_T > 20$ GeV and $|\eta_{det}| < 1.1$ has to satisfy the tight electron requirements, as described in Section 4.3.

- To reject events from the dielectron channel, no second tight electron with $p_T > 15$ GeV and $|\eta_{det}| < 2.5$ can be present.
- To reject events from the electron-muon channel, the event cannot contain any tight muons with $p_T > 15$ GeV.
- The missing transverse energy is required to be $\not\!\!E_T > 20$ GeV. A selection on the difference in the polar angle φ of the leading electron and the missing transverse energy, $\Delta\varphi(e, \not\!\!E_T) > 0.7 \cdot \pi - 0.045 \cdot \not\!\!E_T$, rejects multijet background events.

The additional requirements for the μ+jets channel are:

- The leading muon with $p_T > 20$ GeV and $|\eta_{det}| < 2.0$ has to satisfy the tight muon requirements, as described in Section 4.4.
- Vetoing any additional muons that form an invariant mass 70 GeV$< m_{\mu\mu} <$ 110 GeV with the selected leading muon, rejects $Z \rightarrow \mu\mu$+jets background events.
- To reject events from the dimuon channel, no second muon with $p_T > 15$ GeV of muon-type $|nseg|$=3, with a medium quality track-match can be present.
- To reject events from the electron-muon channel, the event must not contain any tight electrons with $p_T > 15$ GeV.
- The missing transverse energy is required to be $\not\!\!E_T > 25$ GeV. A selection on the difference in the polar angle φ of the leading muon and the missing transverse energy, $\Delta\varphi(\mu, \not\!\!E_T) > 2.1 - 0.035 \cdot \not\!\!E_T$, rejects multijet background.

Events with additional jets or jets of higher p_T have a higher probability of yielding triggers. Trigger effects like these are modeled for Monte Carlo events by measuring trigger efficiencies for leptons and jets in data, and parametrizing these

as a function of p_T. Each Monte Carlo event then gets a weight according to the probability that it would have been triggered.

In Monte Carlo events the efficiency to reconstruct, identify and select leptons is found to be higher than in data. This has to be corrected to agree with the efficiencies measured using collider data. These MC-to-data correction factors are derived typically using a control sample that allows the respective efficiency to be extracted on both MC and collider data. Such factors are denoted by κ, with a descriptive subscript. Apart from corrections for lepton efficiencies, we also reweight all events based on b-fragmentation tuned on LEP data [77].

Since the signal contains two b-quarks in the final state, it is very useful to identify b-jets as described in Section 4.6. In this analysis, we require that in both the e+jets and the μ+jets channel

- at least one jet is tagged by the neural-net b-tagger at the "tight" working point.

Later in the analysis, when separating the $t\bar{t}$ background from $\tilde{t}_1\bar{\tilde{t}}_1$ signal, it is helpful to reconstruct all events to a $t\bar{t}$ hypothesis. For that purpose, we use a kinematic fitter called HITFIT [75]. One jet in the fit is the b-jet from the top quark with a subsequent "hadronic" $W \to \bar{q}q'$ decay, another jet is the b-jet from the top quark with the leptonic $W \to \ell\nu_\ell$ decay, and two are the light jets from the "hadronic" W-boson decay. With four jets, there are twelve possible combinations of jets for a $t\bar{t}$ fit. For each combination, the HITFIT algorithm minimizes a χ^2 statistic with the constraint that both W-boson masses are 80.4 GeV, and that the masses of the supposed reconstructed top quark and antitop quark are the same. The fitter does this by varying the kinematics of the detected objects within their resolutions. Details can be found in Ref. [76]. For each combination of jets, the fit with the lowest χ^2 is taken as the right solution. To limit the number of combinations, information about the b-tags is used. If the event has one b-tag,

HITFIT will take that b-tag as one of the b-quarks in the event, if there are two b-tags, HITFIT will take both b-tagged jets as b-quarks. If there are more than two b-tags in the event, two b-tagged jets will be used as b-quarks in the fit. From all the jet combinations, the one with the lowest χ^2 is chosen again as the correct $t\bar{t}$ assignment. In some cases, there are no solutions, because HITFIT does not even attempt to fit a particular combination of jets, if the hadronic W mass is outside of the range 40 GeV$<$ m_W $<$120 GeV, or if the z-component of the neutrino momentum turns out to be unphysical. As a final selection, we therefore require

- each event to have a convergent HITFIT solution.

While the removal of whole runs or luminosity blocks because of poor data quality can be taken into account in the luminosity calculation, the event-based data quality has to be included in the preselection efficiency. This efficiency was measured in Ref. [78] to be 97.14%, with an insignificant statistical error. A systematic error of 0.5% is assigned to account for any possible dependence on data skims, and this efficiency is considered in addition to the selection efficiencies, the trigger probability and the MC-to-data correction factors.

Tables 6.1 and 6.2 summarize the efficiencies for each of the specific selections, the trigger probability and the MC-to-data correction factors for the signal samples in the order in which the selections were applied, and show the total (product) preselection efficiency for each signal sample. More detailed tables, with the relevant numbers of events, the exclusive and cumulative efficiencies can be found in Appendix A. The total preselection efficiency (ε^{total}) is given for $\tilde{t}_1\bar{\tilde{t}}_1$ events with respect to $\tilde{t}_1\bar{\tilde{t}}_1 \rightarrow b\bar{b}\tilde{\chi}_1^0\tilde{\chi}_1^0\ell\nu_\ell q\bar{q}'$, where ℓ can be an electron or muon from the decay of a W boson (or chargino), including the case where the W boson (or chargino) decays first to a τ lepton. Taking into account all efficiencies and corrections, the number of expected signal events is given in Table 6.3.

Selection or κ	Stop 175/135	Stop 175/120	Stop 175/105	Stop 160/120	Stop 160/105	Stop 145/105
$\geq$4 good jets	39.47 ± 0.22	34.60 ± 0.24	34.96 ± 0.25	29.20 ± 0.20	31.21 ± 0.20	25.81 ± 0.19
Leading jet cut	93.57 ± 0.18	94.20 ± 0.20	95.64 ± 0.18	88.50 ± 0.26	91.90 ± 0.22	85.23 ± 0.30
Loose electron	40.88 ± 0.37	36.66 ± 0.42	32.55 ± 0.42	34.41 ± 0.41	31.34 ± 0.38	28.72 ± 0.42
Muon veto	99.97 ± 0.02	99.98 ± 0.02	100	100	100	99.97 ± 0.03
2nd electron veto	99.96 ± 0.02	99.98 ± 0.02	100	99.98 ± 0.02	99.98 ± 0.02	100
Vertex selection	98.37 ± 0.15	98.21 ± 0.19	98.10 ± 0.22	98.09 ± 0.20	98.67 ± 0.17	98.63 ± 0.20
$\not\!\!E_T$	87.55 ± 0.39	89.72 ± 0.44	89.36 ± 0.49	89.02 ± 0.46	86.87 ± 0.50	86.30 ± 0.60
Triangle selection	93.22 ± 0.32	93.31 ± 0.38	90.61 ± 0.49	92.52 ± 0.41	90.49 ± 0.47	90.40 ± 0.55
Tight electron	88.64 ± 0.42	88.37 ± 0.51	88.28 ± 0.57	87.48 ± 0.54	89.26 ± 0.52	87.75 ± 0.65
Trigger probability	96.06 ± 0.05	95.97 ± 0.06	95.87 ± 0.07	95.51 ± 0.08	95.32 ± 0.09	95.17 ± 0.10
$\kappa_{electron\ reco,\ ID}$	98.51 ± 0.01	98.50 ± 0.02	98.49 ± 0.02	98.51 ± 0.02	98.50 ± 0.02	98.51 ± 0.02
$\kappa_{electron\ likelihood}$	89.09 ± 0.07	89.04 ± 0.08	88.94 ± 0.09	89.05 ± 0.08	89.01 ± 0.08	89.18 ± 0.10
$\kappa_{b-fragmentation}$	96.78 ± 1.04	98.19 ± 1.26	94.13 ± 1.41	98.59 ± 1.31	98.75 ± 1.31	96.79 ± 1.58
$\geq$1 b-tag	54.52 ± 0.82	58.36 ± 1.05	61.34 ± 1.18	54.40 ± 1.09	56.02 ± 1.10	54.40 ± 1.33
HITFIT convergence	95.45 ± 3.03	91.51 ± 3.67	89.33 ± 4.01	91.63 ± 3.96	90.43 ± 3.88	90.30 ± 4.77
Data Quality	97.14 ± 0.50	97.14 ± 0.50	97.14 ± 0.50	97.14 ± 0.50	97.14 ± 0.50	97.14 ± 0.50
ε^{total}	4.43 ± 0.10	3.72 ± 0.10	3.20 ± 0.10	2.51 ± 0.08	2.52 ± 0.08	1.64 ± 0.06

Table 6.1.: Exclusive preselection efficiencies and correction factors in % for all signal mass points in $\tilde{t}_1\bar{\tilde{t}}_1 \rightarrow e$+jets events, with only statistical uncertainties included.

Selection or κ	Stop 175/135	Stop 175/120	Stop 175/105	Stop 160/120	Stop 160/105	Stop 145/105
$\geq$4 good jets	40.10 ± 0.23	34.53 ± 0.24	34.39 ± 0.25	28.69 ± 0.20	29.80 ± 0.20	24.76 ± 0.19
Leading jet cut	93.58 ± 0.18	93.85 ± 0.20	95.95 ± 0.18	88.55 ± 0.26	92.41 ± 0.21	85.67 ± 0.31
Loose muon	38.63 ± 0.37	34.79 ± 0.42	31.86 ± 0.42	34.30 ± 0.41	31.05 ± 0.39	29.23 ± 0.43
Z muon veto	100	100	100	99.98 ± 0.02	99.98 ± 0.02	100
2nd muon veto	100	100	100	99.98 ± 0.02	100	100
Electron veto	99.91 ± 0.04	99.87 ± 0.05	99.95 ± 0.04	99.85 ± 0.06	99.95 ± 0.03	99.88 ± 0.06
Vertex selection	98.37 ± 0.15	98.23 ± 0.20	98.53 ± 0.19	98.31 ± 0.19	98.39 ± 0.19	98.10 ± 0.24
$\not{E}_T$	83.54 ± 0.46	84.95 ± 0.53	84.26 ± 0.59	83.57 ± 0.55	81.78 ± 0.59	79.86 ± 0.71
Triangle selection	92.28 ± 0.36	91.65 ± 0.45	89.25 ± 0.55	91.48 ± 0.46	88.73 ± 0.53	87.63 ± 0.65
Tight muon	83.43 ± 0.52	82.66 ± 0.64	81.05 ± 0.73	81.89 ± 0.66	81.76 ± 0.69	78.71 ± 0.86
Trigger probability	84.45 ± 0.20	84.97 ± 0.23	85.66 ± 0.25	83.44 ± 0.26	84.33 ± 0.25	82.48 ± 0.35
$\kappa_{\mu\ ID\times\ acc\times\ cosmic\ veto}$	97.22 ± 0.16	97.37 ± 0.19	97.22 ± 0.21	97.32 ± 0.18	97.42 ± 0.20	97.23 ± 0.23
$\kappa_{\mu\ track}$	91.80 ± 0.08	91.82 ± 0.10	91.46 ± 0.10	91.56 ± 0.10	91.60 ± 0.10	91.92 ± 0.12
$\kappa_{\mu\ isolation}$	100.20 ± 0.01	100.20 ± 0.02	100.19 ± 0.02	100.22 ± 0.02	100.20 ± 0.02	100.21 ± 0.02
$\kappa_{b-fragmentation}$	98.32 ± 1.14	98.91 ± 1.40	98.10 ± 1.55	91.97 ± 1.41	99.71 ± 1.49	99.40 ± 1.77
$\geq$1 b-tag	57.35 ± 0.88	61.14 ± 1.16	60.39 ± 1.30	55.83 ± 1.23	57.75 ± 1.24	54.83 ± 1.52
HITFIT convergence	94.35 ± 3.16	91.04 ± 4.02	88.07 ± 4.37	89.24 ± 4.36	89.97 ± 4.32	88.29 ± 5.31
Data Quality	97.14 ± 0.50	97.14 ± 0.50	97.14 ± 0.50	97.14 ± 0.50	97.14 ± 0.50	97.14 ± 0.50
ε^{total}	3.57 ± 0.08	2.90 ± 0.09	2.44 ± 0.09	1.78 ± 0.06	1.89 ± 0.06	1.16 ± 0.05

Table 6.2.: Exclusive preselection efficiencies and correction factors in % for all signal mass points in $\tilde{t}_1\bar{\tilde{t}}_1 \rightarrow \mu$+jets events, with only statistical uncertainties included.

Sample	e+jets	μ+jets
Stop 175/135	4.0 ± 0.1	3.1 ± 0.1
Stop 175/120	3.1 ± 0.1	2.3 ± 0.1
Stop 175/105	2.8 ± 0.1	2.0 ± 0.1
Stop 160/120	3.6 ± 0.1	2.4 ± 0.1
Stop 160/105	3.8 ± 0.1	2.7 ± 0.1
Stop 145/105	4.5 ± 0.2	3.0 ± 0.1

Table 6.3.: Expected number of signal events after all preselections for 913 pb^{-1} of data in the e+jets channel and 871 pb^{-1} in the μ+jets channel. The uncertainties are based only on those from the preselection efficiencies.

6.2. Sample Composition

As described in Section 2.3.3, the background processes can be divided into instrumental background, which involves multijet production (sometimes referred to as "QCD"), and the inherent background, which consists of several processes that lead to the same final state as signal. Overall $t\bar{t}$ contribution is estimated using the NLO cross section, but a more sophisticated method to separate $t\bar{t}$ from signal is described in Section 6.3. The inherent background processes with small contributions to the background, namely, Z+jets production, single-top production and diboson production are also estimated using their theoretical cross sections, including the corrections to Z+jets discussed in Section 5.2.2. This section discusses the estimation of mulitjet and W+jets background.

6.2.1. Multijet Background

The contribution from multijet background is determined from data, exploiting the fact that events from signal and inherent backgrounds contain a true isolated lepton, whereas in multijet events the lepton or its isolation are instrumental ar-

tifacts [79]. The procedure is applied for each jet multiplicity ($n = 1, 2, 3, \geq 4$) at three stages: before and after the b-tagging, and, for $n \geq 4$, after convergence in HITFIT convergence.

We define two data samples: the "loose" sample that contains events that fulfill all preselection requirements, except that the lepton does not have to pass the tight electron likelihood or muon isolation requirement, and the "tight" sample, a subset of the former, containing events in which the leptons pass the tight-lepton requirement. The number of events in the loose and tight samples are labeled as N_{loose} and N_{tight}, respectively. N_{sig} is the number of events from signal and all inherent background processes in the loose sample, N_{QCD} the number of multijet events in the loose sample. The efficiency for a true lepton to pass the tight lepton requirement is ε_{sig}, and ε_{QCD} is the same efficiency for a false lepton. Using this notation, we can write:

$$\begin{aligned} N_{loose} &= N_{sig} + N_{QCD} \\ N_{tight} &= \varepsilon_{sig} N_{sig} + \varepsilon_{QCD} N_{QCD}. \end{aligned} \tag{6.1}$$

Since the equations can be written using a 2×2 matrix, the method is sometimes referred to as the "Matrix Method". Solving the linear system of equations for N_{QCD} and N_{sig} yields:

$$N_{sig} = \frac{N_{tight} - \varepsilon_{QCD} N_{loose}}{\varepsilon_{sig} - \varepsilon_{QCD}} \quad \text{and} \quad N_{QCD} = \frac{\varepsilon_{sig} N_{loose} - N_{tight}}{\varepsilon_{sig} - \varepsilon_{QCD}}. \tag{6.2}$$

Since $t\bar{t}$ and W+jets events are expected to dominate the contribution from processes with a true lepton, the efficiency for a lepton to pass the tight lepton selection (ε_{sig}) is determined from those Monte Carlo samples. A contribution of 50% for each sample is assumed in the analysis, and a comparison to the value obtained with a 100% contribution for either is used as a systematic uncertainty

on ε_{sig}. The efficiency measured using the Monte Carlo samples is corrected by the data-to-MC correction factor $\kappa_{electron\ likelihood} = 0.9584 \pm 0.0014$ for electrons and $\kappa_{\mu\ isolation} = 1.0024 \pm 0.0017$ for muons.

The efficiency for a false lepton to pass the tight-lepton selection (ε_{QCD}) is measured in data. Events with low missing transverse energy $\not{E}_T$<10 GeV are assumed to contain no leptons, and are used to determine the ratio of tight-lepton events to loose-lepton events. There is no apparent dependence on jet multiplicity. To improve statistics for determining ε_{QCD}, the final value is obtained from events with two or more jets.

The values of ε_{sig} for different jet multiplicities, and ε_{QCD} before b-tagging, are summarized in Table 6.4.

	e+jets	μ+jets
ε_{sig}(=1 jet)	0.826±0.007±0.047	0.909±0.009±0.019
ε_{sig}(=2 jets)	0.843±0.003±0.019	0.892±0.003±0.009
ε_{sig}(=3 jets)	0.844±0.002±0.001	0.875±0.003±0.005
ε_{sig}(≥4 jets)	0.841±0.003±0.016	0.850±0.003±0.018
ε_{QCD}	0.18±0.02	0.27±0.02

Table 6.4.: ε_{sig} with their statistical and systematic errors for different jet multiplicities, and ε_{QCD} with combined statistical and systematic uncertainties.

After b-tagging, the efficiencies for passing the tight-lepton selection are not expected to change, and the same values are used for estimating multijet background. For ε_{sig}, this is verified in the b-tagged $t\bar{t}$ and W+jets samples. For ε_{QCD}, this kind of study has been performed in the e+jets channel with very limited statistics, and showed no change. The only possible dependence on b-tagging could arise from jets that mimic leptons, which could then be b-tagged. But since the loose lepton criteria already require an isolation from all jets, this cannot occur, and the tight-lepton selection and b-tagging should therefore be independent.

Not only is the size of the multijet background needed in the analysis, but so is the shape of distributions as a function of different variables. For that, we use the data sample that passes the event selections including the loose-lepton selection, but not the tight-lepton selection (the "loose-tight sample").

Figure 6.1 illustrates the results of the Matrix Method for the transverse mass of the leptonic W boson in data and Monte Carlo in the e+jets channel, before b-tagging, for all jet multiplicities. Since the z-component of the neutrino is unknown, the mass of the leptonic W-boson cannot be reconstructed. However, by neglecting the z-components altogether, a quantity called transverse mass can be constructed, which is always smaller than or equal to the W mass [80]. The $t\bar{t}$ and W+jets samples, containing W bosons, show the characteristic edge at the W mass, whereas the multijet background is shifted to lower masses.

6.2.2. W+jets Background

After determining the contribution of all other background sources, the W+jets background is normalized to data, as described in this section. As mentioned in Section 5.2.2, the W+jets sample consists of the subsamples $Wb\bar{b}$, $Wc\bar{c}$, and Wjj, where the heavy-flavor samples get a higher relative contribution than predicted by Alpgen by the factor of $k_{HF} = 1.17 \pm 0.18$. The number of W+jets background events in the selected data sample is therefore:

$$N_{W+jets} = \alpha_W \cdot (\hat{N}_{Wjj} + k_{HF}\hat{N}_{Wc\bar{c}} + k_{HF}\hat{N}_{Wb\bar{b}}), \tag{6.3}$$

where $\hat{N}_{Wxx}$ is the yield predicted by Alpgen, k_{HF} the heavy-flavor scale factor, and α_W the normalization factor to be determined.

The normalization to data is performed before b-tagging by subtracting the other

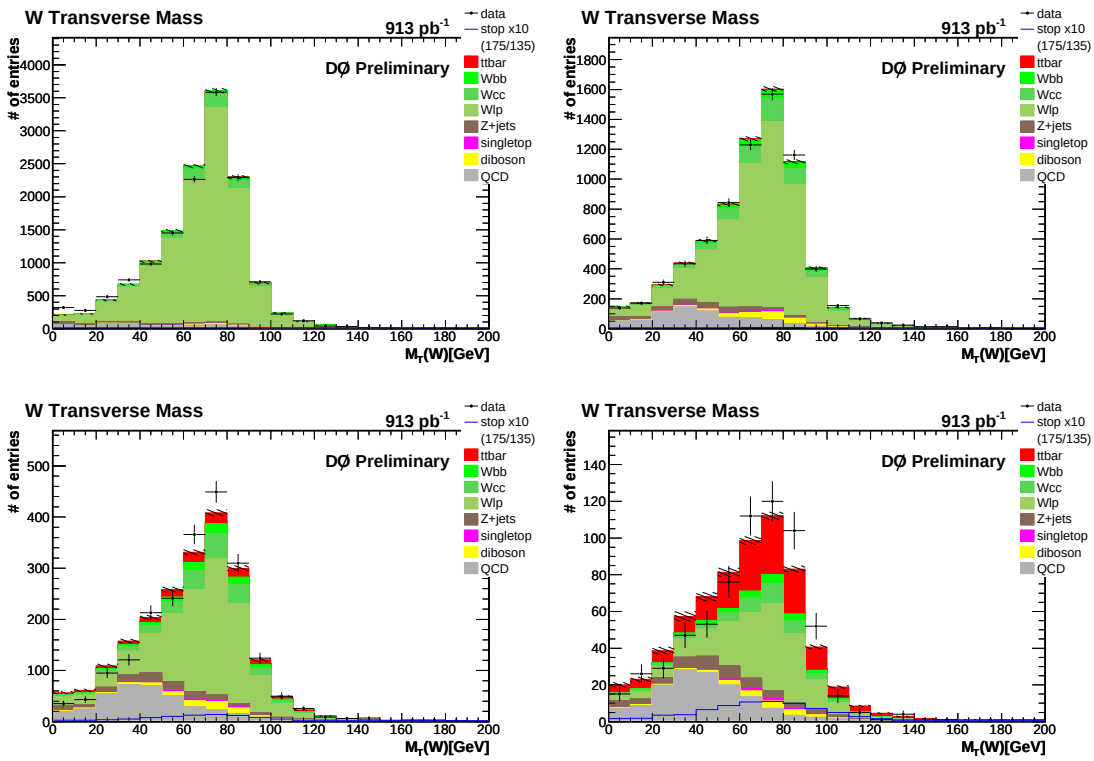

Figure 6.1.: Transverse mass of the W boson (for ℓ and $\not\!\!E_T$) in data and in Monte Carlo events for the e+jets channel, before b-tagging. Top left: events with 1 jet, top right: 2 jets, bottom left: 3 jets, bottom right: 4 or more jets.

known background contributions:

$$N_{W+jets} = N_{data} - N_{multijet} - N_{t\bar{t}} - N_{Z+jets} - N_{singletop} - N_{diboson}. \tag{6.4}$$

By combining Eqs. 6.3 and 6.4 the normalization factor α_W is determined for each jet multiplicity. When normalizing the W+jets background through this procedure, signal is assumed absent. The result is shown together with the event yields before b-tagging in Tables 6.5 and 6.6. By construction, the sum of all backgrounds equals the number of selected events in data. Figure 6.1 shows the results of the overall background estimation before b-tagging, and indicates that

the data are well described.

After b-tagging and convergence in HITFIT, the normalization factor α_W, determined before b-tagging, is applied in Eq. 6.3 to obtain the W+jets yield after b-tagging. The result for all background yields after b-tagging is shown in Tables 6.7 and 6.8. The sum of the background contributions no longer has to be the same as the number of events in data. Figure 6.2 again shows the good agreement of data with Monte Carlo for the transverse mass of the leptonic W boson, this time in the μ+jets channel after b-tagging. Additional data-MC comparisons can be found in Appendix B.

e+jets channel before b-tagging

Sample	=1 jet	=2 jets	=3 jets	≥4 jets
α_W	1.42	1.46	1.32	0.86
$N_{t\bar{t}}$	11.6	71.5	131.9	170.0
$N_{Wb\bar{b}}$	248.3	226.1	84.2	22.2
$N_{Wc\bar{c}}$	764.6	630.4	211.4	45.5
N_{Wjj}	11702.8	4974.1	1102.4	211.4
N_{Z+jets}	238.2	277.2	120.9	50.0
$N_{singletop}$	13.2	39.0	17.5	6.2
$N_{diboson}$	95.0	201.0	65.7	18.1
$N_{multijet}$	506.4	754.8	375.0	139.6
N_{SUM}	13580	7174	2109	663
N_{data}	13580	7174	2109	663

Table 6.5.: Normalization factor α_W for W+jets, and yields of background and data, before b-tagging in the e+jets channel.

6.3. Extraction of Signal

Although the $\tilde{t}_1\bar{\tilde{t}}_1$ and $t\bar{t}$ final states are remarkably similar, they nevertheless exhibit small differences in event kinematics. The differences are combined using

μ+jets channel before b-tagging

Sample	=1 jet	=2 jets	=3 jets	≥4 jets
α_W	1.48	1.60	1.62	1.25
$N_{t\bar{t}}$	7.1	48.3	95.7	137.1
$N_{Wb\bar{b}}$	190.1	204.7	84.7	28.0
$N_{Wc\bar{c}}$	610.8	548.8	219.8	57.2
N_{Wjj}	9754.8	4456.9	1143.1	263.7
N_{Z+jets}	847.6	446.1	160.7	63.2
$N_{singletop}$	9.4	30.0	13.7	4.8
$N_{diboson}$	71.1	169.1	55.1	15.3
$N_{multijet}$	114.2	148.0	65.4	24.6
N_{SUM}	11605	6052	1838	594
N_{data}	11605	6052	1838	594

Table 6.6.: Normalization factor α_W for W+jets, and yields of background and data, before b-tagging in the μ+jets channel.

e+jets channel after b-tagging

Sample	=1 jet	=2 jets	=3 jets	≥4 jets	HITFIT
α_W	1.42	1.46	1.32	0.86	0.86
$N_{t\bar{t}}$	4.9	39.3	77.6	108.3	103.0
$N_{Wb\bar{b}}$	70.6	86.0	35.4	9.1	8.5
$N_{Wc\bar{c}}$	39.5	46.8	20.1	5.0	4.8
N_{Wjj}	124.5	59.0	13.2	4.0	3.8
N_{Z+jets}	2.9	7.5	5.2	3.0	2.8
$N_{singletop}$	5.1	19.3	9.3	3.6	3.1
$N_{diboson}$	3.1	11.6	4.2	1.4	1.4
$N_{multijet}$	16.2	41.1	22.3	11.1	10.7
N_{SUM}	266.8	310.7	187.2	145.6	138.1
N_{data}	255	329	193	145	133

Table 6.7.: Normalization factor α_W for W+jets, and yields of background and data, after b-tagging in the e+jets channel.

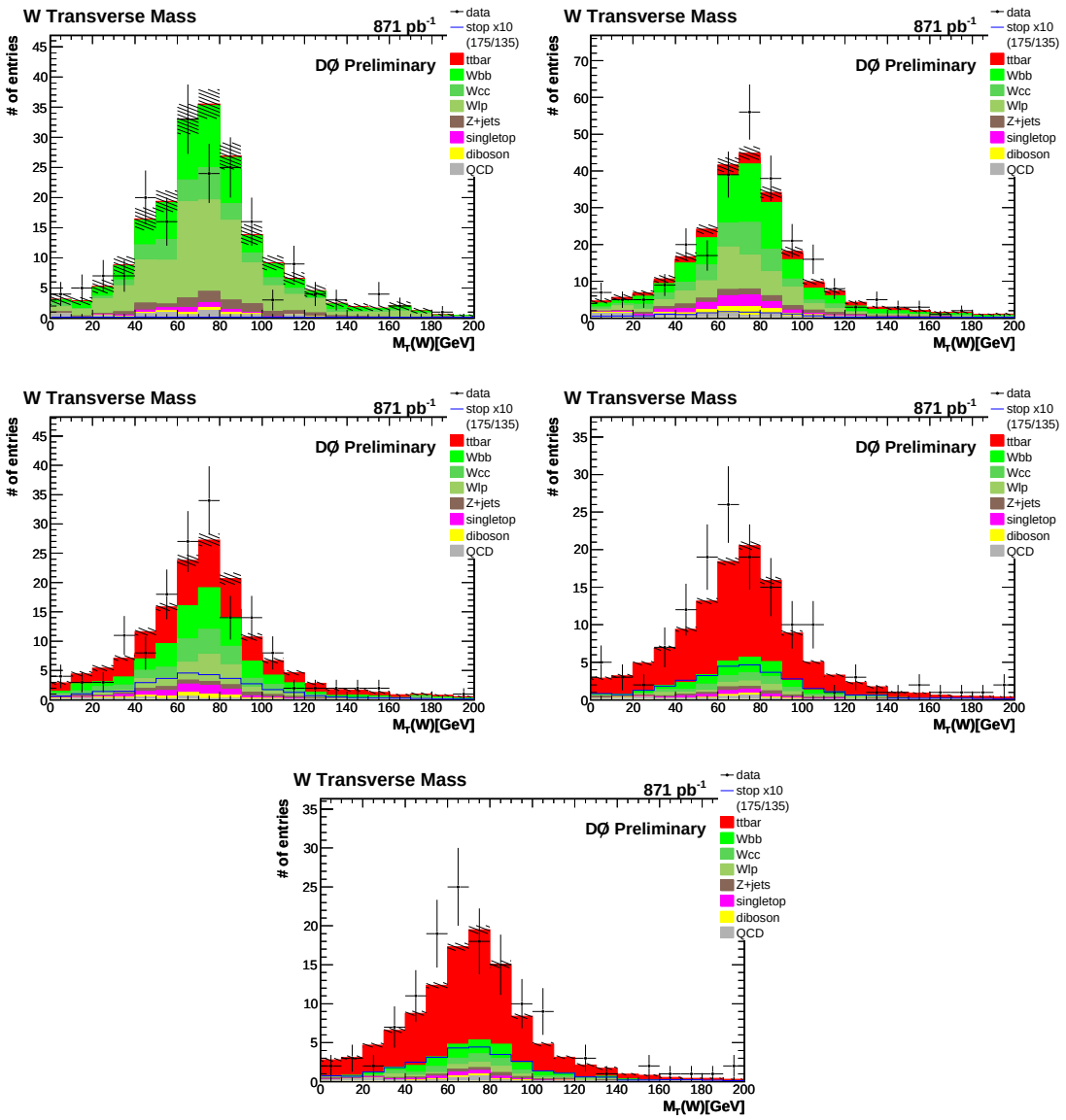

Figure 6.2.: Transverse mass of the W boson (for ℓ and $\not\!\!E_T$) in data and in Monte Carlo events for the μ+jets channel, after b-tagging. Top left: In events with 1 jet, top right: 2 jets, middle left: 3 jets, middle right: 4 or more jets, bottom: 4 or more jets, after convergence in HITFIT.

μ+jets channel after b-tagging

Sample	=1 jet	=2 jets	=3 jets	≥4 jets	HITFIT
α_W	1.48	1.60	1.62	1.25	1.25
$N_{t\bar{t}}$	3.1	27.8	58.5	89.8	84.2
$N_{Wb\bar{b}}$	56.5	79.8	36.1	12.2	11.1
$N_{Wc\bar{c}}$	27.2	39.6	22.2	6.9	6.5
N_{Wjj}	89.0	51.3	19.3	4.4	4.0
N_{Z+jets}	14.3	14.8	6.9	3.9	3.3
$N_{singletop}$	3.7	15.2	7.5	2.9	2.5
$N_{diboson}$	2.8	10.2	3.8	1.4	1.2
$N_{multijet}$	6.6	12.0	3.0	2.9	3.2
N_{SUM}	203.1	250.7	157.5	124.3	116.0
N_{data}	189	265	163	146	135

Table 6.8.: Normalization factor α_W for W+jets, and yields of background and data, after b-tagging in the μ+jets channel.

a multivariate technique to achieve signal-background separation.

6.3.1. Variables for Discriminating Signal from Background

A wide variety of distributions in $\tilde{t}_1\bar{\tilde{t}}_1$ events were compared to those in $t\bar{t}$ events. This included kinematic distributions of single objects such as jets or leptons, angular distributions, invariant masses as well as event variables such as sphericity. Because of additional neutralinos in $\tilde{t}_1\bar{\tilde{t}}_1$ events, more missing transverse energy is expected than in $t\bar{t}$ events. However, because the neutralinos in the event are produced almost back-to-back, no difference is observed, as shown in Fig. 6.3. Most variables show no discriminating power, or are correlated with others. At this point, the kinematic fitter HITFIT, which was described in Section 6.1, becomes useful. Although its purpose is to reconstruct $t\bar{t}$ events, and it fails to

reconstruct stop-quark events correctly because of the neutralinos, which is evident when comparing the HITFIT results with Monte Carlo distributions on parton level, it is nonetheless useful in distinguishing $t\bar{t}$ events from $\tilde{t}_1\bar{\tilde{t}}_1$ events. HITFIT converges on a large fraction of $\tilde{t}_1\bar{\tilde{t}}_1$ events, and therefore does not cause a large loss in efficiency.

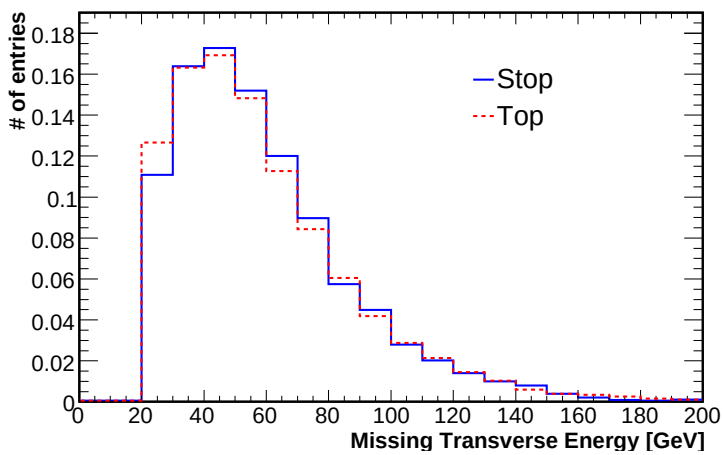

Figure 6.3.: Missing transverse energy in the e+jets channel in $\tilde{t}_1\bar{\tilde{t}}_1$ 175/135 (solid line) and $t\bar{t}$ events (dashed line).

Distributions for $\tilde{t}_1\bar{\tilde{t}}_1$ depend slightly on the masses of the supersymmetric particles. In particular, only the 175/135 mass point has "on-shell" W bosons, whereas all other points have off-shell W bosons. Thus, for each stop-quark mass point, a different subset of the following eleven variables is used in extracting signal:

- The p_T **of the leading** b**-tagged jet** ($p_T(b\text{-jet})$) indicates how much phase space is available for the b-quark from top or stop decay. Since the chargino from the stop quark is heavier than the W boson from the top-quark decay, the b-quark p_T spectrum and consequently the b-jet p_T spectrum is softer in $\tilde{t}_1\bar{\tilde{t}}_1$ events.

- The W **transverse mass** ($M_T(W)$) shows a Jacobian edge for an on-shell W boson in the event. It is reconstructed using the kinematic information for the lepton and $\not{E}_T$. Since most stop-quark mass points have an off-shell W-boson, this quantity is shifted to lower masses.

- $K_{Tmin} = \Delta R_{jj}^{min} E_T^{min}$ provides a measure of the minimum jet-p_T relative to the other in the jet pair that is closest in $\eta - \varphi$ space. Only the four jets of highest p_T are considered in the definition. ΔR_{jj}^{min} is the minimum ΔR distance between a pair of jets, and E_T^{min} is the transverse energy of the lesser jet of that pair.

The following variables have specific designations for jets. All jets, excluding the leading b-tagged jet, are ordered by p_T. The three with highest p_T are called "leading other jet", jet 3 and jet 4.

- The **invariant mass of jet 3 and jet 4** ($m(j,j)$). In $t\bar{t}$ events, these two jets are often the light jets from the $W \to \bar{q}q'$ decay, and the quantity reflects the mass of the W boson. In $\tilde{t}_1\bar{\tilde{t}}_1$ events, a lower mass is reconstructed even for the mass point with on-shell W bosons, and indicates that the two jets do not originate from a W boson.

- The distance in $\eta - \varphi$ space ΔR **between the leading b-tagged jet and the leading other jet** ($\Delta R(b, lead)$) approximates the ΔR between the W boson and the b quark from the same top or stop quark. In $\tilde{t}_1\bar{\tilde{t}}_1$ events, this quantity is much smaller than in $t\bar{t}$ events.

- ΔR **between the lepton and the leading b-tagged jet** ($\Delta R(lep, b)$) approximates the same quantity described above, and constitutes an alternative to the previous variable.

The final variables are provided by the kinematic fitter HITFIT:

- The **top quark mass as reconstructed in** HITFIT (m_t^{hf}) gives the correct top quark mass in $t\bar{t}$ events, but it reconstructs a lower mass in $\tilde{t}_1\bar{\tilde{t}}_1$ events. This happens not only because the stop-quark mass is often lower than the top-quark mass, but also because neutralinos carry away energy, and they are not considered in HITFIT.

- The quantity $\cos\theta^*(b,b)^{hf}$ is constructed by HITFIT using the angle θ^* of the b-jet originating from the hadronic top or stop quark relative to the beam axis in the center-of-mass system of the two b-jets. This variable is a good approximation of the similarly defined $\cos\theta^*(t,t)$, which is different in $t\bar{t}$ and $\tilde{t}_1\bar{\tilde{t}}_1$ events because of the difference in spins. After preselection and HITFIT reconstruction, however, $\cos\theta^*(t,t)^{hf}$ provides less separation than $\cos\theta^*(b,b)^{hf}$.

- The **invariant mass of the b-jets** ($m^{hf}(b,b)$) is reconstructed using the assignments and kinematics of the best fit in HITFIT.

- As mentioned above, the ΔR between the correct pair of W-boson and b-quark assignments in Monte Carlo exhibits good separation. HITFIT does not always assign the pairs correctly, especially in $\tilde{t}_1\bar{\tilde{t}}_1$ events, which is why, for some mass points, ΔR **between the correct** HITFIT **pair of hadronic W-boson and b-jet** ($\Delta R(W,b)^{hf}_{corr}$) gives better separation,

- whereas, for other mass points, the ΔR **between the wrong** HITFIT **pair of hadronic W-boson and b-jet** ($\Delta R(W,b)^{hf}_{wrong}$) gives better separation.

For each stop-quark mass point, we choose an optimal set of variables. The decision is based on achieving best discrimination, while providing least correlation among variables. Table 6.9 lists which variables are used for which mass point.

As an example, Fig. 6.4 shows a comparison of the input variables for $\tilde{t}_1\bar{\tilde{t}}_1$, $t\bar{t}$, and W+jets events for the Stop 175/135 mass point in the μ+jets channel.

$m_{\tilde{t}_1}$	$m_{\tilde{\chi}_1^\pm}$	Variables in Likelihood Discriminant
175 GeV	135 GeV	$p_T(b\text{-jet})$, $\Delta R(b, lead)$, m_t^{hf}, $\cos\theta^*(b,b)^{hf}$
175 GeV	120 GeV	$p_T(b\text{-jet})$, $m(j,j)$, m_t^{hf}, $\Delta R(W,b)^{hf}_{wrong}$
175 GeV	105 GeV	$M_T(W)$, $m(j,j)$, K_{Tmin}, m_t^{hf}, $m^{hf}(b,b)$
160 GeV	120 GeV	$p_T(b\text{-jet})$, $m(j,j)$, m_t^{hf}, $\Delta R(W,b)^{hf}_{corr}$
160 GeV	105 GeV	$p_T(b\text{-jet})$, $M_T(W)$, $m(j,j)$, $\Delta R(lep,b)$, m_t^{hf}
145 GeV	105 GeV	$p_T(b\text{-jet})$, $M_T(W)$, $m(j,j)$, $\Delta R(lep,b)$, m_t^{hf}

Table 6.9.: Variables used in the likelihood discriminant for different signal mass points.

The complete set of plots for each mass point in both channels can be found in Appendix C.1.

Data-MC comparison of the same input variables for the stop 175/135 mass point in the e+jets channel, in the signal bin of $\geq$4 jets, after b-tagging and convergence of HITFIT, is shown in Fig. 6.5. No contribution from signal is added to the Monte Carlo prediction, but the distribution of the variable in the stop 175/135 sample is shown enhanced by a factor of ten. The data-MC comparisons for variables in both channels are displayed in Appendix C.2.

6.3.2. Likelihood Discriminant

After selecting the optimal set of variables that provide good separation and little correlation among each other, the variables are combined in a likelihood discriminant.

Interpreting distributions in any variable x_i in $\tilde{t}_1\bar{\tilde{t}}_1$ signal and $t\bar{t}$ background as probability distributions, a signal probability $P_{sig}(x_i)$ and a background probability $P_{bg}(x_i)$ can be assigned to each event by comparing variable x_i in that event to the distribution of that variable in signal and background. Assuming negligible correlations, the individual probabilities for each variable can be multiplied to

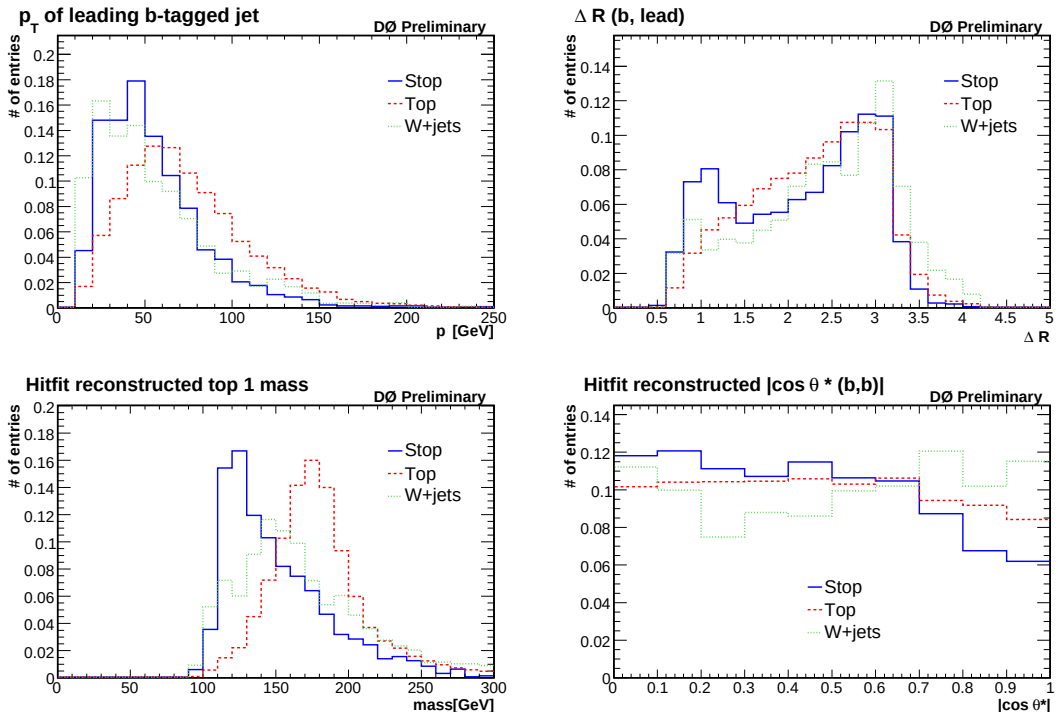

Figure 6.4.: Input variables for the 175/135 mass point in the μ+jets channel.

yield an overall signal and background probability for the event:

$$P_{sig/bg}(\mathbf{x}) = \prod_i P_{sig/bg}(x_i), \tag{6.5}$$

where $\mathbf{x} = (x_1, x_2, ...)$ is the collection of x_i values in this event. A likelihood discriminant $\mathcal{L}(\mathbf{x})$ can be defined as:

$$\mathcal{L}(\mathbf{x}) = \frac{P_{sig}(\mathbf{x})}{P_{sig}(\mathbf{x}) + P_{bg}(\mathbf{x})}. \tag{6.6}$$

The likelihood discriminant $\mathcal{L}(\mathbf{x})$ takes on values between 0 and 1, with 1 being more signal-like and 0 more background-like. Full MC statistics are used to construct the templates and the likelihood discriminant for each sample so as to

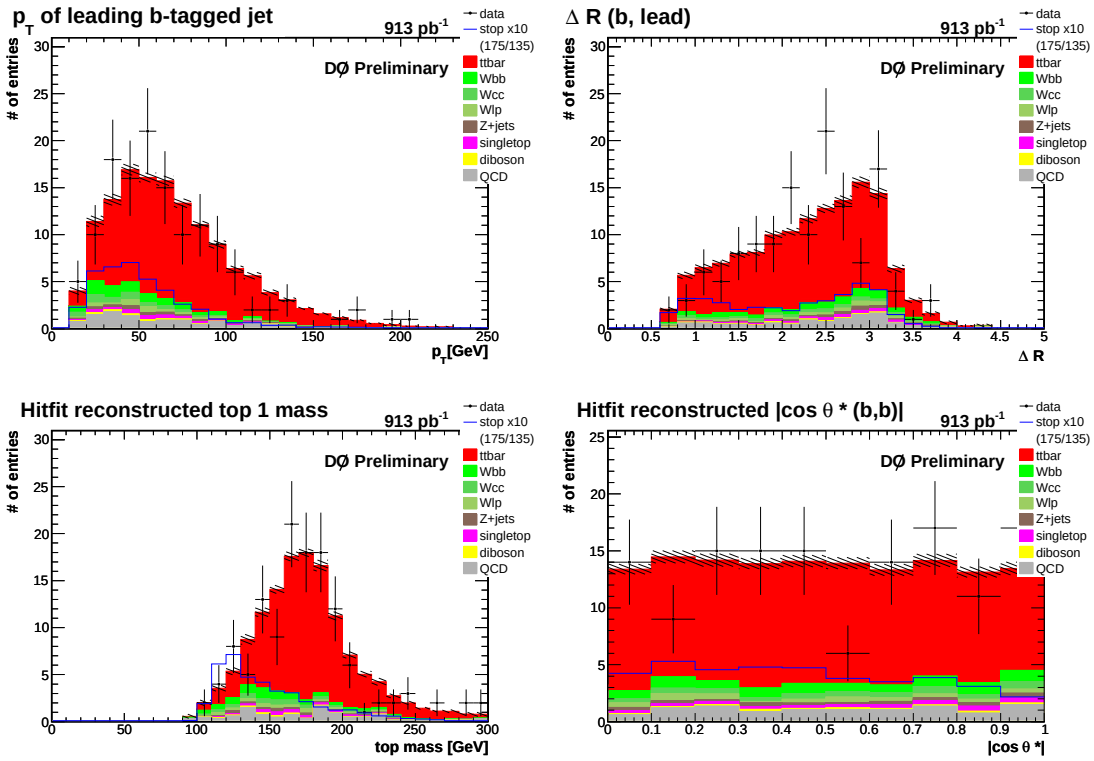

Figure 6.5.: Input variables used in the likelihood discriminant for the 175/135 mass point in data and MC in the e+jets channel.

minimize statistical uncertainty.

Figure 6.6 shows the resulting likelihood discriminants for the 175/135 mass point, comparing $t\bar{t}$ and $\tilde{t}_1\bar{\tilde{t}}_1$ signal for Monte Carlo and data for both the e+jets and the μ+jets events. Similar plots for all mass points can be found in Appendix C.3.

6.3.3. Expected Limits

A Bayesian approach, as described in Section 2.4, is used to extract limits from the distributions in likelihood discriminants.

Before applying the limit extraction method to data, the procedure is evaluated

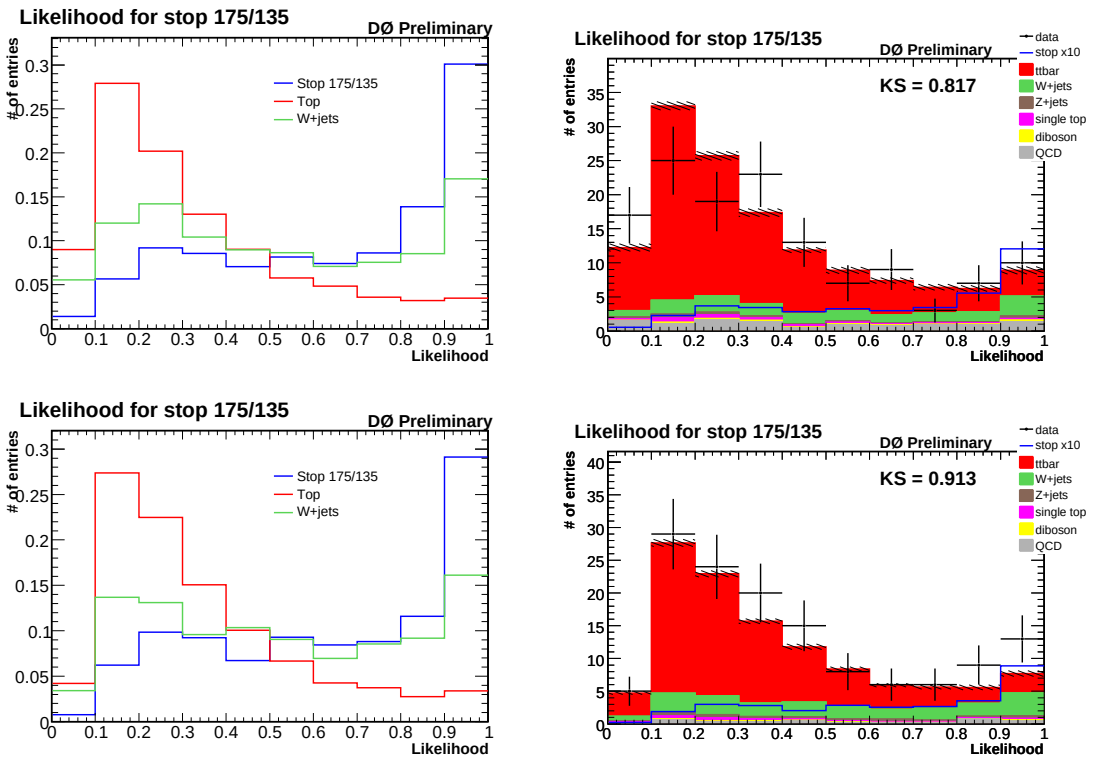

Figure 6.6.: Likelihood discriminant for the 175/135 mass point. The distribution for the 175/135 mass point has been enhanced by a factor of ten and overlaid. Top: in the e+jets channel, bottom: in the μ+jets channel.

on the sum of the preselected Monte Carlo background samples, normalized to their expected yields. That gives an estimate on what limits could be reached without the presence of a contribution from signal. The posterior probability as a function of the $\tilde{t}_1\bar{\tilde{t}}_1$ cross section for the stop 175/135 mass point is shown in Fig. 6.7, and the expected upper limit on the cross section at 95% confidence is defined by the integral of 95% of the area. These results already include systematic uncertainties, as discussed below in Section 6.5. Table 6.10 lists the expected limits for all mass points, with and without systematic uncertainties. The complete set of posterior probabilities can be found in Appendix D.1.

As a cross check, the posterior probability is also calculated as a function of

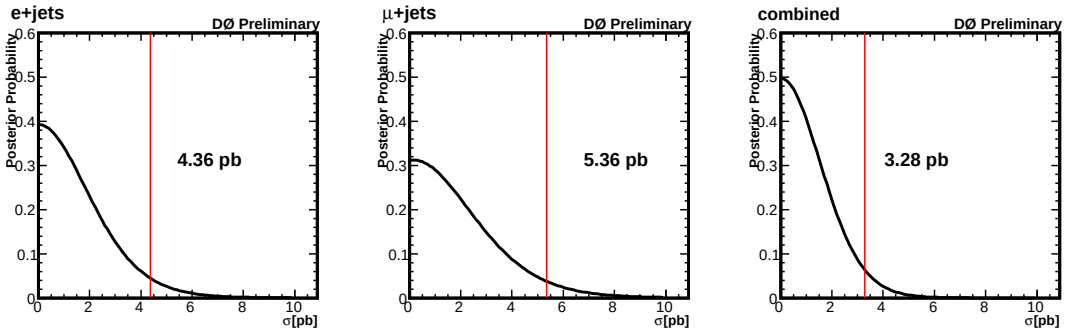

Figure 6.7.: Expected posterior probability as a function of the $\tilde{t}_1\bar{\tilde{t}}_1$ cross section for the 175/135 mass point. Left: For the e+jets channel, middle: for the μ+jets channel, right: for both channels combined.

Sample	e+jets	μ+jets	combined
Statistics only			
Stop 175/135	2.54	3.24	1.91
Stop 175/120	3.85	4.83	2.91
Stop 175/105	4.26	5.59	3.29
Stop 160/120	4.99	7.13	3.93
Stop 160/105	5.05	6.58	3.86
Stop 145/105	7.05	9.73	5.48
With systematic uncertainties			
Stop 175/135	4.36	5.36	3.28
Stop 175/120	6.36	7.72	4.97
Stop 175/105	6.85	7.55	5.16
Stop 160/120	6.79	9.10	5.42
Stop 160/105	6.89	10.26	5.63
Stop 145/105	9.30	11.84	7.27

Table 6.10.: Expected Bayesian limits at 95% confidence on the $\tilde{t}_1\bar{\tilde{t}}_1$ cross section in pb, without and with systematic uncertainties, assuming a $t\bar{t}$ cross section of 6.77 pb.

both the $\tilde{t}_1\bar{\tilde{t}}_1$ and $t\bar{t}$ cross section, as shown in Fig. 6.8. We can again extract the expected limits for the $\tilde{t}_1\bar{\tilde{t}}_1$ cross section at 95% confidence, which yields results similar to those obtained using the standard method, and now we can also evaluate the $t\bar{t}$ cross sections with their uncertainties. Table 6.11 summarizes the results for the expected limits on the $\tilde{t}_1\bar{\tilde{t}}_1$ cross section, and the expected $t\bar{t}$ cross sections. The $t\bar{t}$ cross section is consistently below the input cross section of 6.77 pb, which shows that this method should not be used to extract the $t\bar{t}$ cross section for the Standard Model, where no $\tilde{t}_1\bar{\tilde{t}}_1$ contribution is expected.

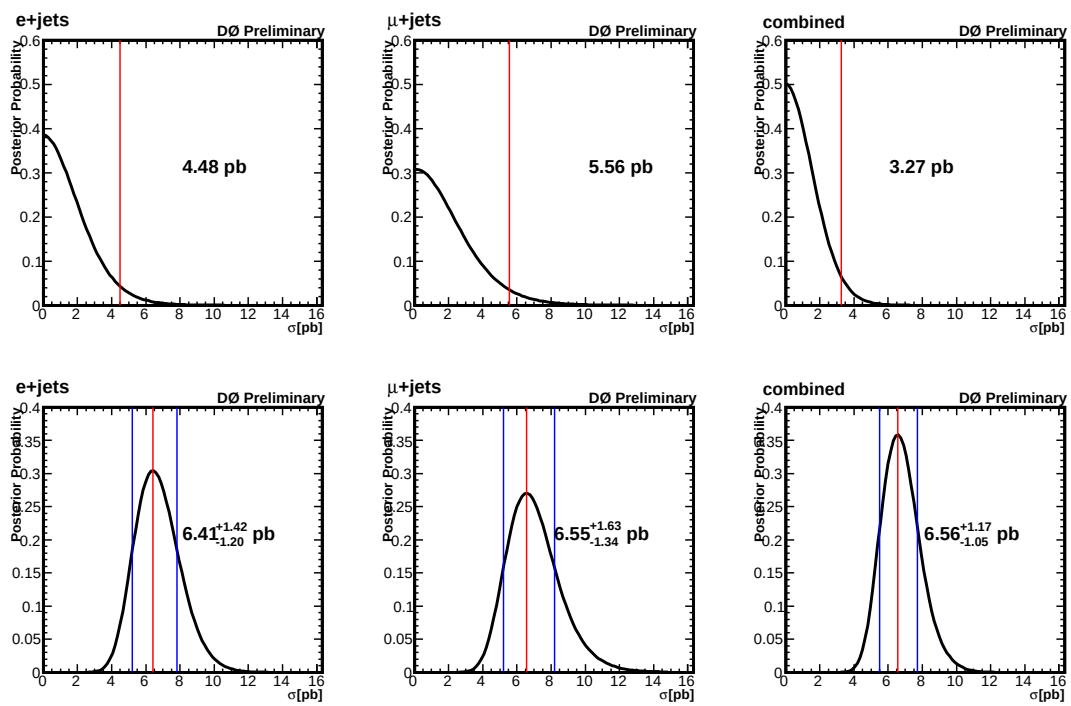

Figure 6.8.: Expected posterior probability for the 175/135 mass point. Top: as a function of the $\tilde{t}_1\bar{\tilde{t}}_1$ cross section, bottom: as a function of the $t\bar{t}$ cross section.

Sample	$\tilde{t}_1\bar{\tilde{t}}_1$ limit			$t\bar{t}$ cross section		
	e+jets	μ+jets	combined	e+jets	μ+jets	combined
Statistics only						
Stop 175/135	3.01	3.90	2.28	$6.40^{+0.82}_{-0.79}$	$6.34^{+0.93}_{-0.89}$	$6.49^{+0.61}_{-0.60}$
Stop 175/120	5.24	6.48	3.95	$6.25^{+0.87}_{-0.86}$	$6.20^{+0.97}_{-0.94}$	$6.39^{+0.64}_{-0.64}$
Stop 175/105	5.74	7.70	4.49	$6.26^{+0.86}_{-0.85}$	$6.17^{+0.98}_{-0.96}$	$6.38^{+0.64}_{-0.64}$
Stop 160/120	6.01	8.72	4.76	$6.38^{+0.83}_{-0.80}$	$6.32^{+0.93}_{-0.90}$	$6.48^{+0.62}_{-0.60}$
Stop 160/105	6.35	8.26	4.85	$6.33^{+0.84}_{-0.81}$	$6.28^{+0.94}_{-0.91}$	$6.44^{+0.63}_{-0.61}$
Stop 145/105	8.19	11.27	6.35	$6.42^{+0.82}_{-0.78}$	$6.38^{+0.92}_{-0.87}$	$6.51^{+0.61}_{-0.58}$
With systematic uncertainties						
Stop 175/135	4.48	5.56	3.27	$6.41^{+1.42}_{-1.20}$	$6.55^{+1.63}_{-1.34}$	$6.56^{+1.17}_{-1.05}$
Stop 175/120	6.70	8.20	5.21	$6.16^{+1.43}_{-1.25}$	$6.20^{+1.64}_{-1.37}$	$6.34^{+1.19}_{-1.06}$
Stop 175/105	7.45	7.96	5.42	$6.12^{+1.46}_{-1.25}$	$6.16^{+1.66}_{-1.35}$	$6.30^{+1.19}_{-1.05}$
Stop 160/120	6.89	9.38	5.50	$6.50^{+1.39}_{-1.24}$	$6.38^{+1.68}_{-1.35}$	$6.56^{+1.19}_{-1.04}$
Stop 160/105	7.10	10.79	5.80	$6.31^{+1.42}_{-1.21}$	$6.32^{+1.75}_{-1.40}$	$6.45^{+1.21}_{-1.05}$
Stop 145/105	9.42	12.19	7.36	$6.50^{+1.39}_{-1.22}$	$6.52^{+1.69}_{-1.34}$	$6.64^{+1.15}_{-1.03}$

Table 6.11.: Expected Bayesian limits at 95% confidence on the $\tilde{t}_1\bar{\tilde{t}}_1$ cross section, and the expected $t\bar{t}$ cross section in pb, without and with systematic uncertainties.

6.4. Closure Tests

To check the validity of the limit-extraction procedure for $\tilde{t}_1\bar{\tilde{t}}_1$ production, we perform two studies on MC events. Two ensembles of pseudo datasets are generated for each mass point:

1. 500 experiments without signal, but with expected backgrounds, with the $t\bar{t}$ background normalized to its theoretical cross section.

2. 100 experiments with expected backgrounds, with the $t\bar{t}$ background normalized to its theoretical cross section, and the predicted $\tilde{t}_1\bar{\tilde{t}}_1$ signal (at NLO) multiplied by a factor of ten.

The first set of experiments determines the expected limits in an alternative way, and is shown to be equivalent to the method presented above. Each MC experi-

ment is treated the same way as the data, including the treatment of systematic uncertainties, and each result enters the ensemble of experiments. The outcome is shown for the 175/135 mass point in Fig. 6.9. The solid vertical line indicates the previously derived expected limit, and agrees well with the mean of the histogram for the experiments in the ensemble. In addition, the dashed vertical line marks the observed limit, which is discussed in Section 7. By comparing the limit in data to the outcome of the MC experiments, we can determine how well the observed limit agrees with the assumption of no contribution from signal. Appendix E contains similar plots for all chosen mass points.

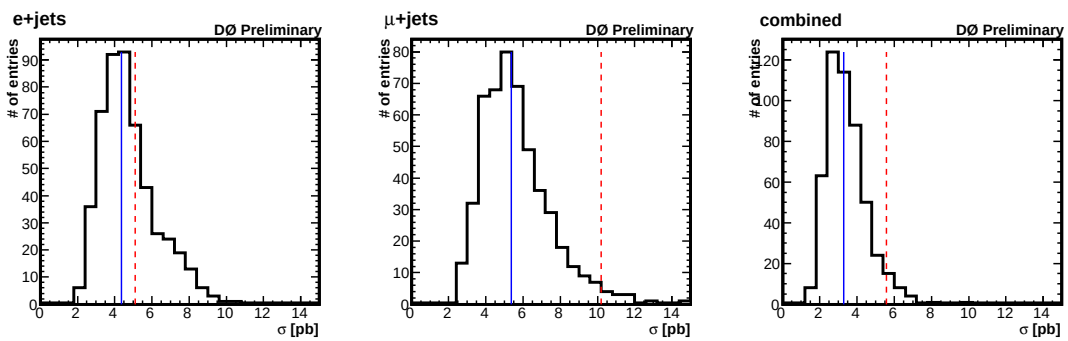

Figure 6.9.: Results for limits in experiments with no signal content for the 175/135 mass point. The expected limit is shown as solid line, the observed limit is shown as dashed line.

The second set of MC experiments is designed to test the ability of the Bayesian method to measure a cross section. Since the predicted NLO cross section is too low to be measured with the given data, the experiments contain a contribution from signal multiplied by a factor of ten. As with the $t\bar{t}$ cross section, the measured value is given by the peak of the posterior probability. The result of each experiment is again used in the ensemble of results, which for the 175/135 mass point is shown in Fig. 6.10. The solid line indicates the input cross section for signal, which, for all mass points, agrees well with the mean, thereby suggesting the ability of the

method to extract a cross section for signal. The results for the other mass points are displayed in Appendix E.

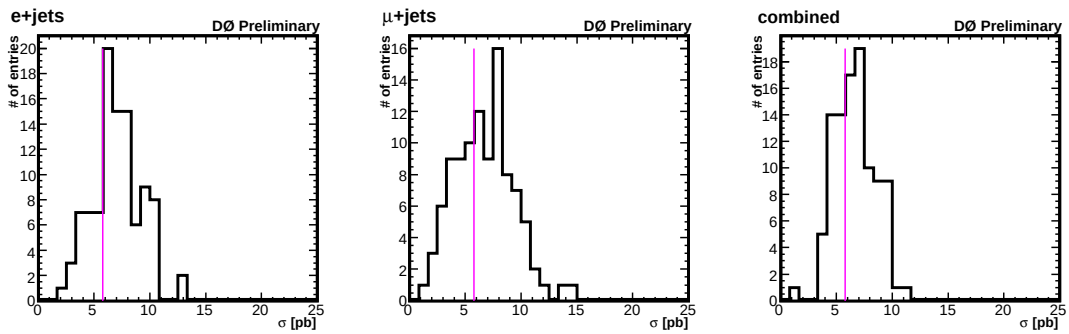

Figure 6.10.: Results for cross sections in experiments when the theoretical signal content for the 175/135 mass point is raised by a factor of ten. The input cross section is shown as a line.

6.5. Systematic Uncertainties

Although the analysis is limited mainly by statistics, a wide range of systematic sources are considered in the uncertainty. These are included in the calculation of posterior probabilities through the prior $\pi(a, \mathbf{b})$ in Eq. 2.11. Technically, this is achieved by sampling a and $\mathbf{b}$ for each bin of the likelihood discriminant from a multivariate Gaussian in the integration. The mean of the Gaussian is given by the estimate yields of each sample in that bin, and the width reflects the uncertainties on each sample. The systematic uncertainties can be categorized into two types, one that changes the yield uniformly for all bins of the likelihood discriminant, and another that affects each bin differently. The latter changes the shape of the distribution in the likelihood discriminant. Tables 6.12 and 6.13 summarize the relative size of all systematic uncertainties on contributions in the e+jets channel, and in the μ+jets channel, respectively. The upper parts of the tables are dedicated

to systematic uncertainties that change the yield uniformly, whereas the lower parts display the uncertainties that affect shape. Correlations of systematics between sources, as indicated in the tables, are taken into account in the procedure.

This section is subdivided into a discussion of systematic uncertainties that change the yield uniformly and those that affect the distribution in the likelihood discriminant.

6.5.1. Systematic Uncertainties on Yields

All systematic uncertainties that affect the yields uniformly are "symmetrized", which means that even if the source changes the yield differently to lower and upper values, the larger effect is used for both directions. It should be noted that W+jets and multijet-background yields are affected only by the uncertainty on their contribution, since they are estimated using data, whereas all other sources of systematic uncertainty arise from estimating the yield using cross sections and efficiencies from Monte Carlo. In the following, each source of systematic uncertainty is discussed in detail.

Luminosity The uncertainty on the integrated luminosity affects all yields uniformly. An uncertainty of 6.1% has been determined previously [57].

Monte Carlo Cross Sections The cross sections used to normalize some of the Monte Carlo samples all have an uncertainty, which is described in Section 5.2.2. For $t\bar{t}$, when including the uncertainty on the cross section due to the uncertainty on the top-quark mass, the relative uncertainty is 18%. For the Z+jets sample, a relative uncertainty of 15% is applied, 12.6% is used for the single-top sample, and 6.8% for the diboson samples.

Source	$\tilde{t}_1\bar{\tilde{t}}_1$	$t\bar{t}$	W+jets	Z+jets	single top	diboson	multijet
Luminosity	6.1	6.1	-	6.1	6.1	6.1	-
MC Cross Section $t\bar{t}$	-	18.0	-	-	-	-	-
MC Cross Section single top	-	-	-	-	12.6	-	-
MC Cross Section Z+jets	-	-	-	15.0	-	-	-
MC Cross Section diboson	-	-	-	-	-	6.8	-
Top Quark Mass	-	4.9	-	-	-	-	-
Matrix Method	-	-	-	-	-	-	21.1
W Normalization	-	-	70.3	-	-	-	-
Primary Vertex Scale Factor	1.12	1.12	-	1.12	1.12	1.12	-
Primary Vertex z Position	1.6	1.6	-	1.6	1.6	1.6	-
Electron Reconstruction and Identification	2.2	2.2	-	2.2	2.2	2.2	-
Electron Track Matching and Likelihood	5.0	5.0	-	5.0	5.0	5.0	-
L1 EM Trigger	1.03	1.03	-	1.03	1.03	1.03	-
L2 EM Trigger	0.02	0.02	-	0.02	0.02	0.02	-
L3 EM Trigger	0.58	0.58	-	0.58	0.58	0.58	-
L3 Jet Trigger	0.05	0.05	-	0.05	0.05	0.05	-
JES down	-23.6 – -5.6	-7.4	-	-15.5	-16.2	-13.9	-
JES up	-3.7 – 17.9	6.3	-	20.4	16.8	29.8	-
W+jets k-factor down	-	-	-	-	-	-	-
W+jets k-factor up	-	-	-	-	-	-	-
b-TRF down	-14.6 – 7.7	-3.3	-0.0	-	-	-	-
b-TRF up	-9.0 – 14.9	4.8	0.0	-	-	-	-

Table 6.12.: Summary of systematic uncertainties and their % effect in the e+jets channel.

Source	$\tilde{t}_1\bar{\tilde{t}}_1$	$t\bar{t}$	W+jets	Z+jets	single top	diboson	multijet
Luminosity	6.1	6.1	-	6.1	6.1	6.1	-
MC Cross Section $t\bar{t}$	-	18.0	-	-	-	-	-
MC Cross Section single top	-	-	-	-	12.6	-	-
MC Cross Section Z+jets	-	-	-	15.0	-	-	-
MC Cross Section diboson	-	-	-	-	-	6.8	-
Top Quark Mass	-	4.2	-	-	-	-	-
Matrix Method	-	-	-	-	-	-	54.2
W Normalization	-	-	30.1	-	-	-	-
Primary Vertex Scale Factor	1.12	1.12	-	1.12	1.12	1.12	-
Primary Vertex z Position	1.6	1.6	-	1.6	1.6	1.6	-
Muon Identification	7.0	7.0	-	7.0	7.0	7.0	-
Muon Tracking	1.5	1.5	-	1.5	1.5	1.5	-
Muon Isolation	2.0	2.0	-	2.0	2.0	2.0	-
Muon Trigger	2.7	2.7	-	2.7	2.7	2.7	-
Jet Trigger	0.2	0.2	-	0.2	0.2	0.2	-
JES down	-27.0 – -8.1	-6.0	-	-36.8	-17.6	-16.4	-
JES up	-10.6 – 19.1	6.1	-	20.3	22.1	26.4	-
W+jets k-factor down	-	-	-	-	-	-	-
W+jets k-factor up	-	-	-	-	-	-	-
b-TRF down	-18.7 – 13.7	-9.2	2.0	-	-	-	-
b-TRF up	-11.9 – 22.5	4.5	0.0	-	-	-	-

Table 6.13.: Summary of systematic uncertainties and their % effect in the μ+jets channel.

Top-Quark Mass To evaluate the effect of the top-quark mass on preselection efficiency, the preselection is applied to $t\bar{t}$ PYTHIA Monte Carlo samples with top-quark masses of 165 GeV and 185 GeV. In the e+jets channel, the efficiency decreases by 7.3% for the sample with a top-quark mass of 165 GeV, and increases by 9.8% for the sample with a top-quark mass of 185 GeV, both relative to 175 GeV. In the μ+jets channel, it decreases by 8.5% and increases by 6.7% for the corresponding mass values. Because we use "symmetric" uncertainties, the larger departure is considered in each channel, that is ±9.8% in the e+jets channel and ±8.5% in the μ+jets channel. But since the uncertainty on the top mass is closer to 5 GeV than the 10 GeV implied in our procedure, only half of the uncertainties are used in the analysis, resulting in a systematic uncertainty of ±4.9% in the e+jets channel and ±4.2% in the μ+jets channel.

Matrix Method The only uncertainty on the multijet yield arises from the Matrix Method. This is evaluated by varying ε_{sig} and ε_{QCD} within their uncertainties. The yield increases when either ε_{sig} or ε_{QCD} is shifted up and decreases when either is shifted down. Consequently, we shift both parameters simultaneously up or down, obtaining a relative increase of 21.1% and decrease of 19.0% in the e+jets channel and an increase of 54.2% and decrease of 47.5% in the μ+jets channel. Again, the uncertainty is symmetrized using the larger shifts, i.e., ±21.1% in the e+jets channel and ±54.2% in the μ+jets channel.

W Normalization Because of its normalization to data, the W+jets background is not affected by the uncertainties from obtaining the event yield through Monte Carlo. The uncertainty on the normalization is estimated by observing the fluctuation in normalization factor α_W for different jet multiplicities. In the e+jets (μ+jets) channel, this normalization factor is measured to be 0.86 (1.28) in the ≥4 jet bin, which is the value used in this analysis. It differs most in the exclusive 2-jet

(3-jet) bin, and has a value of 1.46 (1.64), which converts to a relative uncertainty of 70.3% (27.5%), and is applied as a symmetric uncertainty on the W+jets event yield.

Primary-Vertex Selection The selection of the primary vertex provides two sources of systematic uncertainty to the preselection efficiency. One arises from the difference in the selection efficiency in Monte Carlo and data, and is found to be 1.12% [71]. The second source originates from the fact that the z position of the primary vertex is not simulated accurately, which has been found to cause an uncertainty of 1.6% for the 1 fb^{-1} data [81].

Electron Selection The uncertainty on electron selection stems from the MC-to-data scale factor. This factor is in principal a function of several variables, which is not taken into account in this analysis, but also, the MC used for calculating the scaling is limited in statistics. The electron-reconstruction and identification scale factor depends on p_T and φ, which results in an uncertainty of 2.2% [82]. The scale factors for track matching and likelihood efficiency depend on the number of jets, which provides an uncertainty of 5% [82].

Muon Selection As for the electron selection, the muon selection also derives uncertainties from the MC-to-data scale factors. The uncertainty on the muon identification of 7.0%, and 1.5% on tracking efficiency, arise from the method and limited statistics [82]. The isolation scale factor depends on the number of jets, and leads to an uncertainty of 2% [82].

Trigger Efficiency The systematic uncertainties from triggers have been determined elsewhere, and are taken over for this analysis [83]. In the case of asymmetric uncertainties, the higher uncertainty is used for both directions, as usual.

6.5.2. Systematic Uncertainties Affecting the Shape of the Likelihood

Unlike the systematic uncertainties that change the yield uniformly over all bins of the likelihood discriminant, for the shape-changing uncertainties, asymmetric changes of yields are taken into account.

Again, the multijet background remains unaffected by MC uncertainties, because it is estimated and modeled using data. And although the W+jets background is modeled by Monte Carlo, it is not influenced by any uncertainty that arises prior to its normalization to data.

Jet Energy Scale The effect of uncertainty on the Jet Energy Scale (JES) is evaluated by repeating the complete selection and analysis with the JES correction on jets raised and lowered by one standard deviation σ:

$$\sigma = \sqrt{\sigma^2_{stat,data} + \sigma^2_{sys,data} + \sigma^2_{stat,MC} + \sigma^2_{sys,MC}}. \tag{6.7}$$

The shape and normalization of the distributions in likelihood discriminant for all Monte Carlo samples are affected, except for the W+jets sample, for which the normalization is fixed to its central value. The changed distributions in likelihood discriminant are used in the limit-setting procedure to derive the effect in each bin of the distribution.

Contribution from Heavy Flavor As described in Section 5.2.2, the contribution from heavy-flavor W+jets samples ($Wb\bar{b}$ and $Wc\bar{c}$) are scaled up to improve the description of data. This scale factor $k_{HF} = 1.17 \pm 0.18$ is varied within its uncertainties to produce differently-shaped likelihood-discriminant distributions for the W+jets sample, while the normalization of the W+jets contribution remains fixed.

b-Tagging The uncertainty due to b-tagging is estimated by raising and lowering the tag rate for b-jets by one standard deviation for both the taggability and the tag-rate components for signal $\tilde{t}_1\bar{\tilde{t}}_1$ samples and the largest background, the $t\bar{t}$ sample. Applying this on the considerably smaller background from W+jets would also change the normalization of the W+jets samples, since b-tagging is applied after normalization to data. As it is, the only effect is an almost unnoticeable change in renormalization to data from variation of the $t\bar{t}$ sample.

7. Result and Conclusions

We have presented a search for $\tilde{t}_1\bar{\tilde{t}}_1$ production in the $t\bar{t}$ lepton+jets sample for $\approx$1 fb^{-1} of data. With the Bayesian method thoroughly tested, and systematic uncertainties in place, the result is extracted from data.

The observed posterior probability as a function of the $\tilde{t}_1\bar{\tilde{t}}_1$ cross section for the 175/135 mass point is shown in Fig. 7.1. The line indicates the limit at 95% confidence. The posterior probability peaks away from the origin at a cross section

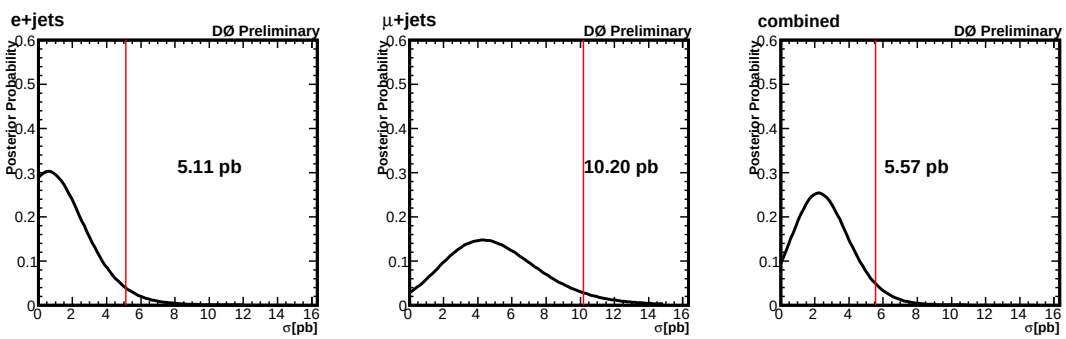

Figure 7.1.: Observed posterior probability as a function of the $\tilde{t}_1\bar{\tilde{t}}_1$ cross section for the 175/135 mass point.

of 4.3 pb in the μ+jets channel, but with an uncertainty of 2.7 pb, which puts a null value within 1.6 standard deviations. Since a signal would be expected in both e+jets and μ+jets channel, and the e+jets channel has no similar excess, we assume that the result in μ+jets corresponds to a small fluctuation up in that channel (see Table 6.8). In addition, the distributions in μ+jets data and Monte

Carlo do not agree as well as in the e+jets channel.

The observed posterior probabilities for all mass points are shown in Appendix D.2. Table 7.1 lists the measured limits at 95% confidence for all mass points and all channels, and compares them to the theoretical cross sections. The results are also illustrated in Fig. 7.2. The upwards fluctuation in the μ+jets channel is observable for all mass points, the only exception being the 175/105 mass point, which is the only one that does not use the p_T of the leading b-tagged jet as input in its likelihood discriminant. As can be seen in Appendix C.2, this variable has a poorer data-MC agreement than all other input variables, but provides very good separation for almost all the mass points, as illustrated in Appendix C.1.

At this point, we cannot exclude any of the analyzed stop masses, since all observed limits are well above theoretical predictions.

Sample	theoretical	e+jets	μ+jets	combined
Statistics only				
Stop 175/135	0.579	2.54	6.52	3.10
Stop 175/120	0.579	3.37	9.48	4.21
Stop 175/105	0.579	3.63	9.40	4.10
Stop 160/120	1.00	4.54	14.08	5.70
Stop 160/105	1.00	5.25	14.58	6.90
Stop 145/105	1.80	7.59	21.37	9.67
With systematic uncertainties				
Stop 175/135	0.579	5.11	10.20	5.57
Stop 175/120	0.579	6.11	12.41	6.58
Stop 175/105	0.579	6.10	9.28	5.55
Stop 160/120	1.00	6.49	15.79	7.45
Stop 160/105	1.00	7.78	20.75	9.71
Stop 145/105	1.80	10.60	24.21	12.32

Table 7.1.: Observed Bayesian limits at 95% confidence on the $\tilde{t}_1\bar{\tilde{t}}_1$ cross section in pb, without and with systematic uncertainties, assuming a $t\bar{t}$ cross section of 6.77 pb.

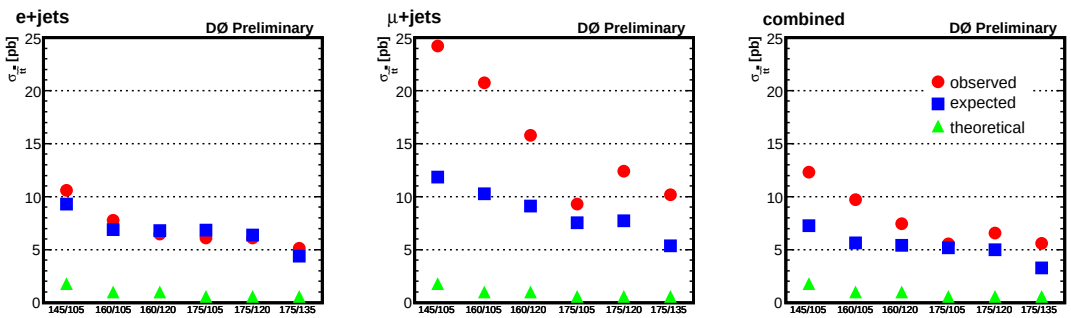

Figure 7.2.: Observed and expected Bayesian limits at 95% confidence, and the theoretical cross section for $\tilde{t}_1\bar{\tilde{t}}_1$ at each mass point, assuming a $t\bar{t}$ cross section of 6.77 pb.

Results are also derived using the cross check, where the posterior probabilities are calculated as function of both the $\tilde{t}_1\bar{\tilde{t}}_1$ and $t\bar{t}$ cross sections. Figure 7.3 shows the posterior probabilities for the 175/135 mass point in different channels. The limits on the $\tilde{t}_1\bar{\tilde{t}}_1$ cross section derived this way agree with those using the standard method. The posterior probabilities for all mass points are displayed in Appendix D.2. Table 7.2 shows the limits on the $\tilde{t}_1\bar{\tilde{t}}_1$ cross section and the results for the extracted $t\bar{t}$ cross section, without and with uncertainties. The results are again illustrated in Fig. 7.4.

Since the extracted limits on the $\tilde{t}_1\bar{\tilde{t}}_1$ cross section are above the NLO prediction in the MSSM, even without taking into account systematic uncertainties, it can be concluded that this kind of search needs more data to become sensitive. However, several improvements of the method can be implemented for the publication of the results of this search.

It has been observed that, for signal samples, there are as many events with three jets as with four or more jets. This can be accommodated by the fact that the jets in $\tilde{t}_1\bar{\tilde{t}}_1$ events have low transverse momentum because of energy carried away by neutralinos, which makes it likelier for these jets not to be reconstructed than

Sample	theoretical	$\tilde{t}_1\bar{\tilde{t}}_1$ limit			$t\bar{t}$ cross section		
	$\sigma_{\tilde{t}_1\bar{\tilde{t}}_1}$	e+jets	μ+jets	combined	e+jets	μ+jets	combined
Statistics only							
Stop 175/135	0.579	3.40	6.98	3.64	$5.91^{+0.82}_{-0.79}$	$6.90^{+1.07}_{-1.03}$	$6.51^{+0.67}_{-0.65}$
Stop 175/120	0.579	4.94	11.09	5.35	$5.95^{+0.84}_{-0.83}$	$6.68^{+1.16}_{-1.13}$	$6.54^{+0.70}_{-0.71}$
Stop 175/105	0.579	4.95	9.54	4.59	$6.07^{+0.82}_{-0.80}$	$7.35^{+1.08}_{-1.07}$	$6.83^{+0.66}_{-0.65}$
Stop 160/120	1.00	5.83	15.01	6.42	$6.07^{+0.82}_{-0.77}$	$6.95^{+1.08}_{-1.04}$	$6.69^{+0.66}_{-0.64}$
Stop 160/105	1.00	7.37	17.22	8.83	$5.81^{+0.83}_{-0.81}$	$6.25^{+1.12}_{-1.06}$	$6.18^{+0.70}_{-0.68}$
Stop 145/105	1.80	9.82	23.17	11.34	$5.88^{+0.82}_{-0.77}$	$6.66^{+1.06}_{-1.00}$	$6.38^{+0.66}_{-0.63}$
With systematic uncertainties							
Stop 175/135	0.579	5.29	10.72	5.59	$5.84^{+1.40}_{-1.17}$	$6.96^{+1.83}_{-1.47}$	$6.36^{+1.23}_{-1.04}$
Stop 175/120	0.579	6.57	12.80	6.90	$5.93^{+1.36}_{-1.18}$	$6.68^{+1.84}_{-1.55}$	$6.45^{+1.22}_{-1.09}$
Stop 175/105	0.579	6.69	9.46	5.64	$5.82^{+1.34}_{-1.15}$	$6.92^{+1.92}_{-1.48}$	$6.14^{+1.16}_{-1.02}$
Stop 160/120	1.00	6.63	16.22	7.64	$6.12^{+1.34}_{-1.18}$	$6.75^{+1.80}_{-1.49}$	$6.51^{+1.20}_{-1.03}$
Stop 160/105	1.00	8.06	21.96	9.98	$5.75^{+1.31}_{-1.13}$	$5.99^{+1.81}_{-1.48}$	$6.01^{+1.16}_{-0.97}$
Stop 145/105	1.80	10.81	24.37	12.56	$5.98^{+1.34}_{-1.16}$	$6.74^{+1.78}_{-1.46}$	$6.46^{+1.20}_{-1.01}$

Table 7.2.: Observed Bayesian limits at 95% confidence on the $\tilde{t}_1\bar{\tilde{t}}_1$ cross section, and the measured $t\bar{t}$ cross section in pb, without and with systematic uncertainties.

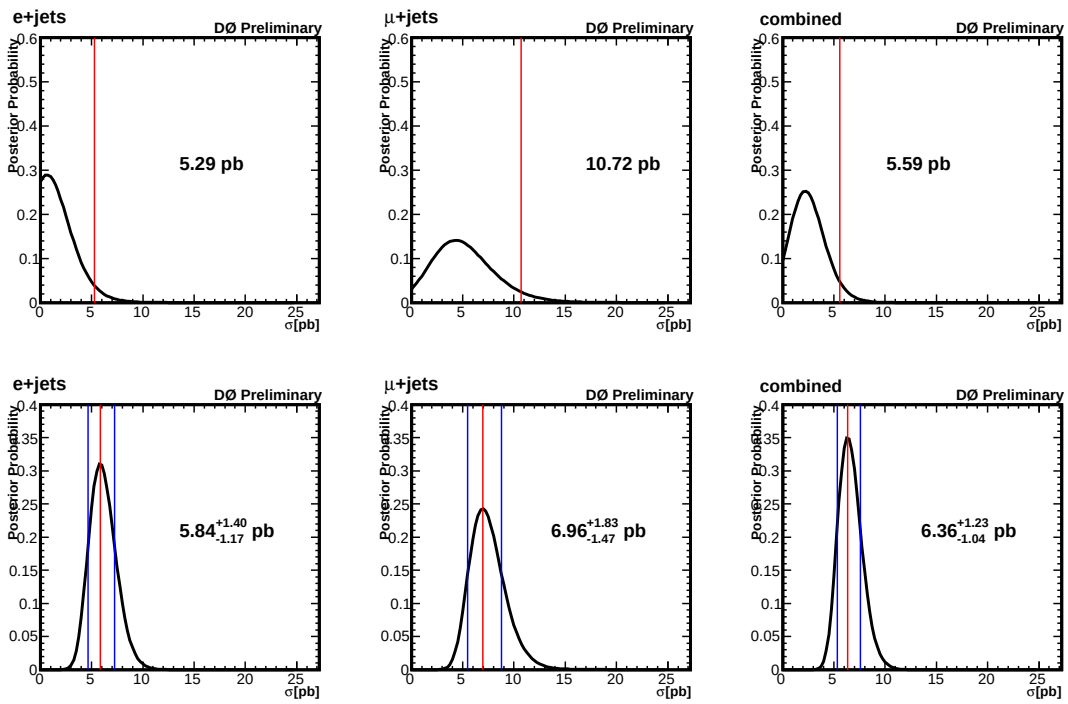

Figure 7.3.: Observed posterior probability for the 175/135 mass point. Top: as a function of the $\tilde{t}_1\bar{\tilde{t}}_1$ cross section, bottom: as a function of the $t\bar{t}$ cross section.

in $t\bar{t}$ events. Although there is a much higher W+jets background in the three-jet multiplicity bin, the $t\bar{t}$ background will be smaller, and including these events should improve the limits. Technically, the analysis can be performed separately in the 3-jet multiplicity bin, and combined with the $\geq$4-jet multiplicity bin during the limit setting procedure, in a similar way as the e+jets and the μ+jets channels are combined. A first look indicates that, although the kinematic fitter HITFIT has to be dropped, enough kinematic differences can be found between $\tilde{t}_1\bar{\tilde{t}}_1$ and $t\bar{t}$ events.

In addition, more stop mass points are being generated to widen the range of the search. It is also desirable to interpolate between the mass points or extrapolate beyond them, which is not possible using the current method, since it uses

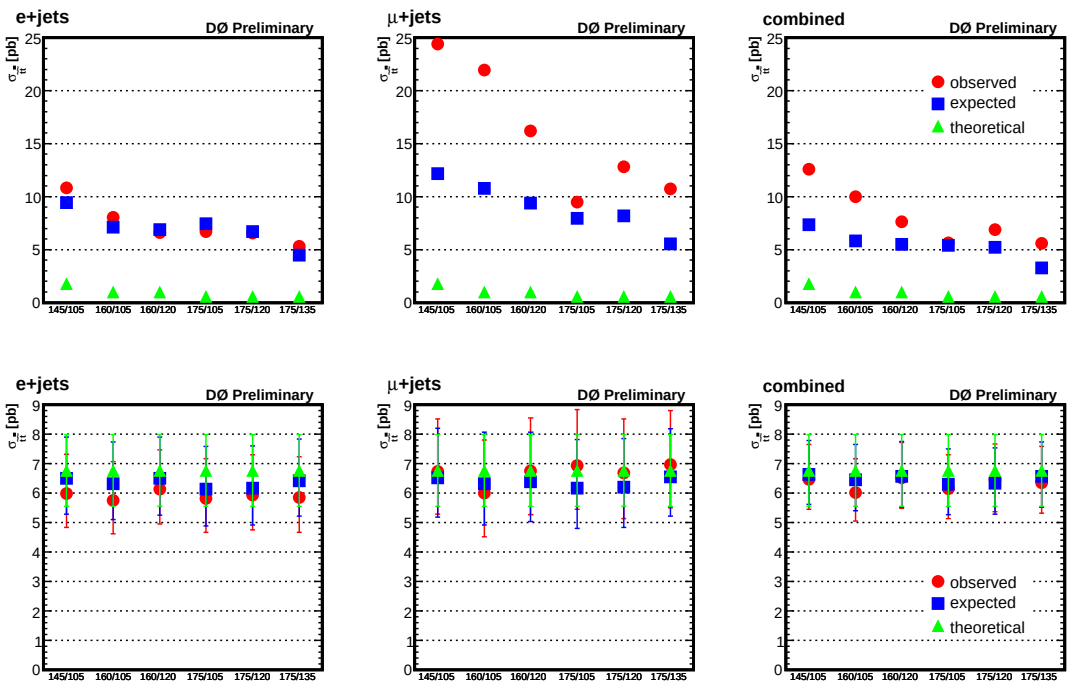

Figure 7.4.: Top: Observed and expected Bayesian limits at 95% confidence on the $\tilde{t}_1\bar{\tilde{t}}_1$ cross section, and the theoretical cross section for $\tilde{t}_1\bar{\tilde{t}}_1$ at each mass point. Bottom: Observed, expected and theoretical cross section for $t\bar{t}$.

different likelihood discriminants for each point. This is necessary, because the $\tilde{t}_1\bar{\tilde{t}}_1$ signal samples differ significantly from each other. But it has been found that samples with the same mass difference $\Delta m = m_{\tilde{t}_1} - m_{\tilde{\chi}_1^\pm}$ look sufficiently similar to derive a single likelihood discriminant for them. This would enable the aforementioned interpolation and extrapolation procedure, and thereby improve limits on $\tilde{t}_1\bar{\tilde{t}}_1$ production.

Bibliography

[1] D. Griffiths, *Introduction to Elementary Particles*, Wiley (1987).

F. Halzen, A. Martin, *Quarks and Leptons*, Wiley (1984).

[2] F. Abe *et al.* (CDF Collaboration), *Observation of the Top Quark in $p\bar{p}$ Collisions with the Collider Detector at Fermilab*, Phys. Rev. Lett. **74**, 2626 (1995), hep-ex/9503002.

S. Abachi *et al.* (DØ Collaboration), *Observation of the Top Quark*, Phys. Rev. Lett. **74**, 2632 (1995), hep-ex/9503003.

F. Abe *et al.* (CDF Collaboration), *Study of $t\bar{t}$ Production in $p\bar{p}$ Collisions Using Total Transverse Energy*, Phys. Rev. Lett. **75**, 3997 (1995), hep-ex/9506006.

[3] H. Baer, X. Tata, *Weak Scale Supersymmetry: From Superfields to Scattering Events*, Cambridge University Press (2006).

[4] J. R. Ellis, S. Rudaz, *Search For Supersymmetry In Toponium Decays*, Phys. Lett. B **128**, 248 (1983).

[5] F. Englert, R. Brout, *Broken Symmetry and the Mass of Gauge Vector Mesons*, Phys. Rev. Lett. **13**, 321 (1964).

G. S. Guralnik, C. R. Hagen, T. W. B. Kibble, *Global Conservation Laws and Massless Particles*, Phys. Rev. Lett. **13**, 585 (1964).

P. W. Higgs, *Broken Symmetries and the Masses of Gauge Bosons*, Phys. Rev. Lett. **13**, 508 (1964).

P. W. Higgs, *Broken Symmetries, Massless Particles and Gauge Fields*, Phys. Lett. **12**, 132 (1964).

[6] B. Webber, private communication (2007).

[7] M. Carena, M. Quiros, C.E.M. Wagner, *Opening the Window for Electroweak Baryogenesis*, Phys. Lett. **B380**, 81 (1996).

M. Carena, M. Quiros, C.E.M. Wagner, *Electroweak baryogenesis and Higgs and stop searches at LEP and the Tevatron*, Nucl. Phys. **B524**, 3 (1998).

[8] N. Kidonakis, R. Vogt, *Next-to-next-to-leading order soft-gluon corrections in top quark hadroproduction*, Phys. Rev. D **68**, 114014 (2003).

[9] CDF Collaboration, *Combination of Top Pair Production Cross Section Results*, CDF Note 8148 (2006). `http://www-cdf.fnal.gov/physics/new/top/2006/xs_combo/`.

[10] DØ Top Quark Physics Results (2007), `http://www-d0.fnal.gov/Run2Physics/top/top_public_web_pages/top_public.html`.

[11] V. M. Abazov *et al.* (DØ Collaboration), *Evidence for production of single top quarks and first direct measurement of —V(tb)—*, Phys. Rev. Lett. **98**, 181802 (2007), hep-ex/0612052.

[12] W. Beenakker *et al.*, *Stop Production at Hadron Colliders*, Nucl. Phys. B515 (1998) 3-14.

[13] W. Beenakker *et al.*, *PROSPINO: A Program for the Production of Supersymmetric Particles in Next-to-leading Order QCD*, arXiv:hep-ph/9611232v1 (1996).

PROSPINO homepage `http://www.ph.ed.ac.uk/~tplehn/prospino/`.

[14] C. Boehm, A. Djouadi, Y. Mambrini, *Decays of the lightest top squark*, Phys. Rev. D **61**, 095006 (2000).

A. Djouadi, Y. Mambrini, *Three-body decays of top and bottom squarks*, Phys. Rev. D **63**, 115005 (2001).

[15] W. M. Yao *et al.* (Particle Data Group), *Review of particle physics*, J. Phys. G **33**, 1 (2006).

[16] H. Baer, F. E. Paige, S. D. Protopopescu, X. Tata, *ISAJET 7.48: A Monte Carlo event generator for p p, anti-p p, and e+ e- reactions*, hep-ph/0001086 (2000).

[17] LEPSUSYWG, ALEPH, DELPHI, L3 and OPAL experiments, note LEPSUSYWG/07-05 (`http://lepsusy.web.cern.ch/lepsusy/Welcome.html`).

[18] A.A. Affolder *et al.* (CDF Collaboration), *Search for scalar top quark production in $p\bar{p}$ collisions at $\sqrt{s}$=1.8 TeV*, Phys. Rev. Lett. **84**, 5273 (2000).

[19] CDF Collaboration, *Search for Direct Pair Production of Scalar Top and Scalar Bottom Quarks in $p\bar{p}$ Collisions at $\sqrt{s}$=1.96 TeV*, CDF Note 8411 (2006).

[20] DØ Collaboration, *Search for the pair production of scalar top quarks in acoplanar charm jet + Missing transverse energy final state in $p\bar{p}$ collisions at $\sqrt{s}$=1.96 TeV*, DØ Note 5436-CONF (2007). (`http://www-d0.fnal.gov/Run2Physics/WWW/results/prelim/NP/N56/`)

[21] V. Abazov *et al.* (DØ Collaboration), *Search for the lightest scalar top quark*

in events with two leptons in $p\bar{p}$ collisions at $\sqrt{s}$=1.96 TeV, hep-ex/0707.2864 (2007).

[22] R. T. Cox, *Probability, Frequency and Reasonable Expectation*, Am. J. Phys. **14**, 1 (1946).

H. Jeffreys, *Theory of Probability*, 3rd edition, Oxford University Press (1961).

E. T. Jaynes and L. Bretthorst, *Probability Theory, the Logic of Science*, Oxford (2003).

A. O'Hagan, *Kendall's Advanced Theory of Statistics, Volume 2B: Bayesian Inference*, Oxford (1994).

[23] G. J. Feldman and R. D. Cousins, *A Unified approach to the classical statistical analysis of small signals*, Phys. Rev. D **57**, 3873 (1998).

[24] T. Junk, *Confidence level computation for combining searches with small statistics*, Nucl. Instrum. Meth. A **434**, 435 (1999).

A. L. Read, *Modified Frequentist Analysis of Search Results (The CL_S Method)*, CERN Yellow Report 2000-005.

[25] V. Büscher *et al.*, *Recommendation of the Ad-Hoc Committee on Limit-Setting Procedures to be Used by DØ in Run II*, DØ Note 4629 (2004).

[26] S. Jain *et al.*, *Limits using a Bayesian approach in the package "top_statistics"*, DØ Note 5123 (2006).

[27] Fermilab Beams Division, *Run II Handbook*, Fermilab Beams Division Run II webpage, `http://www-bd.fnal.gov/lug/`.

[28] V. M. Abazov *et al.* (The DØ Collaboration), *The Upgraded DØ Detector*, Nucl. Instrum. Meth. A **565**, 463 (2006), FERMILAB-PUB-05-341-E (2005).

[29] E. Kajfasz (for the DØ Collaboration), *DØ Silicon Microstrip Tracker for Run IIa*, Nucl. Instrum. Meth. A **511**, 16-19 (2003).

[30] L. Groers, *DØ Calorimeter Upgrades for Tevatron Run II*, DØ Note 4240, Proceedings for the IXth International Conference on Calorimetry in Particle Physics, Annecy, France, Oct 9-14, 2000.

[31] S. Abachi *et al.* (The DØ Collaboration), *Beam Tests of the DØ Uranium Liquid Argon End Calorimeters*, FERMILAB-PUB-92-162 (1992), DØ Note 1434 (1992).

[32] B. Abbott *et al.* (The DØ Collaboration), *A Measurement of the W Boson Mass*, Phys. Rev. D **58** 092003 (1998), hep-ex/9712029.

[33] S. Abachi *et al.* (The DØ Collaboration), *The DØ Detector*, Nucl. Instrum. Meth. A **338**, 185 (1994).

[34] A. Brandt *et al.* (The DØ Collaboration), *A forward proton detector at DØ*, FERMILAB-PUB-97-377 (1997).

[35] C. C. Miao (The DØ Collaboration), *The DØ Run II luminosity monitor*, Nucl. Phys. Proc. Suppl. **78**, 342 (1999).

[36] T. L. Edwards *et al.* (The DØ Collaboration), *Determination of the Effective Inelastic $p\bar{p}$ Cross-Section for the DØ Run II Luminosity Measurement*, FERMILAB-TM-2278-E (2004).

[37] G. C. Blazey, *The DØ Run II Trigger*, FERMILAB-CONF-97-395-E (1997).

[38] DØ Algorithm webpage, `http://www-d0.fnal.gov/Run2Physics/WWW/algorithm.htm`.

[39] A. Khanov, private communication (2007).

[40] A. Khanov, *HTF: Histogramming Method for Finding Tracks. The Algorithm Description.*, DØ Note 3778 (2000).

[41] G. Borrisov, *Ordering a Chaos or... Technical Details of AA Tracking*, All DØ Meeting February 28, 2003 `http://www-d0.fnal.gov/atwork/adm/d0_private/2003-02-28/adm_talk.ps`.

[42] R. E. Kalman, *A New Approach to Linear Filtering and Prediction Problems*, J. Bas. Eng. **82D** 35 (1960).

R. E. Kalman, R. S. Brucy, *New Results in Linear Filtering and Prediction Theory*, J. Bas. Eng. **83D** 95 (1961).

P. Billoir, *Track Fitting With Multiple Scattering: A New Method*, Nucl. Instrum. Meth. A **225**, 352 (1984).

R. Frühwirth, *Application Of Kalman Filtering To Track And Vertex Fitting*, Nucl. Instrum. Meth. A **262**, 444 (1987).

H. Greenlee, *The D0 Kalman Track Fit*, DØ Note 4303 (2003).

[43] A. Schwartzmann, C. Tully, *Primary Vertex Reconstruction by Means of Adaptive Vertex Fitting*, DØ Note 4918 (2005).

[44] A. Schwartzmann, M. Narain, *Probabilistic Primary Vertex Selection*, DØ Note 4042 (2002).

[45] J. Kozminski *et al.*, *Electron Likelihood in p14*, DØ Note 4449 (2004).

[46] L. Wang *et al.*, *Electron Likelihood Efficiency in p17*, DØ Note 5114 (2006).

[47] DØ Muon Identification Webpage, `http://www-d0.fnal.gov/phys_id/muon_id/d0_private/muonid_dh.html`.

[48] P. Calfayan *et al.*, *Muon Identification Certification for p17 data*, DØ Note 5157 (2006).

[49] G. C. Blazey *et al.*, *Run II Jet Physics*, Proceedings of the Physics at RUN II: QCD and Weak Boson Physics Workshop, Batavia, Illinois (1999), hep-ex/0005012.

G. C. Blazey *et al.*, *Run II Jet Physics*, DØ Note 3750 (2000).

[50] A. Harel, *Jet ID Optimization*, DØ Note 4919 (2005).

[51] DØ p17 Preliminary Jet Energy Scale Webpage, `http://www-d0.fnal.gov/phys_id/jes/public/plots_v7.1/`.

[52] D. Boline, L. Feligioni, M. Narain, *Update on b-quark jet identification with Secondary Vertex reconstruction using DØreco version p14-Pass2 Samples*, DØ Note 4796 (2005).

b-ID Secondary Vertex Tagger p14-pass2 Certification Results webpage, `http://www-d0.fnal.gov/phys_id/bid/d0_private/certification/p14Pass2/SVT/secvertex_v4_frames.html`.

[53] K. Hanagaki, J. Kasper, *Identification of b-jet by Soft Muon*, DØ Note 4867 (2005).

Soft Lepton (muon) tagging method webpage, `http://www-d0.fnal.gov/phys_id/bid/d0_private/certification/p14Pass2/SLT/SLT_v1_1.html`.

[54] R. Demina *et al.*, *Measurement of b-tagging efficiency and mis-tagging rates with CSIP method*, DØ Note 4432 (2004).

Counting Signed Impact Parameter tagging method webpage, `http://www-d0.fnal.gov/phys_id/bid/d0_private/certification/p14/CSIP/CSIP_v2.html`.

[55] D. Bloch, B. Clément, *Update of the JLIP b-tagger Performance in p14/Pass2 with JES 5.3*, DØ Note 4824 (2005).

Jet Lifetime Probability (JLIP) b-tag Certification webpage, `http://www-d0.fnal.gov/phys_id/bid/d0_private/certification/p14Pass2/JLIP/Jetprob_v1.html`.

[56] T. Scanlon, *A Neural Network b-tagging Tool*, DØ Note 4889 (2005).

M. Anastasoaie, S. Robinson, T. Scanlon, *Performance of the NN b-tagging Tool on p17 Data*, DØ Note 5213 (2006).

[57] B. Casey *et al.*, *Determination of the Effective Inelastic $p\bar{p}$ Cross-Section for the DØ Luminosity Measurement Using Upgraded Readout Electronics*, DØ Note 4958 (2005).

G. Snow, *Adjustments to the Measured Integrated Luminosity in Run IIa*, DØ Note 5139 (2006).

T. Andeen *et al.* (DØ Collaboration), *The DØ experiment's integrated luminosity for Tevatron Run IIa*, Fermilab-TM-2365 (2007).

[58] DØ Top Triggers, `http://www-d0.fnal.gov/Run2Physics/top/d0_private/wg/triggers/triggers.html`.

[59] `top_cafe` package homepage, `http://www-d0.fnal.gov/Run2Physics/top/d0_private/wg/top_cafe/doxydoc/html`.

[60] S. M. Ulam, *Adventures of a Mathematician*, University of California Press (1991).

[61] T. Sjöstrand, L. Lönnblad, S. Mrenna, P. Skands, *PYTHIA 6.3: Physics and manual*, arXiv:hep-ph/0308153 (2003).

[62] M.L. Mangano *et al.*, *ALPGEN, a Generator for Hard Multiparton Processes in Hadronic Collisions*, JHEP **0307**, 001 (2003).

[63] E.E. Boos *et al.*, *Method for simulating electroweak top-quark production events in the NLO approximation: SingleTop event generator*, Phys. Atom. Nucl. **69**, 1317 (2006).

[64] J. Pumplin *et al.*, *New Generation of Parton Distributions with Uncertainties from Global QCD Analysis*, JHEP **0207**, 012 (2002).

[65] S. Höche *et al.*, *Matching Parton Showers and Matrix Elements*, arXiv:hep-ph/0602031 (2006).

[66] B. Andersson, G. Gustafson, G. Ingelman, T. Sjostrand, *Parton Fragmentation And String Dynamics*, Phys. Rept. **97**, 31 (1983).

[67] Y. Fisyak, J. Womersley, *D0 GEANT Simulation of the Total Apparatus Response*, DØ Note 3191 (1997).

[68] S. Agostinelli *et al.* (GEANT4 Collaboration), *GEANT4: A simulation toolkit*, Nucl. Instrum. Meth. A **506**, 250 (2003).

[69] D0SIM User Manual, DØ Note 407 (1986).

[70] Y. Peters *et al.*, *Study of the W+Jets heavy flavor scale factor in p17*, DØ Note 5406 (2007).

[71] B. Martin *et al.*, *Measurement of the $t\bar{t}$ production cross section at $\sqrt{s}$=1.96 TeV in the ee final state using p17 dataset*, DØ Note 5386 (2007).

[72] DØ Collaboration, *A Search for $ZH(\rightarrow \ell^+\ell^- b\bar{b})$ Production with the DØ Detector in $p\bar{p}$ Collisions at $\sqrt{(s)}$=1.96 TeV*, DØ Note 5275-CONF (2006).

[73] Z. Sullivan, *Understanding single-top-quark production and jets at hadron colliders*, Phys. Rev. D **70**, 114012 (2004).

[74] L. Christofek *et al.*, *Probability Calculation for Multi-object Trigger Configurations*, DØ Note 4882 (2005).

M. Agelou *et al.*, *Top Trigger Efficiency Measurements and the top_trigger package*, DØ Note 4512 (2004).

`caf_trigger` webpage, `http://www.phys.ualberta.ca/~kwchan/d0/caf_trigger/readme.html`.

[75] S. Snyder, *Measurement of the Top Quark Mass at DØ*, Doctoral Thesis, State University of New York at Stony Brook (1995).

M. Demarteau *et al.*, *p17 parton level corrections and resolutions for hitfit*, DØ Note 5418 (2007).

[76] A. Harel, *Top Charge Asymmetry*, DØ Note 5393 (2007).

[77] Y. Peters *et al.*, *Reweighting of the fragmentation function for the DØ Monte Carlo*, DØ Note 5325 (2007).

[78] S.-J. Park, M. Begel, *Efficiency of the Data Quality Calorimeter Flags*, DØ Note 5324 (2007).

[79] E. Barberis *et al.*, *The Matrix Method and its Error Calculation*, DØ Note 4564 (2004).

[80] J. Smith, W. L. van Neerven, J. A. M. Vermaseren, *The Transverse Mass And Width Of The W Boson*, Phys. Rev. Lett. **50**, 1738 (1983).

[81] H. Schellman, *The longitudinal shape of the luminous region at DØ*, DØ Note 5142 (2006).

[82] D. Cho *et al.*, *Measurement of the $t\bar{t}$ Production Cross Section at $\sqrt{s}$=1.96 TeV in the Lepton+Jets Final State using Neural Network b-tagging algorithm on 1 fb^{-1} of DØ Data*, DØ Note 5335 (2007).

[83] J. Brunelle *et al.*, *Measurement of the $t\bar{t}$ Production Cross Section at $\sqrt{s}$=1.96 TeV in the Lepton+Jets Final State using a Topological Method on 1 fb^{-1} of DØ Data*, DØ Note 5249 (2006).

A. Tables of Preselection Efficiencies

Tables A.1 through A.12 show the event yields, exclusive and cumulative selection efficiencies, and correction factors for the $\tilde{t}_1\bar{\tilde{t}}_1$ signal samples for all mass points in the order in which the selections have been applied. For details about the selection, refer to Section 6.1.

Selection or κ	Events left	Exclusive selection efficiency[%]	Cumulative selection efficiency[%]
	47670		
$\geq$4 good jets	18815	39.47 ± 0.22	39.47 ± 0.22
Leading jet cut	17606	93.57 ± 0.18	36.93 ± 0.22
Loose electron	7197	40.88 ± 0.37	15.10 ± 0.16
Muon veto	7195	99.97 ± 0.02	15.10 ± 0.16
2nd electron veto	7192	99.96 ± 0.02	15.09 ± 0.16
Vertex selection	7075	98.37 ± 0.15	14.84 ± 0.16
$\not{E}_T$	6194	87.55 ± 0.39	12.99 ± 0.15
Triangle selection	5774	93.22 ± 0.32	12.11 ± 0.15
Tight electron	5118	88.64 ± 0.42	10.74 ± 0.14
Trigger probability		96.06 ± 0.05	10.31 ± 0.14
$\kappa_{electron\ reco,\ ID}$		98.51 ± 0.01	10.16 ± 0.13
$\kappa_{electron\ likelihood}$		89.09 ± 0.07	9.05 ± 0.12
$\kappa_{b-fragmentation}$		96.78 ± 1.04	8.76 ± 0.15
$\geq$1 b-tag		54.52 ± 0.82	4.77 ± 0.10
HITFIT convergence		95.45 ± 3.03	4.56 ± 0.10
Data Quality		97.14 ± 0.50	4.43 ± 0.10
ε^{total}			4.43 ± 0.10

Table A.1.: Preselection efficiencies and corresponding κ factors in % in $\tilde{t}_1\bar{\tilde{t}}_1 \rightarrow e$+jets events for the 175/135 mass point. Only statistical uncertainties are included.

Selection or κ	Events left	Exclusive selection efficiency[%]	Cumulative selection efficiency[%]
	46561		
$\geq$4 good jets	18669	40.10 ± 0.23	40.10 ± 0.23
Leading jet cut	17470	93.58 ± 0.18	37.52 ± 0.22
Loose muon	6749	38.63 ± 0.37	14.49 ± 0.16
Z muon veto	6749	100	14.49 ± 0.16
2nd muon veto	6749	100	14.49 ± 0.16
Electron veto	6743	99.91 ± 0.04	14.48 ± 0.16
Vertex selection	6633	98.37 ± 0.15	14.25 ± 0.16
$\not{E}_T$	5541	83.54 ± 0.46	11.90 ± 0.15
Triangle selection	5113	92.28 ± 0.36	10.98 ± 0.15
Tight muon	4266	83.43 ± 0.52	9.16 ± 0.13
Trigger probability		84.45 ± 0.20	7.74 ± 0.11
$\kappa_{\mu\ ID\times\ acc\times\ cosmic\ veto}$		97.22 ± 0.16	7.53 ± 0.11
$\kappa_{\mu\ track}$		91.80 ± 0.08	6.92 ± 0.10
$\kappa_{\mu\ isolation}$		100.20 ± 0.01	6.94 ± 0.10
$\kappa_{b-fragmentation}$		98.32 ± 1.14	6.80 ± 0.13
$\geq$1 b-tag		57.35 ± 0.88	3.90 ± 0.09
HITFIT convergence		94.35 ± 3.16	3.68 ± 0.09
Data Quality		97.14 ± 0.50	3.57 ± 0.08
ε^{total}			3.57 ± 0.08

Table A.2.: Preselection efficiencies and corresponding κ factors in % in $\tilde{t}_1\bar{\tilde{t}}_1 \rightarrow \mu$+jets events for the 175/135 mass point. Only statistical uncertainties are included.

Selection or κ	Events left	Exclusive selection efficiency[%]	Cumulative selection efficiency[%]
	40448		
$\geq$4 good jets	13993	34.60 ± 0.24	34.60 ± 0.24
Leading jet cut	13182	94.20 ± 0.20	32.59 ± 0.23
Loose electron	4833	36.66 ± 0.42	11.95 ± 0.16
Muon veto	4832	99.98 ± 0.02	11.95 ± 0.16
2nd electron veto	4831	99.98 ± 0.02	11.94 ± 0.16
Vertex selection	4745	98.21 ± 0.19	11.73 ± 0.16
$\not{E}_T$	4257	89.72 ± 0.44	10.52 ± 0.15
Triangle selection	3972	93.31 ± 0.38	9.82 ± 0.15
Tight electron	3510	88.37 ± 0.51	8.68 ± 0.14
Trigger probability		95.97 ± 0.06	8.33 ± 0.13
$\kappa_{electron\ reco,\ ID}$		98.50 ± 0.02	8.20 ± 0.13
$\kappa_{electron\ likelihood}$		89.04 ± 0.08	7.31 ± 0.12
$\kappa_{b-fragmentation}$		98.19 ± 1.26	7.18 ± 0.15
$\geq$1 b-tag		58.36 ± 1.05	4.19 ± 0.11
HITFIT convergence		91.51 ± 3.67	3.83 ± 0.11
Data Quality		97.14 ± 0.50	3.72 ± 0.10
ε^{total}			3.72 ± 0.10

Table A.3.: Preselection efficiencies and corresponding κ factors in % in $\tilde{t}_1\bar{\tilde{t}}_1 \rightarrow e$+jets events for the 175/120 mass point. Only statistical uncertainties are included.

Selection or κ	Events left	Exclusive selection efficiency[%]	Cumulative selection efficiency[%]
	40658		
$\geq$4 good jets	14039	34.53 ± 0.24	34.53 ± 0.24
Leading jet cut	13175	93.85 ± 0.20	32.40 ± 0.23
Loose muon	4584	34.79 ± 0.42	11.27 ± 0.16
Z muon veto	4584	100	11.27 ± 0.16
2nd muon veto	4584	100	11.27 ± 0.16
Electron veto	4578	99.87 ± 0.05	11.26 ± 0.16
Vertex selection	4497	98.23 ± 0.20	11.06 ± 0.16
$\not{E}_T$	3820	84.95 ± 0.53	9.40 ± 0.15
Triangle selection	3501	91.65 ± 0.45	8.61 ± 0.14
Tight muon	2894	82.66 ± 0.64	7.12 ± 0.13
Trigger probability		84.97 ± 0.23	6.05 ± 0.11
$\kappa_{\mu\ ID\times\ acc\times\ cosmic\ veto}$		97.37 ± 0.19	5.90 ± 0.11
$\kappa_{\mu\ track}$		91.82 ± 0.10	5.42 ± 0.10
$\kappa_{\mu\ isolation}$		100.20 ± 0.02	5.43 ± 0.10
$\kappa_{b-fragmentation}$		98.91 ± 1.40	5.37 ± 0.12
$\geq$1 b-tag		61.14 ± 1.16	3.28 ± 0.10
HITFIT convergence		91.04 ± 4.02	2.99 ± 0.09
Data Quality		97.14 ± 0.50	2.90 ± 0.09
ε^{total}			2.90 ± 0.09

Table A.4.: Preselection efficiencies and corresponding κ factors in % in $\tilde{t}_1\bar{\tilde{t}}_1 \rightarrow \mu$+jets events for the 175/120 mass point. Only statistical uncertainties are included.

Selection or κ	Events left	Exclusive selection efficiency[%]	Cumulative selection efficiency[%]
	36722		
$\geq$4 good jets	12837	34.96 ± 0.25	34.96 ± 0.25
Leading jet cut	12277	95.64 ± 0.18	33.43 ± 0.25
Loose electron	3996	32.55 ± 0.42	10.88 ± 0.16
Muon veto	3996	100	10.88 ± 0.16
2nd electron veto	3996	100	10.88 ± 0.16
Vertex selection	3920	98.10 ± 0.22	10.67 ± 0.16
$\not{E}_T$	3503	89.36 ± 0.49	9.54 ± 0.15
Triangle selection	3174	90.61 ± 0.49	8.64 ± 0.15
Tight electron	2802	88.28 ± 0.57	7.63 ± 0.14
Trigger probability		95.87 ± 0.07	7.31 ± 0.13
$\kappa_{electron\ reco,\ ID}$		98.49 ± 0.02	7.20 ± 0.13
$\kappa_{electron\ likelihood}$		88.94 ± 0.09	6.41 ± 0.12
$\kappa_{b-fragmentation}$		94.13 ± 1.41	6.02 ± 0.14
$\geq$1 b-tag		61.34 ± 1.18	3.69 ± 0.11
HITFIT convergence		89.33 ± 4.01	3.30 ± 0.10
Data Quality		97.14 ± 0.50	3.20 ± 0.10
ε^{total}			3.20 ± 0.10

Table A.5.: Preselection efficiencies and corresponding κ factors in % in $\tilde{t}_1\bar{\tilde{t}}_1 \rightarrow e$+jets events for the 175/105 mass point. Only statistical uncertainties are included.

Selection or κ	Events left	Exclusive selection efficiency[%]	Cumulative selection efficiency[%]
	37001		
$\geq$4 good jets	12724	34.39 ± 0.25	34.39 ± 0.25
Leading jet cut	12209	95.95 ± 0.18	33.00 ± 0.24
Loose muon	3890	31.86 ± 0.42	10.51± 0.16
Z muon veto	3890	100	10.51 ± 0.16
2nd muon veto	3890	100	10.51 ± 0.16
Electron veto	3888	99.95 ± 0.04	10.51 ± 0.16
Vertex selection	3831	98.53 ± 0.19	10.35 ± 0.16
$\not{E}_T$	3228	84.26 ± 0.59	8.72 ± 0.15
Triangle selection	2881	89.25 ± 0.55	7.79 ± 0.14
Tight muon	2335	81.05 ± 0.73	6.31 ± 0.13
Trigger probability		85.66 ± 0.25	5.41 ± 0.11
$\kappa_{\mu\ ID\times\ acc\times\ cosmic\ veto}$		97.22 ± 0.21	5.26 ± 0.11
$\kappa_{\mu\ track}$		91.46 ± 0.10	4.82 ± 0.10
$\kappa_{\mu\ isolation}$		100.19 ± 0.02	4.83 ± 0.10
$\kappa_{b-fragmentation}$		98.10 ± 1.55	4.72 ± 0.12
$\geq$1 b-tag		60.39 ± 1.30	2.85 ± 0.09
HITFIT convergence		88.07 ± 4.37	2.51 ± 0.09
Data Quality		97.14 ± 0.50	2.44 ± 0.09
ε^{total}			2.44 ± 0.09

Table A.6.: Preselection efficiencies and corresponding κ factors in % in $\tilde{t}_1\bar{\tilde{t}}_1 \rightarrow \mu$+jets events for the 175/105 mass point. Only statistical uncertainties are included.

Selection or κ	Events left	Exclusive selection efficiency[%]	Cumulative selection efficiency[%]
	52505		
$\geq$4 good jets	15332	29.20 ± 0.20	29.20 ± 0.20
Leading jet cut	13569	88.50 ± 0.26	25.84 ± 0.19
Loose electron	4669	34.41 ± 0.41	8.89 ± 0.12
Muon veto	4669	100	8.89 ± 0.12
2nd electron veto	4668	99.98 ± 0.02	8.89 ± 0.12
Vertex selection	4579	98.09 ± 0.20	8.72 ± 0.12
$\not{E}_T$	4076	89.02 ± 0.46	7.76 ± 0.12
Triangle selection	3771	92.52 ± 0.41	7.18 ± 0.11
Tight electron	3299	87.48 ± 0.54	6.28 ± 0.11
Trigger probability		95.51 ± 0.08	6.00 ± 0.10
$\kappa_{electron\ reco,\ ID}$		98.51 ± 0.02	5.91 ± 0.10
$\kappa_{electron\ likelihood}$		89.05 ± 0.08	5.27 ± 0.09
$\kappa_{b-fragmentation}$		98.59 ± 1.31	5.19 ± 0.11
$\geq$1 b-tag		54.40 ± 1.09	2.82 ± 0.08
HITFIT convergence		91.63 ± 3.96	2.59 ± 0.08
Data Quality		97.14 ± 0.50	2.51 ± 0.08
ε^{total}			2.51 ± 0.08

Table A.7.: Preselection efficiencies and corresponding κ factors in % in $\tilde{t}_1\bar{\tilde{t}}_1 \rightarrow e$+jets events for the 160/120 mass point. Only statistical uncertainties are included.

Selection or κ	Events left	Exclusive selection efficiency[%]	Cumulative selection efficiency[%]
	52379		
$\geq$4 good jets	15029	28.69 ± 0.20	28.69 ± 0.20
Leading jet cut	13308	88.55 ± 0.26	25.41 ± 0.19
Loose muon	4565	34.30 ± 0.41	8.72 ± 0.12
Z muon veto	4564	99.98 ± 0.02	8.71 ± 0.12
2nd muon veto	4563	99.98 ± 0.02	8.71 ± 0.12
Electron veto	4556	99.85 ± 0.06	8.70 ± 0.12
Vertex selection	4479	98.31 ± 0.19	8.55 ± 0.12
$\not{E}_T$	3743	83.57 ± 0.55	7.15 ± 0.11
Triangle selection	3424	91.48 ± 0.46	6.54 ± 0.11
Tight muon	2804	81.89 ± 0.66	5.35 ± 0.10
Trigger probability		83.44 ± 0.26	4.47 ± 0.08
$\kappa_{\mu\ ID\times\ acc\times\ cosmic\ veto}$		97.32 ± 0.18	4.35 ± 0.08
$\kappa_{\mu\ track}$		91.56 ± 0.10	3.98 ± 0.07
$\kappa_{\mu\ isolation}$		100.22 ± 0.02	3.99 ± 0.07
$\kappa_{b-fragmentation}$		91.97 ± 1.41	3.68 ± 0.09
$\geq$1 b-tag		55.83 ± 1.23	2.05 ± 0.07
HITFIT convergence		89.24 ± 4.36	1.83 ± 0.06
Data Quality		97.14 ± 0.50	1.78 ± 0.06
ε^{total}			1.78 ± 0.06

Table A.8.: Preselection efficiencies and corresponding κ factors in % in $\tilde{t}_1\bar{\tilde{t}}_1 \rightarrow \mu$+jets events for the 160/120 mass point. Only statistical uncertainties are included.

Selection or κ	Events left	Exclusive selection efficiency[%]	Cumulative selection efficiency[%]
	51718		
$\geq$4 good jets	16139	31.21 ± 0.20	31.21 ± 0.20
Leading jet cut	14832	91.90 ± 0.22	28.68 ± 0.20
Loose electron	4649	31.34 ± 0.38	8.99 ± 0.13
Muon veto	4649	100	8.99 ± 0.13
2nd electron veto	4648	99.98 ± 0.02	8.99 ± 0.13
Vertex selection	4586	98.67 ± 0.17	8.87 ± 0.13
$\not{E}_T$	3984	86.87 ± 0.50	7.70 ± 0.12
Triangle selection	3605	90.49 ± 0.47	6.97 ± 0.11
Tight electron	3218	89.26 ± 0.52	6.22 ± 0.11
Trigger probability		95.32 ± 0.09	5.93 ± 0.10
$\kappa_{electron\ reco,\ ID}$		98.50 ± 0.02	5.84 ± 0.10
$\kappa_{electron\ likelihood}$		89.01 ± 0.08	5.20 ± 0.09
$\kappa_{b-fragmentation}$		98.75 ± 1.31	5.13 ± 0.11
$\geq$1 b-tag		56.02 ± 1.10	2.87 ± 0.08
HITFIT convergence		90.43 ± 3.88	2.60 ± 0.08
Data Quality		97.14 ± 0.50	2.52 ± 0.08
ε^{total}			2.52 ± 0.08

Table A.9.: Preselection efficiencies and corresponding κ factors in % in $\tilde{t}_1\bar{\tilde{t}}_1 \rightarrow e$+jets events for the 160/105 mass point. Only statistical uncertainties are included.

Selection or κ	Events left	Exclusive selection efficiency[%]	Cumulative selection efficiency[%]
	51765		
$\geq$4 good jets	15425	29.80 ± 0.20	29.80 ± 0.20
Leading jet cut	14255	92.41 ± 0.21	27.54 ± 0.20
Loose muon	4426	31.05 ± 0.39	8.55 ± 0.12
Z muon veto	4425	99.98 ± 0.02	8.55 ± 0.12
2nd muon veto	4425	100	8.55 ± 0.12
Electron veto	4423	99.95 ± 0.03	8.54 ± 0.12
Vertex selection	4352	98.39 ± 0.19	8.41 ± 0.12
$\not{E}_T$	3559	81.78 ± 0.59	6.88 ± 0.11
Triangle selection	3158	88.73 ± 0.53	6.10 ± 0.11
Tight muon	2582	81.76 ± 0.69	4.99 ± 0.10
Trigger probability		84.33 ± 0.25	4.21 ± 0.08
$\kappa_{\mu\ ID\times\ acc\times\ cosmic\ veto}$		97.42 ± 0.20	4.10 ± 0.08
$\kappa_{\mu\ track}$		91.60 ± 0.10	3.76 ± 0.07
$\kappa_{\mu\ isolation}$		100.20 ± 0.02	3.77 ± 0.07
$\kappa_{b-fragmentation}$		99.71 ± 1.49	3.75 ± 0.09
$\geq$1 b-tag		57.75 ± 1.24	2.17 ± 0.07
HITFIT convergence		89.97 ± 4.32	1.95 ± 0.07
Data Quality		97.14 ± 0.50	1.89 ± 0.06
ε^{total}			1.89 ± 0.06

Table A.10.: Preselection efficiencies and corresponding κ factors in % in $\tilde{t}_1\bar{\tilde{t}}_1 \rightarrow \mu$+jets events for the 160/105 mass point. Only statistical uncertainties are included.

Selection or κ	Events left	Exclusive selection efficiency[%]	Cumulative selection efficiency[%]
	53060		
$\geq$4 good jets	13697	25.81 ± 0.19	25.81 ± 0.19
Leading jet cut	11674	85.23 ± 0.30	22.00 ± 0.18
Loose electron	3353	28.72 ± 0.42	6.32 ± 0.11
Muon veto	3352	99.97 ± 0.03	6.32 ± 0.11
2nd electron veto	3352	100	6.32 ± 0.11
Vertex selection	3306	98.63 ± 0.20	6.23 ± 0.11
$\not{E}_T$	2853	86.30 ± 0.60	5.38 ± 0.10
Triangle selection	2579	90.40 ± 0.55	4.86 ± 0.09
Tight electron	2263	87.75 ± 0.65	4.26 ± 0.09
Trigger probability		95.17 ± 0.10	4.06 ± 0.08
$\kappa_{electron\ reco,\ ID}$		98.51 ± 0.02	4.00 ± 0.08
$\kappa_{electron\ likelihood}$		89.18 ± 0.10	3.57 ± 0.07
$\kappa_{b-fragmentation}$		96.79 ± 1.58	3.44 ± 0.09
$\geq$1 b-tag		54.40 ± 1.33	1.88 ± 0.07
HITFIT convergence		90.30 ± 4.77	1.69 ± 0.06
Data Quality		97.14 ± 0.50	1.64 ± 0.06
ε^{total}			1.64 ± 0.06

Table A.11.: Preselection efficiencies and corresponding κ factors in % in $\tilde{t}_1\bar{\tilde{t}}_1 \rightarrow e$+jets events for the 145/105 mass point. Only statistical uncertainties are included.

Selection or κ	Events left	Exclusive selection efficiency[%]	Cumulative selection efficiency[%]
	52806		
$\geq$4 good jets	13073	24.76 ± 0.19	24.76 ± 0.19
Leading jet cut	11200	85.67 ± 0.31	21.21 ± 0.18
Loose muon	3274	29.23 ± 0.43	6.20 ± 0.11
Z muon veto	3274	100	6.20 ± 0.11
2nd muon veto	3274	100	6.20 ± 0.11
Electron veto	3270	99.88 ± 0.06	6.19 ± 0.11
Vertex selection	3208	98.10 ± 0.24	6.08 ± 0.10
$\not{E}_T$	2562	79.86 ± 0.71	4.85 ± 0.09
Triangle selection	2245	87.63 ± 0.65	4.25 ± 0.09
Tight muon	1767	78.71 ± 0.86	3.35 ± 0.08
Trigger probability		82.48 ± 0.35	2.76 ± 0.07
$\kappa_{\mu\ ID\times\ acc\times\ cosmic\ veto}$		97.23 ± 0.23	2.69 ± 0.06
$\kappa_{\mu\ track}$		91.92 ± 0.12	2.47 ± 0.06
$\kappa_{\mu\ isolation}$		100.21 ± 0.02	2.48 ± 0.06
$\kappa_{b-fragmentation}$		99.40 ± 1.77	2.46 ± 0.07
$\geq$1 b-tag		54.83 ± 1.52	1.35 ± 0.06
HITFIT convergence		88.29 ± 5.31	1.19 ± 0.06
Data Quality		97.14 ± 0.50	1.16 ± 0.05
ε^{total}			1.16 ± 0.05

Table A.12.: Preselection efficiencies and corresponding κ factors in % in $\tilde{t}_1\bar{\tilde{t}}_1 \rightarrow \mu$+jets events for the 145/105 mass point. Only statistical uncertainties are included.

B. Control Plots

This appendix shows the data-MC agreement in distributions for selected control variables: p_T of the highest p_T (leading) jet, η of the leading jet, lepton p_T, missing transverse energy $\not\!\!E_T$, W transverse mass and the sphericity of the event. The variables are shown in both e+jets and μ+jets channel for events with four or more jets before b-tagging, then after b-tagging and finally in the signal bin after b-tagging and HITFIT convergence. The signal contribution is not included in the Monte Carlo distributions, but as an example the corresponding histograms for the Stop 175/135 mass point are overlaid ten times enhanced.

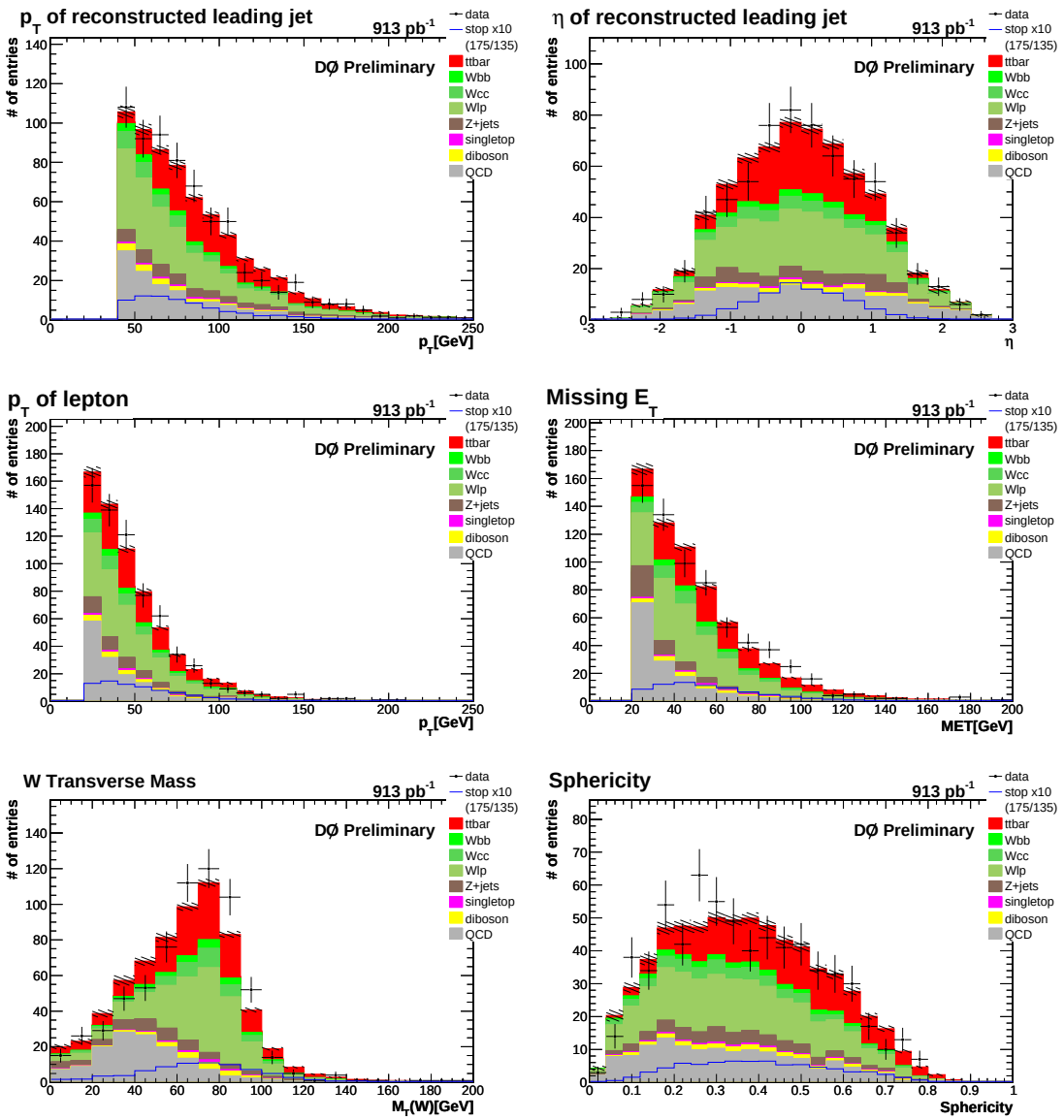

Figure B.1.: Comparison of data and MC in the e+jets channel for $\geq$4 jets, before b-tagging.

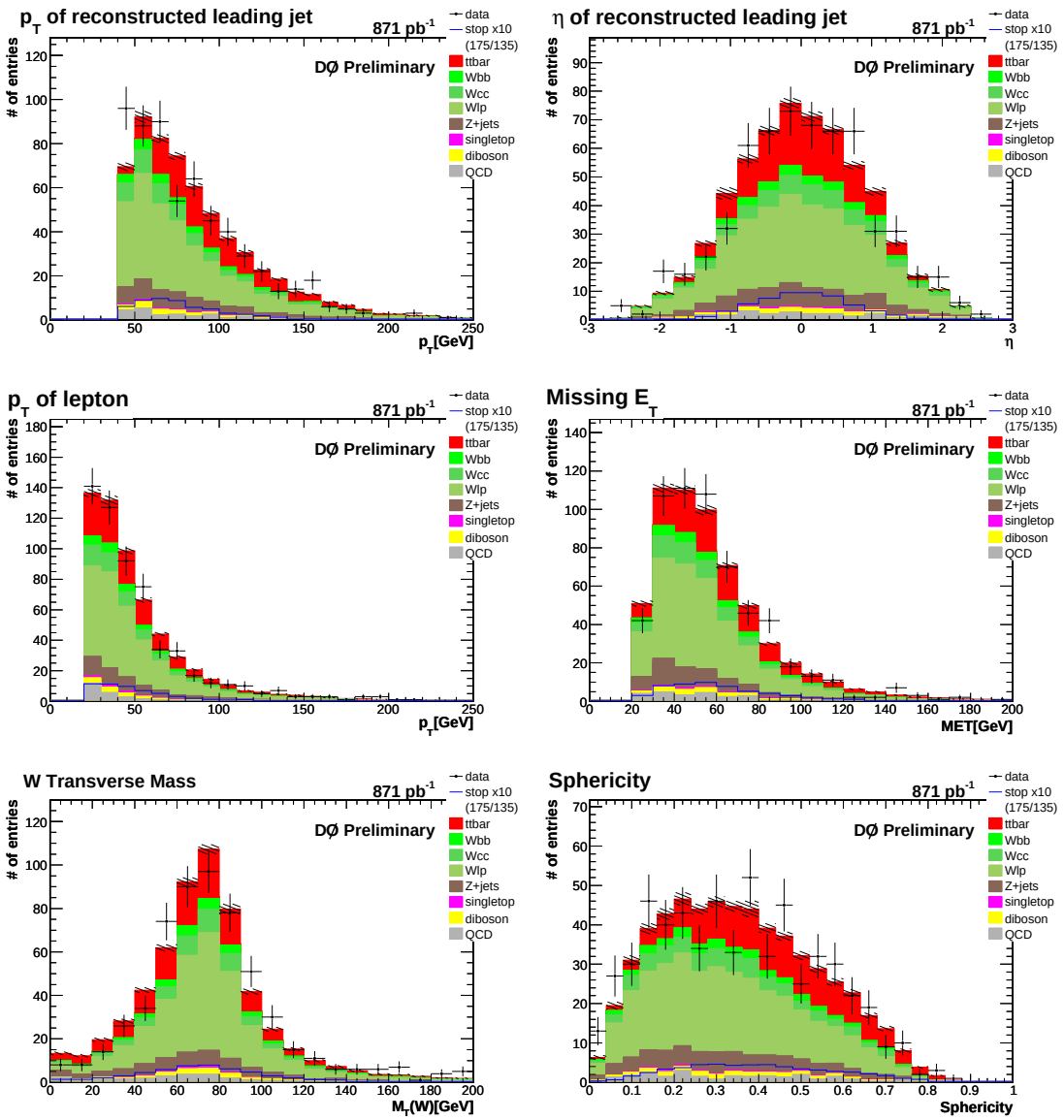

Figure B.2.: Comparison of data and MC in the μ+jets channel for $\geq$4 jets, before b-tagging.

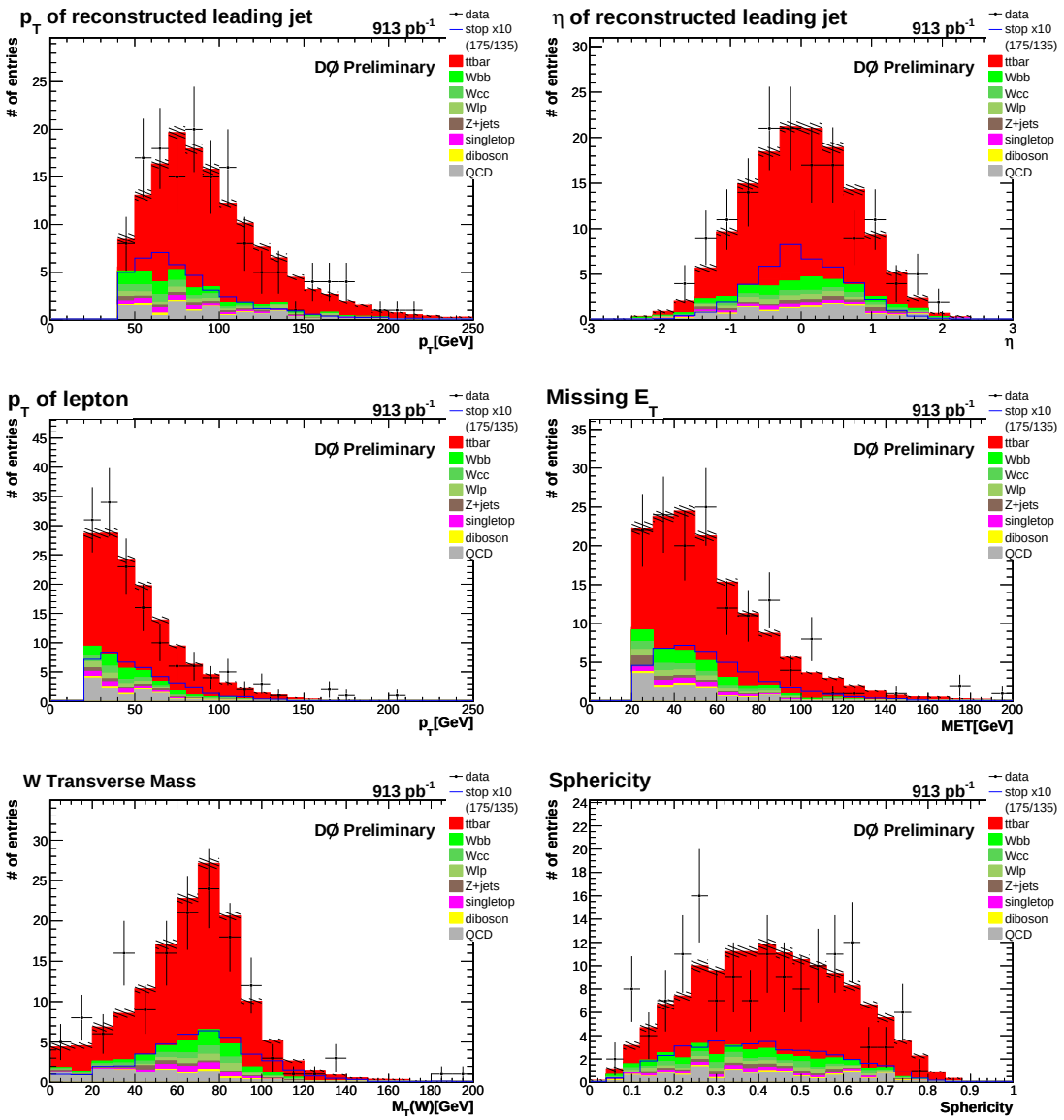

Figure B.3.: Comparison of data and MC in the e+jets channel for $\geq$4 jets, after b-tagging.

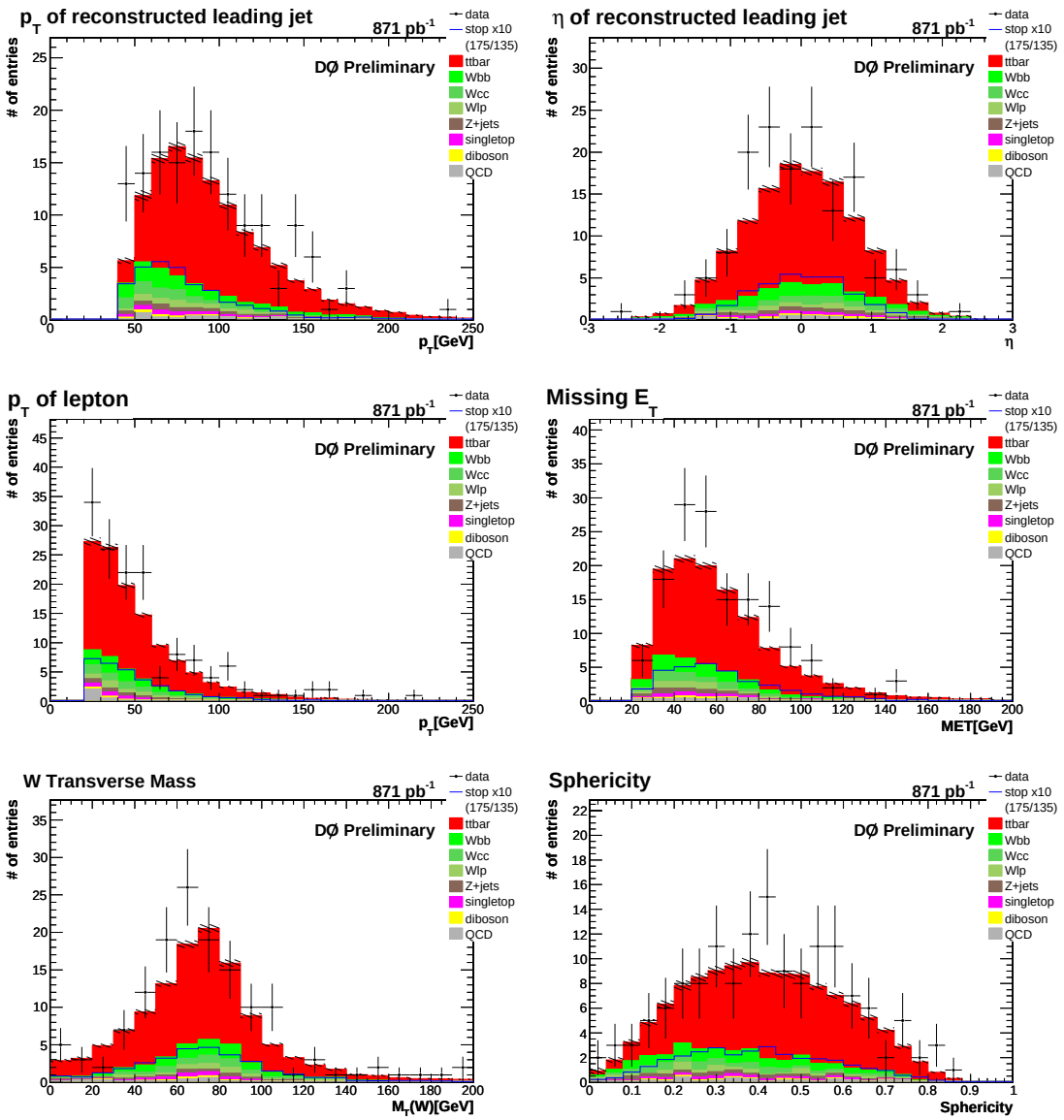

Figure B.4.: Comparison of data and MC in the μ+jets channel for $\geq$4 jets, after b-tagging.

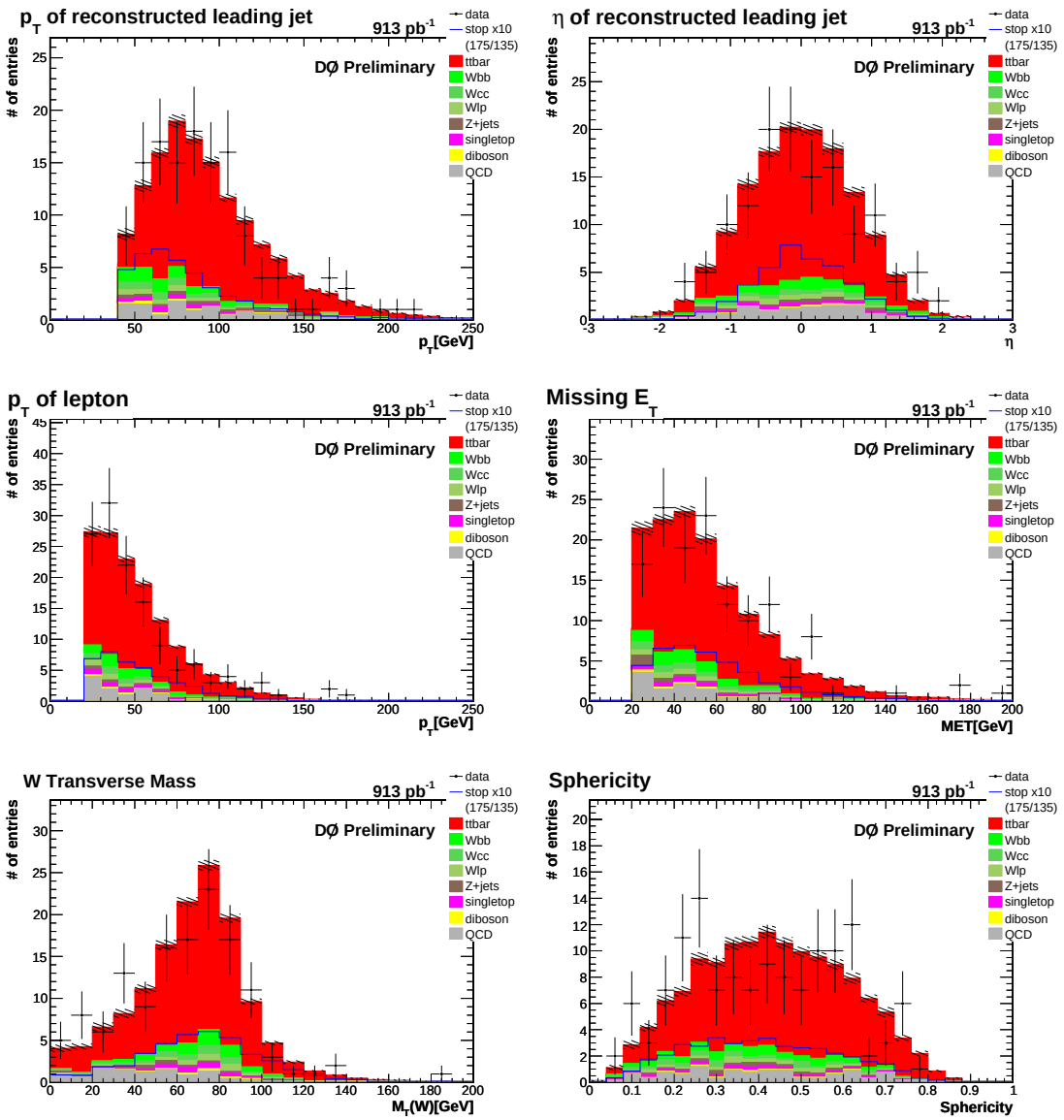

Figure B.5.: Comparison of data and MC in the e+jets channel for $\geq$4 jets, after b-tagging and after obtaining convergence in HITFIT.

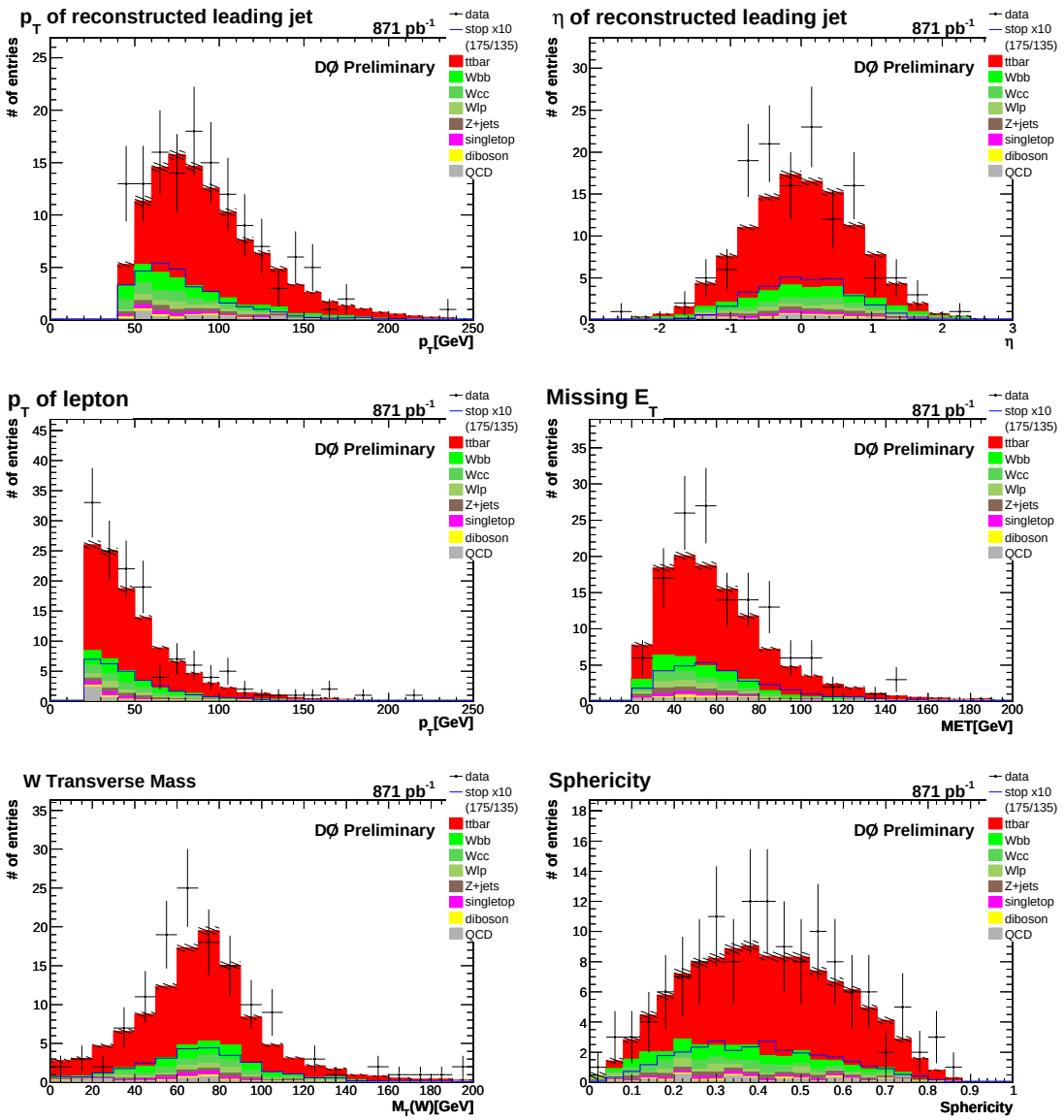

Figure B.6.: Comparison of data and MC in the μ+jets channel for $\geq$4 jets, after b-tagging and after obtaining convergence in HITFIT.

C. Likelihood Discriminant

This appendix shows the complete set of plots for all $\tilde{t}_1\bar{\tilde{t}}_1$ signal mass points related to the likelihood discriminant.

C.1. Variables for Discriminating Signal from Background

First the input variables are displayed as comparison between the $\tilde{t}_1\bar{\tilde{t}}_1$, $t\bar{t}$, and W+jets samples. For details about the variables, refer to Section 6.3.1.

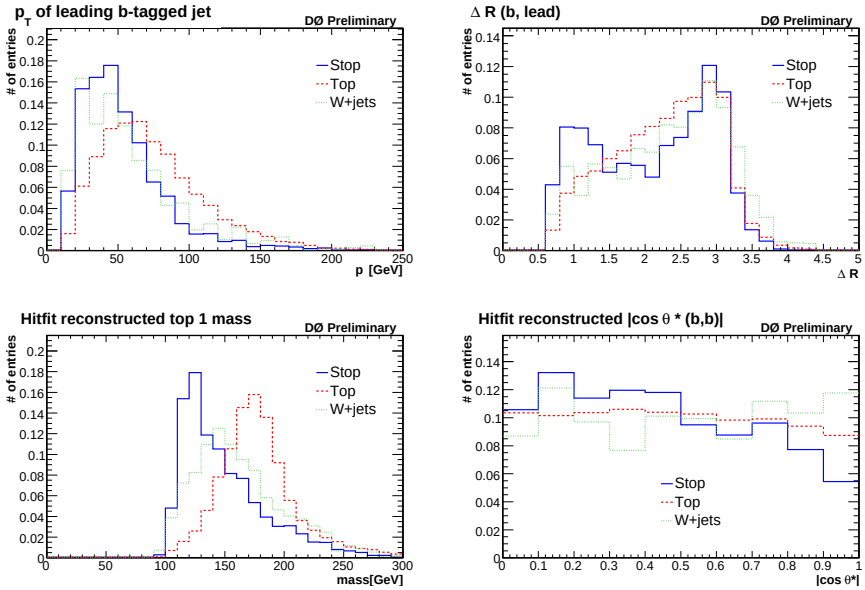

Figure C.1.: Input variables for the 175/135 mass point in the e+jets channel.

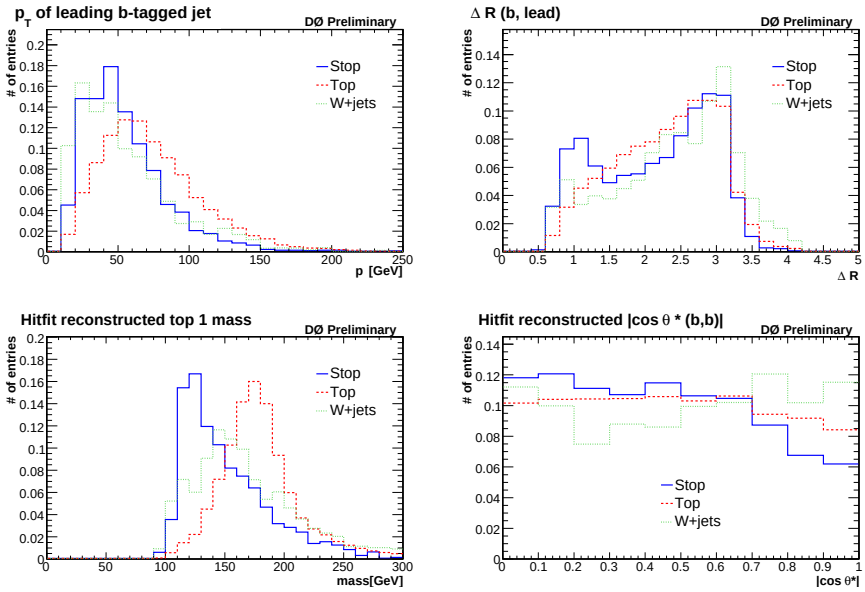

Figure C.2.: Input variables for the 175/135 mass point in the μ+jets channel.

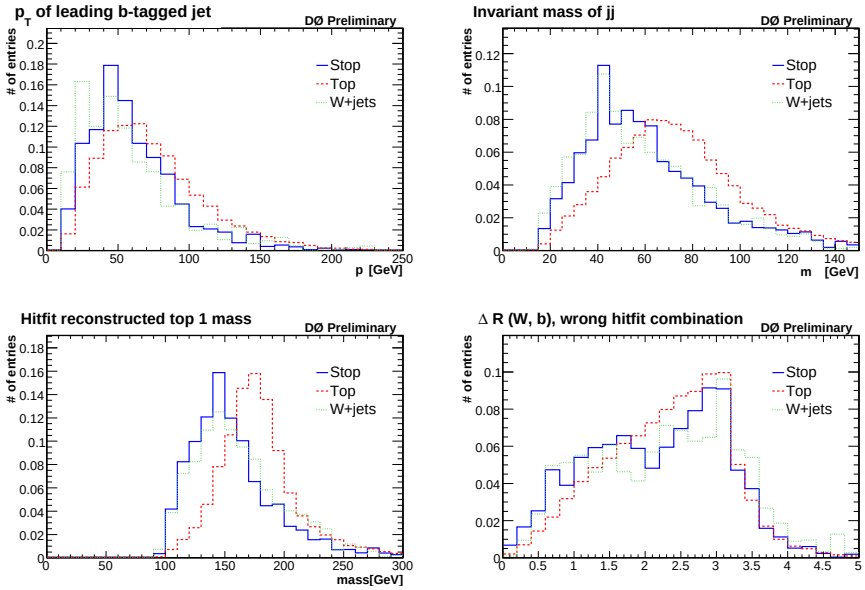

Figure C.3.: Input variables for the 175/120 mass point in the e+jets channel.

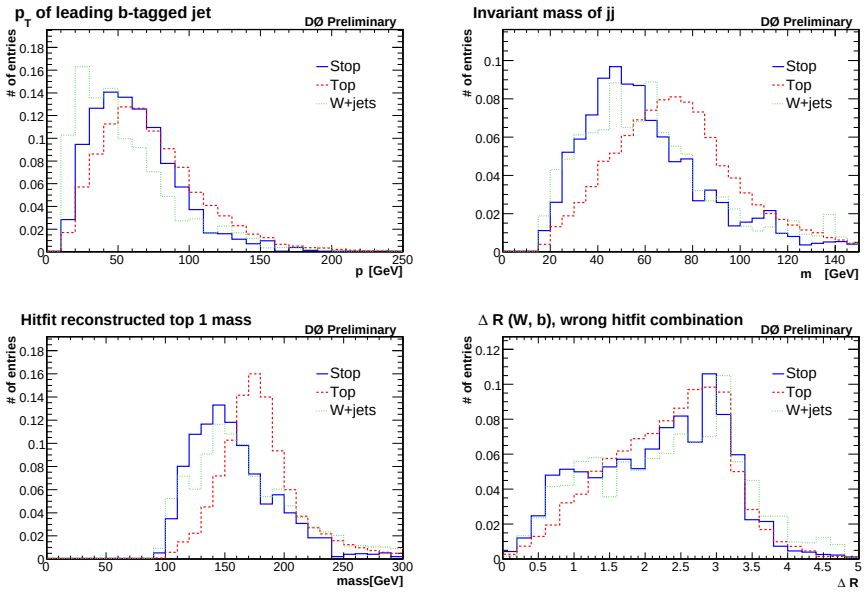

Figure C.4.: Input variables for the 175/120 mass point in the μ+jets channel.

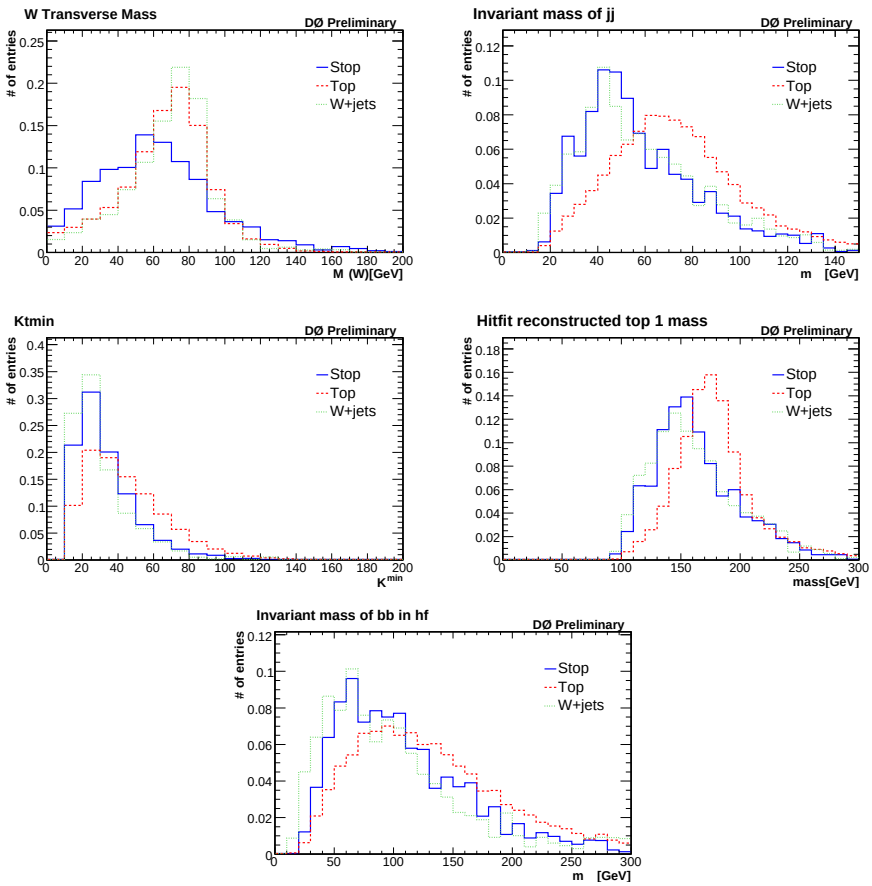

Figure C.5.: Input variables for the 175/105 mass point in the e+jets channel.

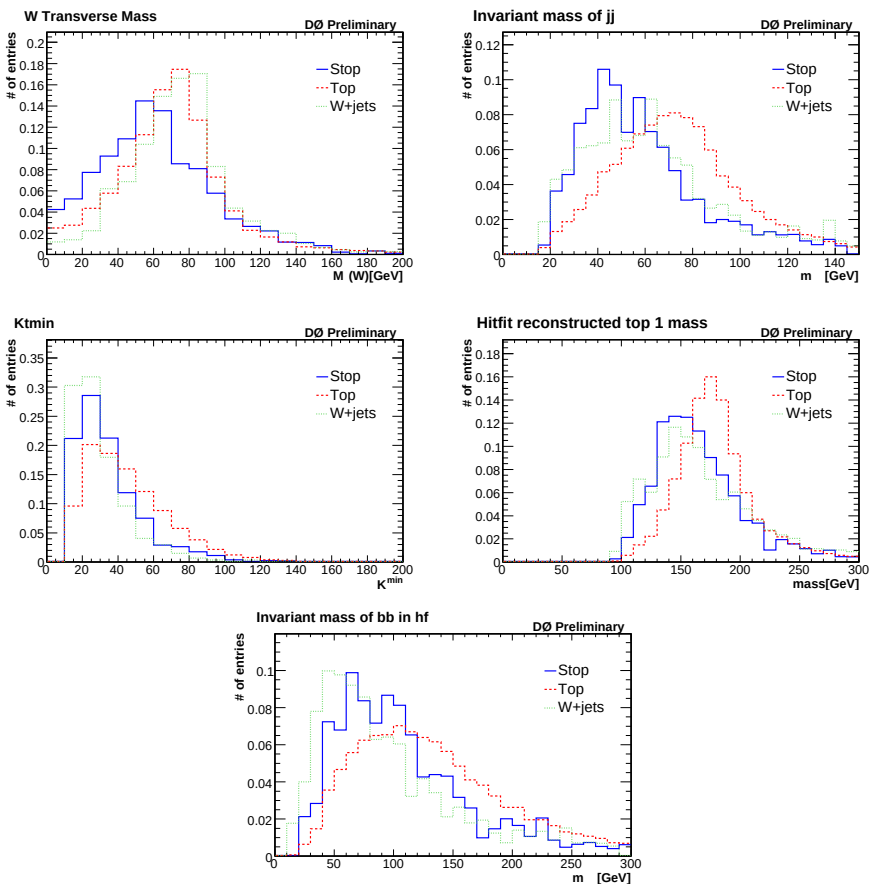

Figure C.6.: Input variables for the 175/105 mass point in the μ+jets channel.

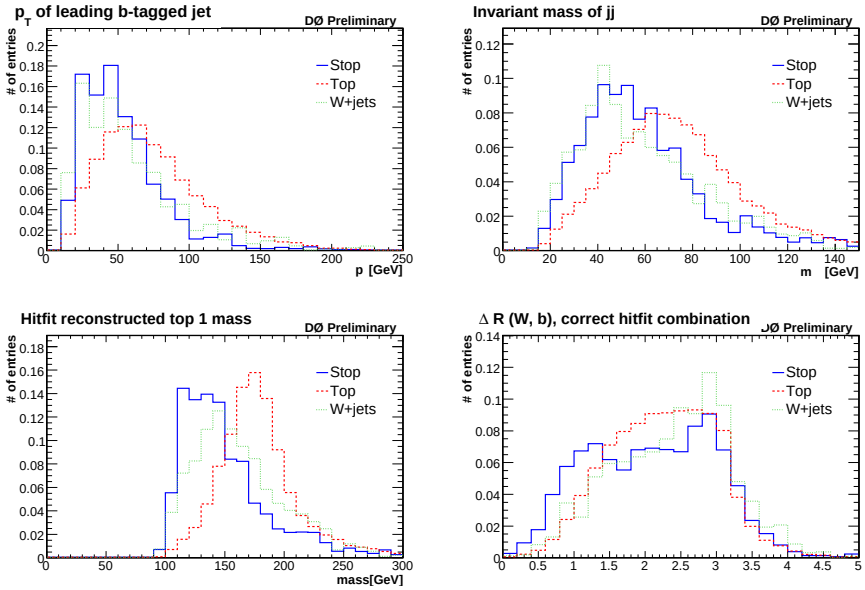

Figure C.7.: Input variables for the 160/120 mass point in the e+jets channel.

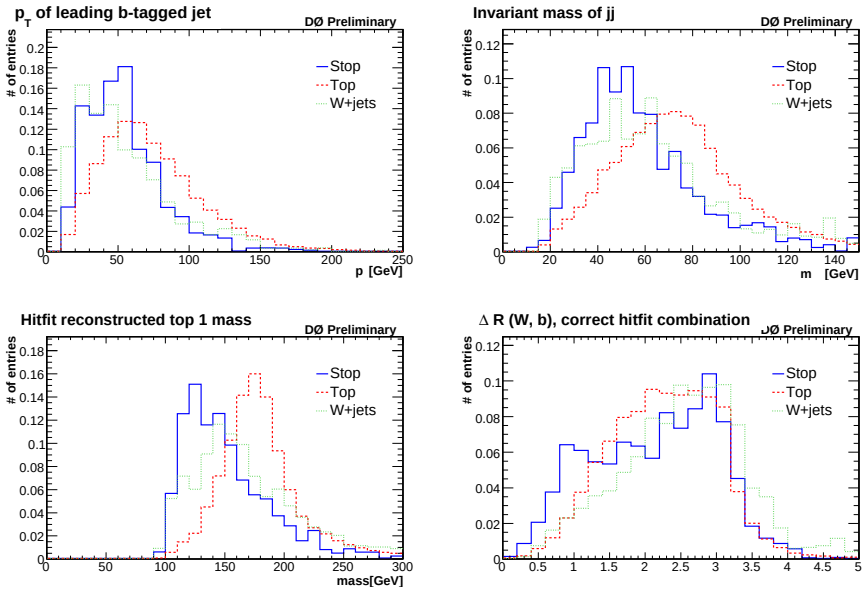

Figure C.8.: Input variables for the 160/120 mass point in the μ+jets channel.

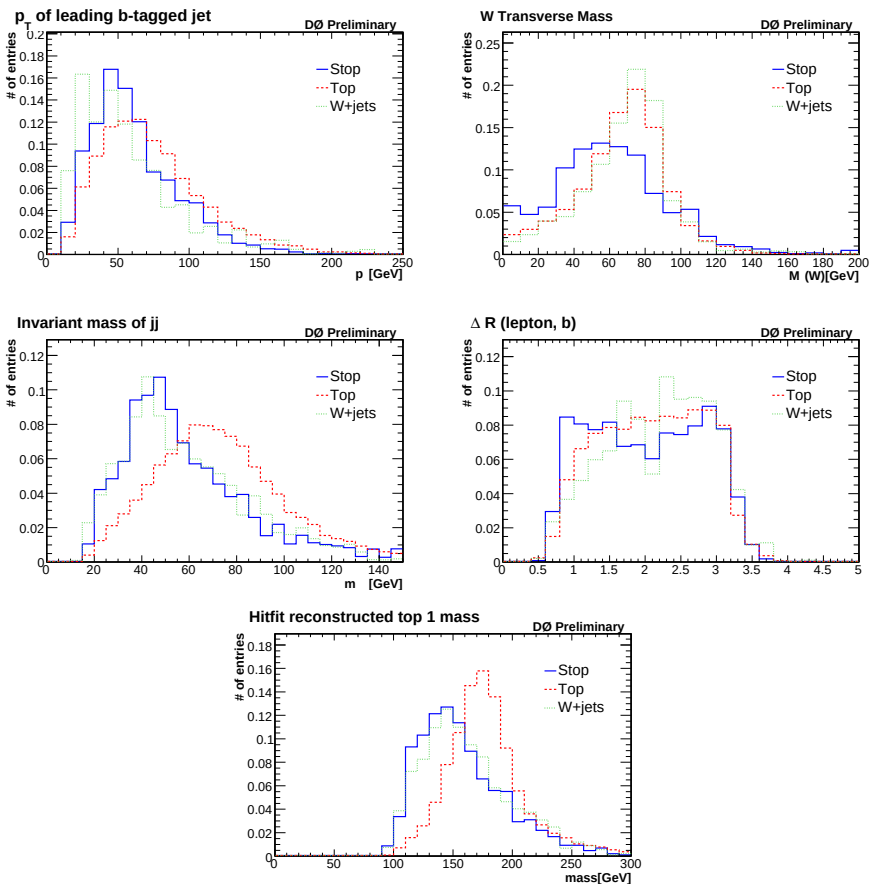

Figure C.9.: Input variables for the 160/105 mass point in the e+jets channel.

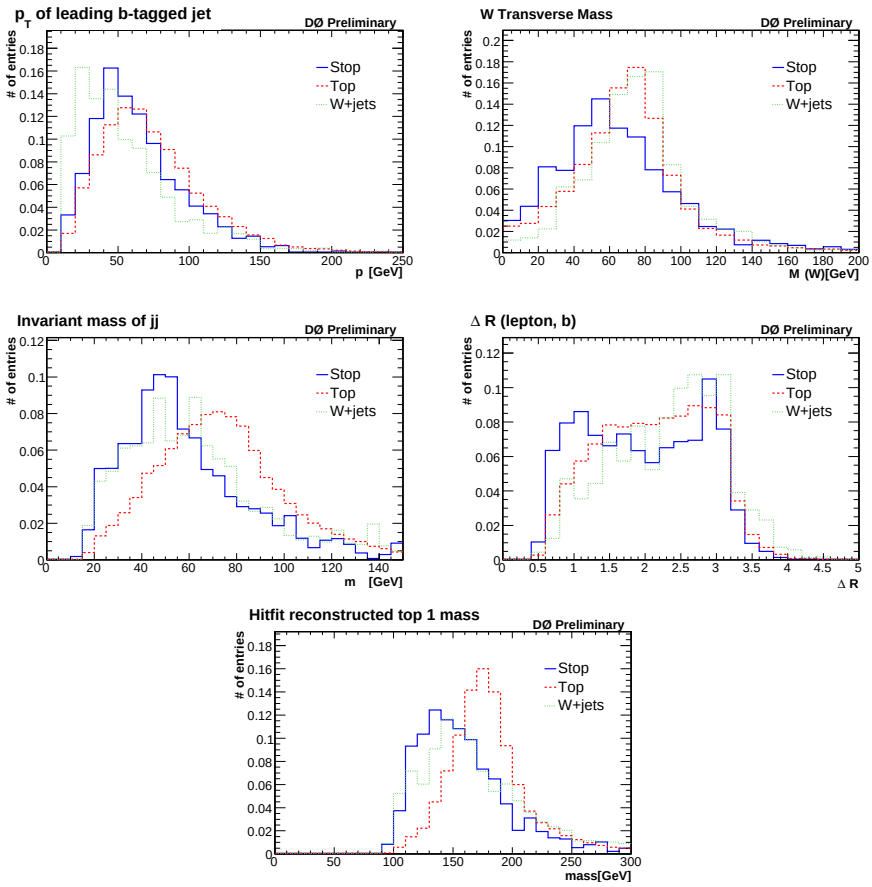

Figure C.10.: Input variables for the 160/105 mass point in the μ+jets channel.

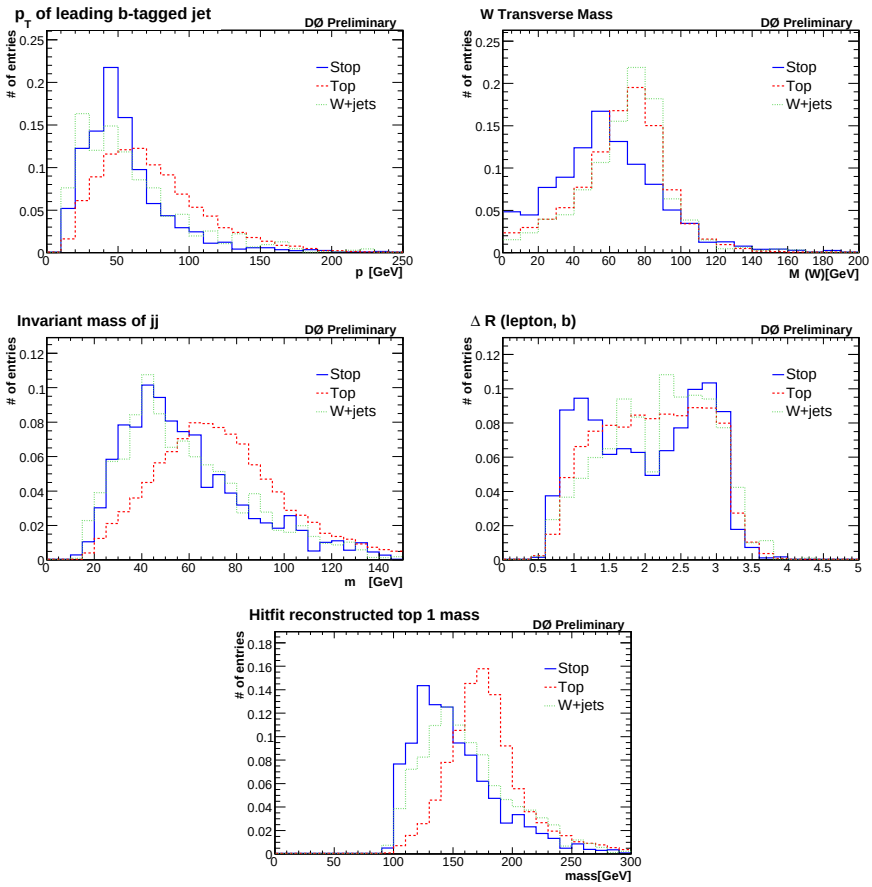

Figure C.11.: Input variables for the 145/105 mass point in the e+jets channel.

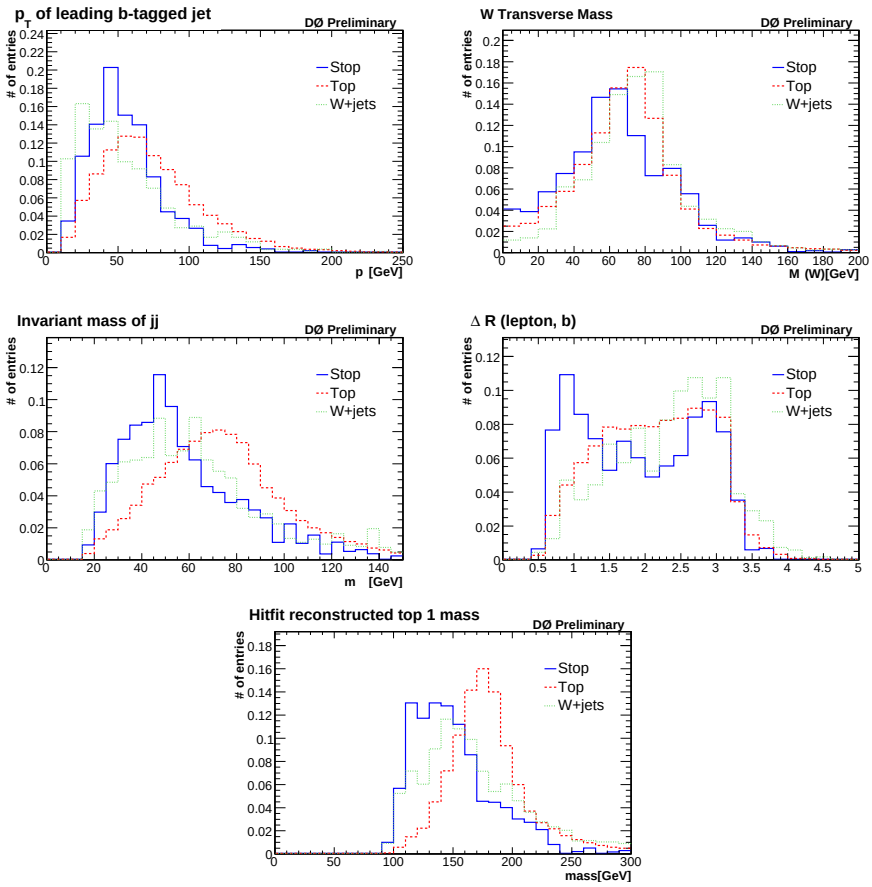

Figure C.12.: Input variables for the 145/105 mass point in the μ+jets channel.

C.2. Comparison of Input Variables in Data and MC

This section shows the data-MC agreement of the input variables for the likelihood discriminants for each mass point in the signal jet multiplicity bin with four or more jets after b-tagging and after HITFIT convergence. The signal contribution is not included in the Monte Carlo distributions, but as an example the corresponding histograms for the 175/135 mass point are overlaid ten times enhanced. For details about the variables, refer to Section 6.3.1.

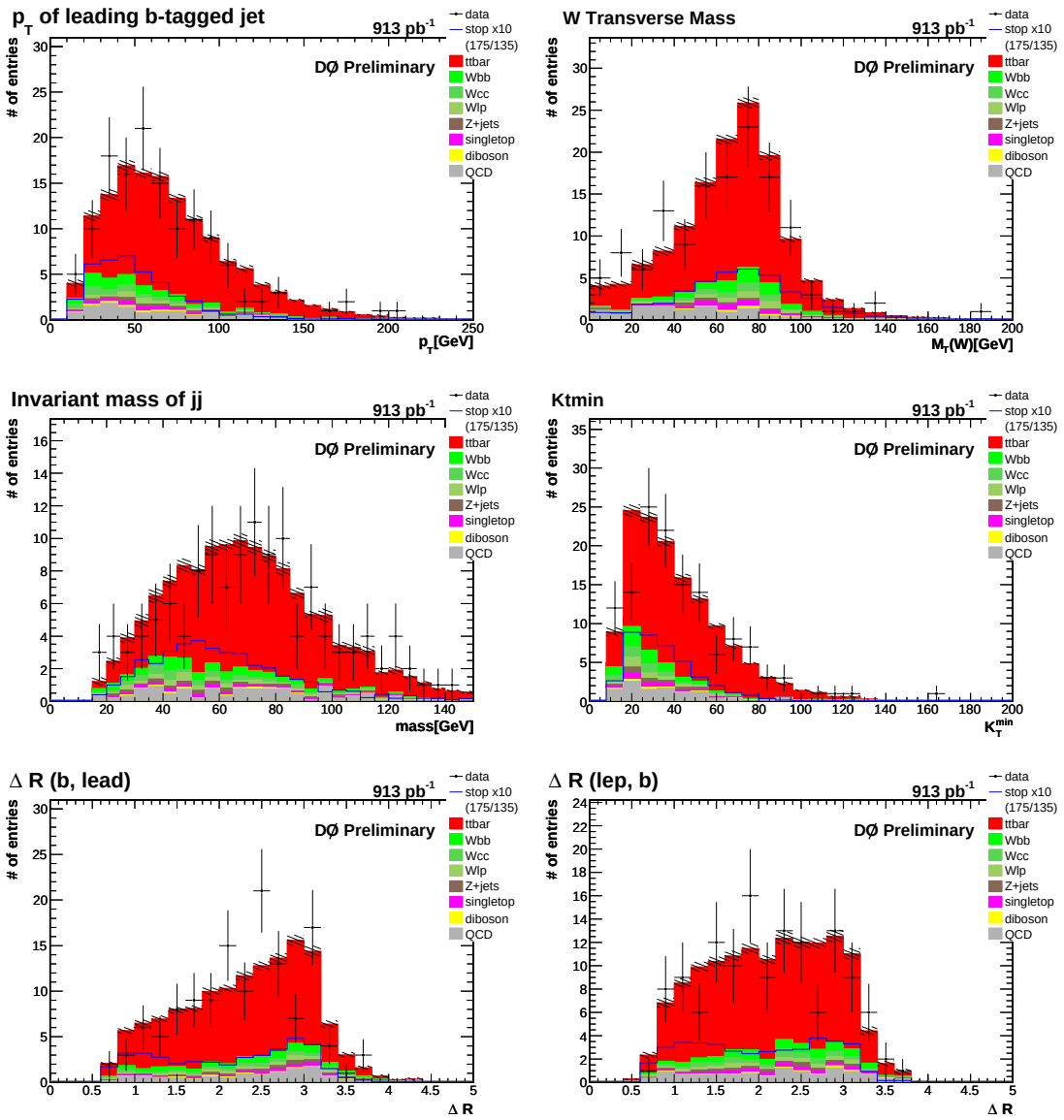

Figure C.13.: Input variables used in the likelihood discriminants in data and MC in the e+jets channel.

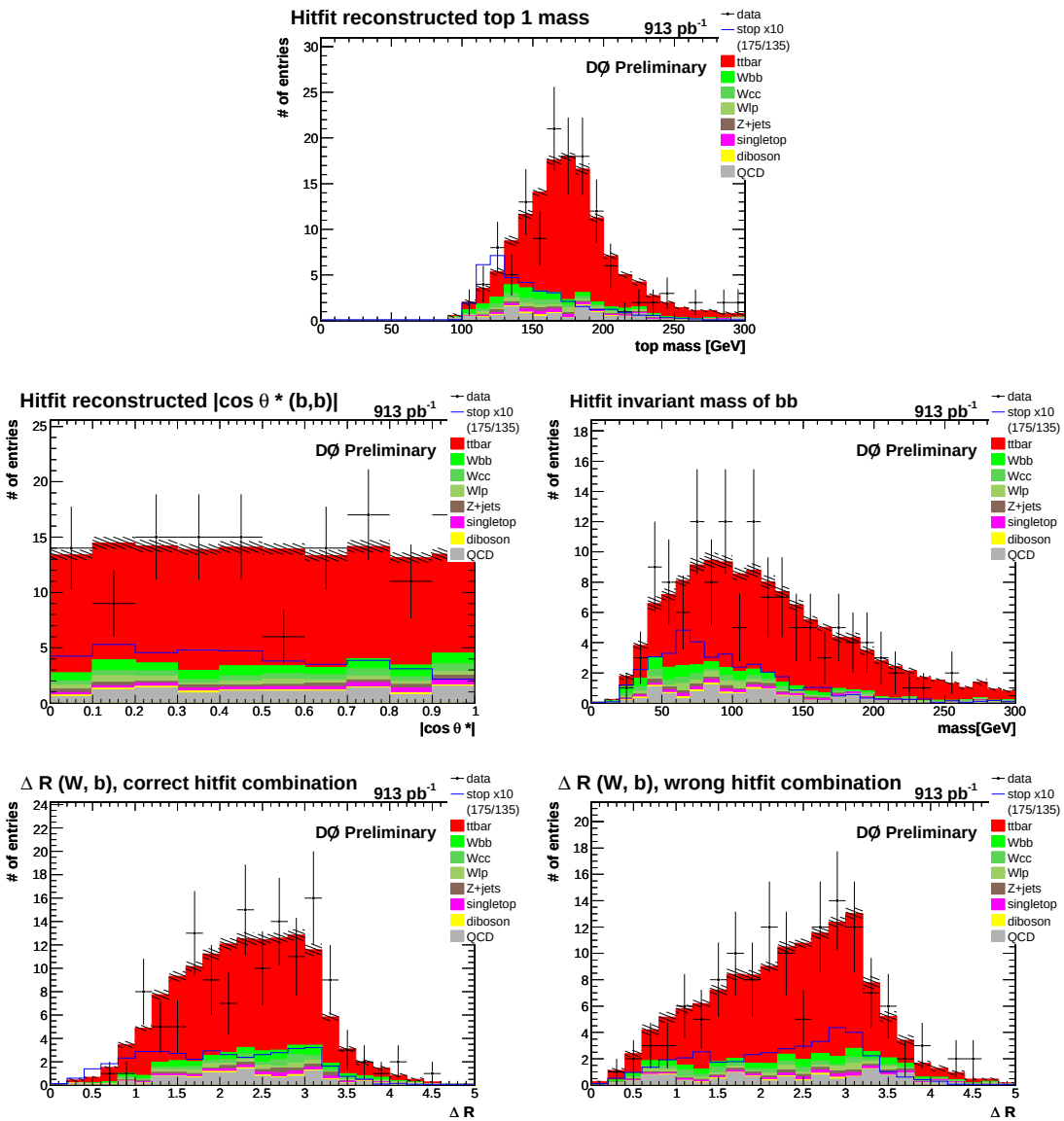

Figure C.14.: Input variables used in the likelihood discriminants in data and MC in the e+jets channel.

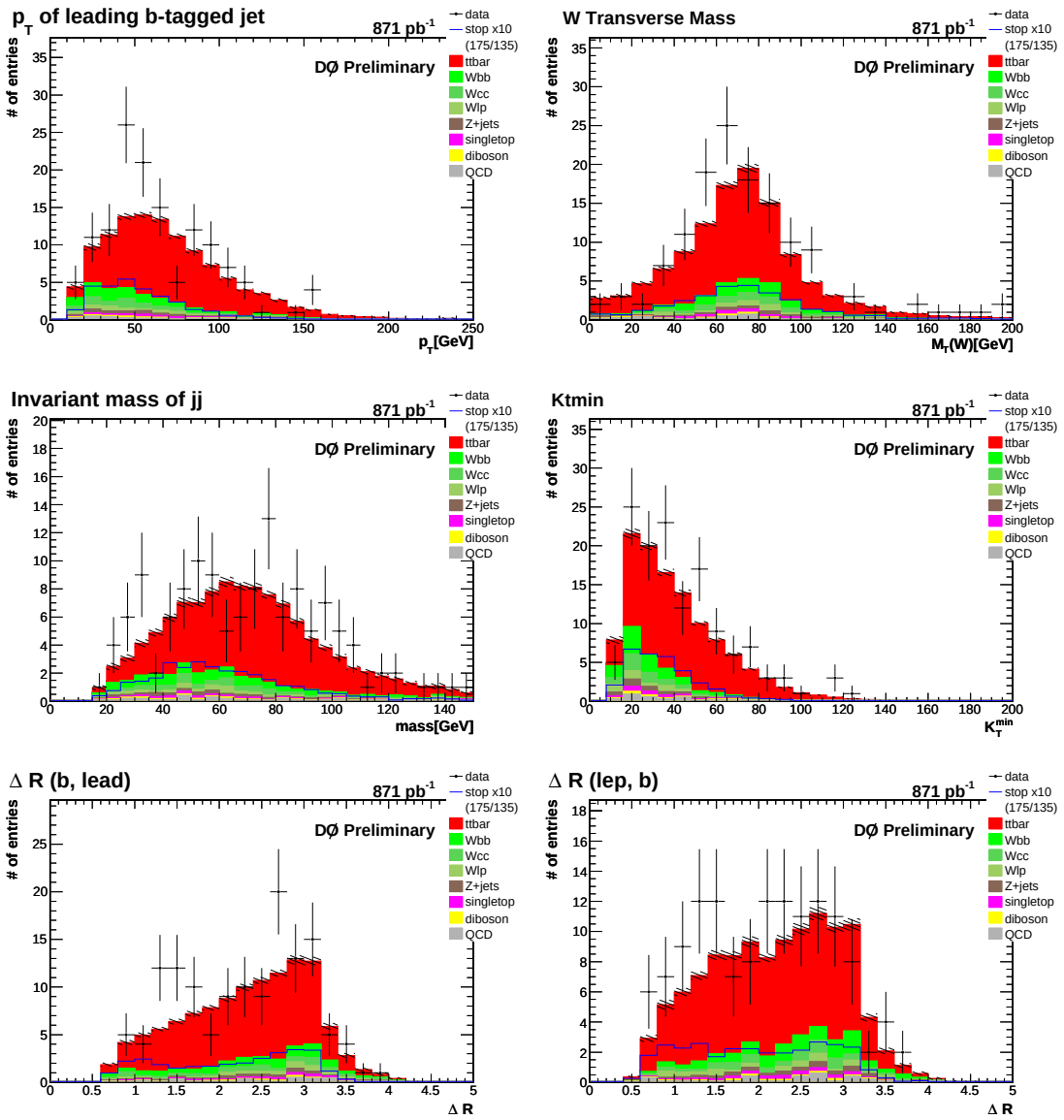

Figure C.15.: Input variables used in the likelihood discriminants in data and MC in the μ+jets channel.

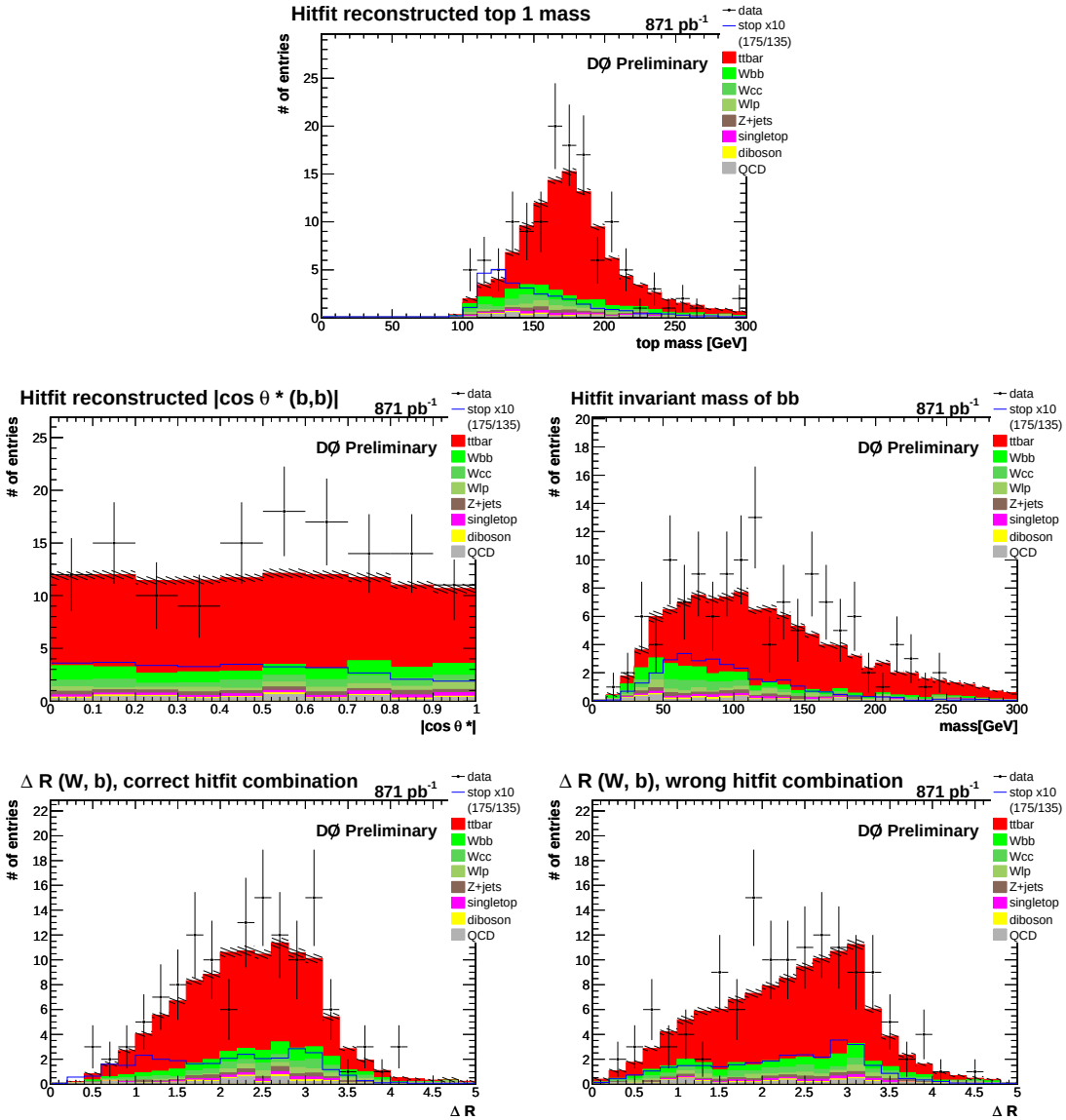

Figure C.16.: Input variables used in the likelihood discriminants in data and MC in the μ+jets channel.

C.3. Likelihood Discriminant

In this section the resulting likelihood discriminant distributions for each mass point as a comparison between $\tilde{t}_1\bar{\tilde{t}}_1$ signal, the $t\bar{t}$ background, and the W+jets background as well as a comparison between the Monte Carlo prediction and the data are shown. For details about the construction of the likelihood discriminant, refer to Section 6.3.2.

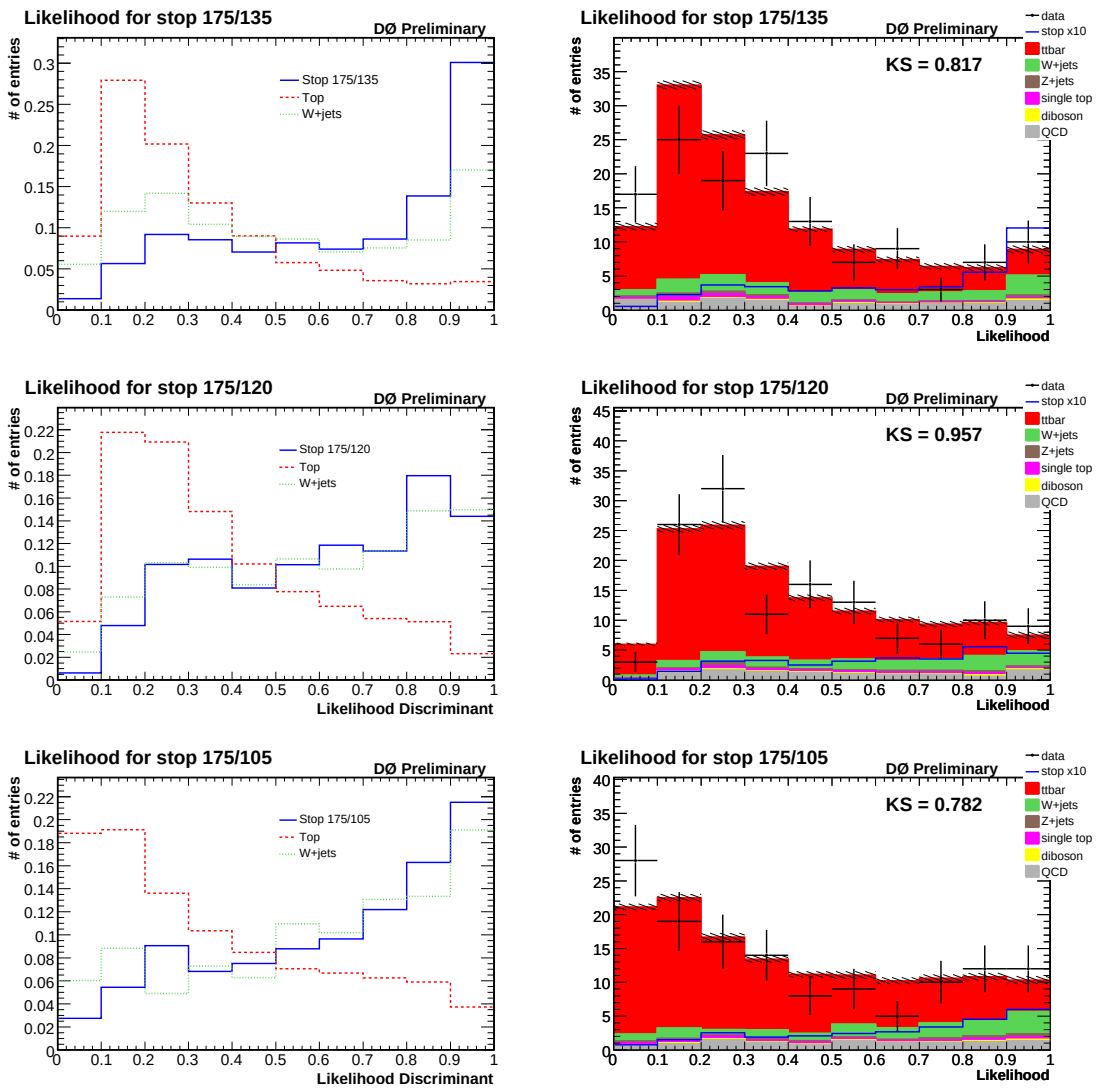

Figure C.17.: Likelihood discriminants in the e+jets channel for different mass points. Top: Stop 175/135, middle: Stop 175/120, bottom: Stop 175/105.

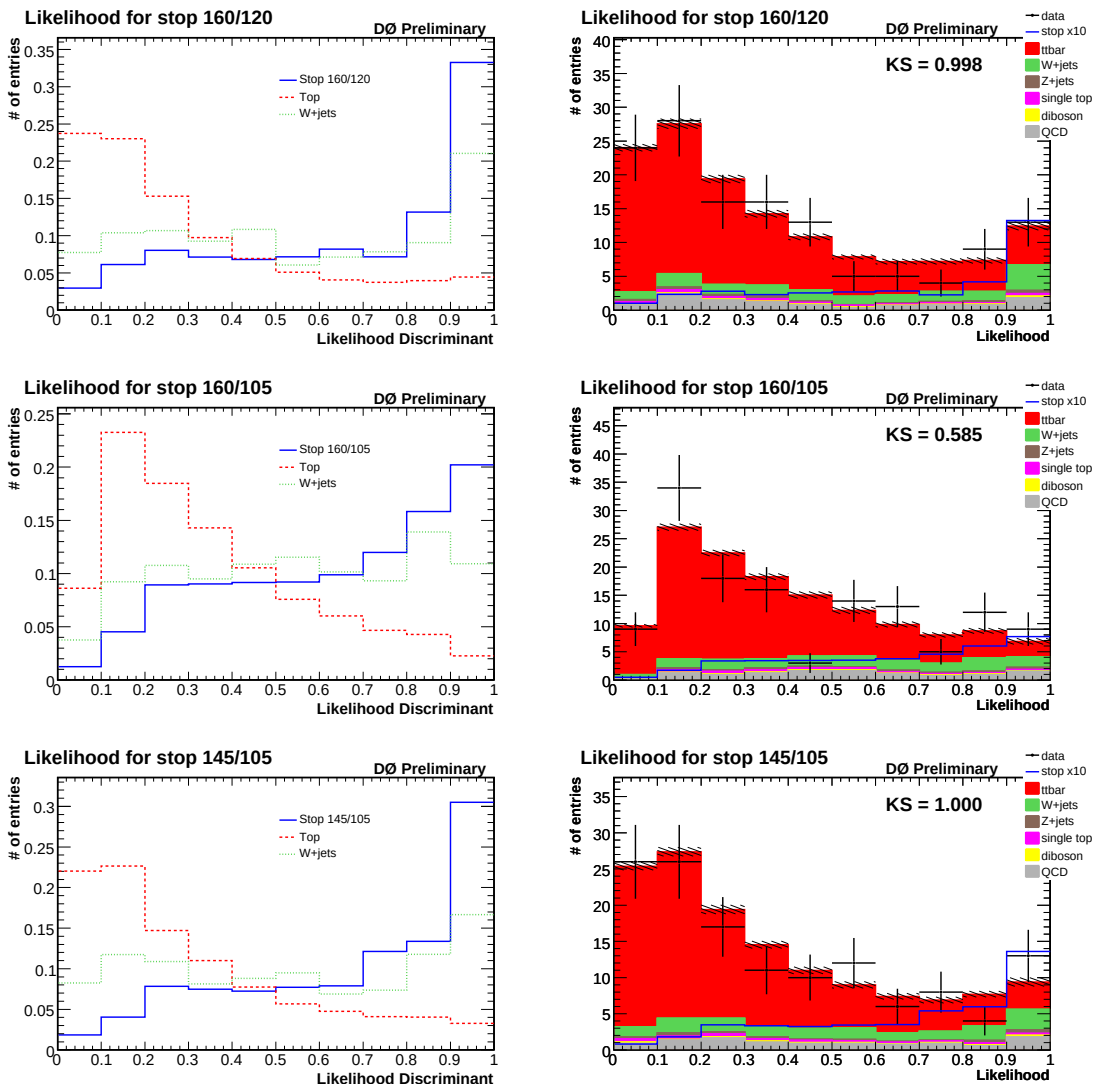

Figure C.18.: Likelihood discriminants in the e+jets channel for different mass points. Top: Stop 160/120, middle: Stop 160/105, bottom: Stop 145/105.

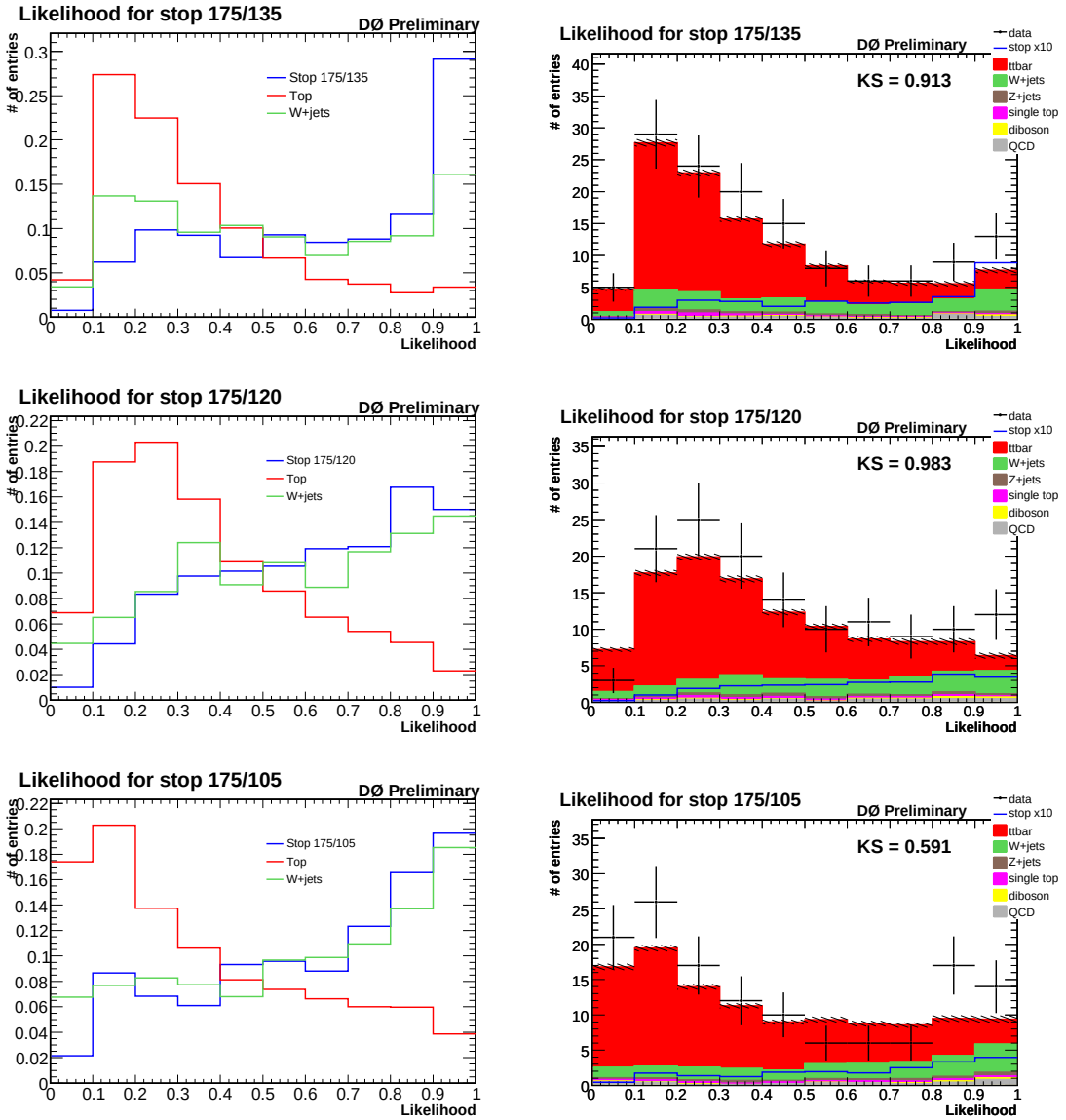

Figure C.19.: Likelihood discriminants in the μ+jets channel for different mass points. Top: Stop 175/135, middle: Stop 175/120, bottom: Stop 175/105.

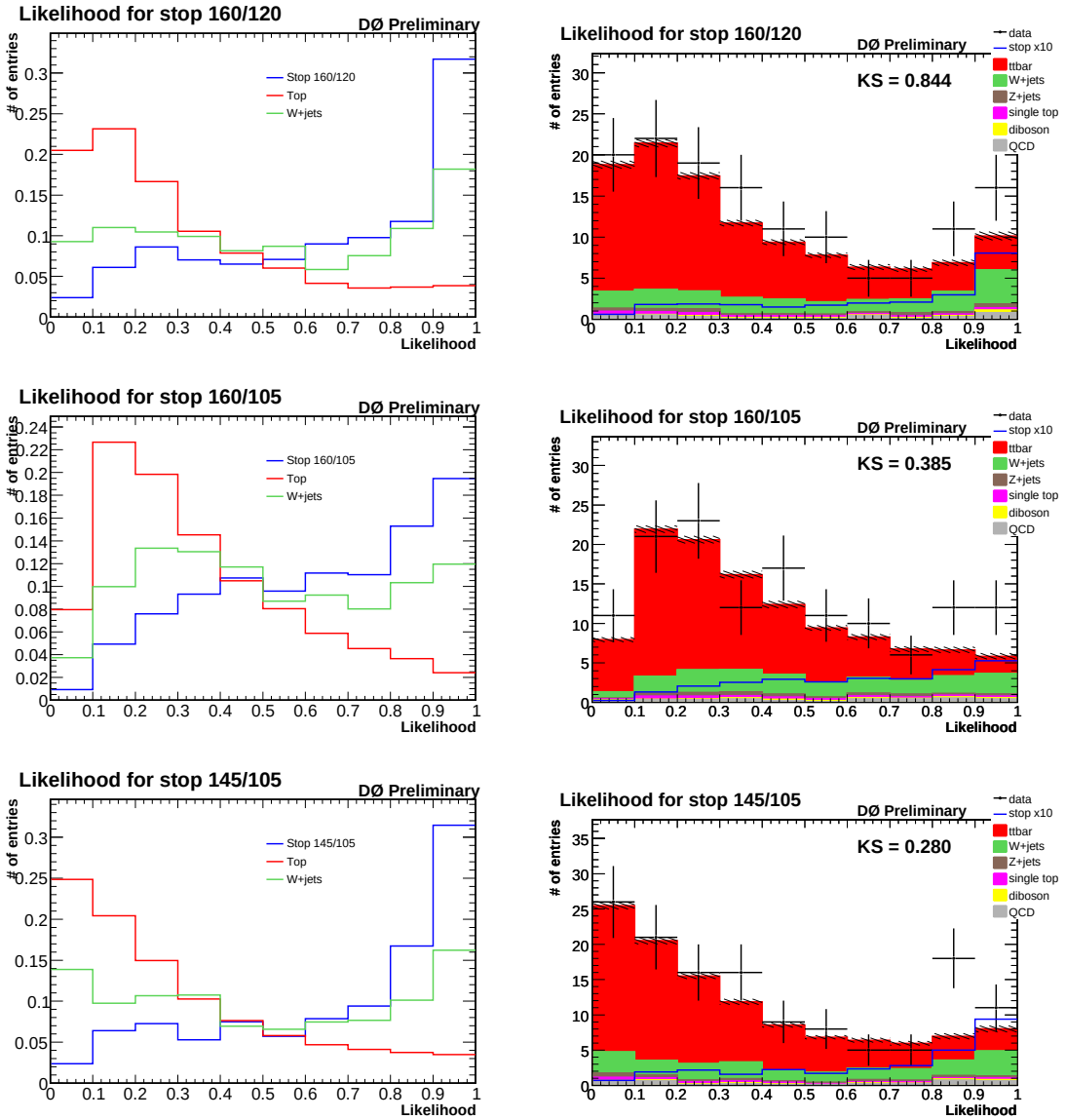

Figure C.20.: Likelihood discriminants in the μ+jets channel for different mass points. Top: Stop 160/120, middle: Stop 160/105, bottom: Stop 145/105.

D. Posterior Probabilities

This appendix shows the posterior probability funtions. The first part is dedicated to the expected ones that are extracted on a Monte Carlo sample with no signal conribution, and the second part to the observed ones measured on data. For each part there are two sets of plots. The first set shows the posterior probabilities as a function of the $\tilde{t}_1\bar{\tilde{t}}_1$ cross section, and the $t\bar{t}$ cross section is fixed to its theoretical value of 6.77 pb. The red solid line and number in each plot indicate the 95% confidence level limit. The second set of plots shows the posterior probabilities as a function of both the $\tilde{t}_1\bar{\tilde{t}}_1$ cross section and as a function of the $t\bar{t}$ cross section. In the latter case the red line indicates the most probable value for the $t\bar{t}$ cross section and the blue lines mark the 1σ band around it.

D.1. Expected Posterior Probabilities

The following plots show the expected posterior probabilities measured on a Monte Carlo sample with no signal contribution.

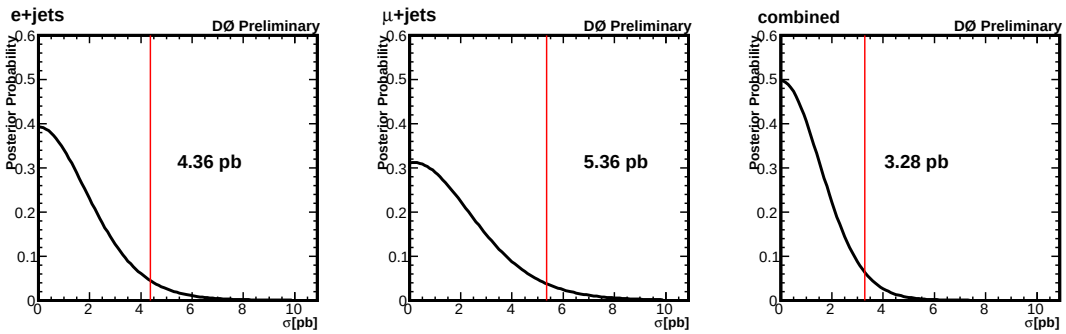

Figure D.1.: Expected posterior probability as a function of the $\tilde{t}_1\bar{\tilde{t}}_1$ cross section for the 175/135 mass point.

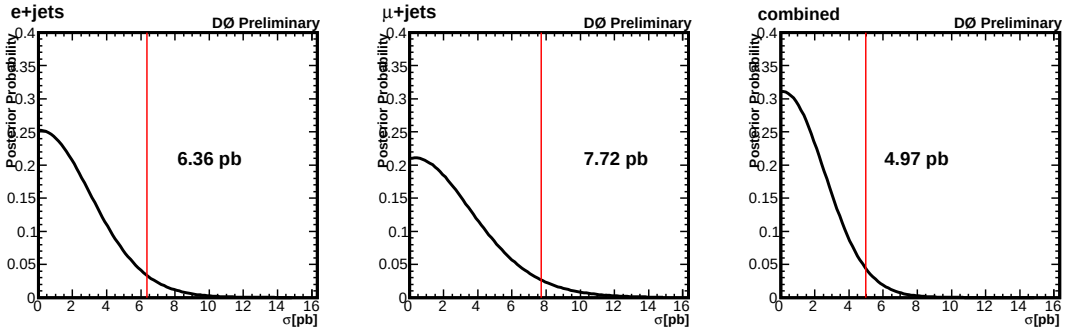

Figure D.2.: Expected posterior probability as a function of the $\tilde{t}_1\bar{\tilde{t}}_1$ cross section for the 175/120 mass point.

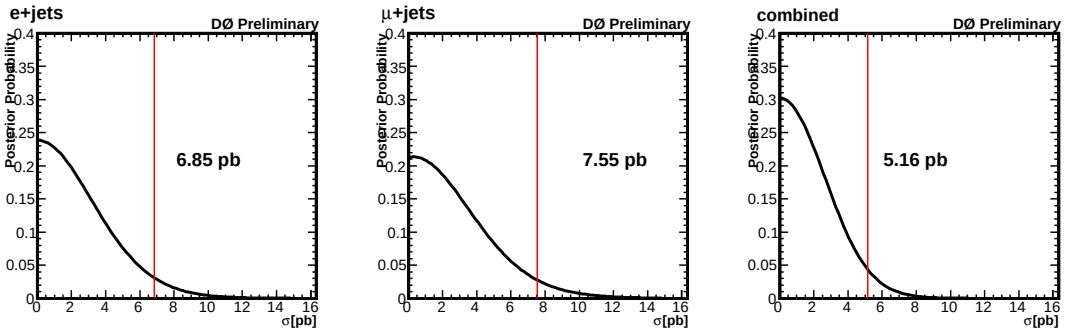

Figure D.3.: Expected posterior probability as a function of the $\tilde{t}_1\bar{\tilde{t}}_1$ cross section for the 175/105 mass point.

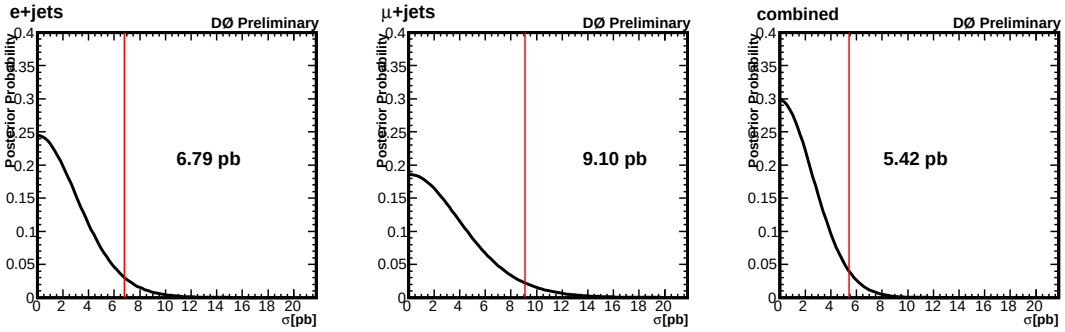

Figure D.4.: Expected posterior probability as a function of the $\tilde{t}_1\bar{\tilde{t}}_1$ cross section for the 160/120 mass point.

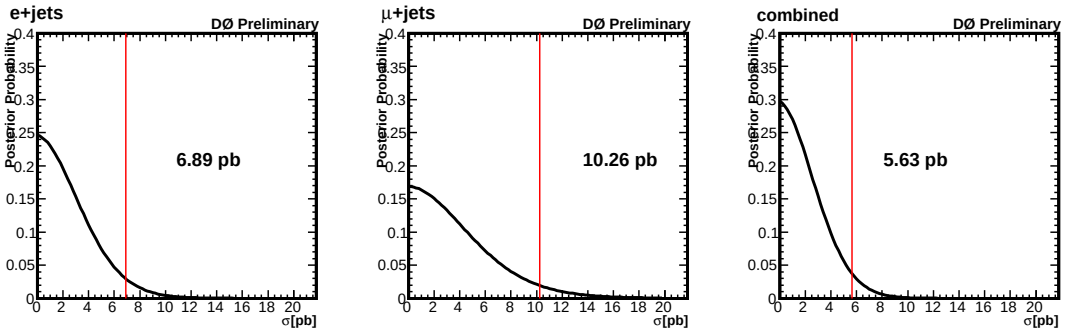

Figure D.5.: Expected posterior probability as a function of the $\tilde{t}_1\bar{\tilde{t}}_1$ cross section for the 160/105 mass point.

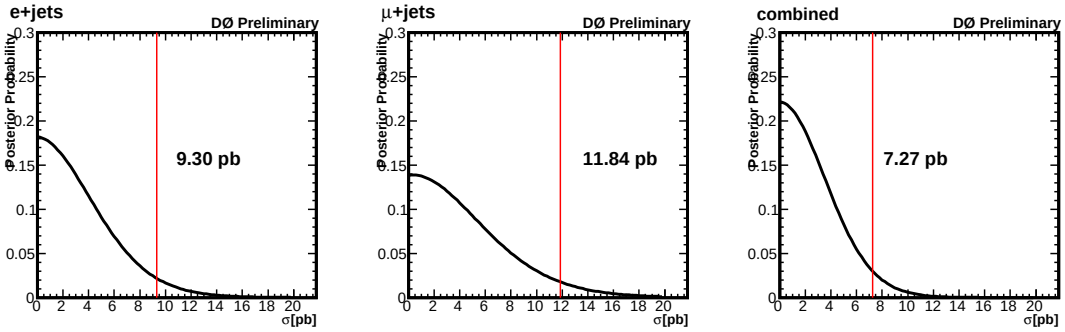

Figure D.6.: Expected posterior probability as a function of the $\tilde{t}_1\bar{\tilde{t}}_1$ cross section for the 145/105 mass point.

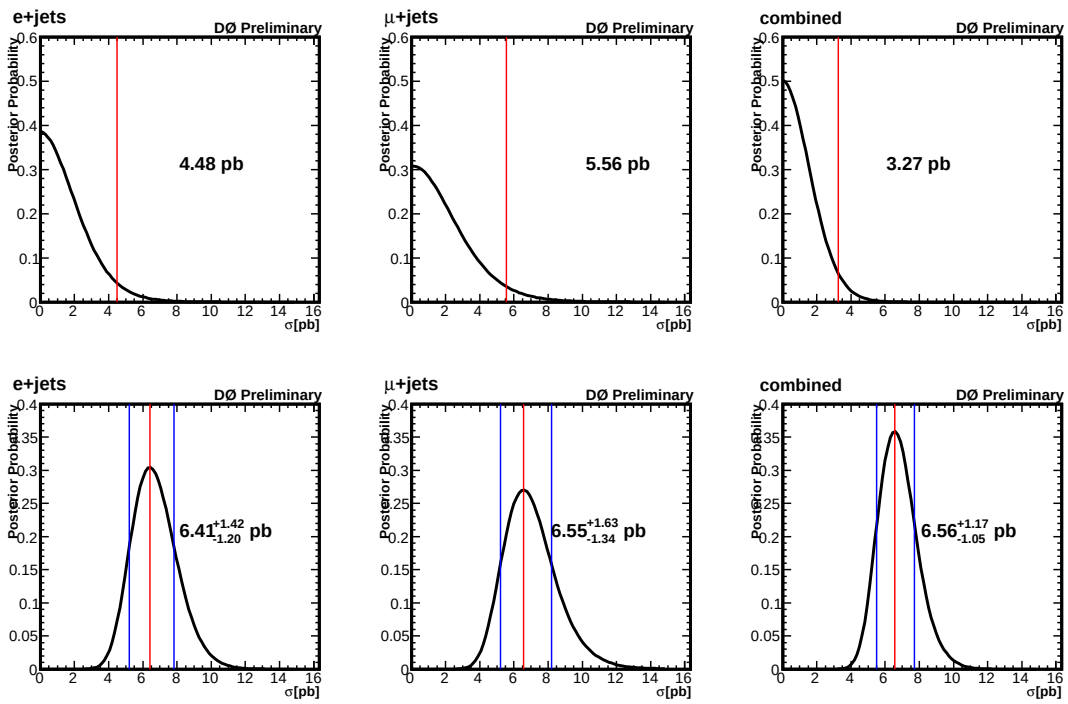

Figure D.7.: Expected posterior probability for the 175/135 mass point. Top: as a function of the $\tilde{t}_1\bar{\tilde{t}}_1$ cross section, bottom: as a function of the $t\bar{t}$ cross section.

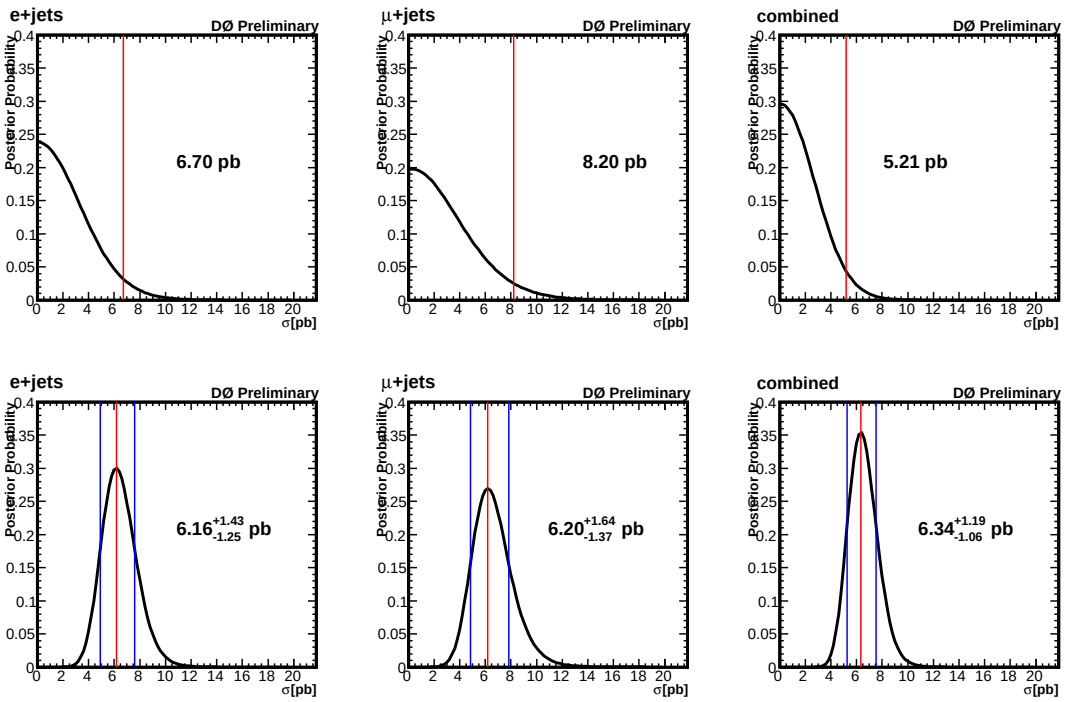

Figure D.8.: Expected posterior probability for the 175/120 mass point. Top: as a function of the $\tilde{t}_1\bar{\tilde{t}}_1$ cross section, bottom: as a function of the $t\bar{t}$ cross section.

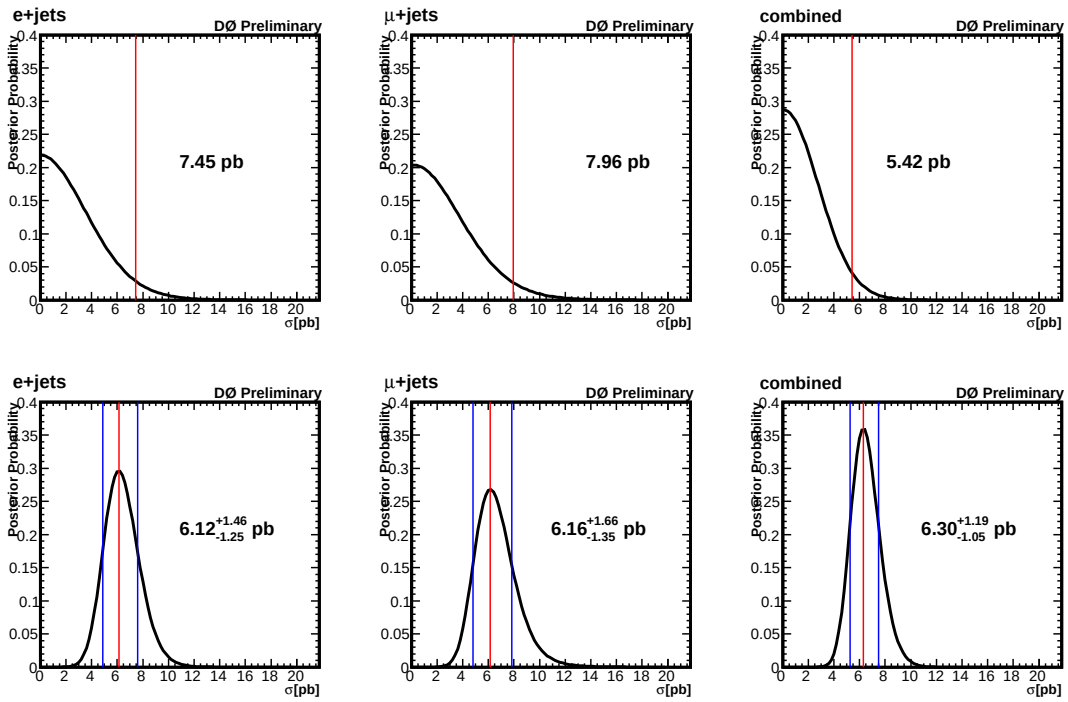

Figure D.9.: Expected posterior probability for the 175/105 mass point. Top: as a function of the $\tilde{t}_1\bar{\tilde{t}}_1$ cross section, bottom: as a function of the $t\bar{t}$ cross section.

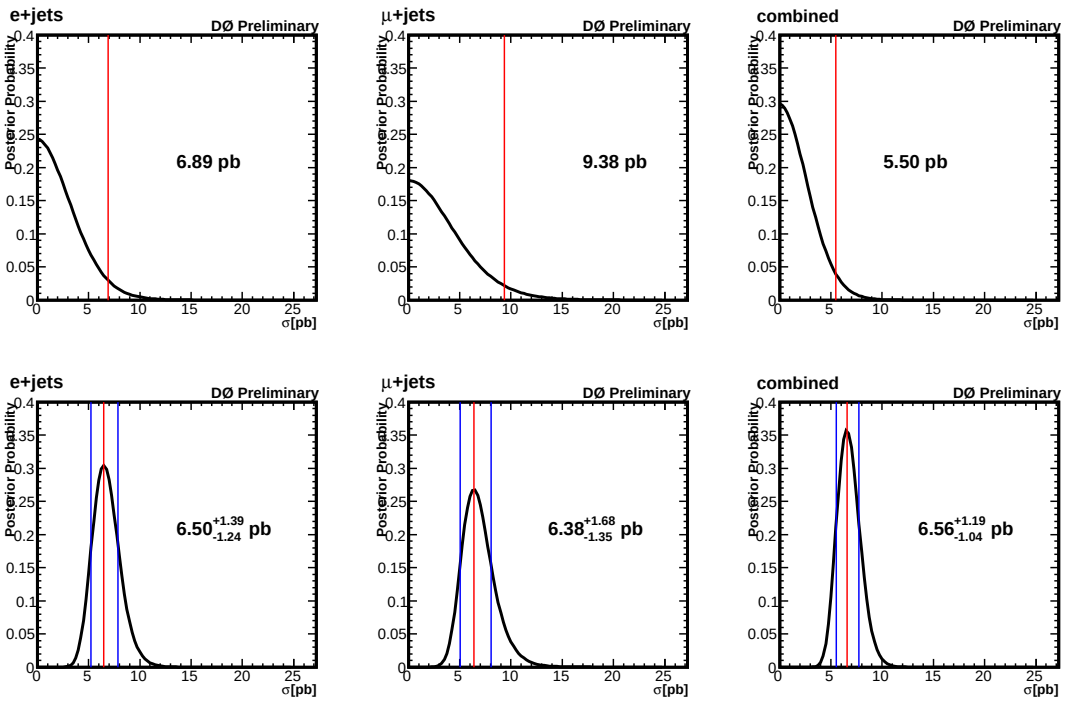

Figure D.10.: Expected posterior probability for the 160/120 mass point. Top: as a function of the $\tilde{t}_1\bar{\tilde{t}}_1$ cross section, bottom: as a function of the $t\bar{t}$ cross section.

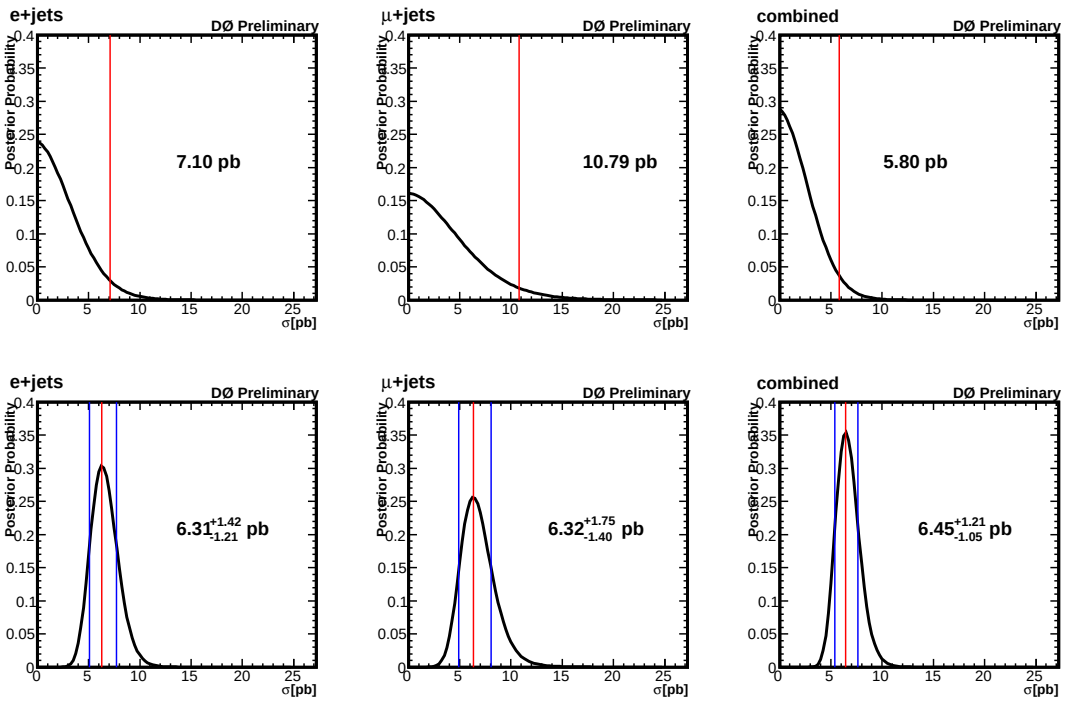

Figure D.11.: Expected posterior probability for the 160/105 mass point. Top: as a function of the $\tilde{t}_1\bar{\tilde{t}}_1$ cross section, bottom: as a function of the $t\bar{t}$ cross section.

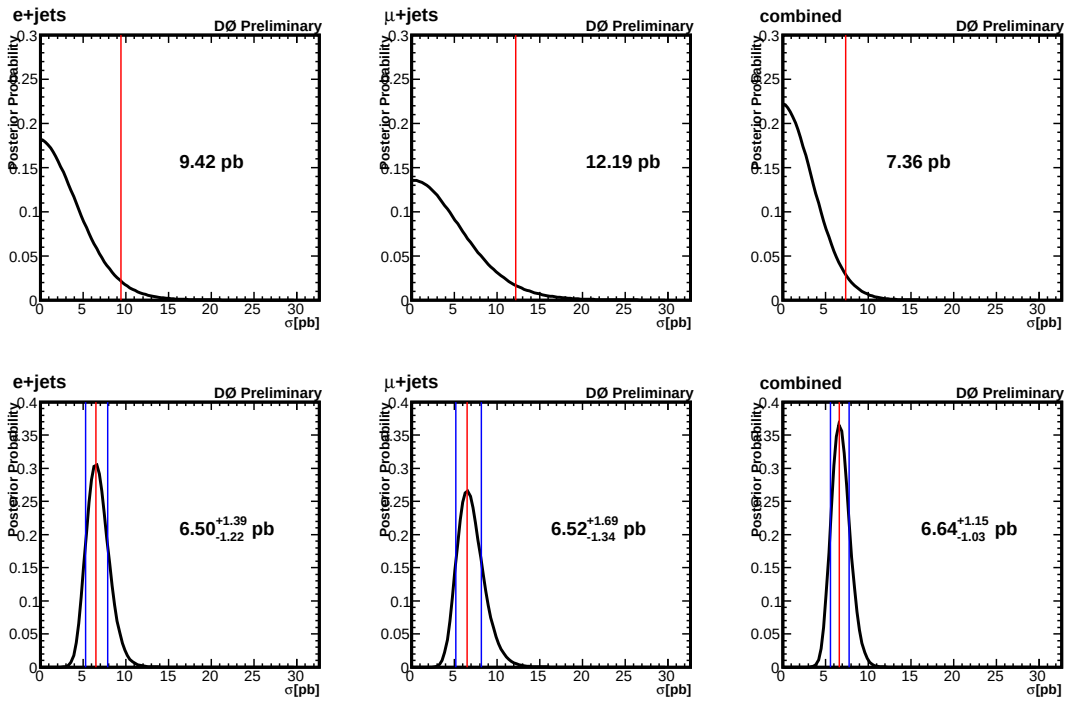

Figure D.12.: Expected posterior probability for the 145/105 mass point. Top: as a function of the $\tilde{t}_1\bar{\tilde{t}}_1$ cross section, bottom: as a function of the $t\bar{t}$ cross section.

D.2. Observed Posterior Probabilities

The following plots show the observed posterior probabilities measured on data.

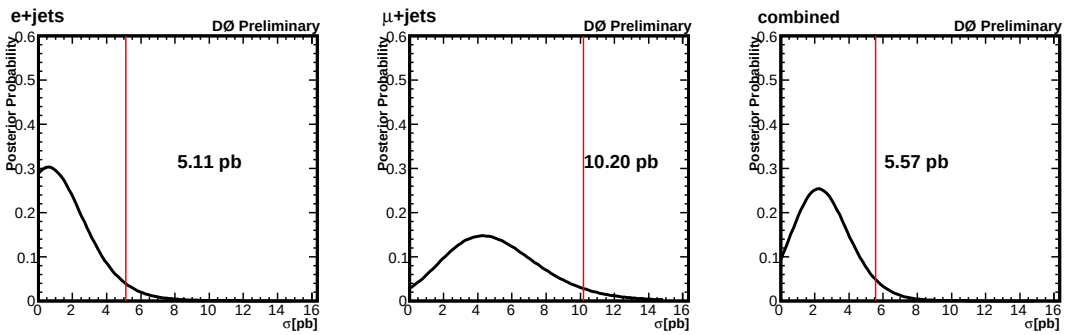

Figure D.13.: Observed posterior probability as a function of the $\tilde{t}_1\bar{\tilde{t}}_1$ cross section for the 175/135 mass point.

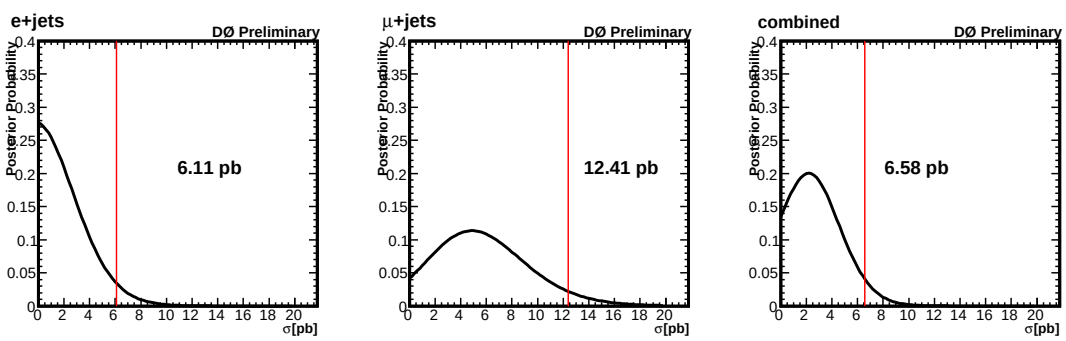

Figure D.14.: Observed posterior probability as a function of the $\tilde{t}_1\bar{\tilde{t}}_1$ cross section for the 175/120 mass point.

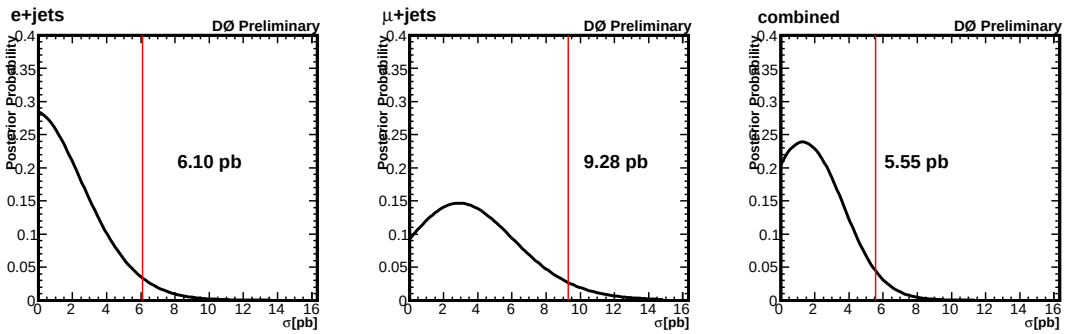

Figure D.15.: Observed posterior probability as a function of the $\tilde{t}_1\bar{\tilde{t}}_1$ cross section for the 175/105 mass point.

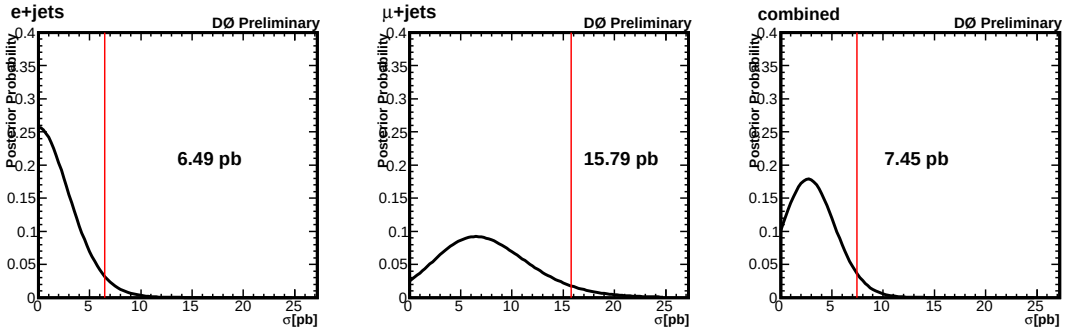

Figure D.16.: Observed posterior probability as a function of the $\tilde{t}_1\bar{\tilde{t}}_1$ cross section for the 160/120 mass point.

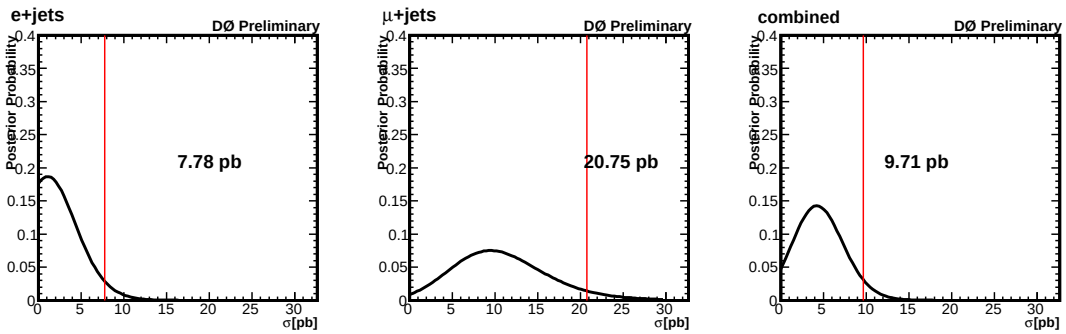

Figure D.17.: Observed posterior probability as a function of the $\tilde{t}_1\bar{\tilde{t}}_1$ cross section for the 160/105 mass point.

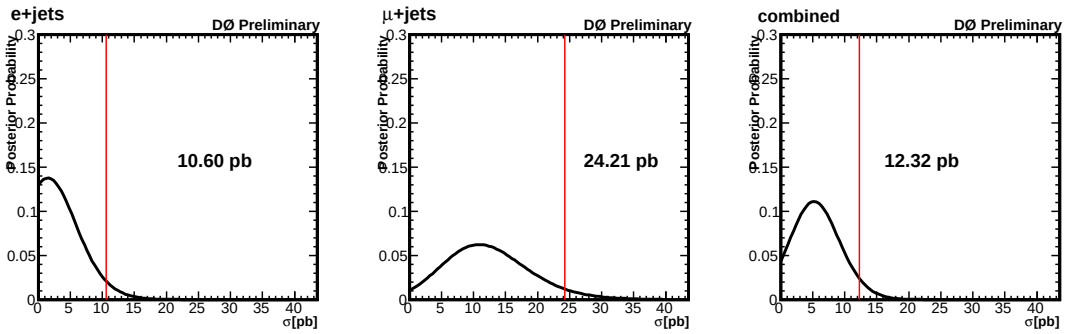

Figure D.18.: Observed posterior probability as a function of the $\tilde{t}_1\bar{\tilde{t}}_1$ cross section for the 145/105 mass point.

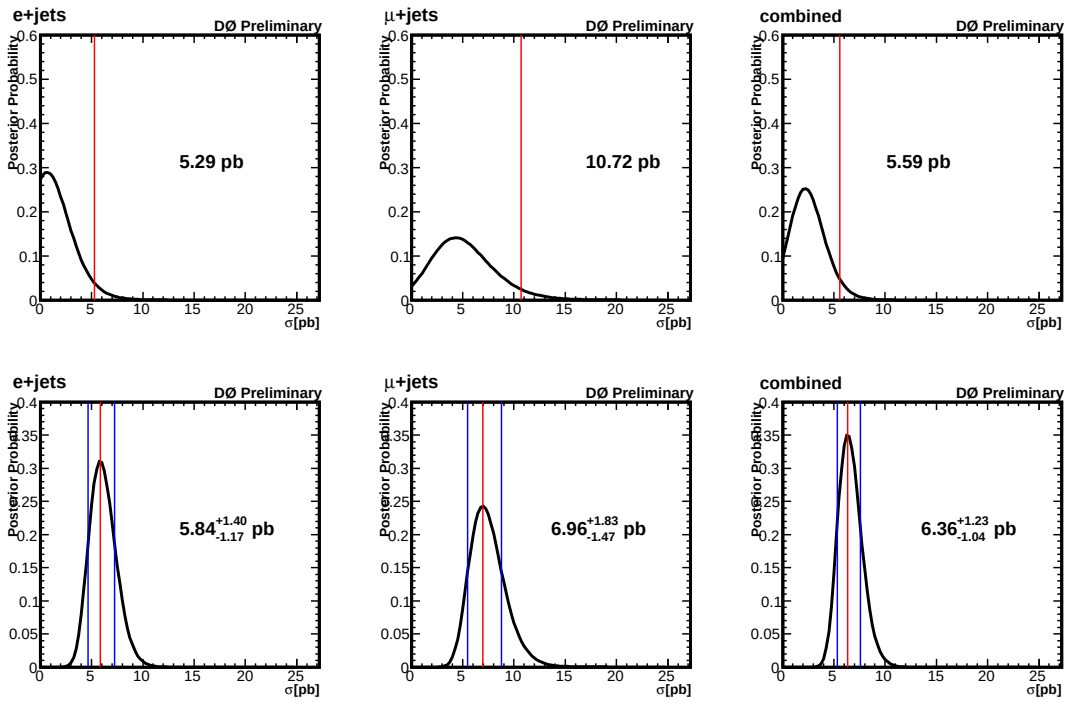

Figure D.19.: Observed posterior probability for the 175/135 mass point. Top: as a function of the $\tilde{t}_1\bar{\tilde{t}}_1$ cross section, bottom: as a function of the $t\bar{t}$ cross section.

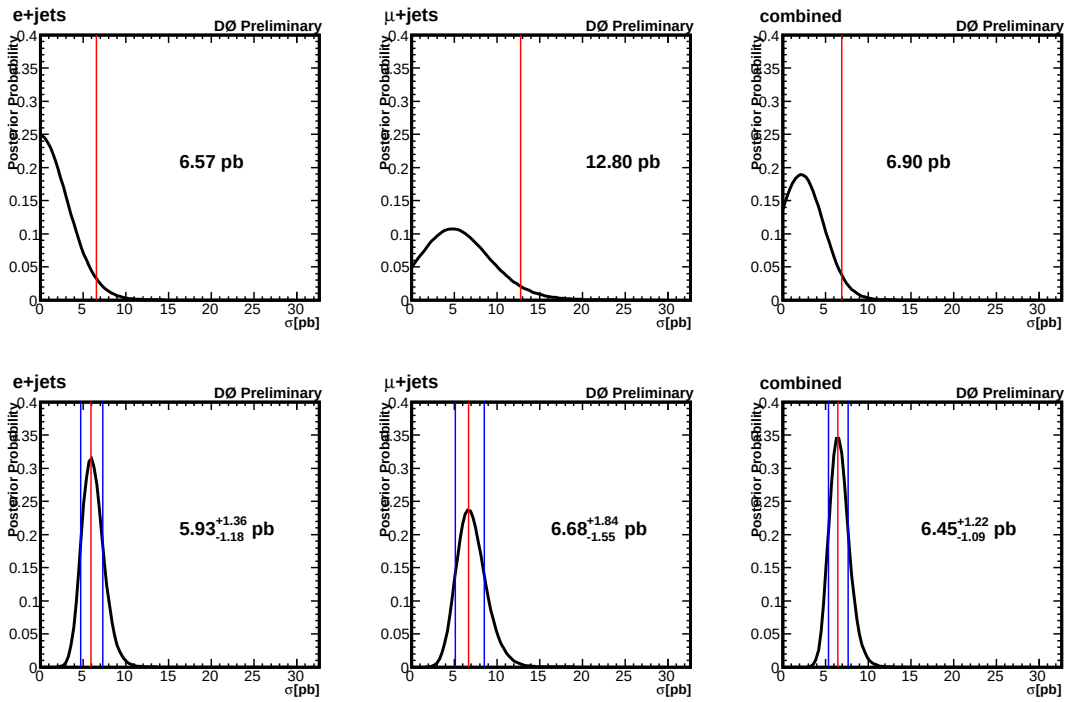

Figure D.20.: Observed posterior probability for the 175/120 mass point. Top: as a function of the $\tilde{t}_1\bar{\tilde{t}}_1$ cross section, bottom: as a function of the $t\bar{t}$ cross section.

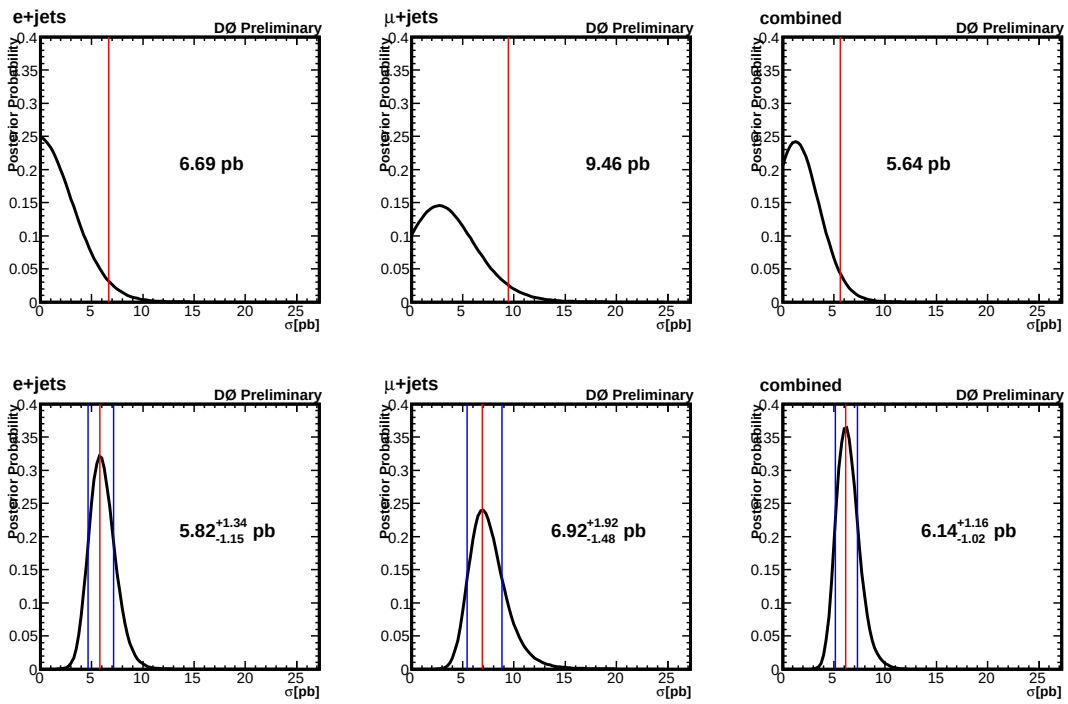

Figure D.21.: Observed posterior probability for the 175/105 mass point. Top: as a function of the $\tilde{t}_1\bar{\tilde{t}}_1$ cross section, bottom: as a function of the $t\bar{t}$ cross section.

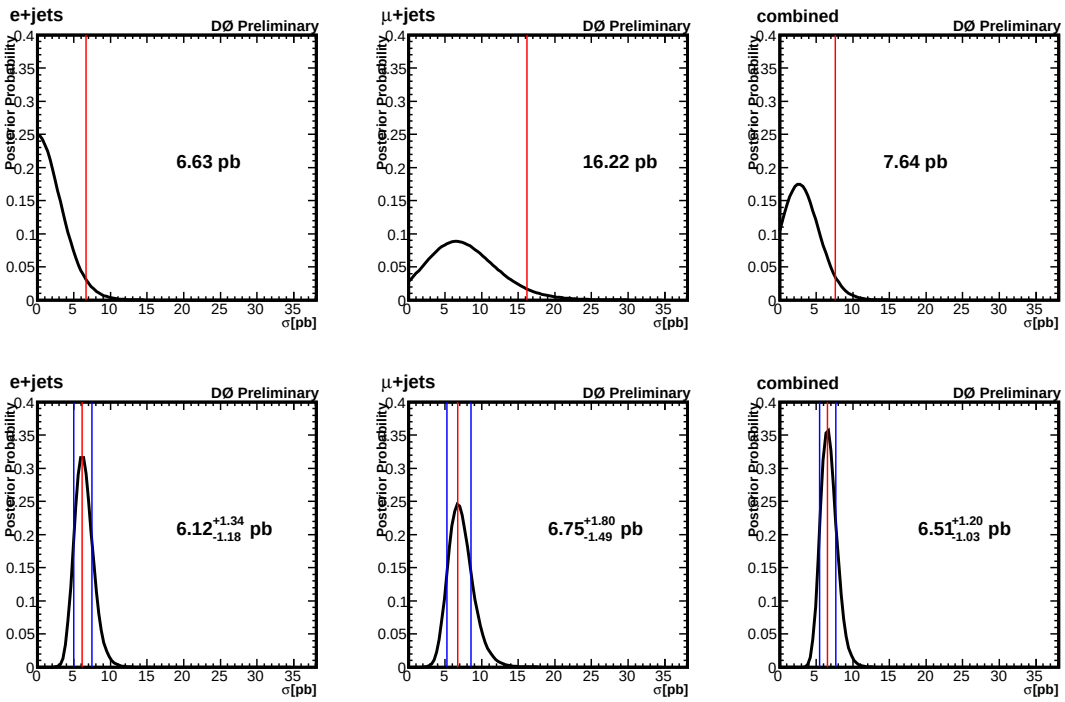

Figure D.22.: Observed posterior probability for the 160/120 mass point. Top: as a function of the $\tilde{t}_1\bar{\tilde{t}}_1$ cross section, bottom: as a function of the $t\bar{t}$ cross section.

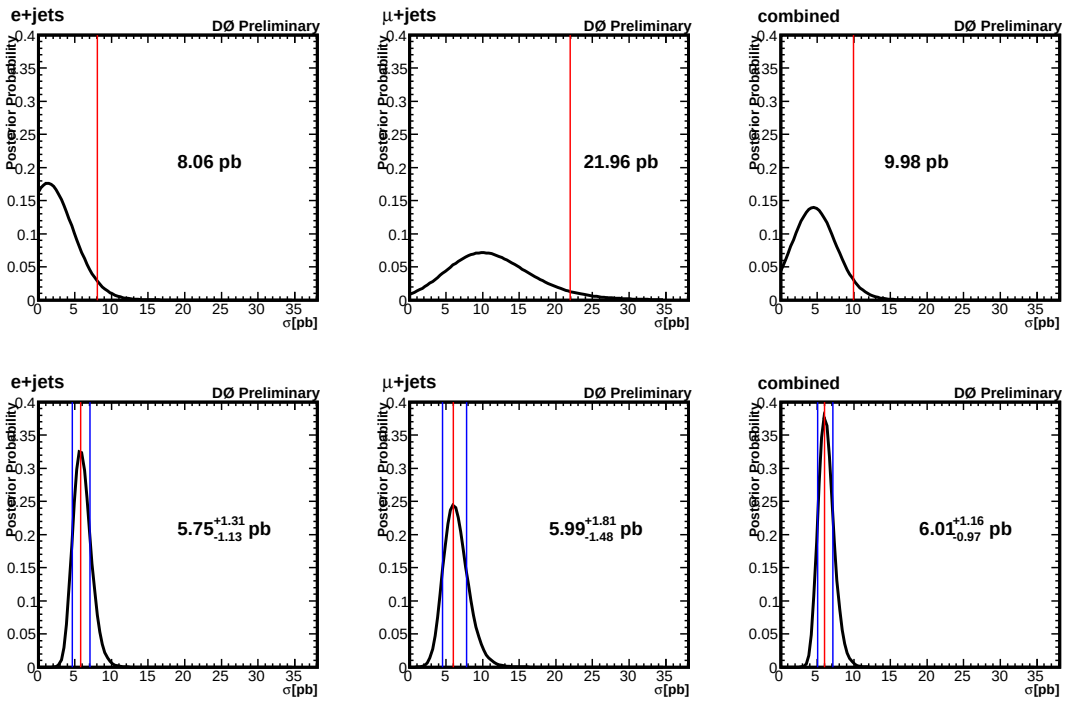

Figure D.23.: Observed posterior probability for the 160/105 mass point. Top: as a function of the $\tilde{t}_1\bar{\tilde{t}}_1$ cross section, bottom: as a function of the $t\bar{t}$ cross section.

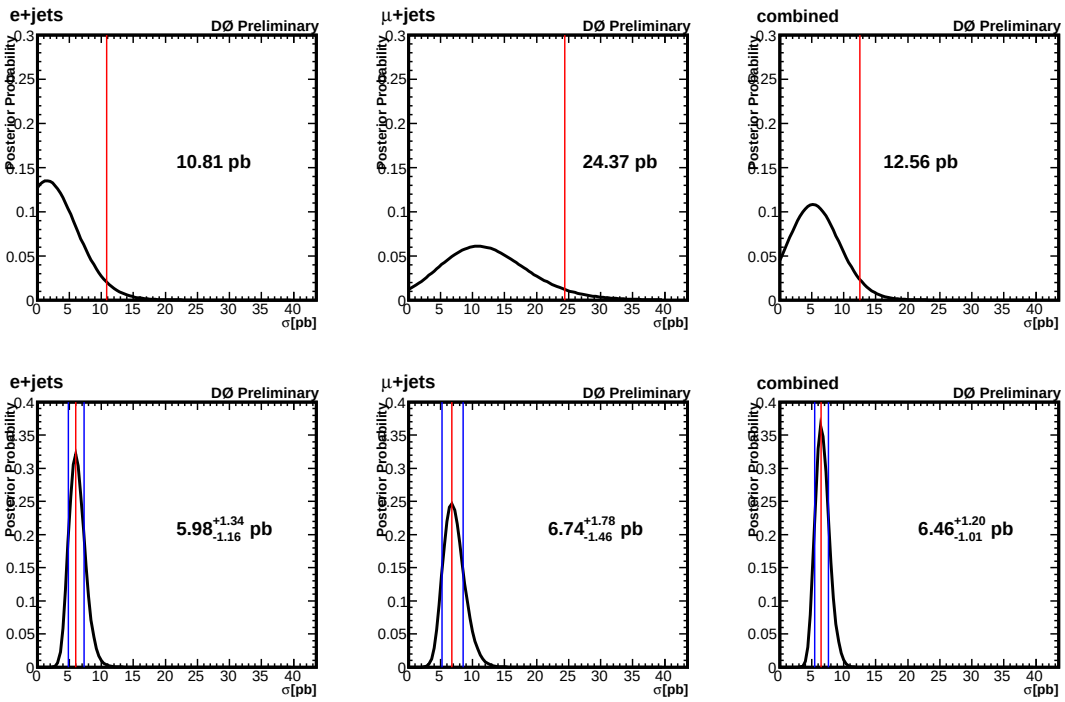

Figure D.24.: Observed posterior probability for the 145/105 mass point. Top: as a function of the $\tilde{t}_1\bar{\tilde{t}}_1$ cross section, bottom: as a function of the $t\bar{t}$ cross section.

E. Results of Ensemble Tests

This appendix displays the results of the ensemble tests for all signal mass points. The first set of plots shows the distributions of the measured limits in the pseudo datasets without any signal content. The second set shows the distributions of the measured cross sections in the pseudo datasets with ten times the theoretical signal content.

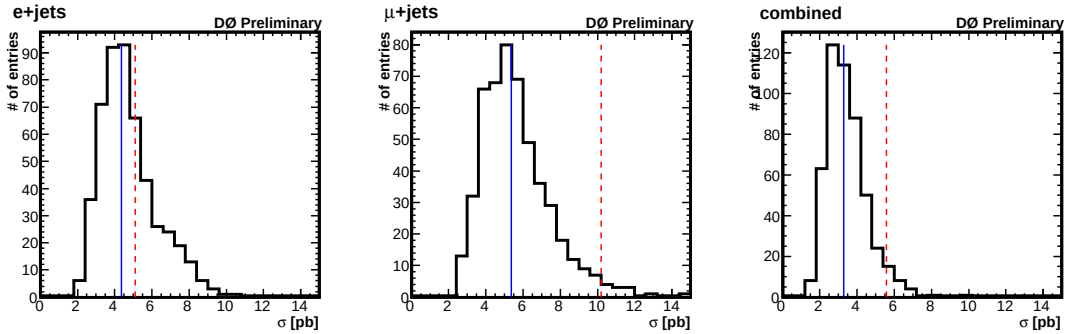

Figure E.1.: Results for limits in experiments with no signal content for the 175/135 mass point. The expected limit is shown as solid blue line, the observed limit is shown as dashed red line.

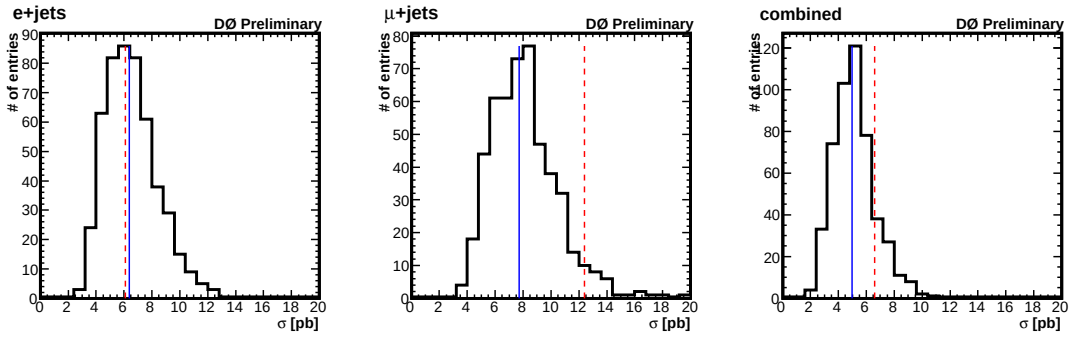

Figure E.2.: Results for limits in experiments with no signal content for the 175/120 mass point. The expected limit is shown as solid blue line, the observed limit is shown as dashed red line.

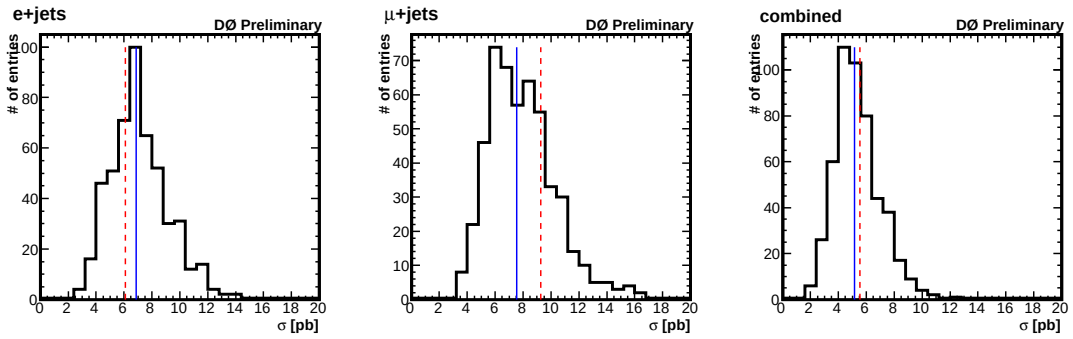

Figure E.3.: Results for limits in experiments with no signal content for the 175/105 mass point. The expected limit is shown as solid blue line, the observed limit is shown as dashed red line.

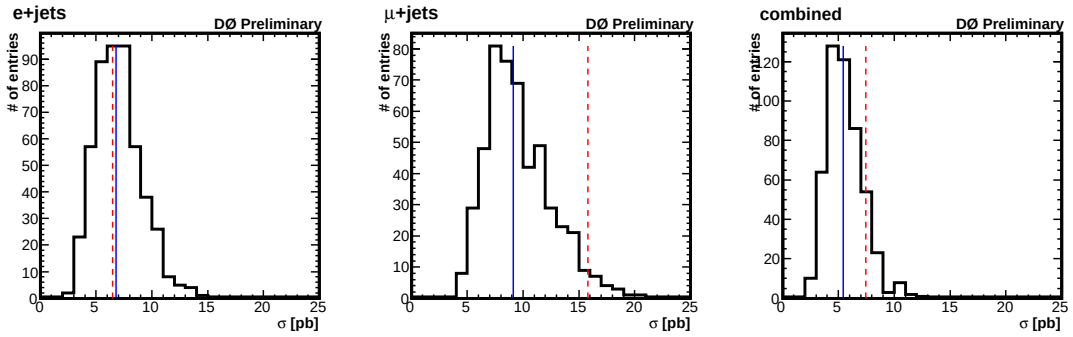

Figure E.4.: Results for limits in experiments with no signal content for the 160/120 mass point. The expected limit is shown as solid blue line, the observed limit is shown as dashed red line.

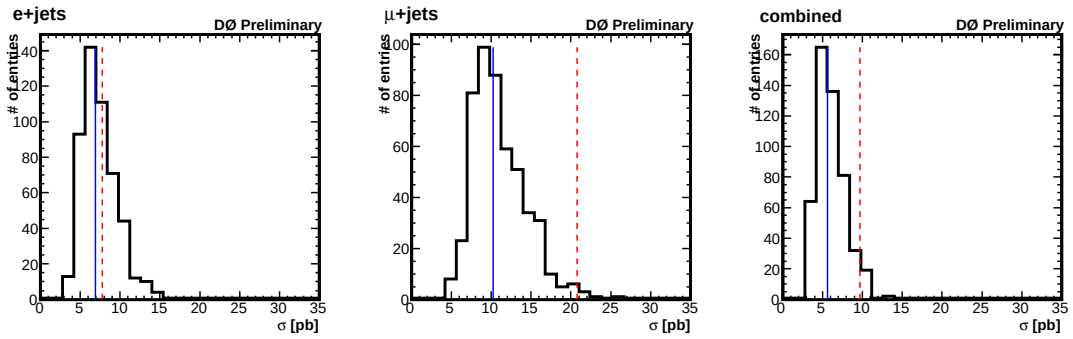

Figure E.5.: Results for limits in experiments with no signal content for the 160/105 mass point. The expected limit is shown as solid blue line, the observed limit is shown as dashed red line.

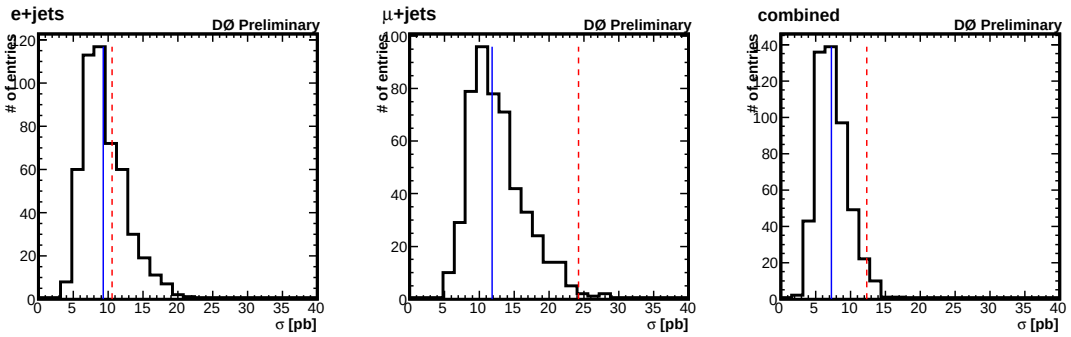

Figure E.6.: Results for limits in experiments with no signal content for the 145/105 mass point. The expected limit is shown as solid blue line, the observed limit is shown as dashed red line.

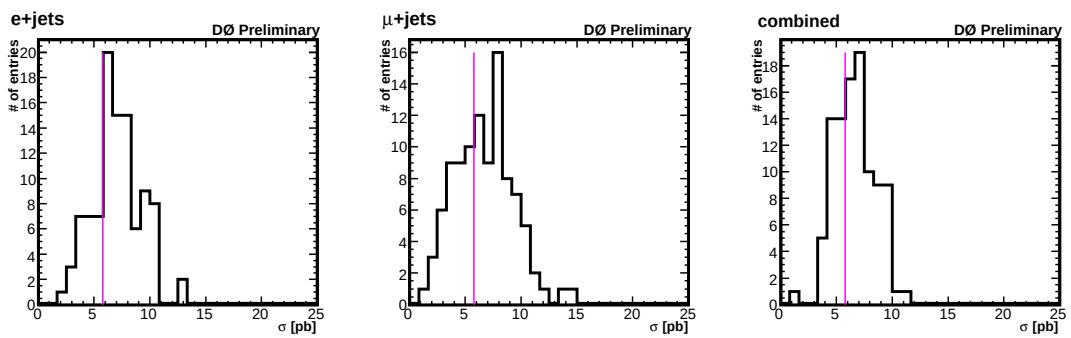

Figure E.7.: Results for cross sections in experiments when the theoretical signal content for the 175/135 mass point is raised by a factor of ten. The input cross section is shown as purple line.

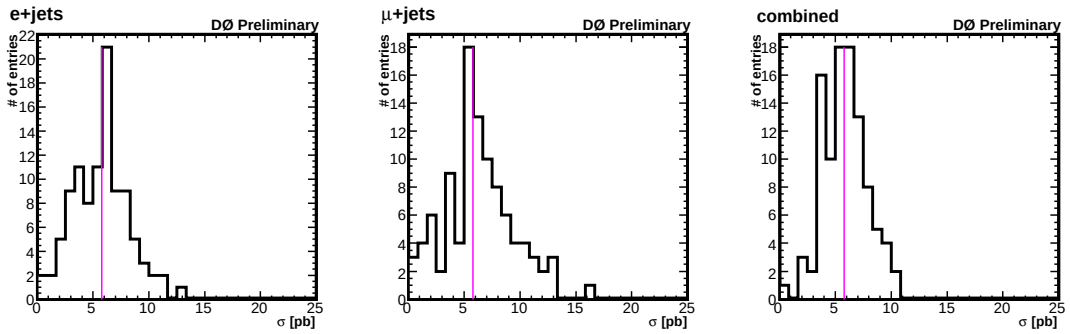

Figure E.8.: Results for cross sections in experiments when the theoretical signal content for the 175/120 mass point is raised by a factor of ten. The input cross section is shown as purple line.

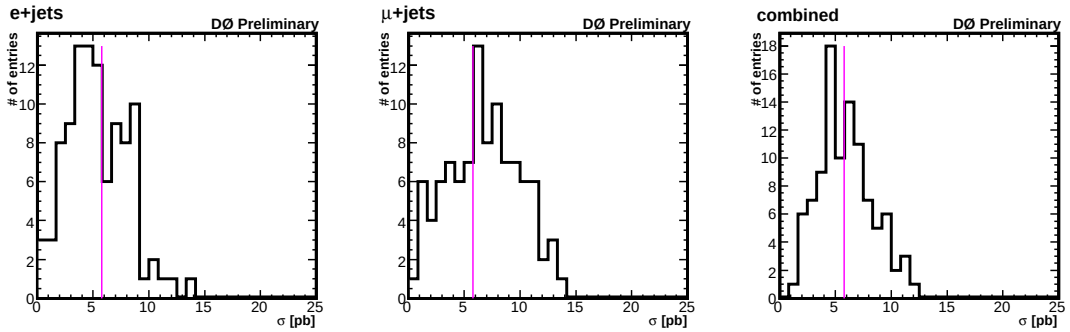

Figure E.9.: Results for cross sections in experiments when the theoretical signal content for the 175/105 mass point is raised by a factor of ten. The input cross section is shown as purple line.

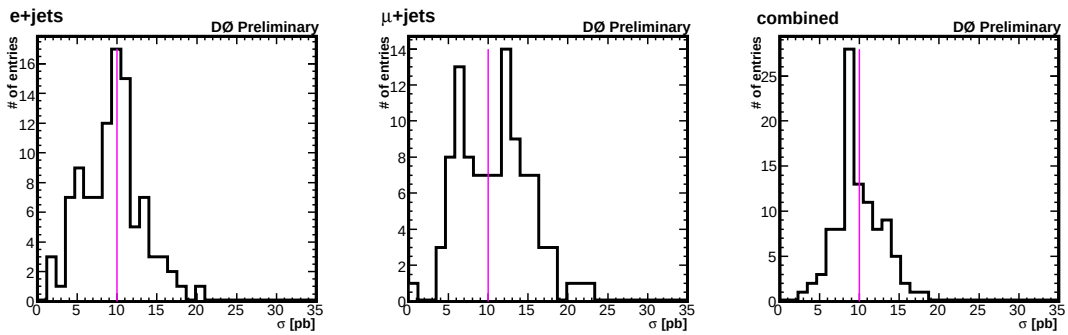

Figure E.10.: Results for cross sections in experiments when the theoretical signal content for the 160/120 mass point is raised by a factor of ten. The input cross section is shown as purple line.

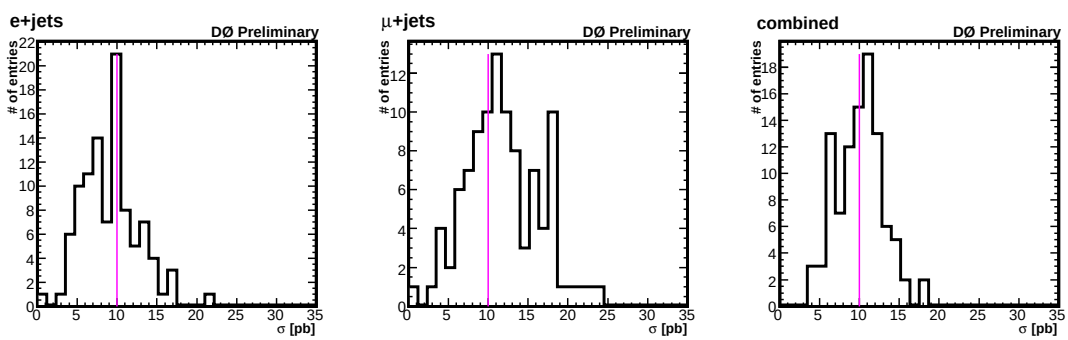

Figure E.11.: Results for cross sections in experiments when the theoretical signal content for the 160/105 mass point is raised by a factor of ten. The input cross section is shown as purple line.

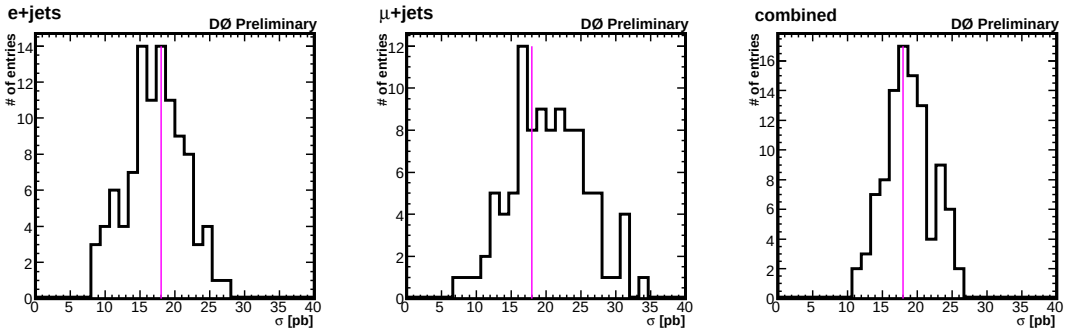

Figure E.12.: Results for cross sections in experiments when the theoretical signal content for the 145/105 mass point is raised by a factor of ten. The input cross section is shown as purple line.